Drag Reduction Performance and Turbulent Structure of Polymeric Solutions in Wall-bounded Turbulent Flows

by

Mohammad Mohammadtabar

A thesis submitted in partial fulfillment of the requirements for the degree of

Doctor of Philosophy

Department of the Mechanical Engineering

University of Alberta

Abstract

The higher drag of turbulent flows relative to laminar flows requires greater pumping power and results in a higher transportation cost. For this reason, reducing drag in turbulent pipe flows is of interest. Among various methods, the use of long-chain polymers has attracted more attention due to the small quantity of polymer required for drag reduction (DR). This technique was used in the Alaska oil pipeline, where the operators saved about $300 million per year through reduced pumping costs. Drag reducing polymers can have a flexible or a rigid molecular structure. Most biopolymers are categorized as rigid polymers. The general objective of this research is to investigate potential use of biopolymers instead of the commonly used synthetic polymers. To achieve this goal, the comparison of drag reduction performance and mechanisms of flexible and rigid polymers is necessary. Several techniques were used for the investigations including pressure loss measurements in flow loops to characterize drag reduction, rheometers for measuring shear and extensional viscosity, and a planar and stereoscopic particle image velocimetry (PIV) for characterization of turbulent structures in polymer solutions. It was observed that drag reduction was proportional to the relaxation time and Weiseenberg number. Polymer solutions with larger ratio of storage over loss modulus also led to a larger DR due to their stronger elastic behavior. In turbulent channel flow, the spatial correlation of the fluctuating velocity field shows that increasing polymer concentration increases the spatial coherence of streamwise fluctuations in the streamwise direction while they appear to have opposite sign in the wall-normal direction. The proper orthogonal decomposition (POD) of velocity fluctuations shows that the inclined shear layer structure of Newtonian wall flows becomes horizontal at the point of maximum drag reduction (MDR) and does not contribute to turbulence production. The investigations of rigid and flexible polymer solutions at a similar DR showed different profiles of

streamwise Reynolds stress, while wall-normal Reynolds stresses and Reynolds shear stresses of polymer solutions were approximately the same. In addition, turbulent structures of one solution (SF polymers) at MDR were experimentally characterized. At MDR, the low and high speed streaks were elongated and thickened relative to those found in a turbulent Newtonian flow.

The comparison of drag reduction performance and turbulent structures of rigid and flexible polymers (even at the same DR) showed the availability of different drag reduction mechanisms in polymer solutions with different molecular structures. To further investigate the effect of flexible and rigid polymers on turbulent structures, tomographic PIV can be used to characterize important parameters such as production and dissipation term of kinetic energy budget of turbulence. By using these measurements, drag reduction mechanisms existed in the literature can be effectively evaluated and a potential new drag reduction mechanism can be developed.

Preface

This thesis includes the design and construction of pipe and channel flow loops, the experimental investigation of DR mechanisms, and rheology measurements.

The design and construction of pipe and channel flow loops are carried out by the author under supervision of Dr. Sina Ghaemi and Dr. Sean Sanders and explained in Chapter 3.

All the experiments including pressure drop measurements, the planar and stereo PIV measurements, data analysis, and interpretation of results are conducted by the author under supervision of Dr. Sina Ghaemi and Dr. Sean Sanders and clarified in Chapters 3-6.

All rheology measurements are carried out by the author under the supervision of Dr. Sina Ghaemi and Dr. Sean Sanders, except the extensional viscosity measurements which were carried out by Dr. Bayode Owolabi at the Department of Civil and Environmental Engineering of the University of Alberta. All the results are presented in Chapters 4-6.

Some of the results (Chapter 5) are published in "Physics of Fluids" journal as follows:

"Reproduced from [M. Mohammadtabar, R.S. Sanders, S. Ghaemi, "Turbulent structures of non-Newtonian solutions containing rigid polymers," Physics of Fluids 29, 103101 (2017).], with the permission of AIP Publishing."

Acknowledgement

To my late mother Tahereh Nemati, I know you waited a long time for my PhD graduation and my deepest regret is that I couldn’t make it when you were among us. I really appreciate all your encouragement and support.

I would like to express my deepest gratitude to my supervisors Dr. Sina Ghaemi and Dr. Sean Sanders for their guidance, advice, and support.

I would like to gratefully acknowledge financial support provided by Natural Sciences and Engineering Research Council of Canada (NSERC) and Alberta Innovates-Technology Futures (AITF), also the NSERC Industrial Research Chair in Pipeline Transport Process (PTP) for providing the funding for the work.

I am grateful to my colleague, Masoud Ebrahimian, who helped me to go through the last series of my PhD experiments.

My special gratitude goes out to my wife, Neda, my daughter, Deniz and my son, Dara, for their support and patience throughout my PhD program.

Contents

List of Figures

List of Tables

Nomenclature

a^k	Temporal coefficient of proper orthogonal decomposition
C_f	Friction coefficient
C_{uu}	Spatial correlation of streamwise velocity fluctuation
C_{vv}	Spatial correlation of wall-normal velocity fluctuation
D_{mid}	Midpoint diameter of the filament (m)
F_z	Tensile force (N)
G	Elasticity modulus (Pa)
G^*	Viscoelasticity modulus (Pa)
G'	Storage modulus (Pa)
G''	Loss modulus (Pa)
H	Height of channel (m)
Re	Reynolds number
U, V, W	Streamwise, wall-normal, and spanwise mean velocity profiles (m/s)
u, v, w	Streamwise, wall-normal, and spanwise velocity fluctuations (m/s)
U^+, V^+, W^+	Mean velocity profiles normalized with friction velocity
u^+, v^+, w^+	Velocity fluctuations normalized with friction velocity
u_τ	Friction velocity (m/s)
W_C	Width of channel (m)
x, y, z	Streamwise, wall-normal, and spanwise coordinate system (m)
$\langle \rangle$	Ensemble average

Greek Letters

ΔP_p	Pressure drop of polymer solutions (Pa)
ΔP_w	Pressure drop of water (Pa)
δ_υ	Wall unit (m)
ε	Hencky strain
$\dot{\varepsilon}$	Strain rate (1/s)
η_e	Extensional viscosity (Pa.s)
η_s	Solvent kinematic viscosity (m^2/s)

ρ	Density of fluid (kg/m^3)
σ	Surface tension (Pa)
τ_0	Sinusoidal stress (Pa)
τ_{21}	Stress amplitude
τ_w	Shear stress at the wall (Pa)
$\langle\tau_p\rangle$	Polymer stress (Pa)
$\langle\tau_{Re}\rangle$	Reynolds stress (Pa)
$\langle\tau_s\rangle$	Viscous stress (Pa)
λ	Relaxation time (S)
μ_w	Shear viscosity at the wall (Pa.s)
μ_s	Solvent shear viscosity (Pa.s)
φ^k	Normalized mode
ω	Angular frequency (rad/s)
ω_x, ω_y, ω_k	Streamwise, wall-normal, and spanwise vorticity fluctuations (1/s)

List of Abbreviations

CaBER	Capillary break-up extensional rheometer
CMC	Carboxymethyl cellulose
DR	Drag reduction
HDR	High drag reduction
JPDF	Joint probability density function
LDV	Laser doppler velocimetry
LDR	Low drag reduction
MDR	Maximum drag reduction
PAM	Polyacrylamide
PEO	Polyethylene Oxide
PIB	Polyisobutylene
PIV	Particle image velocimetry
POD	Proper orthogonal decomposition
XG	Xanthan gum
SF	SuperFloc
SNR	Signal to noise ratio
SOC	Sum of Correlation

Chapter 1. Introduction

Turbulent pipe flows play an important role in firefighting, irrigation, sewers, heating and cooling, and long distance oil transport (Han & Choi 2017). The higher drag of turbulent flows compared to laminar flow requires greater pumping power and results in a higher transportation cost. There are several additives for drag reduction in liquid flows such as fibers, surfactants, micro-bubbles, and polymers. The latter has been the most common technique used in oil pipelines because small quantities of polymer can significantly reduce drag (Abubakar *et al.* 2014). For example, Warholic *et al.* (2001) observed 43% drag reduction (DR) using 1.24 part per million (ppm) of a long-chain polymer, while DR as large as 80% was obtained by Virk (1975) using only 110 ppm.

The DR amount depends on several parameters such as concentration, molecular structure, chain flexibility, and molecular weight (MW) of the polymer, and solvent properties such as its temperature, pH, and salt content. There is some consensus in the literature regarding the effect of some of these parameters. It is known that DR increases with increase of polymer concentration up to an optimum concentration; above this concentration, DR decreases due to increasing solution shear viscosity (Abubakar *et al.* 2014; Hoyt 1989). Virk (1975) observed that DR is larger for polymers with greater molecular weight (i.e., longer chain). The effect of temperature has been observed to depend on the structure of the polymer: when temperature was increased from 5 to 35ºC, Interthal & Wilski (1985) observed that DR using polyethylene oxide (PEO) decreased from 70 to 50% while DR using polyacrylamide (PAM) did not change. Pereira & Soares (2012) observed similar variations of DR due to changes in concentration, molecular weight, and temperature for PAM and PEO through extensive tests using a double-gap cylindrical geometry.

Polymers are generally classified as flexible or rigid polymers, based on their molecular structure. Examples of flexible polymers include PAM and PEO, while the typical rigid polymers used for DR include xanthan gum (XG), and Carboxymethyl cellulose (CMC). Sandoval *et al.* (2015) and Soares *et al.* (2015a) investigated DR and degradation of both flexible and rigid polymers (PEO, PAM, and XG) in a pipe flow. They concluded that the flexible polymers provide better DR than rigid polymers, while deterioration in performance of the rigid polymers due to mechanical degradation was negligible in comparison with flexible polymers.

Two different mechanisms have been proposed to explain DR using polymers in turbulent flows. The first mechanism is based on the larger extensional viscosity of a drag-reducing solution and the second mechanism is based on the viscoelastic properties of the solution. Lumley (1969) hypothesized that, due to the stretching of polymer molecules in a turbulent flow, the extensional component of viscosity is large and damps the turbulence fluctuations (Teng *et al.* 2018). This hypothesis has been challenged since strain rate in a turbulent flow fluctuates, and therefore, the molecules can coil back when strain rate decreases (White & Mungal 2008). De Gennes (1986) proposed the second mechanism, in which DR is associated with the viscoelastic properties of the polymer solution. According to this theory, the partially stretched molecules absorb the turbulent kinetic energy in the near-wall region, and release it farther away from the wall where the strain rate is small. This mechanism is hypothesized to terminate the turbulent energy cascade at a larger length scale relative to dissipative scale of a Newtonian turbulent flow (White & Mungal 2008). However, these DR mechanisms have been proposed for flexible polymers, and their validity for rigid polymers with negligible chain flexibility has yet to be evaluated (Pereira *et al.* 2013).

It is currently of interest to replace synthetic polymers with biopolymers, such as Guar Gum, Xanthan Gum (XG), Okra, Aloe Vera, and Glycogen. Biopolymers are generated from living organisms and are bio degradable, i.e. they break down into natural products such as water, gases, and salts. Therefore, the use of biopolymers results in the reduction of the environmental footprint associated with the producing, consuming and disposal of drag-reducing polymers. The general objective of this research is to investigate potential use of bio polymers with rigid structure, along with the associated drag reduction mechanism. To achieve this goal, comparing the DR mechanism of both rigid and flexible polymers is necessary. The thesis aims to experimentally investigate DR mechanisms of rigid and flexible polymer solutions through characterization of solution rheology and PIV measurements. As a first step, dependency of DR on the rheology for both polymer solutions is investigated. The rheology of polymer solutions involves measuring shear viscosity, extensional viscosity, and viscoelastic properties. To isolate the effect of shear viscosity, a wide range of flexible polymers (three grades of PAM and PEO) and rigid polymers (XG and CMC) has been selected and their concentrations are adjusted to produce a similar shear viscosity. The relationship of DR and degradation with extensional and viscoelastic rheology is investigated. The measurements indicated that DR of rigid and flexible polymers is independent of shear viscosity.

There are many studies about using flexible polymers as drag reducers, while only a few investigators used bio polymers with rigid structure. Hence, as a second step, DR mechanism of a bio polymer (XG) solution at different concentrations (different DR) is studied by comparing turbulent structures of water and polymer solutions using a planar PIV. The effect of XG concentration on the spatial correlation of wall-normal and streamwise velocity fluctuations is also investigated. Proper orthogonal decomposition (POD) is also used to extract dominant turbulent structures in both Newtonian and non-Newtonian flows.

The literature suggests a considerable difference between turbulent structures for flows involving solutions of rigid and flexible polymers. However, the previous studies were carried out at different experimental condition and turbulent structures were compared at different DR percentage (pressure drop) and Reynolds number. For an appropriate comparison of turbulent structures, the evaluation should be carried out at when both rigid and flexible polymers produce an identical condition. Therefore, the mean velocity profiles, Reynolds stresses, polymer stresses, and the spatial correlation of streamwise velocity fluctuations for rigid and flexible polymer solutions at similar DR are experimentally investigated in this thesis using planar and stereo PIV.

The objectives of this research can be summarized as follows:

- Investigate the rheology of drag-reducing solutions of flexible and rigid polymers.
- Study turbulent structures of flows of bio polymer (rigid structure) solutions.
- Characterize turbulent structures of rigid and flexible polymer solutions at identical DR.
- Compare turbulent structures of flexible polymer solutions at MDR with those found in water.

This dissertation is organized in a paper-based format and will be presented in seven chapters. The second chapter starts with an introduction of the basic concepts of turbulent pipe and channel flows, and then it focuses on polymer drag reducers in turbulent pipe and channel flows, followed by rheology characterization in non-Newtonian flows. The third chapter describes the design and the construction of the flow loop used for the experiments. The polymer preparation, rheological measurements (shear viscosity, extensional viscosity, and viscoelastic properties), and pressure drop measurements are discussed. The planar and stereo PIV, which were used for flow measurements, are also explained in this chapter. In Chapter 4, the results and discussion from the manuscript entitled “Rheology of drag-reducing solutions of flexible and rigid polymers” are explained. The second manuscript entitled as “Turbulent structures of non-Newtonian solutions containing rigid polymers” is discussed in Chapter 5. Chapter 6 presents the results and discussion originally included in the manuscript entitled “Turbulence mechanisms of rigid and flexible polymers at an identical DR and turbulent structures at MDR”. Chapter 7 describes the main conclusions of the current study and presents recommendations for future work.

Chapter 2. Literature review

The basic concepts of turbulent channel flows for Newtonian and non-Newtonian flows are discussed. Literature about polymer drag reduction and degradation is reviewed in detail. The importance of molecular structure in polymer drag reducers is explained in the “rigid and flexible polymers” section. The effect of DR on the mean velocity profiles, Reynolds stresses, vorticity fluctuations, streamwise velocity streaks and quasi-streamwise vortices for both rigid and flexible polymer solutions are detailed. The relationship between DR and rheology of polymer solutions, which consists of the measurements of shear viscosity, extensional viscosity, and viscoelastic properties, is presented. Finally, mechanisms of MDR in the literature are introduced and compared.

2.1 Turbulent channel flow

Turbulent channel flow is classified as an internal flow where the flow is bounded by solid surfaces. A schematic of a rectangular channel with height H (= 2δ), width W_c and length L, along a coordinate system (x, y and z) are shown in Figure 2.1. The length of the channel is large relative to the height of the channel (L / H >> 1). At large x, the mean velocity profile is independent of streamwise direction which shows the formation of a fully developed flow. The large aspect ratio (W_c / H >> 1) also indicates that the flow is independent of spanwise direction (remote from the side walls). In this section, some basics of turbulent channel flow are described in detail based on Pope (2000).

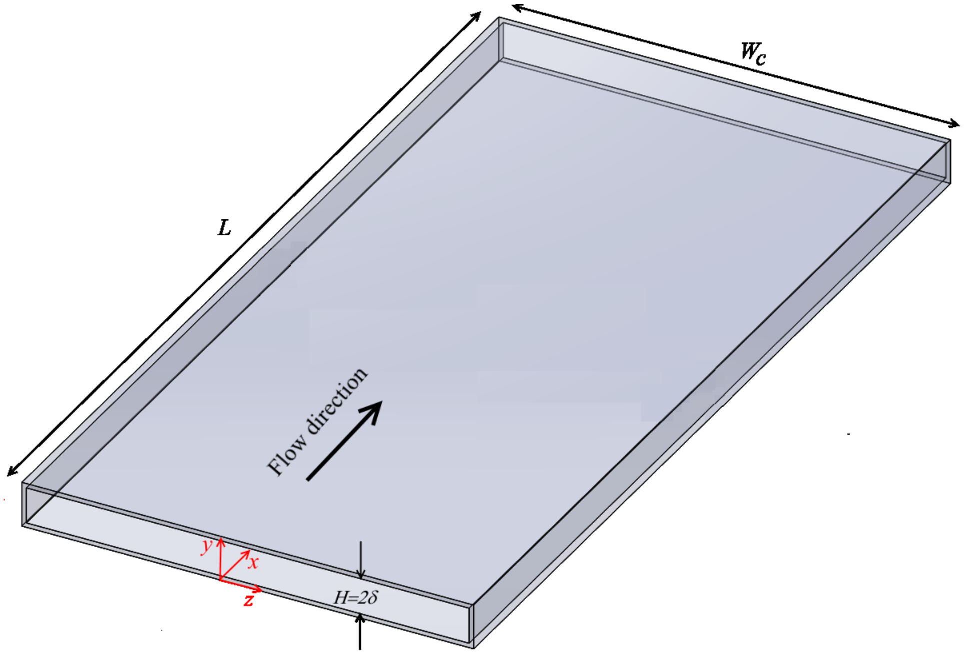

Figure 2-1. A schematic of the turbulent channel flow. The coordinate system is shown in the picture.

The instantaneous and fluctuating velocity vectors are defined as $\boldsymbol{U_i}$ and $\boldsymbol{u_i}$ where the index i refers to velocity components. Here, U and u (i = 1) are streamwise instantaneous and fluctuating velocity, V and v (i = 2) are wall-normal instantaneous and fluctuating velocity, and W and w (i = 3) are spanwise instantaneous and fluctuating velocity. The fluctuating velocity can be obtained from the instantaneous velocity using Reynolds decomposition as

$$\boldsymbol{u_i} = \boldsymbol{U_i} - \langle \boldsymbol{U_i} \rangle \tag{2.1}$$

where $\langle \boldsymbol{U_i} \rangle$ shows an ensemble average of $\boldsymbol{U_i}$ over time. To characterize the flow regime in the channel, Reynolds number is defined as

$$Re = \frac{U_b H}{\upsilon_s} \tag{2.2}$$

where U_b and υ_s are bulk velocity and kinematic viscosity, respectively. The flow is assumed laminar for Re < 1,350 while it is presumed as a turbulent flow for Re > 1,800 although transitional effects exist in the flow until Re = 3000 (Pope 2000). The flow is assumed steady, incompressible, fully-developed, and independent of spanwise direction, thus the continuity equation is simplified to

$$\frac{\partial \langle V \rangle}{\partial \mathrm{y}} = 0 \tag{2.3}$$

The wall-normal velocity, $\langle V \rangle$, is zero at the walls ($y = 0$ and $y = H$). Hence, the integration of Equation (2.3) using boundary conditions mentioned above results in $\langle V \rangle = 0$. The streamwise and wall-normal mean-momentum equations simplify as

$$-\frac{\partial \langle P \rangle}{\partial x} - \rho \frac{\mathrm{d}\langle uv \rangle}{\mathrm{d}y} + \mu_s \frac{\mathrm{d}^2 \langle U \rangle}{\mathrm{d}y^2} = 0 \tag{2.4}$$

$$-\rho \frac{\partial \langle v^2 \rangle}{\partial y} - \frac{\partial \langle P \rangle}{\partial y} = 0 \tag{2.5}$$

where μ_s is the shear viscosity of solvent. By integrating Equation (2.5) in the y direction and applying the boundary condition of $\langle v^2 \rangle_{y=0} = 0$, this equation can be written as

$$\langle v^2 \rangle + \frac{\langle P \rangle}{\rho} = \frac{P_w(x)}{\rho} \tag{2.6}$$

where P_w is the mean pressure at the channel wall. By applying the x derivative to Equation (2.6),

$$\frac{\partial \langle P \rangle}{\partial x} = \frac{\mathrm{d}P_w}{\mathrm{d}x} \tag{2.7}$$

Thus, equation (2.4) can be written as

$$\frac{\mathrm{d}\tau}{\mathrm{d}y} = \frac{\mathrm{d}P_w}{\mathrm{d}x}, \text{and} \qquad \tau = \rho \nu_s \frac{\mathrm{d}\langle U \rangle}{\mathrm{d}y} - \rho \langle uv \rangle \tag{2.8}$$

The shear stress, τ, is a function of y while P_w is a function of x, thus $\mathrm{d}\tau/\mathrm{d}y$ and $\mathrm{d}P_w/\mathrm{d}x$ are constant. With boundary conditions of $\tau = \tau_w$ at $y = 0$, and $\tau = 0$ at $y = H/2$, the solution to equation (2.8) is

$$\tau_w = - \frac{H}{2}\left(\frac{dP}{dx}\right) \tag{2.9}$$

$$\tau = \tau_w(1 - \frac{2y}{H}) \tag{2.10}$$

The skin-friction velocity can be obtained from

$$C_f = {\tau_w}\Big/{(\frac{1}{2}\rho U_b^2)} \tag{2.11}$$

The key parameters in a wall-bounded shear flow near the wall are the viscosity and the wall shear stress. The inner scales can be written from these parameters as

$$u_\tau = \sqrt{\frac{\tau_w}{\rho}}\ , \qquad \tau_w = \mu_s \frac{\mathrm{d}\langle U \rangle}{\mathrm{d}y} \tag{2.12}$$

$$\delta_\upsilon = \frac{\upsilon}{u_\tau} \tag{2.13}$$

where u_τ and δ_υ denote the friction velocity (wall velocity scale) and the viscous length (wall unit), respectively. The friction Reynolds number can be obtained from

$$Re_\tau = \frac{\delta}{\delta_\upsilon} \tag{2.14}$$

The velocity profile and the distance from the wall can be normalized using the inner scales as

$$u^+ = \frac{\langle U \rangle}{u_\tau} \tag{2.15}$$

$$y^{+} = \frac{y}{\delta_v} \tag{2.16}$$

The molecular viscosity affects the shear stress in the viscous wall region ($y^{+} < 50$) while the effect of viscosity is negligible in the outer layer ($y^{+} > 50$). In the viscous sublayer ($y^{+} < 5$), the Reynolds shear stress, $-\rho\langle uv\rangle$, can be neglected relative to the viscous stress, $\mu_s\,\mathrm{d}\langle U\rangle/\mathrm{d}y$.

The mean velocity profiles in wall-bounded flows can be modeled based on y^{+} as

For viscous sublayer: $u^{+} = y^{+}$ $\quad y^{+} < 5$ (2.17)

For log-law region: $u^{+} = \frac{1}{\kappa}\ln y^{+} + B$ $\quad y^{+} > 30$ and $y/\delta < 0.3$ (2.18)

Where $B = 5.2$ and $\kappa = 0.41$, and their variations are within 5%. The transitional layer which connects viscous sublayer and log-law region (von-Karman law) is denoted as a buffer layer ($5 < y^{+} < 30$) (Pope 2000).

The shear viscosity of polymer solutions is a function of shear rate and its value decreases with increasing shear rate (shear-thinning behaviour). Therefore, the shear viscosity at the wall, μ_w, is used to define Reynolds numbers in non-Newtonian flows (Ptasinski *et al.* 2001, 2003; Warholic *et al.* 1999)

$$Re_w = \frac{\rho U_b H}{\mu_w}\,. \tag{2.19}$$

The total stress in polymer solutions consists of a Newtonian part due to the solvent and a polymeric part (Ptasinski *et al.* 2001; Warholic *et al.* 1999). Therefore, the total stress can be defined as

$$\tau_{total} = \tau^{(s)} + \tau^{(p)} = \mu_s \frac{\mathrm{d}\langle U\rangle}{\mathrm{d}y} - \rho\langle uv\rangle + \tau^{(p)} \tag{2.20}$$

where $\tau^{(p)}$ is the mean polymeric stress.

2.2 Polymer drag reduction

Drag reduction (DR) in turbulent flow can be achieved through the addition of drag reducer agents such as fibers, surfactants, microbubbles, and polymers (Abubakar *et al.* 2014). A small quantity of high-molecular weight polymers can reduce drag significantly, while higher concentrations for other drag reducer agents are needed to produce an identical DR (Abubakar *et al.* 2014). Polymer drag reducer was used in Tans-Alaska oil pipeline and about 50% DR was obtained using 10 ppm of an oil-soluble polymer. The capacity was increased from 1.45 to 2.1 million barrel per day (Jubran *et al.* 2007). The addition of polymers in the flow is assessed through two ways: (a) measuring pressure drop at constant flow rate and (b) measuring flow rate at constant pressure drop. Most experimental studies of polymer additives have been carried out at the same flow rate. The percentage of DR for polymer solutions at constant flow rate can be obtained by

$$\mathrm{DR}(\%) = \left(1 - \frac{\Delta P_{polymer}}{\Delta P_{water}}\right) \times 100 \tag{2.21}$$

where ΔP_{water} and $\Delta P_{polymer}$ are the pressure drop measured for water and polymer solutions, respectively (Abubakar *et al.* 2014).

The DR increases with the increase of polymer concentration up to an optimum concentration; above this concentration, DR decreases due to increasing solution shear viscosity (Abubakar *et al.* 2014; Hoyt 1989). The reason behind this is that the addition of polymer solution reduces the Reynolds shear stress ($-\rho\langle uv\rangle$), which is the main source of turbulence generation until the magnitude of Reynolds shear stress reaches zero at the optimum concentration. Above this concentration, further increase in the polymer concentration has no effect on the Reynolds shear stress and increases the shear viscosity, which increases the drag (i.e., wall shear stress $\tau_w = \mu_w \mathrm{d}\langle U\rangle/\mathrm{d}y$). For brevity, the maximum drag reduction achieved at the optimum concentration is called MDR.

A remaining issue in the practical application of polymer solutions is the gradual decrease of DR due to the scission of the long chain polymer molecules (Vanapalli *et al.* 2006). This is known as mechanical degradation and occurs under high shear conditions. Den Toonder *et al.* (1995) showed that Superfloc-A110 is more resistant to degradation than Separan AP-273 and Polyox WSR-301. They also concluded that a disc pump has less influence on degradation than a centrifugal pump. Vanapalli *et al.* (2006) hypothesized that the scission process is due to the local stress generated by the smallest eddies of the turbulent flow. It has also been observed that rigid polymers are more resistant to mechanical degradation than flexible polymers (Escudier *et* *al.* 2009; Pereira *et al.* 2013), although their DR is smaller. Hadri *et al.* (2011) presented the critical temperature above which increase in temperature results in more degradation, and below which increase in temperature delays the degradation. Nakken *et al.* (2001), Lee *et al.* (2002), and Vanapalli *et al.* (2006) for different polymer solutions demonstrated that the mean molecular weight reaches its asymptotic value during the scission of polymer chains, which explains why there is also an asymptote for the degradation. Liberatore *et al.* (2004) studied the effect of degradation of polyacrylamide solutions on molecular weight distribution. They clarified that there are some long time intervals over which drag reduction attenuates at constant molecular weight distribution. Henaut *et al.* (2012) used a rheometer and flow loop in order to investigate the polymer degradation phenomenon in crude oil. They demonstrated that there is a link between flow dissipated energy and degradation kinetics. Soares *et al.* (2015b) argued that rigid polymers are not subject to the scission process, and the decrease in DR of rigid polymer that is typically observed in the early stages of experiment is associated with de-aggregation of polymer agglomerates. Vonlanthen & Monkewitz (2013) developed a model for degradation of PEO based on a cascade in molecular weight distribution induced by molecular scission. However, such degradation models are based on the polymer molecular structure. It is therefore not known if the rheology of the polymer solution can be used to predict the mechanical degradation of the solution.

If mechanical degradation is too severe for a given practical application, it may be possible is to use rigid polymers like Gar Gum, XG, or Glycogen. Another way to decrease the degradation is to combine the flexible polymers with rigid polymers. For example, Sandoval & Soares (2016) showed that combinations of PAM and XG, or PEO and XG, not only increases the amount of drag reduction, but also delays the degradation compared to a single polymer solution.

2.3 Rigid and flexible polymers

Polymers are generally classified as flexible or rigid polymers, based on their molecular structure. Examples of flexible polymers include polyacrylamide (PAM) and polyethylene oxide (PEO). The PAM polymer, as a flexible synthetic polymer made from acrylamide subunits, has a wide range of applications in water treatment, papermaking process, and the flocculation of solid particles dispersed in a medium (Han & Choi 2017; Xiong *et al.* 2018). Most biopolymers such as Guar Gum, XG, sodium alginate, glycogen, and starch are categorized as rigid polymers. Among these, XG has a wide range of applications in food production, cosmetics, pharmaceutical and oil industries. The XG polymer is an extracellular polysaccharide which is made by the bacterium Xanthomonas camperstris (Kim *et al.* 1998). It shows a stable organized helical conformation which is the reason for its rigid structure at moderate temperature and low ionic forces (Pereira *et al.* 2013). Under saline conditions, or at high temperatures, its configuration changes to a coiled structure which is associated with smaller drag reduction capability (Pereira *et al.* 2013). The drag reduction obtained by XG, similar to the performance observed when flexible polymers are used, increases as its concentration and molecular weight increase (Bewersdorff & Singh 1988; Sohn *et al.* 2001). However, the transient performance (DR versus time) for flexible and rigid polymers has been observed to be significantly different (Pereira *et al.* 2013). Sandoval *et al.* (2015) and Soares *et al.* (2015b) investigated DR and degradation of both flexible and rigid polymers (PEO, PAM, and XG) in a pipe flow. They concluded that the flexible polymers provide better DR than rigid polymers, while deterioration in performance of the rigid polymers due to mechanical degradation was negligible in comparison with flexible polymers. The DR can be increased by grafting flexible PAM onto rigid backbones of XG (Abubakar *et al.* 2014; Singh *et al.* 1991). Singh *et al.* (1991) showed that copolymers with longer and fewer PAM branches increase DR more than those with shorter and more PAM branches.

2.4 The effect of DR on turbulent flow

The effect of rigid and flexible polymers on the mean velocity profile and turbulent intensities has been investigated in the literature. Warholic *et al.* (1999) achieved a wide range of DR (10-69%) using 0.25-50 ppm of a flexible polymer (Percol 727, a copolymer of PAM and sodium acrylamide). They defined low and high DR (LDR and HDR) regimes, based on the logarithmic section of the mean velocity profile and the magnitude of streamwise Reynolds stress. The logarithmic section of the mean velocity profile for LDR stayed parallel with the von-Karman log-law of Newtonian flows, but shifted upwards. However, at HDR, the slope of logarithmic section increased (smaller κ, where κ is the von Karman constant) in addition to its upward shift.

For measurements carried out at $Re = 20{,}000$ (based on the half height of the channel and water viscosity), Warholic *et al.* (1999) also investigated the variation of the normalized streamwise Reynolds stress, $\langle u^2 \rangle / u^2_\tau$, where u_τ is the friction velocity of the corresponding flow (polymer solutions and the Newtonian counterpart). They observed that $\langle u^2 \rangle / u^2_\tau$ is larger than the Newtonian flow for LDR, while it is smaller than $\langle u^2 \rangle / u^2_\tau$ of the Newtonian flow at HDR. The peak of $\langle u^2 \rangle / u^2_\tau$ increased by 26% relative to the Newtonian flow at DR = 38%, while it reduced by 33% at DR = 69%. An attenuation of both normalized wall-normal Reynolds stress, $\langle v^2 \rangle / u^2_\tau$, and Reynolds shear stress, $\langle uv \rangle / u^2_\tau$, was observed with increasing DR at LDR and HDR regimes. The peak of $\langle v^2 \rangle / u^2_\tau$ and $\langle uv \rangle / u^2_\tau$, at MDR (DR = 69%), was reduced by 74% and 91%, respectively. The latter results confirmed the existence of a "shear deficit", which shows that the total shear stress in drag reducing flow is greater than the sum of viscous shear stress and the Reynolds shear stress. The shear deficit is equivalent to polymeric stresses. Ptasinski *et al.* (2001) also carried out LDV measurements on the turbulent pipe flow of a flexible PAM polymer (Superfloc A110). They observed a similar trend in variations of turbulence statistics with increasing DR although a larger $<uv>$ residual (maximum of 0.014 N/m^2 at 69% DR) was observed at MDR compared to the findings of Warholic *et al.* (1999); maximum of 0.005 N/m^2 at 65% DR.

Gampert *et al.* (2005) investigated the turbulent intensities of both flexible PAM polymer (Praestol 2300) and rigid polymer (XG) in turbulent channel flow at $Re \sim 30{,}000$. They observed the same trend as the literature in the variation of Reynolds stresses for flexible polymer. For the rigid polymer solution, the variations were negligible (~ ±10%), although DR range was also small (7-17%) using 30-120 ppm of XG. The Reynolds stresses in turbulent flows of rigid XG polymer solutions were investigated by Escudier *et al.* (2009) and Jaafar and Poole (2011). The LDV measurements of Escudier *et al.* (2009) demonstrated that the spanwise Reynolds stress ($<w^2>/u^2_\tau$) is independent of the extent of DR, but $<v^2>/u^2_\tau$ decreases with increasing DR, and $<u^2>/u^2_\tau$ increases as DR increases when DR $\leq$ 59%. Any further increase in DR results in smaller values of $<u^2>/u^2_\tau$. As mentioned above, the Reynolds stresses were normalized with the friction velocity of the polymer solution; therefore, the trends are also affected by the variation of friction velocity with DR.

The vorticity fluctuations of Newtonian flow are modified due to the addition of polymer solutions (Dallas *et al.* 2010). Kim *et al.* (2007) presented their DR mechanism based on the vortex retardation. They showed that the torque produced by polymer stress opposes the rotation of quasi-streamwise vortices and hairpin vortices which are the source of Reynolds shear stress production. Li *et al.* (2015) used direct numerical simulation (DNS) and finitely extensible nonlinear elastic-Peterlin (FENE-P) model and showed that the ratio of the convective time scale of streamwise vorticity fluctuation to vortex rotation time is an important parameter for DR and its universality of MDR; independent of type of polymer, geometry, and concentration (Virk *et al.* 1967). These studies show that vorticity fluctuation is a key parameter for DR mechanism.

Li *et al.* (2006) used DNS and investigated the effect of DR on the vorticity fluctuations in the channel flow at Re_τ = 180. They observed that the magnitude of streamwise vorticity fluctuations, normalized with the friction velocity of polymer solution, reduces with increasing DR, while attenuation of wall-normal and spanwise vorticity fluctuations was bounded to the near wall regions ($y^+ < 30$). The magnitude of the peak in streamwise, wall normal, and spanwise vorticity fluctuations at DR = 71%, decreased by 83%, 30%, and 36%, respectively. Dallas *et al.* (2010) also used DNS and FENE-P model without using any assumptions and captured the strong polymer-turbulence dynamics interactions at three different Reynolds numbers ($Re_c = U_cH/2\upsilon_0$ = 2750, 4250, and 10400, where $U_c = 3/2U_b$). They studied the vorticity fluctuations of polymer solutions in the channel flow at Re_c = 4250. They observed a reduction of streamwise vorticity fluctuations in the whole channel (~70% reduction of the peak value at DR of 64.5%). The attenuation of wall-normal and spanwise vorticity fluctuations for the near wall region ($y/H < 0.1$, where H is the channel height) was also verified. The peak value of wall-normal and spanwise vorticity fluctuations, at MDR (DR = 64.5%), was reduced by 70% and 60%, respectively. In addition to the large difference observed in the reduction of peak value of wall-normal and spanwise vorticity fluctuations for these two studies, other discrepancies also exist. The magnitude of wall-normal vorticity fluctuations in the study of Dallas *et al.* (2010) at DR = 62% and 64.5% was reduced in the whole channel, while the reduction of intensity in the Li *et al.* (2006) study was only observed in the near-wall region. At $y/H > 0.2$, the magnitude of normalized spanwise vorticity fluctuations with the friction velocity of polymers in the work of Dallas *et al.* (2010) at DR = 62% and 64.5% is lower than that at DR = 57.3%, while it was an increasing function of DR at $y^+>30$ in the work of Li *et al.* (2006). As mentioned above, Dallas *et al.* (2010) carried out their investigation at a constant Re_c, while the results of Li *et al.* (2006) were obtained at a constant Re_τ. Therefore further investigation of vorticity fluctuations, especially an experimental study, is essential.

Prevalent structures in the wall-bounded turbulent flows include streamwise velocity streaks and quasi-streamwise vortices. In the self-sustaining cycle of wall turbulence in Newtonian flow, quasi-streamwise vortices extract energy from the mean velocity profile and generate streamwise velocity streaks; in turn, an instability in the high and low speed streaks results in formation of quasi-streamwise vortices (White & Mungal 2008). The addition of polymers into Newtonian flows alters streamwise velocity streaks and quasi-streamwise vortices (White & Mungal 2008). The number and strength of quasi-streamwise vortices decrease with increasing DR (White & Mungal 2008). In addition, the streamwise velocity streaks become thickened in polymer solutions (White *et al.* 2004; White & Mungal 2008). The addition of polymers in the turbulent flow disrupts the turbulence regeneration cycle (Dubief *et al.* 2004). However, the mechanism of this disruption is not clearly understood and relates to the interactions between polymers and turbulence.

2.5 Rheology of polymer solutions

Many previous investigations have characterized polymer solutions using shear viscosity. This is perhaps due to the availability of equipment and the traditional characterization of non-Newtonian liquids using shear viscometers, although shear viscosity appears to have little relevance to the DR mechanisms proposed by Lumley (1969) and De Gennes (1986). The shear viscosity of polymer solutions reduces with the increase of shear rate (shear-thinning behaviour). The shear-thinning behavior of polymer solutions has been confirmed by many investigators (Escudier *et al.* 2009; Ptasinski *et al.* 2003; Warholic *et al.* 1999)

A detailed review of the literature shows that there are only a few measurements of extensional viscosity and viscoelasticity of drag-reducing polymer solutions. Due to experimental limitations, these measurements were made at polymer concentrations at least an order of magnitude higher than that needed for maximum DR.

Escudier *et al.* (1998) observed that the DR of high concentration solutions of XG, CMC, and PAM (minimum of 2000 ppm) is proportional to their extensional viscosity at small shear rates

(~10 1/s). This suggests a relationship between DR and extensional viscosity; however, polymer concentration was too large and the corresponding shear rate (i.e., ~10 1/s) is a few orders of magnitude smaller than the mean shear rate of a turbulent flow. The measurements were carried out using an opposed-nozzle rheometer, which is not accurate to obtain extensional viscosity (Dontula *et al.* 1997). Jaffar *et al.* (2009) used a capillary break-up extensional rheometer (CaBER) to characterize extensional viscosity by measuring the diameter of a thinning filament for non-ionic polysaccharide at concentrations of 1000 to 5000 ppm. From the filament diameter, they estimated the relaxation time (λ) and Trouton ratio (the ratio of extensional viscosity to shear viscosity). They observed a large Trouton ratio for all the polymer concentrations, which confirmed the dominance of non-Newtonian extensional behavior of the solutions. Pereira *et al.* (2013) also used CaBER and observed a larger relaxation time for PEO than that of PAM at identical concentrations. They could not measure the relaxation time of XG since filament diameter did not follow the exponential decay proposed by Entov & Hinch (1997). Recently, Owolabi *et al.* (2017) used CaBER for measurement of extensional viscosity in PAM solutions at low polymer concentrations (150-350 ppm), and investigated the variation of DR with Weissenberg number (Wi), defined as the product of λ and mean turbulent wall shear rate. They observed that DR rapidly increases with Wi and reaches an asymptote of about 64% when $Wi > 6$.

A summary of the investigations reporting measurements of λ is presented in Table 2-1. The table shows that a limited number of extensional viscosity measurements have been reported, and that most of the measurements were made at concentrations higher than that needed for maximum drag reduction (MDR).

Oscillatory tests can measure the storage modulus (G') and the loss modulus (G'') to characterize the linear viscoelastic properties of a polymer solution. Nakken *et al.* (2001) observed that G' and G'' moduli of a poly α-olefins polymer solution at 5000 ppm increased with increasing oscillation frequency. Pereira & Soares (2012) associated larger value of DR of PEO relative to PAM to a larger storage modulus (G'). However, due to experimental limitations, measurement of G' was conducted for a 10,000 ppm polymer solution while DR was measured at 2 to 50 ppm. Pereira *et al.* (2013) also conducted oscillatory measurements for a wide range of concentrations that were higher than the concentration used for drag measurement. Escudier *et al.* (2001)

investigated the effect of polymer preparation procedure through measurement of G' and G'' moduli. The oscillatory measurements of Jaffar *et al.* (2009) for rigid polysaccharide solutions showed that G' is smaller than G'' (i.e., viscous behavior) when the polymer concentration is less than 2000 ppm, while G' is larger than G'' (i.e., elastic behavior) at higher concentrations. They also observed that the dependency of G' and G'' on frequency is smaller at higher concentrations. Therefore, extrapolation of oscillatory viscoelastic measurements to lower concentration, in which drag is measured, may not be straightforward. Wyatt *et al.* (2011) showed that DR and G' modulus of XG solutions depend on the concentration of the master solution used for preparation of the final solution. Based on oscillatory measurements of a 60 ppm XG solution prepared from master solutions with different concentration, they showed that a larger G' results in higher DR. The change in DR was associated with the residual entanglements that are still sustained after diluting the concentrated master solution.

A summary of investigations of oscillatory measurements, including solution concentration and the DR values are presented in Table 2-1. In these investigations, oscillatory measurements were carried out at concentrations higher than that used for drag reduction measurements.

Table 2-1. A summary of the literature that has reported extensional viscosity and oscillatory measurements of drag-reducing polymer solutions.

Source	Polymer type	Concentration for DR (ppm)	DR%	Oscillatory tests	Concentration for oscillatory tests (ppm)	Extensional viscosity	Concentration for extensional viscosity (ppm)
Nakken *et al.* (2001)	Poly α-olefin A	1-12	1-35	Yes	5000	No	NA
Pereira *et al.* (2012)	PEO, PAM	2-50	12-24, 2-20	Yes	10000	No	NA
Pereira *et al.* (2013)	PEO, PAM, XG	2-100	15-20, 7-21, 0.5-27	Yes	1000-10000 2500-10000 250-10000	Yes	1000-10000 2500-10000 100-10000
Escudier *et al.* (2001)	XG, CMC	NA	NA	Yes	2500, 4000	No	NA
Jaffar *et al.* (2009)	Scleroglucan	750	47, 55	Yes	750, 5000	Yes	1000
Escudier *et al.* (1999)	CMC, XG, PAA	2500-4000 2000 1250-2000	NA	No	NA	Yes	2500-4000 2000 1250-2000
Owolabi *et al.* (2017)	PAA	250	72	No	NA	Yes	250
Wyatt *et al.* (2010)	XG	60	11-16	Yes	60 (from 500 to 4000 ppm master solution)	No	NA

2.6 Mechanisms of MDR

The increase in polymer concentration leads to higher DR until MDR is achieved, which is also known as the Virk asymptote (Virk 1971). Further increase in the polymer concentration results in higher solution viscosity and drag increase (Abubakar *et al.* 2014; Hoyt 1989). The Virk asymptote is independent of polymer properties, which suggests its universality (Virk 1975). Benzi *et al.* (2005) and Procaccia *et al.* (2008) presented a model for MDR which depends on Reynolds shear stresses and eddy viscosities. Based on the experimental results of Warholic *et al.* (1999), they assumed that Reynolds shear stresses is approximately zero at MDR and presented a limit to the slope of log-law velocity profile. On the other hand, many experimental works observed non-zero Reynolds shear stress at MDR (Li *et al.* 2006; Min *et al.* 2003; Ptasinski *et al.* 2003). In addition this model was not able to address the source of turbulence production at MDR.

Xi & Graham (2012) investigated Newtonian and viscoelastic turbulence in a minimal channel flow using DNS. The turbulence in a minimal channel flow was characterized into two alternating time intervals, including high (active turbulence) and low (hibernating turbulence) friction. They showed that hibernating turbulence shares the same statistical (e.g. mean velocity and velocity fluctuations) and structural (e.g. weak vortices) features with MDR, and its frequency increases with increasing polymer elasticity. They concluded that MDR is a marginal state of hibernating turbulence. This is in agreement with the work of Procaccia *et al.* (2008) in which turbulence at MDR was limited to the edge between laminar and turbulent flows.

Samanta *et al.* (2013) proposed another explanation for MDR using experimental investigations in pipe flow and DNS results in channel flow. They introduced a secondary instability, known as elasto-inertial instability (EII), based on the interaction of elasticity and inertia at high polymer concentrations. The EII is the dominant instability that moves the natural transition point to lower *Re* relative to Newtonian flow. They concluded that DR is finally limited by the EII, which resists the flow to be laminar and becomes a new source of turbulence at MDR.

Choueiri *et al.* (2018) carried out PIV measurements in the turbulent pipe flow with increasing polymer concentration at a constant *Re*. They observed that increase in PAM concentration at *Re* = 5250 results in reduction of friction factor until MDR at 60 ppm is obtained. Further increase in concentration up to 80 ppm did not affect MDR. However, a different trend was observed at *Re* = 3150. The MDR was achieved by using 20 ppm and the full laminar region was observed by adding 25 ppm. The flow stayed laminar by increasing the concentration up to 40 ppm. Further increase in PAM polymer up to 60 ppm leads to triggering EII, which results in transmission of laminar flow to MDR at 60 ppm concentration. The turbulent structures consist of bursts separated by quiescent regions for PAM solution at 20 ppm, while streamwise elongated streaks are dominated at 60 ppm concentration.

In summary, turbulent structures at MDR depend on the regime of flow (transitional or turbulent flows) and *Re* number is a key parameter in their characterization. Further experiments at high *Re* number are needed to compare turbulent structures with those found in low *Re* number.

Chapter 3. Experimental Setup

The experimental setup used in this research consists of pipe and channel flow loops. Both of them were designed and constructed by the author. A brief explanation about the design and construction of flow loops is presented in this section.

The DR produced by polymer additives was characterized by measuring pressure drop in a turbulent pipe and channel flow loops. The preparation procedure of the polymer solutions and the measurements of shear viscosity, extensional viscosity, and storage and viscous modulus are also detailed here.

In addition, two series of PIV measurements were carried out in this research. The first one is a planar PIV and focuses on the effect of XG concentrations on the turbulent structures, while the second one consists of both planar and stereo PIV and highlights the comparison of turbulent structures in rigid and flexible polymer solutions at an identical DR, as well as visualization of turbulent structures in Newtonian flow and polymer solution at MDR.

3.1 Pipe flow setup

The DR measurements were conducted in a pipe with nominal diameter of D = 25.4 mm at a flow rate of 21.9 L/min. The schematic of the flow loop, presented in Figure 3-1, shows the two pressure ports for measurement of pressure drop (ΔP), the reservoir, and the pump. The upstream pressure port is located at x = 1.5 m, where the origin of x is at the flange shown in Figure 3-1. This distance results in a flow development L/D = 59 to ensure a fully developed flow (Çengel 2014). The downstream pressure port is at x = 2.5 m, which results in 0.032 ± 0.002 psi pressure drop between the two ports for flow of water at Q = 21.9 L/min.

A Validyne differential pressure transducer with 0.5 psi diaphragm was used for the measuring the pressure drop. The signal was sampled at 2 Hz through a LabVIEW (National Instruments) interface. A progressive cavity pump (Moyno, model 36704) and a variable frequency drive were used to circulate the flow. Flow rate was measured using a magnetic flow meter (Omega, FLR 8340D).

The Reynolds number of the flow is $Re = U_bD/\upsilon$ = 20,600, where U_b, and υ are the bulk velocity and kinematic viscosity of water, respectively. The flow rate was kept constant during the experiments, which resulted in a constant U_b of 0.72 m/s for water and polymer solutions. A constant temperature of 25±0.5°C was also maintained. The pipes were completely washed after each polymer experiment, followed by pressure drop measurement with water to ensure no contamination from the previous test occurred. The wall shear stress is calculated using $\tau_w = \Delta P\, D/\, 4L$, where L =1 m is the distance between the pressure ports. The calculated wall shear stress for the Newtonian (water) flow is 1.4 Pa. The DR% can be obtained using the equation presented in Chapter 2 (2-21).

A moving average with kernel of 500 data points (at 2 Hz) was applied to the pressure data recorded for 2 hours. The average pressure drop of the first 500 data point is referred to as DR_0. The concentrated solution was gradually added to the mixing tank while the flow loop operated for five minutes to homogenously mix the polymer solution before the start of the data acquisition.

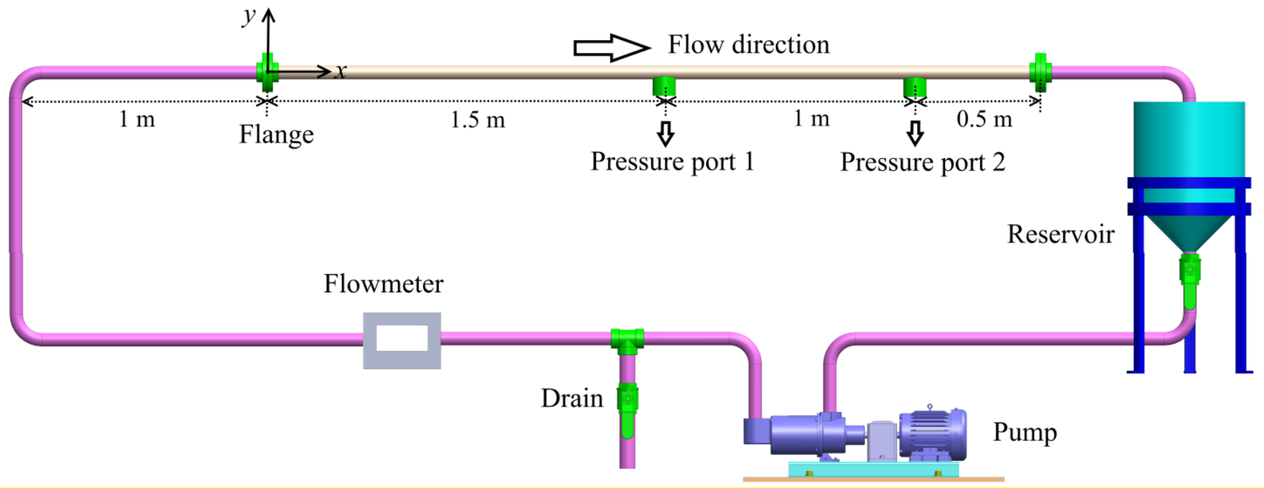

Figure 3-1. Schematic of the flow loop used for the drag reduction experiments.

3.2 Channel flow setup

The measurements were carried out in the test-section of a closed-circuit flow loop with rectangular cross-section of 60×10 mm^2 ($W \times H$) and hydraulic diameter of D_h = 17.1 mm. The total length of the rectangular channel is 1200 mm (120H) while the measurements are carried out 845 mm (84.5H) downstream of the channel entrance to obtain a fully developed channel flow. There is a settling chamber upstream of the test-section followed by a contraction section with area ratio of 1:9 and a diffuser downstream of the test section as shown in Figure 3-2.

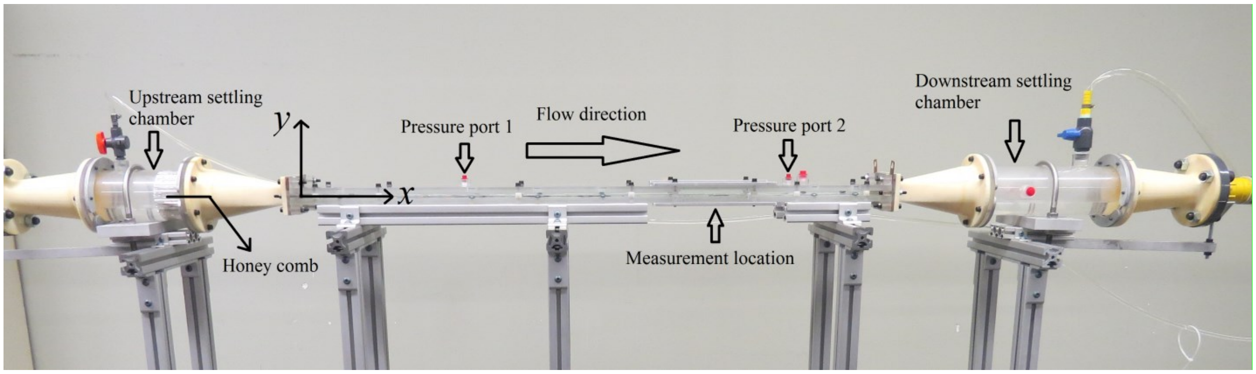

Figure 3-2. The test-section of the present study, which has a rectangular cross-section formed by glass side walls and acrylic top and bottom walls.

Figure 3-3 shows an exploded view of channel test section. The top and bottom plates of the test section are made from cast acrylic while the sidewalls are glass to minimize distortion of high-magnification PIV images.

Figure 3-4 shows an exploded view of settling chambers with expansion section, settling chamber, and contraction sections. The upstream settling chamber has a honeycomb structure to break down the large eddies and a fine mesh to increase the uniformity of the flow at the entrance of the test-section.

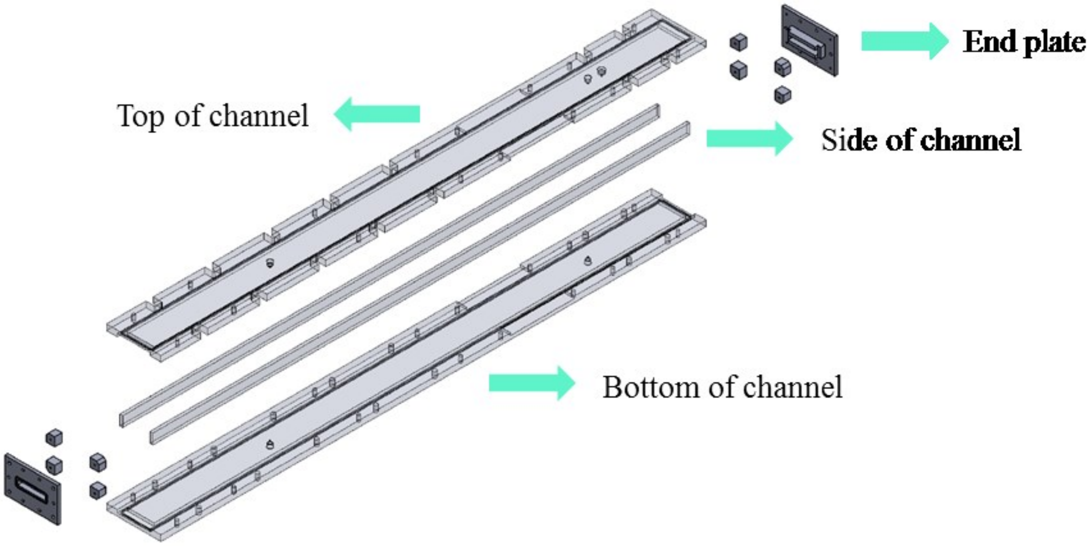

Figure 3-3. The 3D exploded view of a channel test section.

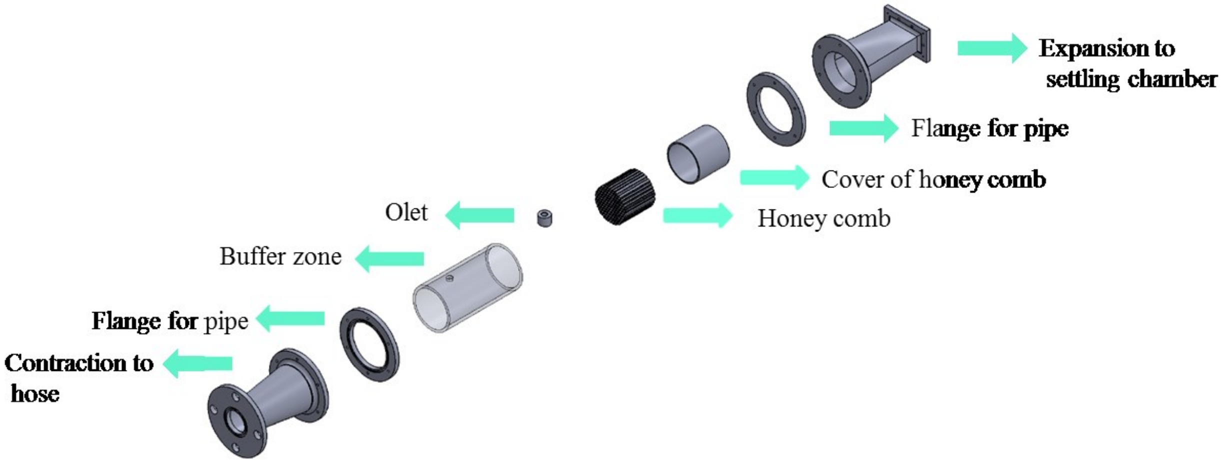

Figure 3-4. The 3D exploded view of settling chambers with expansion to settling chamber and contraction to hose.

The 2D drawings of the test section, flanges, O-rings, expansion, contractions, and settling chambers are prepared using Solidworks software and are presented in Appendix A.

A Validyne differential pressure transducer with 0.5 psi diaphragm was used to measure the pressure drop between pressure ports 1 and 2, as shown in Figure 3-2. The high-pressure port is located at $x = 0.3$ m from the entrance of test section (the coordinate system is shown in Figure 3-2) to ensure fully developed flow (Çengel 2014), and the low-pressure port is installed at $x = 1$ m. The pressure transducer is calibrated using pressure calibrator DPI 610. The voltage output for both pressure drop measurement and flow rate is read using a data acquisition card (National Instruments 9219) with 24-bit resolution and logged using LabVIEW. The data collection frequency for pressure drop measurement was 2 Hz.

The flow loop has a 70 L reservoir connected to a Moyno pump (Model 36704). Previous investigations have shown rapid degradation of polymers when centrifugal or gear pumps are used (Den Toonder 1995). A variable frequency driver (VFD) is used to control the pump speed while a magnetic flow meter (Omega, FLR 8340D) measures the flow rate. Flow rate data were collected at a frequency of 2 Hz.

3.3 Polymer preparation and rheology

A wide range of flexible and rigid polymers was selected for this research. Flexible PAM polymers with different molecular weights and monomers are chosen: Magnafloc 5250 (BASF Corp.), Superfloc A-110 (Kemira), and Superfloc A-150 (Kemira), and a PEO polymer (Sigma-Aldrich). These are high molecular weight anionic polymers (1-20 million Daltons), which are used in mineral processing and tailings thickening (BASF). Superfloc A-150 has a higher molecular weight and anionic charge relative to Superfloc A-110 (Kemira). The PEO has a linear structure and a molecular weight of about 8 million Da (SIGMA-ALDRICH). Two rigid polymers with non-linear structures were selected including XG and CMC polymers. The abbreviation used to refer to each polymer, the supplier, and polymer structures are shown in Table 3-1.

The XG is a biopolymer made from the process of fermentation of Xanthomonas by gram-negative bacteria (Papagianni *et al.* 2001). The XG polymer has a linear main-chain of (1-4)-β-D glucose backbone, connected to a trisaccharide side-chain on every second D-glucose. The rigidity of the polymer is produced by the charged trisaccharide side-chain which folds back around main chain of (1-4)-β-D glucose (Bewersdorff & Singh 1988). Based on the literature, the molecular weight of XG polymer is between 2×10^6 and 5×10^7 g/mol (Papagianni *et al.* 2001).

A high-concentration, master solution is prepared using a low shear magnetic stirrer. The required amount of polymer powder is accurately weighed (Mettler Toledo, AB104-S) with precision of 0.1 mg. The polymer and water were gradually added to a beaker (~2 L) while the magnetic stirrer mixed the solution at 300-400 rpm. This procedure prevents aggregation of polymer molecules and lump formation. The length of the magnetic stir bar was 60-70% of the beaker diameter to promote homogenous mixing. After 2 hours of mixing, a vacuum pump was applied to remove air bubbles from the solution. The master solution was added to ~ 68 L of water to obtain the desired final concentration in the flow loop.

Table 3-1. Polymers listed as part of the current study.

Polymer	Abbreviation	Manufacturer	Polymer structure
Superfloc A-150	SF-150	Kemira	Flexible
Superfloc A-110	SF-110	Kemira	Flexible
Magnafloc 5250	MF	BASF Corporation	Flexible
Polyethylene oxide	PEO	Sigma-Aldrich	Flexible
Xanthan gum	XG	Not Available	Rigid
Carboxy methyl cellulose	CMC	Not Available	Rigid

3.3.1 Shear viscosity

A rheometer (RheolabQC, Anton Paar) with a double gap cylinder (DG42) was used to measure the shear viscosity of polymer solutions at a maximum shear rate of 1000 (1/s). A water bath was used to maintain the temperature at 25±0.02˚C during the measurements. The small gap of this rheometer, 1 mm, is suitable for viscosity measurements of low viscosity fluids at high shear rate. The accuracy of viscosity measurements is estimated to be ± 2% (Schramm 1994). The inner cylinder (bob) turns while the outer cylinder (cup) remains stationary. The rheometer (DG42) measures shear viscosity from 10^{-4} to 7×10^3 Pa.s over a range of shear rates from 4×10^{-2} to 9×10^3 s^{-1}. The shear viscosity for a rheometer with double gap can be obtained as $\eta = T(r-$

$R)/(2\pi L r^3 \Omega)$, where η, T, r, R, L, and Ω are shear viscosity, torque on inner cylinder, inner radius, outer radius, length of bob, and angular velocity of bob (Morrison 2001). Hence, shear viscosity is calculated by measuring T and Ω.

3.3.2 Extensional viscosity

A HAAKE CaBER (Thermo Scientific) was used to characterize the extensional viscosity of the polymer solutions. To make a measurement, a droplet of polymer solution was placed between two circular plates with 6 mm diameter and 3 mm distance. The top plate is suddenly lifted to stretch the polymer solution and form a filament. The final gap size is 9 mm with a strike time of 50 ms. The laser micrometer monitored the middle of the filament at a frequency of 10 kHz. The produced filament becomes thinner and finally breaks up due to the capillary force. The midpoint diameter of the filament (D_{mid}) was recorded using a laser micrometer as a function of time (Thermo Scientific 2006), as it evolves with time through under the balance of viscous, elastic, tensile, and capillary forces, following (Renardy 1995; Yarin 1993)

$$3\eta_s\left(-\frac{2}{D_{mid}}\frac{dD_{mid}}{dt}\right)=\frac{4F_z}{\pi D_{mid}^2}-(\tau_{zz}-\tau_{rr})-\frac{2\sigma}{D_{mid}} \tag{3.1}$$

where σ, F_z, η_s are surface tension, tensile force on the ends of the filament, and solvent viscosity, respectively. The term on the left side is viscous stress while the terms on the right denote stresses from tensile, elastic, and capillary forces, respectively. The τ_{zz} and τ_{rr} terms refer to normal stresses in the axial and radial directions, respectively. The elastic force is modeled using the upper-convected Maxwell model to correlate polymer stress with the deformation rate (F. Olsson 1993) to yield (Thermo Scientific 2006)

$$D_{mid} = D_0(GD_0/\sigma)^{1/3}\exp(-t/3\lambda) \tag{3.2}$$

Here D_0, G, and λ stand for the midpoint diameter at $t = 0$, elasticity modulus, and the relaxation time of fluid, respectively. The relaxation time (λ) is estimated by fitting Chapter (3.2) on the linear section of a semi-logarithmic plot of D_{mid} as a function of time. Hencky strain and strain rate are also calculated using

$$\varepsilon(t) = 2\ln(D_0/D_{mid}(t)), \text{ and} \tag{3.3}$$

$$\dot{\varepsilon}(t) = -\frac{2}{D_{mid}(t)}(dD_{mid}(t)/dt), \tag{3.4}$$

Respectively (Anna & McKinley 2002). The apparent extensional viscosity is estimated as (Anna & McKinley 2002; McKinley & Tripathi 2002)

$$\eta_E(\varepsilon) = \frac{(2X-1)\sigma}{dD_{mid}/dt} \tag{3.5}$$

where X is an axial correction factor based on the local shape of filament assumed to be 0.71 according to McKinley *et al.* (McKinley & Tripathi 2002). The polymer solution surface tension (σ) typically was assumed to be the similar to that of water (73×10^{-3} N/m). This assumption is confirmed by Miller *et al.* (2009) in which they showed that the surface tension of a polymer solution at a high concentration (10,000 ppm) is nearly identical to the surface tension of water.

3.3.3 Storage and loss modulus

The viscoelasticity modulus is defined as $G^*=G'+iG''$, where G' and G'' are the elastic and viscous modulus, respectively. The elastic modulus refers to the elastic storage of energy, while viscous modulus indicates loss of energy due to viscous dissipation (Morrison 2001). Oscillatory tests were conducted by applying time dependent shear rate as a cosine function (Morrison 2001). The motion of rotor of geometry followed $b(t) = h\gamma_0 \sin(\omega t)$, where $b(t)$, h, γ_0, and ω are the rotor displacement, geometric gap, strain amplitude, and angular frequency of motion, respectively. The shear stress produced from this motion, at low strain amplitudes, is (Morrison 2001)

$$-\tau_{21} = \tau_0 \sin(\omega t + \delta) = (\tau_0 \cos\delta)\sin\omega t + (\tau_0 \sin\delta)\cos\omega t \tag{3.6}$$

where τ_{21} and τ_0 are the sinusoidal and peak stress amplitude, respectively. δ is the phase angle which is defined as the phase difference between the applied strain and the stress response. The first term represents the component of the shear stress that is in the phase with imposed strain (i.e., sin ωt) while the second term is in phase with the imposed strain rate (i.e., cos ωt). It is known that shear stress is proportional to strain in elastic materials (Hooke's law) and is proportional to shear rate in a Newtonian fluid. Therefore, the shear stress in Equation (3.6) has an elastic part that is proportional to strain and a Newtonian part that is proportional to strain rate. Therefore, the elastic and loss modulus are obtained by decomposing and dividing Equation (3.6) by the peak strain amplitude (γ_0) (Morrison 2001)

$$G'(\omega) = \frac{\tau_0}{\gamma_0}\cos\delta \quad \text{and} \quad G''(\omega) = \frac{\tau_0}{\gamma_0}\sin\delta. \tag{3.7}$$

For a Newtonian fluid, $G' = 0$ and $G'' = \mu\omega$, where μ is the shear (dynamic) viscosity, while for a Hookean solid $G'' = 0$ and $G' = G$. The G' and G'' moduli are both nonzero in a viscoelastic material (Morrison 2001).

The oscillatory tests to determine G' and G'' were carried out using Discovery Hybrid Rheometer (DHR-2) (TA Instruments) with a concentric cylinder (TA-Instruments 2019). Both amplitude and frequency sweep tests were conducted. The minimum measurable torque using this rheometer was 0.002 µN.m (TA-Instruments 2019). The measured torque in the current study varied from 0.1 µN.m to 640 µN.m. In the amplitude sweep tests, a fixed angular frequency (0.628 rad/s) was used while the stress was slowly increased from 0.00085 to 0.0673 Pa. In the frequency sweep tests, a fixed oscillation displacement of 0.1 rad was applied and the angular frequency was varied from 0.628 to 18.84 rad/s.

3.4 Planar particle image velocimetry

3.4.1 Planar PIV for XG investigation of Chapter 5

Planar PIV measurement at relatively high image magnification (M = 1.3) was carried out across the full height channel. A Nd:YAG laser (Solo III-15, New Wave Research) with 532 nm wave length, and maximum output of 50 mJ over 3-4 ns pulse was applied for illumination. A combination of cylindrical and spherical lenses was used to form a laser sheet having a thickness of ~ 1 mm. The laser sheet was directed through the bottom wall of the test section to cover an x-y plane at the mid-span of the cross-section. A CCD camera (Imager proX, LaVision GmbH) with sensor size of 2048×2048 pixel and pixel size of 7.4×7.4 µm^2 with 14-bit resolution was employed to capture the scattered light reflected from 2 µm silver coated spherical glass beads. The tracers have a density of 4 g/cm^3 (SG02S40 Potters Industries) and relaxation time $\tau_s = d_p^2\rho_p/18\mu$, ~ 10^{-6} s, where d_p is the tracer particle diameter, ρ_p is tracer particle density, and µ is viscosity of water. The camera is equipped with a Sigma SLR objective lens with a focal length of *f* = 105 mm at an aperture opening of *f* /11. The current PIV measurement has the digital resolution of 179 pix/mm. Field of view of the image is 11.5×11.5 mm^2 and depth-of-field is set to approximately 1 mm. An ensemble of 6,000 PIV image pairs is recorded in double-frame mode with laser pulse separation of 110 μs synchronized using a programmable timing unit (PTU9, LaVision GmbH) controlled by DaVis 8.2.

The minimum intensity of the ensemble of images was subtracted from individual images in order to improve the signal-to-noise ratio. The resulting images were multiplied by a constant to utilize the 14-bit resolution before normalizing the images by the average of the ensemble. The ensemble of correlation (EC) technique (Meinhart *et al.* 2000) with final interrogation window (IW) size of 8×8 pix (45×45 μm^2) and 75 percent overlap was applied to obtain the mean velocity profile. The high spatial-resolution of this technique allows measurement of the velocity gradient within the viscous sublayer and subsequent estimates of the wall shear rate, as was mentioned previously. The turbulence statistics are obtained from a multi-pass correlation algorithm applied to double-frame recordings with final interrogation windows of 32×32 pix (0.18×0.18 mm^2, $7.9\lambda_0 \times 7.9\lambda_0$) with 75 percent overlap. The PIV processing was conducted in DaVis 8.2 (LaVision GmbH). The smallest eddy size in wall turbulence which should be resolved to obtain accurate turbulence statistics is ~$20\lambda_0$ (~455 μm) according to Stanislas *et al.* (2008). This eddy size is larger than the IW size ($7.9\lambda_0$) demonstrating the adequate spatial resolution of the current PIV system. A summary of the measurement parameters can be found in Table 3-2.

Table 3-2. Imaging and processing parameters of the planar PIV system.

Data set	6,000	
Magnification	1.3	
Digital resolution	179 pix/mm	
Δt (μs)	110	
Measurement field (Δx, Δy)	2048×2048 pix 11.5×11.5 mm^2 $505.5\ \lambda_0\times505.5\ \lambda_0$	
Velocity evaluation	double-frame correlation	ensemble of correlations
Spatial resolution (x, y)	32×32 pix 180×180 μm^2 $7.9\ \lambda_0\times7.9\ \lambda_0$	8×8 pix 45×45 μm^2 $2.0\ \lambda_0\times2.0\ \lambda_0$
Window overlap	75 %	75 %

3.4.2 Planar PIV for investigation of rigid and flexible polymer solutions in Chapter 6

A planar-PIV with relatively high image magnification (M = 1.37) was used to characterize 2D flow statistics in the channel flow. A dual-cavity Nd:YLF laser (DM20-527, Photonics Industries) with 527 nm wavelength, and maximum energy of 20 mJ per pulse (at frequency of 1 kHz) for each cavity of laser was used to generate a laser sheet with approximately 1 mm thickness. The laser sheet generated by the combination of cylindrical and spherical lenses was directed to the middle of the channel to illuminate the *x*-*y* plane across the full height of the channel. For imaging, a CMOS high-speed camera (Phantom v611) was used, with sensor size of 1280×800 pixel, pixel size of 20×20 μm^2, and 12-bit resolution. A Sigma SLR objective lens with a focal length of f = 105 mm at an aperture opening of $f/11$ was used to image a 5.6×10.5 mm^2 field-of-view (FOV). The digital resolution of image was 69 pix/mm, and the depth of field was obtained approximately 1 mm. The laser and camera were synchronized using a programmable timing unit (PTU X, LaVision GmbH) controlled by DaVis 8.4 (LaVision

GmbH). Again, silver-coated 2 μm spherical glass beads (SG02S40 Potters Industries) with density of 4 g/cm^3 were selected as tracer particles. A total of 5000 image sets were collected at a repetition rate of 20 set/s. Each image set included four single-frame time-series of images at an acquisition rate of 10 kHz The signal-to-noise ratio (SNR) was improved by using subtract time filter and applying subtract minimum. PIV sum-of-correlation (Meinhart *et al.* 2000) with a final interrogation window (IW) size of 4×4 pix (58×58 μm^2, $6.8\lambda_0 \times 6.8\lambda_0$) and 75 percent overlap was used to obtain the mean velocity profile. The turbulence statistics were obtained using PIV time-series sliding sum-of-correlation with multi-pass algorithm and a final interrogation window (IW) size of 16×16 pixel (0.233×0.233 mm^2, $27\lambda_0 \times 27\lambda_0$) at 75% overlap in Davis 8.4 (LaVision GmbH). Time filter and correlation in sliding sum-of-correlation were taken one. It gives one vector field from four single-frame images of each cycle.

3.5 Stereoscopic particle image velocimetry

The streamwise vorticity was characterized in the *y-z* plane using stereoscopic particle image velocimetry (stereo-PIV) for the investigations of Chapter 6. The stereo-PIV consisted of two CMOS high-speed cameras (Phantom v611) placed at an angle of about 90° respect to each other, as shown in Figure 3-5. A prism filled with water was used to reduce image distortion caused by the inclined viewing angle of the cameras. The cameras were also equipped with scheimpflug adapters to align the focus plane with the laser sheet. A field of view of 18.7×11.2 mm^2 with digital resolution of 38 pix/mm was obtained using a Sigma SLR objective lens with a focal length of f = 105 mm at an aperture opening setting of f/22, which produces depth-of-focus of approximately 6.7 mm. The same dual-cavity Nd:YLF laser used in planar-PIV was used to produce a laser sheet with the thickness of approximately 1.5 mm. The thickness of laser is adjusted to capture the small motion of tracer particles in the in-phase *y-z* plane and to accommodate the large out-of-plane motion of the tracer particles. The same tracer particles used in planar-PIV was used to carry out stereo-PIV. A 3D calibration target (type 025-3.3) was used to perform the initial calibration of imaging system. The mapping of the calibration image was conducted using a pinhole model in Davis 8.4 (LaVision GmbH). A self-calibration procedure was applied in Davis 8.4 (LaVision GmbH) as described by Wieneke (2005), with a root-mean-square (RMS) fit of 0.45 pixel for camera 1 and 0.72 pixel for camera 2. A total of 2850 image sets at a rate of 20 sets/s were collected. Each set included six time-resolved images at an acquisition rate of 5 kHz. The signal-to-noise ratio (SNR) was improved by using subtract time filter and applying subtract minimum. The velocity vectors were obtained using PIV time-series sliding sum-of-correlation with multi-pass algorithm and a final interrogation window (IW) size of 12×12 pixel (0.318×0.318 mm^2, $37\lambda_0 \times 37\lambda_0$) at 75% overlap in Davis 8.4 (LaVision GmbH). Time filter and correlation in sliding sum-of-correlation were set to two and one, respectively, which give one vector field from six single-frame images of each cycle. The vorticity field was attained by calculating the velocity gradient using a second order central difference method.

A set of 8500 time-resolved images at an acquisition rate of 5 kHz were recorded to obtain the turbulent structures at MDR. Time filter and correlation in sliding sum-of-correlation were taken one. The multi-pass algorithm were used to reach a final interrogation window (IW) size of 48×48 pixel (1.272×1.272 mm^2, $148\lambda_0 \times 148\lambda_0$) at 75% overlap in Davis 8.4 (LaVision GmbH).

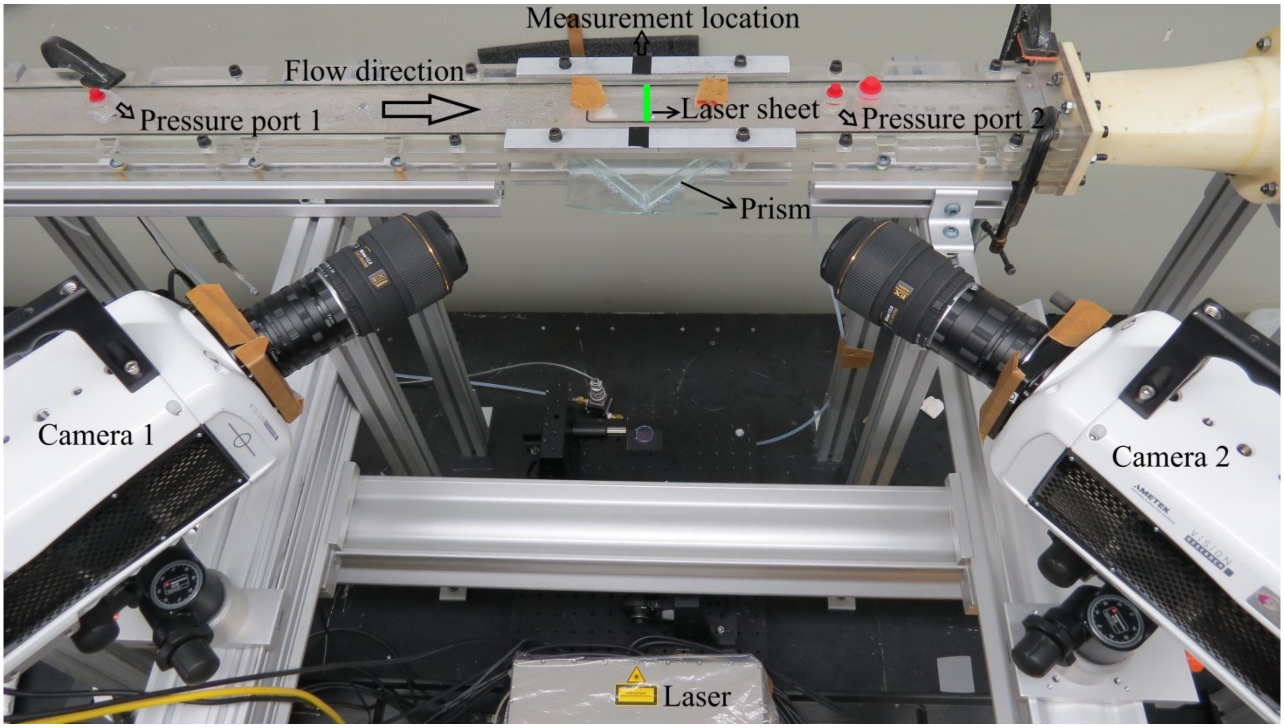

Figure 3-5. An image of the test section equipped with the stereo-PIV measurement system. The pressure ports, pressure transducer, high-speed cameras, measurement location, and the center of coordinate system are shown in this image.

3.6 Uncertainty analysis

Statistical convergence of second and higher order turbulence statistics at y^+_0 =25 is analyzed for flow of water and XG solution at 100 ppm concentration (XG-100) and presented in Figure 3-6. Most of the statistics reach a plateau after about 4,000 PIV data points. The random error is calculated as the standard deviation of the last 1,000 data points and shown in Table 3-3. The table also presents the difference of maximum and minimum of the last 1,000 data points and the mean value.

Table 3-3. Estimation of random error based on statistical convergence of last 1,000 PIV data points for water and XG-100. The "Max-Min" column shows maximum minus minimum of the value.

	Water			XG-100		
	Mean	Standard deviation	Max-Min	Mean	Standard deviation	Max-Min
$\langle u^2\rangle / u_{\tau 0}^2$	4.23	0.0070	0.025	6.68	0.0098	0.0422
$\langle v^2\rangle / u_{\tau 0}^2$	0.53	0.0004	0.002	0.25	0.0004	0.0015
$\langle uv\rangle / u_{\tau 0}^2$	-0.61	0.0014	0.005	-0.37	0.0014	0.0058
$\langle u^2 \mathrm{v}\rangle / u_{\tau 0}^3$	0.75	0.0040	0.018	-0.10	0.0050	0.0222
$\langle u^3\rangle / u_{\tau 0}^3$	-3.76	0.0225	0.087	1.86	0.1930	0.637
$\langle u^4\rangle / u_{\tau 0}^4$	53.4	0.1016	0.365	108	0.3178	1.36

This analysis shows that the number of data points (6000 PIV data points) is sufficient for the statistical convergence of the second and higher order turbulence statistics.

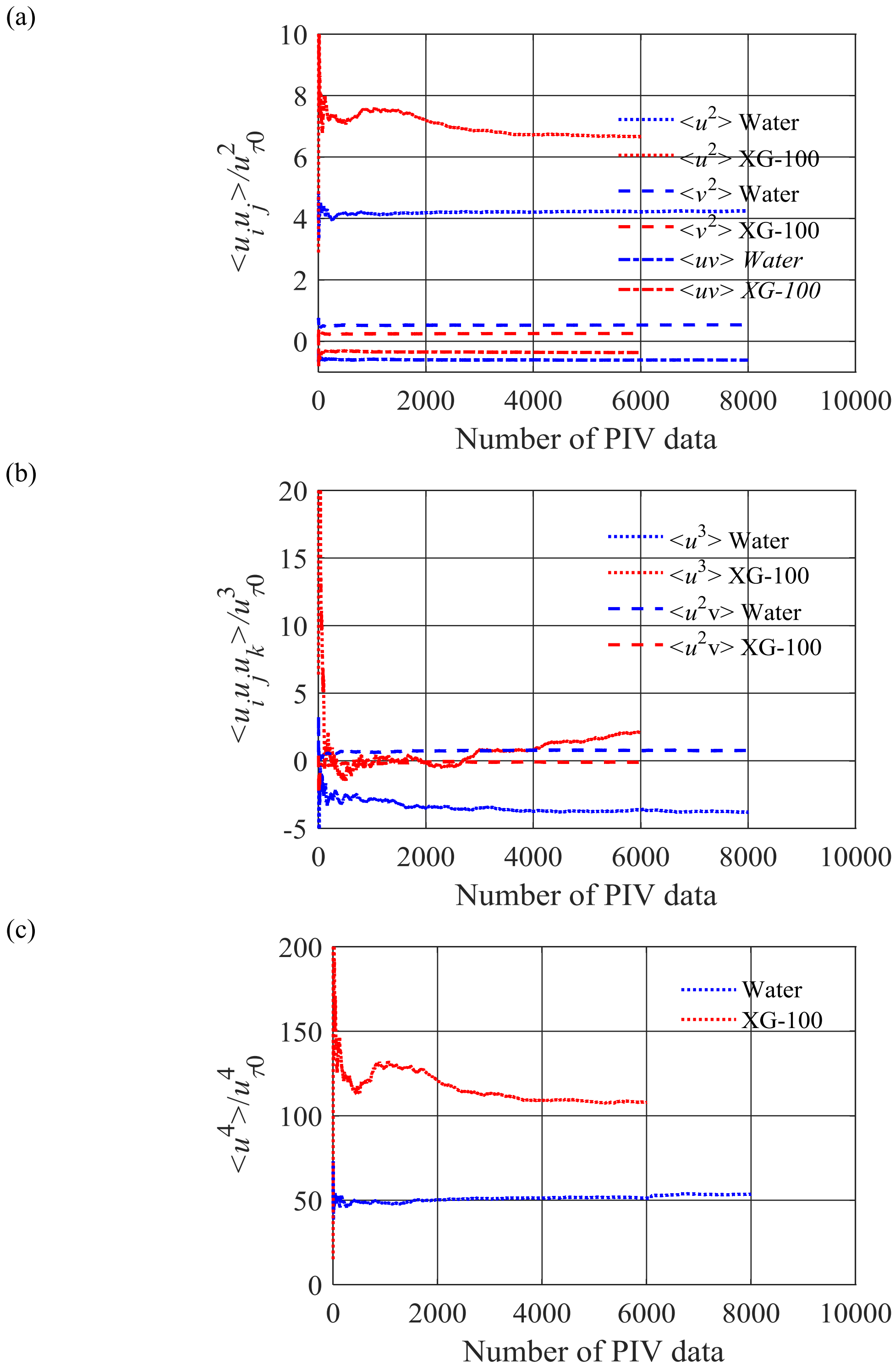

Figure 3-6. Statistical convergence of (a) $<u^2>/ u^2_{\tau 0}$,$<v^2>/ u^2_{\tau 0}$, and $<uv>/ u^2_{\tau 0}$, (b) $<u^3>/ u^3_{\tau 0}$, and $<u^2\mathrm{v}>/ u^3_{\tau 0}$, and (c) $<u^4>/ u^4_{\tau 0}$ at y^+_0=25 for water and XG-100 versus number of PIV data points.

Chapter 4. Rheology of drag-reducing solutions of flexible and rigid polymers

4.1 Introduction

The DR amount depends on the molecular structure (rigidity and flexibility) of the polymer additives. Flexible polymers provide better DR performance relative to rigid polymers. On the other hand, the flexible polymers are more susceptible to mechanical degradation compared to rigid polymers (Pereira *et al.* 2013). Both of the DR mechanisms (De Gennes 1986; Lumley 1967) have been proposed for flexible polymers, and their validity for rigid polymers with negligible chain flexibility has to be evaluated (Pereira *et al.* 2013). The first step for this evaluation is to fully characterize the rheology of rigid and flexible polymer solutions in terms of extensional viscosity (η_E) and viscoelasticity.

Many previous investigations have characterized polymer solutions using shear viscosity. This is perhaps due to the availability of equipment and the traditional characterization of non-Newtonian liquids using shear viscometers, although shear viscosity appears to have little relevance to the DR mechanisms proposed by Gennes 1986 and Lumley 1967. A detailed review of the literature shows that there are only a few measurements of extensional viscosity and viscoelasticity of drag-reducing polymer solutions. Due to experimental limitations, these measurements were made at polymer concentrations at least an order of magnitude higher than that needed for maximum DR. A summary of the investigations reporting measurements of λ was presented in Table 2-1. The table showed that a limited number of extensional viscosity measurements have been reported, and that most of the measurements were made at concentrations higher than that needed for maximum drag reduction (MDR).

Oscillatory tests can measure the storage modulus (G') and the loss modulus (G'') to characterize the linear viscoelastic properties of a polymer solution. The dependency of DR on the storage and loss modulus has been investigated by a few investigators. A summary of investigations of oscillatory measurements, including solution concentration and the DR values are presented in

Table 2-1. In these investigations, oscillatory measurements were carried out at concentrations higher than that used for drag reduction measurements.

A remaining issue in the practical application of polymer solutions is the gradual decrease of DR due to the scission of the long chain polymer molecules (Vanapalli *et al.* 2006). This is known as mechanical degradation and occurs under high shear conditions. It is not known if the rheology of the polymer solution can be used to predict the mechanical degradation of the solution.

Among the investigations of Table 2-1, only Owolabi *et al.* (2017) observed a direct relationship between extensional viscosity and DR. However, this work was carried out only using PAM and no oscillatory measurements were conducted. In other investigations summarized in Table 2-1, solution rheology was characterized at concentrations higher than that used for DR tests. Another issue that makes it difficult to draw any conclusion from these studies arises from the fact that all the rheological properties (i.e., shear viscosity, extensional viscosity and viscoelasticity) varied for the different solutions tested. This makes it more challenging to identify the primary parameters that correlate with DR.

In the current investigation, we isolate the effect of shear viscosity to study the effects of extensional viscosity and viscoelasticity. This is carried out by adjusting the concentration of different rigid and flexible polymers, through trial and error, to obtain the same shear viscosity. Three grades of PAM and a PEO polymer with flexible molecular structure, and XG and CMC with rigid structure are used. The drag reduction of these polymer solutions, which have a common shear viscosity, is measured in a turbulent pipe flow. Their extensional viscosity and viscoelastic properties are measured using CaBER and oscillatory tests at the same polymer concentration that was used for DR tests. The rate of mechanical degradation of the polymer solutions is also evaluated by monitoring pressure drop in the pipe loop to seek a relationship with solution rheology.

4.2 Experimental conditions

The DR measurements were carried out in the pipe flow setup (discussed in Chapter 3) at a flow rate of 21.9 L/min. The flow rate was kept constant during the experiments, which resulted in a constant U_b of 0.72 m/s for water and polymer solutions. The Reynolds number of the

Newtonian flow is $Re = U_b D/\upsilon$ = 20,600. The wall shear stress is calculated using $\tau_w = \Delta P\ D/ 4L$, where L =1 m is the distance between the pressure ports. The calculated wall shear stress for the Newtonian (water) flow is 1.4 Pa. Drag reduction percentage can be obtained using equation (2.21). A moving average with kernel of 500 data points (at 2 Hz) was applied to the pressure data recorded for 2 hours. The average pressure drop of the first 500 data point is referred to as DR_0.

Three grades of PAM (Magnafloc 5250 (BASF Corp.), Superfloc A-110 (Kemira), and Superfloc A-150 (Kemira)) and a PEO polymer (Sigma-Aldrich) with flexible molecular structure, and XG and CMC with rigid structure are used in this investigation. The concentrations of these polymers are adjusted to produce an identical shear viscosity.

4.3 Results and discussion

In this section, we first select a reference polymer solution based on the DR performance of SF-150. The shear viscosity of this solution determines the target value at which the other flexible and rigid polymer solutions will be tested. Secondly, we measure DR and the extent of mechanical degradation for each of the polymer solutions. Finally, the extensional viscosity and viscoelastic properties of the solutions are investigated to evaluate their relationship with DR and mechanical degradation.

4.3.1 Determination of the reference shear viscosity

Drag reduction of SF-150 solutions at 20, 30, 40, and 50 ppm is shown in Figure 4-1. The 20 ppm tests are repeated here to provide an indication of the uncertainty of the process. The discrepancy of the two tests is about 2% over the 2 hours of measurement. This error originates from both polymer preparation and pressure measurement uncertainty. It is observed that at 20 ppm, an initial DR of ~58% is obtained, which reduces to 37% due to mechanical degradation after 2 hours of circulation in the flow loop. The drag reduction at 30 ppm also starts at ~60%, similar to the 20 ppm solution; however, less mechanical degradation is observed in this case. The mechanical degradation at 40 ppm is negligible and DR remains about 60-62% during the measurement period. The slight increase of DR is associated with further mixing of the solution within the flow loop. Drag reduction at 50 ppm is smaller due to its higher shear viscosity or possibly due to solution preparation procedure. We therefore select SF-150 at 20 ppm as the reference flexible polymer since it is more prone to degradation than the higher concentration SF-150 solutions. The polymer solutions with low MW (e.g. PEO) need to be made at higher concentrations than those with high MW (e.g. SF-150) to provide similar shear viscosity. Therefore, the selection of the lower SF-150 concentration allows us to use lower concentrations of low MW polymers at identical shear viscosity. This helps us to keep all the polymer solutions at dilute conditions, where the polymer molecules do not interact with each other.

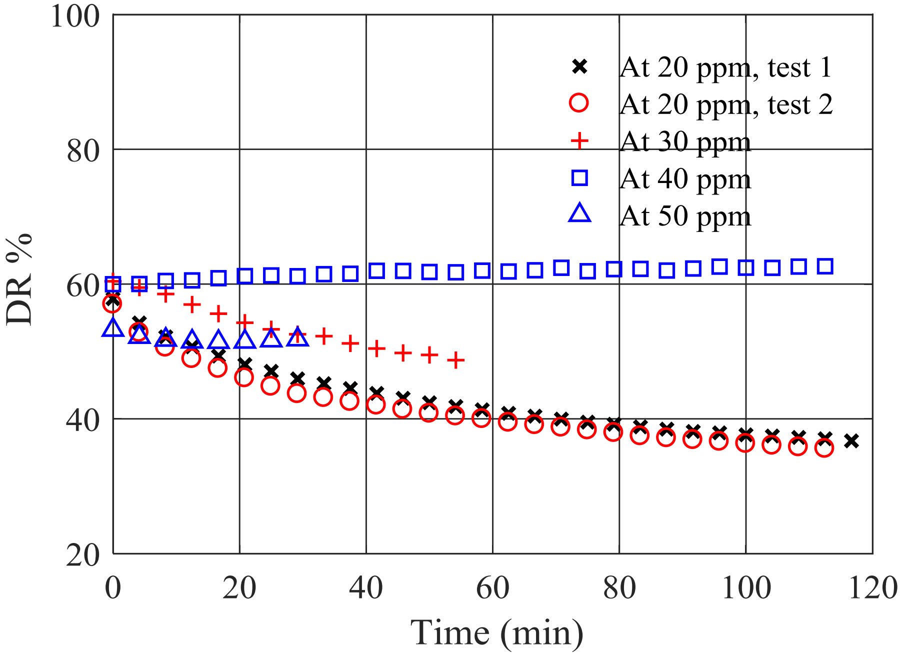

Figure 4-1. Drag reduction of SF-150 polymer solutions tested at different concentrations. The test at 20 ppm is repeated to evaluate the uncertainty of the polymer mixing procedure and pressure drop measurements.

The shear viscosity of the reference polymer solution (20 ppm of SF-150) was measured using the double-gap rheometer described in section 3.3. Then, the concentration of the other polymer solutions was varied by trial and error to produce the same shear viscosity. This procedure for magnafloc (MF) and PEO is illustrated in Figure 4-2, which shows shear viscosity measurements of MF solutions (22, 26, and 28 ppm), and PEO solutions (50, 100, 170, 185, and 200 ppm). Comparison of Figures 4-2(a) and (b) shows that a larger change in concentration of PEO is required with respect to MF to result in a similar change in shear viscosity. This is attributed to the larger MW of MF.

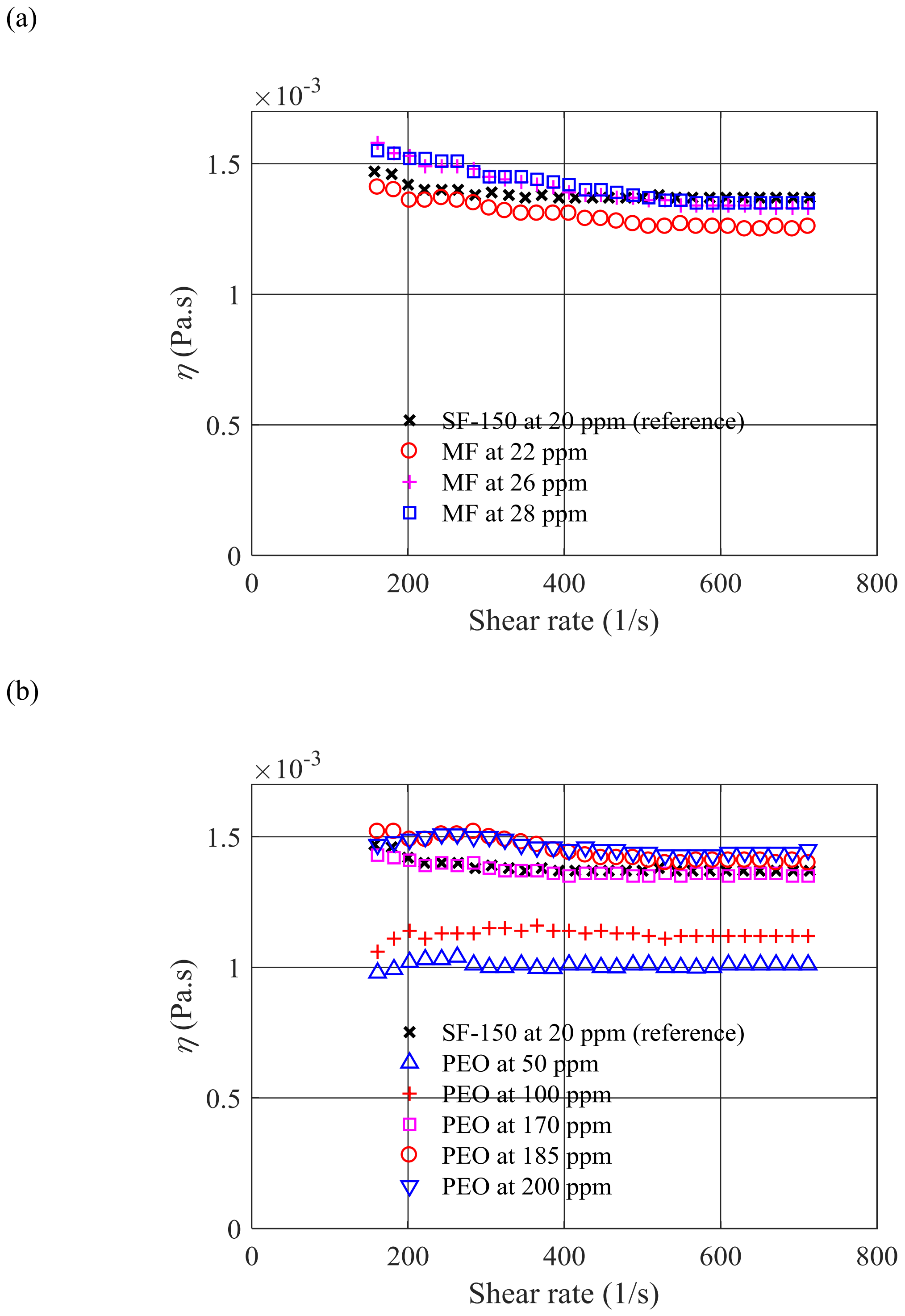

Figure 4-2. Variation in shear viscosity of (a) MF and (b) PEO solutions with concentration. The shear viscosity of the reference 20 ppm SF-150 solution at is also shown for comparison.

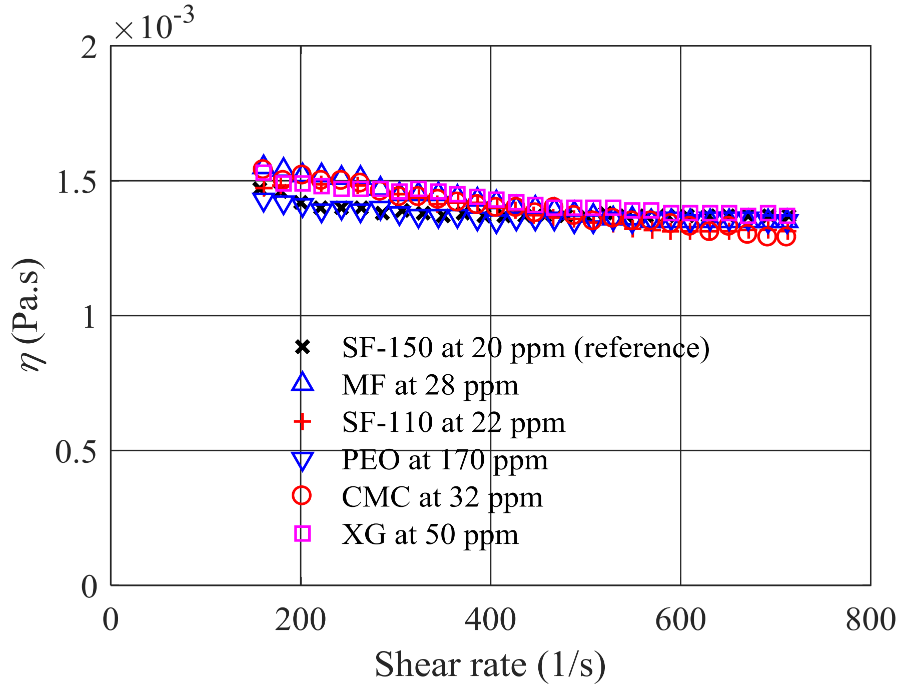

Figure 4-3. Shear viscosity of each polymer solution at its adjusted concentration. The maximum difference in shear viscosity between the reference polymer and the other polymer solutions is 5%, occurring at low shear rate of ~200 1/s.

Similar trial and error experiments have been carried out for all the polymers to obtain the concentration required to produce the same shear viscosity as the reference case. For each polymer, this concentration is referred to as the "adjusted" concentration. The shear viscosity of each polymer solution at its adjusted concentration is demonstrated in Figure 4-3. It can be observed that the measured shear viscosities are within 5% of that of the reference SF-150 solution. The adjusted concentration is used to investigate DR, mechanical degradation, and the solution rheology, as described in the next sections. The adjusted polymer concentrations used in the current study are lower than the overlap concentration (*c**) reported in the literature for PEO, XG, and CMC solutions. Escudier *et al.* (2009) obtained *c** of 670 ppm for XG and 300 ppm for polyacrylamide solutions. Thus, polyacrylamide solutions (20-28 ppm) and XG (50 ppm) solutions used in this study can be considered dilute. Dinic *et al.* (2015) also estimated *c** of 1700 ppm for PEO solution which is also much larger than the 170 ppm PEO used in this study.

4.3.2 Drag reduction and mechanical degradation

The DR of each polymer solution at its adjusted concentration, measured over 2 hours, is shown in Figure 4-4. For all the polymers, the maximum value of DR is found at the beginning of the test, followed by a gradual reduction due to mechanical degradation. The initial DR of PEO is the lowest among the flexible polymers (~44%) and its DR capability disappears after 20 min. The SF-150 has the highest DR up to 45 min, when degradation reduces its DR slightly below that of MF, showing that it is slightly more susceptible to mechanical degradation than MF. Drag reduction of both SF-150 and MF is greater than that of SF-110, as they have larger MW. Mechanical degradation of SF-110 and SF-150 solutions follows similar trends. XG and CMC present similar DR of about 10% with negligible loss of performance, which is consistent with the measurements of Soares *et al.* (2015a). The mechanical degradation of the solutions is characterized as DR change per time ($\Delta DR/\Delta t$, %/min), estimated over the measurement time and shown in Table 4-1. The results show that the flexible polymers have the largest initial DR_0 of 50-58% with a degradation rate of 12-17%/min. PEO has DR_0 of 44% while its degradation rate per unit time is significant at about 174%/min. The rigid polymers have a small DR of 10-12% with negligible degradation of 1.4 to 3.0%/min. This investigation clearly shows that both DR and mechanical degradation are independent of the solution shear viscosity.

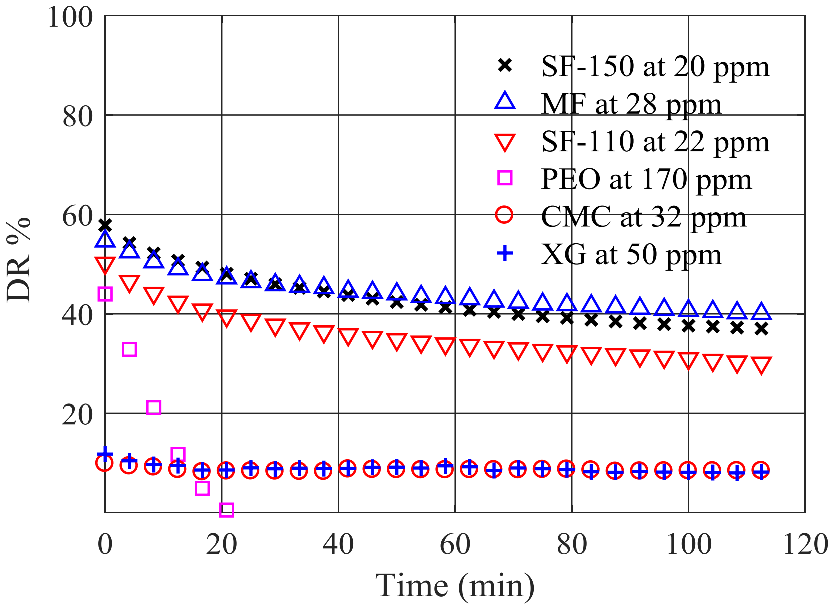

Figure 4-4. Drag reduction of flexible and rigid polymer solutions as the solution circulates in the flow loop. All polymer solutions have the same shear viscosity (see Figure 4-3).

4.3.3 Extensional viscosity

The variation in filament diameter as a function of time, as obtained from CaBER measurements, is demonstrated in Figure 4-5. The reference time of $t = 0$ is set when the top plate reaches the final 9 mm gap. The filament of the XG and CMC (rigid polymers) broke at about $t = 0$, which indicates that those polymer solutions have negligible extensional viscosity. At $t > 0$, SF-150 and PEO have the thickest and the thinnest filaments, respectively. MF has a greater filament diameter than SF-110. The break up time for SF-150 and SF-110 are 0.1 and 0.07 s while it is 0.08 s for MF. PEO maintains the thinnest filament that stretches beyond 0.12 s.

An exponential decay of filament diameter based on Equation (3.2) should appear to be linear in the semi-logarithmic plot of Figure 4-5. Therefore, the relaxation time of the polymer solutions is calculated by fitting Equation (3.2) on the linear section of the data of Figure 4-5. The magnitude of each estimated relaxation time is shown in Table 4-1. The results show that PEO has the largest relaxation time, followed by SF-150, MF, and then SF-110. The relaxation time of the rigid polymers is expected to be smaller than 1 ms and thus not measurable using the CaBER system as the filament quickly ruptured (Campo-Deaño & Clasen 2010; Dinic *et al.* 2015; Rodd *et al.* 2005).

The high relaxation time of SF-150, MF, and SF-110 is correlated with their larger DR_0 values shown in Table 4-1. However, the correlation of high DR_0 with high λ does not seem to apply to PEO; this polymer solution has the lowest DR_0 of 44% among the flexible polymer solutions while it has the largest value of λ. The discrepancy can be explained by the high degradation rate of PEO ($\Delta DR/\Delta t$ = 174 %/min). An assumed initially high DR of PEO could have quickly degraded within the first five minutes of circulation in the loop before the start of the data acquisition. An extrapolation of PEO data in Figure 4-4 to 5 min before the start of data acquisition results in ~65% DR which is in agreement with its higher λ. The smaller DR of XG and CMC polymers is also consistent with their negligible λ (i.e., filament immediately ruptured).

The Weissenberg number can be calculated as $Wi = \lambda \times d\langle U\rangle/dy$, where $\langle U\rangle$ and $d\langle U\rangle/dy$ are mean velocity and shear rate at the wall, respectively. The wall shear rate is obtained from $d\langle U\rangle/dy = \tau_w / \mu_w$, where μ_w is the shear viscosity of the polymer solution at the wall. As mentioned earlier, τ_w is determined from pressure drop measurements. Since polymer solutions lose their DR performance due to mechanical degradation, pressure drop measurements within first 5 minutes of data acquisition are used to calculate τ_w. The viscosity at the wall (μ_w) is estimated from the shear viscosity measurements of Figure 4-3, and is approximately 1.4 mPa.s for shear rate varying from 400-700 1/s. The estimated magnitudes of $d<U>/dy$ and Wi for the flexible polymer solutions are presented in Table 4-1. As expected, an inverse relationship between DR_0 and the mean velocity gradient at the wall is observed here: the larger the DR_0, the smaller the value of $d<U>/dy$. As Table 4-1 shows, Wi of PEO is larger than that of the other flexible polymers while Wi of XG ad CMC should be negligible. Therefore, similar to the previous discussion of the relationship between λ and DR_0, larger DR_0 can be associated with larger Wi. Again, PEO is the exception here due to its high degradation rate.

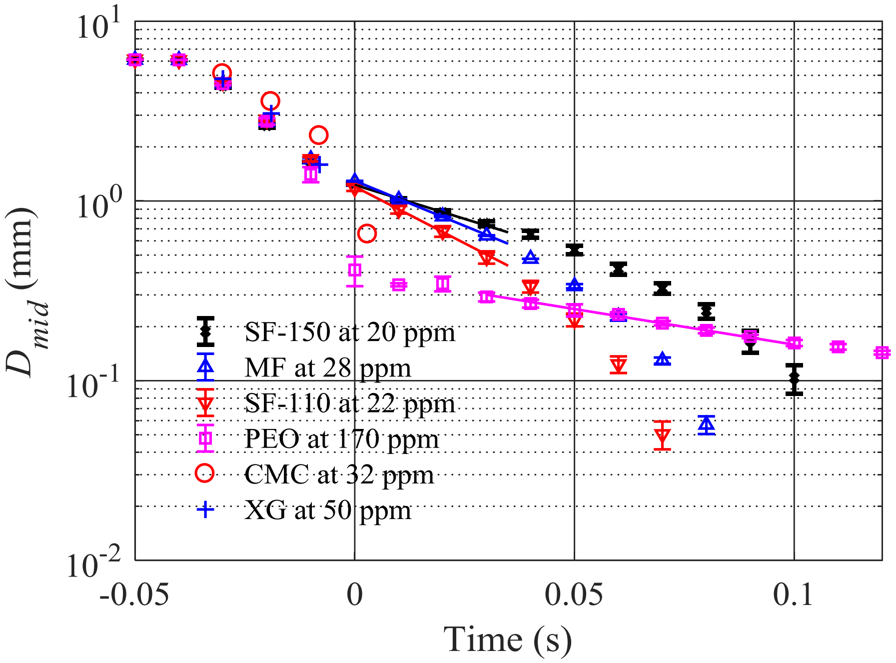

Figure 4-5. Temporal evolution of filament diameter of each polymer solution at its adjusted concentration, measured using a CaBER. The XG and CMC filaments ruptured before the top plate reached the final separation distance. Only one out of 100 data points is presented for the clarity of the plot. The error bars represent the standard deviation of filament diameters based on five measurements.

Table 4-1. Relaxation time, wall shear rate, Weissenberg number, DR_0 (at $t = 0$), $\Delta DR/\Delta t$, and averages of G' and G'' for flexible and rigid polymer solutions. All polymer solutions have the same shear viscosity.

Polymer solutions	Relaxation time (ms)	Wall shear rate (1/s)	Weissenberg number (Wi)	DR_0	$\Delta DR/\Delta t$ (%/min)
SF-150	19	407	8	58	17
MF	14	448	6	55	12
SF-110	11	486	5	50	17
PEO	36	528	19	44	174
XG	Not Available	Not Available	Not Available	12	3
CMC	Not Available	Not Available	Not Available	10	1

The dependency of DR with *Wi* number was evaluated by Owolabi *et al.* (2017). They used two types of PAM solutions: FloPAM at three concentrations (150, 250, and 350 ppm) and Separan at 250 ppm and they measured DR in a cylindrical pipe, a rectangular channel, and a square duct. They proposed an empirical equation to predict DR as a function of *Wi* and a critical Weissenberg, $Wi_c = 0.5$, which indicates the onset of DR. This equation shows increase of DR when *Wi* increases up to ~6, beyond which an asymptotic behavior at DR of ~64% is observed independent of *Wi*. An estimation of DR, based on the Owolabi *et al.* (2017) model, shows that this model overestimates DR of SF-150, MF, and SF-110 by 10, 17, and 27% with respect to the measurements. It should be noted that the uncertainty of Owolabi *et al.* (2017) appears to be about ±8% as some of the their experimental results for $Wi \sim 5$ fall in the range of 59-75% DR. Another reason for the discrepancy is the mechanical degradation of the polymer solutions and the change in their λ and *Wi* values within the first 5 min of flow circulation before data acquisition and during the data acquisition process. Although Owolabi *et al.* (2017)'s model was proposed based on experiments using PAM, applying the model to PEO results in 45% overestimation of DR. The discrepancy is largely associated with the rapid mechanical degradation of PEO and consequent change in its rheology. Nevertheless, the evaluation suggests correlation of DR with both λ and *Wi*. Comparison of different polymers ability for DR based on λ can be straightforward since it only requires CaBER measurements. However, DR prediction based only on λ may not be feasible since the shear rate of the flow field, which is included in

Wi, also plays an important role. An accurate estimation of shear rate, i.e. $d<U>/dy$, for the polymer flow requires measurement of pressure drop or velocity profile in the pipe flow of the polymer solution.

The strain rate and extensional viscosity obtained from Equations (3.4) and (3.5) are used to generate Figure 4-6 for the flexible polymers. It is observed that η_E slightly increases with strain rate for the PAM solutions. However, for PEO, η_E rapidly reduces with increasing strain rate. This indicates strain-rate hardening behavior of MF, SF-110 and SF-150, while PEO has strain-rate thinning behavior. Two important conclusions are drawn from this figure. First, the magnitude of η_E at the strain rate of ~ 200 1/s is larger in SF-150 relative to that in MF and SF-110 solutions and PEO has the lowest value of η_E among the flexible polymers. This behavior agrees with the DR trends; polymer solutions with higher extensional viscosity show more DR. The strain rate of 200 1/s is relevant to the shear rate present in turbulent pipe flow as its magnitude is close to the mean $d<U>/dy$ seen in Table 4-1. Secondly, the substantial mechanical degradation of PEO solution can be associated with its strain-rate thinning behavior. The PAM solutions with strain-rate hardening behavior did not show any significant degradation.

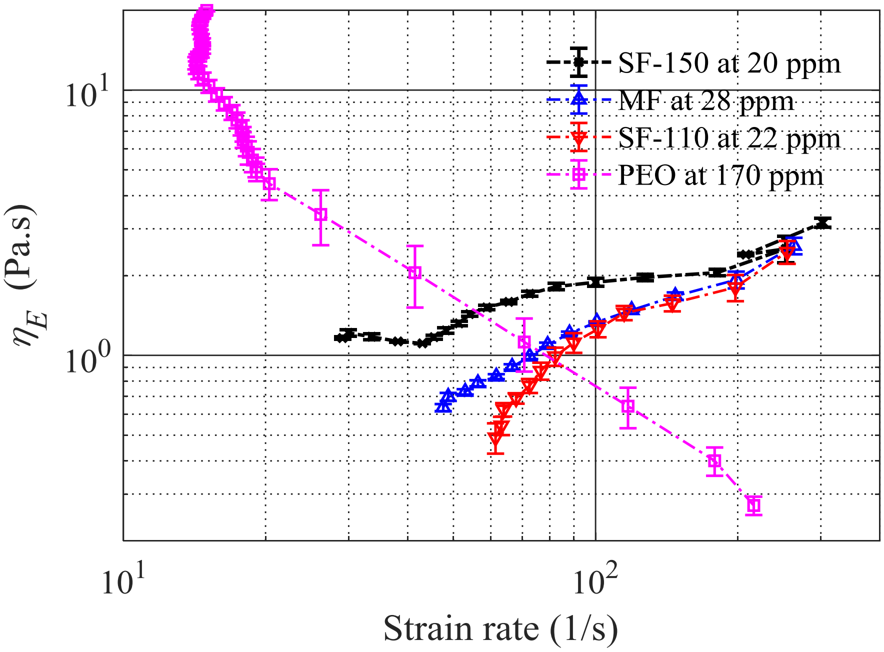

Figure 4-6. Variation of extensional viscosity with strain rate for the flexible polymer solutions. The PAM polymers show strain-rate hardening behavior while PEO shows strain-rate thinning. Only one out of 50 data points is presented for the clarity of the plot. The error bars represent the standard deviation of the values based on five measurements.

4.3.4 Oscillatory rheology

Measurement of storage modulus (G'), loss modulus (G''), and their ratio (G'/G'') for the stress and frequency sweep tests are shown in Figures 4-7 and 4-8, respectively. The ratio G'/G'' indicates whether the solution will dissipate ($G'/G'' < 1$) or temporarily store ($G'/G'' > 1$) the energy. For a fixed oscillation angular frequency of 0.628 rad/s in Figure 4-7(a) and (b), with increasing stress, G' and G'' of all polymer solutions are constant (linear region) at stress smaller than 0.01 Pa and then gradually decrease. The linear region observed in Figure 4-7(a) and (b) is called as linear viscoelastic region (LVR).The PAM solutions (SF-110, SF-150, and MF) have the largest values of G' and G'', while PEO has the smallest values. The G' and G'' of the rigid polymers (XG and CMC) fall between the PAM solutions and PEO. As shown in Figure 4-7(a), the magnitude of G' for the polymer solutions is larger than G' of water for stress smaller than 0.03 Pa. For higher stress, G' for water and some of the polymer solutions have the same magnitude, showing large uncertainty of the measurements at stress larger than 0.03 Pa. Figure 4-7(b) shows that polymer solutions have greater G'' compared with water over the entire range of strain rates.

Due to smaller G' and G'', the rigid polymers cannot store or dissipate turbulence fluctuations and produce a smaller DR, while PAM polymers with larger G' and G'' moduli produce higher DR. The small G' and G'' of PEO is not correlated with its relatively high DR. A smaller ratio of G'/G'' is observed for CMC and XG solutions in Figure 4-7(c), which indicates greater viscous dissipation than elastic behavior. The larger G'/G'' ratio for SF-150, SF-110, and MF solutions shows the higher elasticity of these polymer solutions, which is correlated with their better DR performance. Therefore, it can be concluded that solutions with large G'/G'' produce larger DR due to their dominant elastic behavior. This is expected since a large viscous dissipation (i.e., small G'/G'') converts turbulent kinetic energy into heat, which is not desirable for DR.

The measured G' and G'' from the frequency sweep tests at a fixed oscillation displacement of 0.1 rad are shown in Figure 4-8. The G' and G'' of all polymer solutions increase with increasing oscillation angular frequency, which indicates stronger viscoelastic behavior at higher angular frequencies. In Figures 4-8(a) and (b), the PAM polymers are shown to have the largest G' and G'', PEO has the smallest moduli across all the frequencies, while those of rigid XG and CMC polymers fall between PEO and PAM polymer solutions. Figures 4-8(a) and (b) show that G' and

G'' for water increase with increasing angular frequency. As shown in Figure 4-8(a), the magnitude of G' for polymer solutions and water approaches the same value at about 9.42 rad/s. Hence, only the measurements for smaller than 9.42 rad/s are reliable. In Figure 4-8(b), G'' for polymer solutions is larger than G'' of water solution across the investigated angular frequency range. The larger modulus of PAM polymers also suggests that G' and G'' are related with DR. Again, the PEO solution appears as an anomaly in this trend. The trend of G'/G'' observed in Figure 4-7(c) is also verified in Figure 4-8(c).

For a Newtonian fluid, $G' = 0$ and $G'' = \mu\omega$, where μ is the shear (dynamic) viscosity, while for a Hookean solid $G'' = 0$ and $G' = G$. The G' and G'' moduli are both nonzero in a viscoelastic material (Morrison 2001). For water (a Newtonian fluid), the theoretical G'' can be obtained as $G'' = \mu\omega$. The shear viscosity for water is known at the temperature of 25°C (~ 0.0009 Pa.s). Hence, theoretical G'' for water shown by dash line in Figure 4-8(b) shows the uncertainty of the experimental results. At angular frequencies smaller than 2.5 rad/s, the experimental results follow the theoretical results while the uncertainty increases with the increase of angular frequency at ω larger than 2.5 rad/s.

The variation of G' and G'' with oscillation angular frequency depends on the polymer type and concentration. Morrison (2001) defined four zones based on oscillatory shear measurements of a high MW linear homopolymer. A terminal zone was defined to refer to the low frequency end of the spectrum (~10^{-11} to 10^{-8} 1/s), where G' is proportional to ω^2 and G'' is proportional to ω. This proportionality is consistent with a theoretical model of linear viscoelasticity (Morrison 2001), and results in $G'' > G'$. At higher angular frequencies, G'' becomes smaller than G', and both are independent of angular frequency. This zone is referred to as the rubbery regime and is followed by transition to a glassy zone. The latter zone was reported in the angular frequency range of 0.1 to 1000 rad/s for the homopolymers (Morrison 2001), and is also characterized with $G'' < G'$. The important feature of this spectrum is the change from the viscous dominated behavior ($G'' > G'$) of the terminal regime, at the low frequency end of the spectrum, to the glassy zone with dominant elastic behavior ($G'' < G'$), at the high frequency end of the spectrum. As shown in Figure 4-8(c), for most of the polymer solutions, G'/G'' is slightly smaller than one, indicating that viscous effects are stronger than the elastic behavior in the linear viscoelastic limit. The PAM and PEO solutions have larger G'/G'' ratios than the rigid polymers, which results in stronger elastic behavior and higher DR. Due to fast mechanical degradation, DR of PEO is smaller than PAM solutions in spite of its larger G'/G''.

Escudier *et al.* (2001) measured G' and G'' for 2500 ppm XG solution and 4000 ppm CMC solution in the frequency range of 0.007-70 rad/s (~ 0.001-11 Hz). They observed G' and G'' of XG increase with increasing frequency from 0.01 to 5 Pa and from 0.05 to 4 Pa, respectively. The G' and G'' of CMC also increased from 0.0008 to 5 Pa and from 0.003 to 7 Pa, respectively. A smaller increase of G' and G'' with oscillation frequency is observed for the rigid XG polymers.

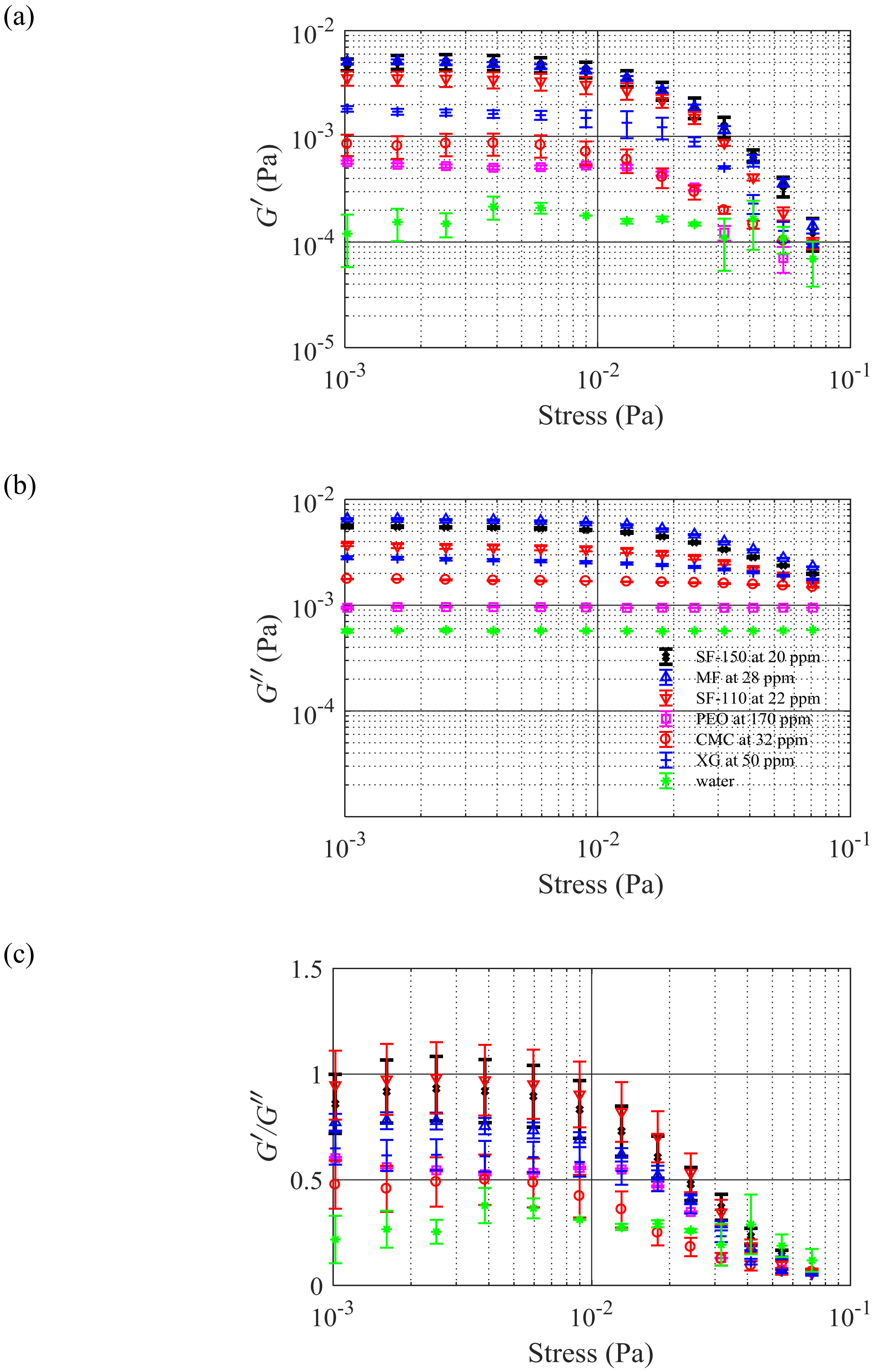

Figure 4-7. (a) Storage modulus, (b) loss modulus, (c) the ratio of storage to loss modulus for polymer solutions as a function of stress during a stress sweep test with constant oscillation angular frequency of 0.628 rad/s. The error bars represent the variation of *G′*,*G″, and G′*/*G″* based on five independent measurements.

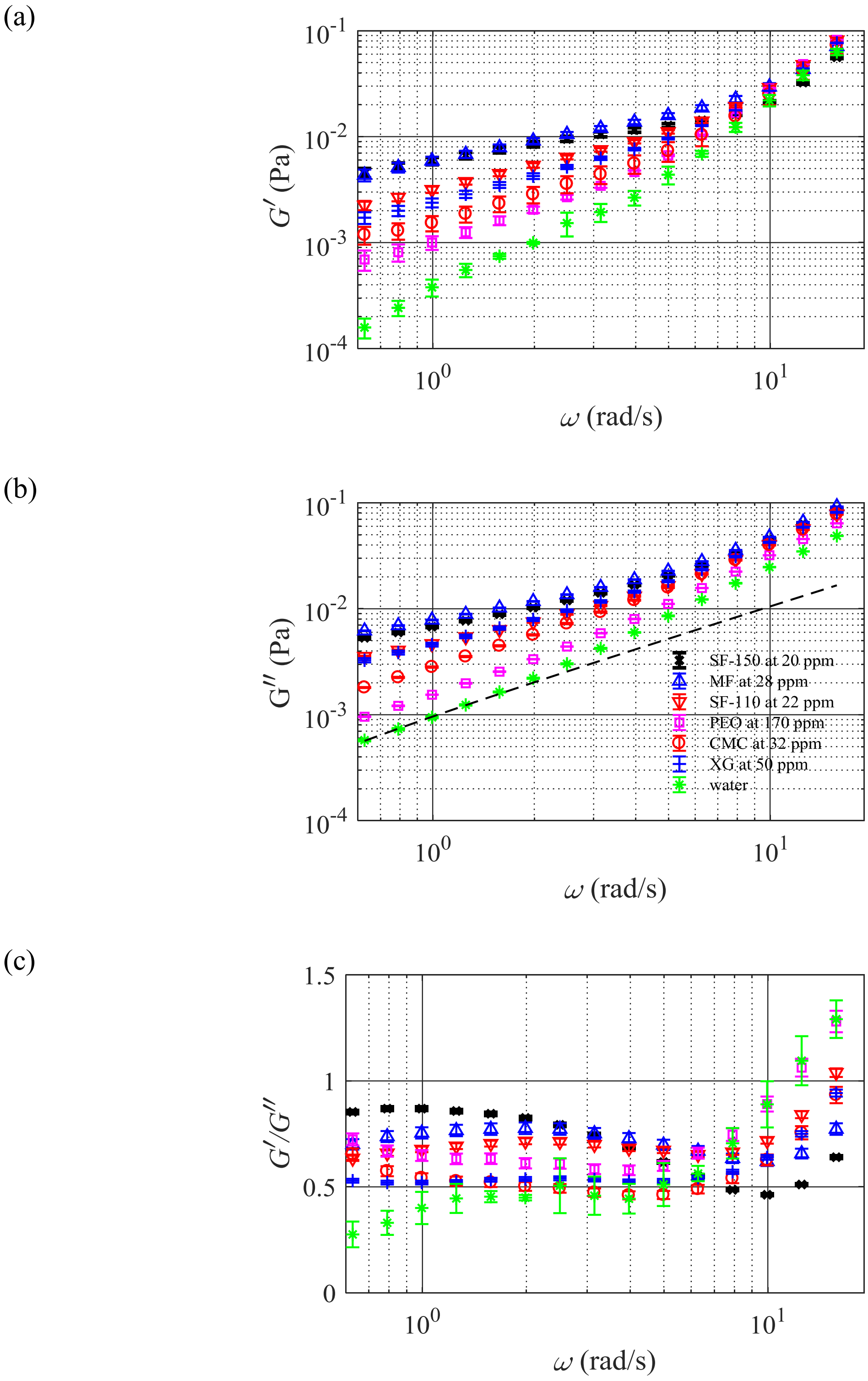

Figure 4-8. (a) Storage modulus, (b) loss modulus, (c) the ratio of storage to loss modulus for polymer solutions as a function of angular frequency during a frequency sweep test with oscillation displacement of 0.1 rad. The error bars represent the variation of G', G'', *and* G'/G'' based on five measurements. The dashed line in Figure 4-8(b) shows theoretical results for water.

4.4 Conclusion

The concentration of the flexible and rigid polymers was adjusted to make solutions with an identical shear viscosity. Under this circumstance, the flexible PAM solutions showed larger DR performance relative to rigid polymers. The rigid polymers demonstrated negligible degradation of DR over a period of 2 hours, while the PAM polymers showed a moderate degradation, and DR of PEO quickly diminished over 20 min. Drag reduction was proportional to the relaxation time, Weissenberg number, and extensional viscosity at high shear rate (~200 1/s). Oscillatory tests also showed that the polymer solutions with larger storage and loss modulus produce a larger DR. The large mechanical degradation of PEO was associated with a significant reduction of extensional viscosity with increase of strain rate (i.e. strain-rate thinning), and a smaller storage and loss moduli.

Chapter 5. Turbulent structures of non-Newtonian solutions containing rigid polymers

5.1 Introduction

In the literature, several polymers with different structures have been investigated to evaluate drag reduction (DR) performance and provide insight into the DR mechanisms. Most of these polymers are synthetic such as polyethylene (PEO), polyacrylamide (PAM) and polyisobutylene (PIB) and have been successfully tested in both pilot-scale and industrial applications (Abubakar *et al.* 2014). It is currently of interest to replace these additives with biopolymers, such as Guar Gum, Xanthan Gum (XG), Okra, Aloe Vera, and Glycogen. Biopolymers are generated from living organisms and are bio degradable, i.e. they break down into natural products such as water, gases, and salts. Therefore, the use of biopolymers results in the reduction of the environmental footprint associated with the producing, consuming and disposal of drag-reducing polymers (Abdulbari *et al.* 2014).

Among rigid polymers, XG has a wide range of applications in the food production, cosmetics, pharmaceutical and oil industries. It shows a stable organized helical conformation which is the reason for its rigid structure at moderate temperature and low ionic forces (Pereira *et al.* 2013). The drag reduction obtained by XG, similar to the performance observed when flexible polymers are used, increases as its concentration and molecular weight increases (Bewersdorff & Singh 1988; Sohn *et al.* 2001). However, the transient performance (DR versus time) for flexible and rigid polymers has been observed to be significantly different (Pereira *et al.* 2013).

The effect of flexible polymers on turbulence structures has received more attention in the literature due to their superior DR performance. On the other hand, there are only a few studies about using rigid polymer as a drag reducer. The objective of the current investigation is to characterize the turbulent structure of a representative rigid biopolymer, XG, at a relatively low Reynolds number (*Re* = 7,200 for Newtonian flow), and to quantify differences in the turbulent structures at a range of polymer concentrations up to (and including) the concentration providing

MDR. High spatial-resolution PIV is conducted to investigate the DR mechanism by studying (and comparing) the turbulent structure of water and polymer solutions. In this study, and in contrast with most of the results presented in the literature, the Reynolds stresses are normalized using a common friction velocity ($u_{\tau 0}$ of Newtonian flow) to more clearly identify the physical variations in the turbulent flows. The investigation is extended to higher-order moment of velocity fluctuation and conditional average of Reynolds shear stress to identify the relationship between reduction of turbulence production and turbulent coherent structures. In addition, the length-scales and spatial organization of turbulent motions are characterized using spatial-correlation and Proper Orthogonal Decomposition (POD).

5.2 Flow properties

The measurements were conducted in the channel flow setup (discussed in Chapter 3) at a constant flow rate of 21.9 L/min. The flow rate was kept constant during the experiments, which resulted in a constant bulk velocity of 0.61 m/s for water and polymer solutions The Reynolds number of the Newtonian flow is $Re = U_b H/\upsilon$ = 7,200. The inner scaling of the turbulent Newtonian channel flow (water) can be estimated using Blasius' law estimating the friction-factor as $C_f = 0.0791(U_b D_h/\upsilon)^{-1/4} \sim 0.0075$. The estimated C_f is applied to calculate the wall shear stress as $\tau_{w0} = 0.5\rho U_b^2 C_f \sim 1.53$ Pa and the friction velocity is therefore $u_{\tau 0} = (\tau_{w0}/\rho)^{0.5} \sim 0.039$ m/s. The estimated wall unit is $\lambda_0 = \upsilon/u_{\tau 0}$ = 22.8 μm and $Re_\tau = u_{\tau 0}H/(2\upsilon)$ = 220 (Bhushan 2012).The rigid polymer used in this study is xanthan gum (XG), whose structure is effectively discussed in Chapter 3.

5.3 Polymer characterization

The wall shear stress of polymer solutions is also estimated using pressure drop measurement as $\tau_w^* = (\Delta P\ WH) / (2L(W+H))$. As mentioned previously, the experiments of the current study are carried out at a constant flow rate and the percentage of drag reduction (DR) achieved for each polymer solution is obtained using the equation presented in Chapter 2 (2-21).

The wall shear stress can also be obtained using $\tau_w = \mu_w d\langle U\rangle/dy$, where μ_w and $d\langle U\rangle/dy$ are dynamic viscosity and shear rate of polymer solution at the wall, respectively (Escudier *et al.* 2009; Ptasinski *et al.* 2001). Here, the shear rate at the wall is estimated using high-spatial resolution PIV measurement; specifically, by producing a best-fit linear regression of the near-wall velocity points. The estimated shear rate is used to obtain the corresponding near-wall viscosity (μ_w) from viscosity measurement presented in Figure 5-1. Finally, wall shear stress is calculated by multiplying viscosity (μ_w) and shear rate ($d<U>/dy$) at the wall. It is important to note that the application of a constant near-wall viscosity for non-Newtonian flows is an approximation (Housiadas & Beris 2004). The shear stress obtained from PIV is within 15% of that estimated based on pressure drop. The variation of wall-shear stress over the corners and the side walls of a finite duct introduces error in the latter method. A rheometer with a double gap cylinder (RheolabQC, Anton Paar USA Inc.) is used to measure the viscosity of each solution up to shear-rate of 1000 (1/s) (Schramm 1994). The estimated inner-wall scaling of the polymer and water channel flows and the relevant parameters are shown in Table 5-1. As Table 5-1 shows, drag reduction clearly increases with increasing XG concentration.

The Fanning friction factor versus Reynolds number ($Re_w = \rho U_b D_h/\mu_w$) for water and polymer solutions is shown in Figure 5-2. The Fanning friction factor is calculated through $C_f = 16/Re_w$ for laminar flow and $1/C_f^{\ 1/2} = 4\log_{10}(Re_w\ C_f^{\ 1/2}) - 0.4$ (Prandtl-Karman equation) for turbulent flow (Abubakar *et al.* 2014; Escudier *et al.* 2009). Virk et al. (Virk 1975) showed the point of MDR using polymers reaches an asymptote which can be modeled as $1/C_f^{\ 1/2} = 19\log_{10}(Re_w\ C_f^{\ 1/2}) - 32.4$ on the Fanning plot. The friction factor for water is in good agreement with Prandtl-Karman equation for turbulent flows. It is also observed in Figure 5-2 that the friction factor decreases with increasing polymer concentration. For brevity, the XG concentrations of 75 ppm, 100 ppm, and 125 ppm are indicated as XG-75, XG-100, XG-125, respectively. It should be noted that MDR was reached at XG-125 (i.e. a polymer concentration of 125 ppm). It can be seen in Figure 5-2 that the friction factor for this condition (XG-125) overlaps with the Virk's asymptote. Further evidence of the turbulent regime for polymeric flows is provided using spectral analysis in spatial domain in section 5.4.7.

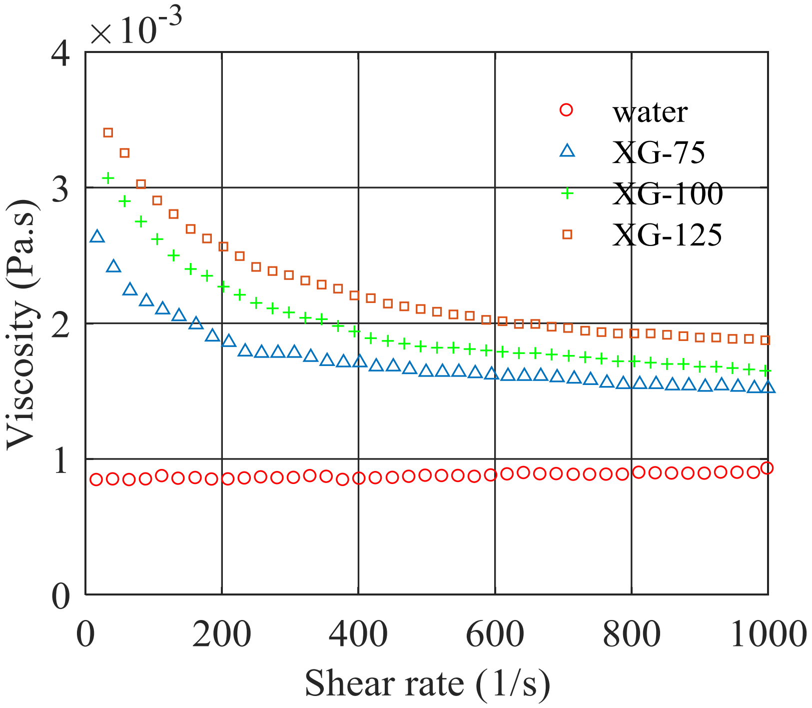

Figure 5-1. Rheological characterization of water and polymer solutions showing the effect of XG polymer concentration on the solution viscosity.

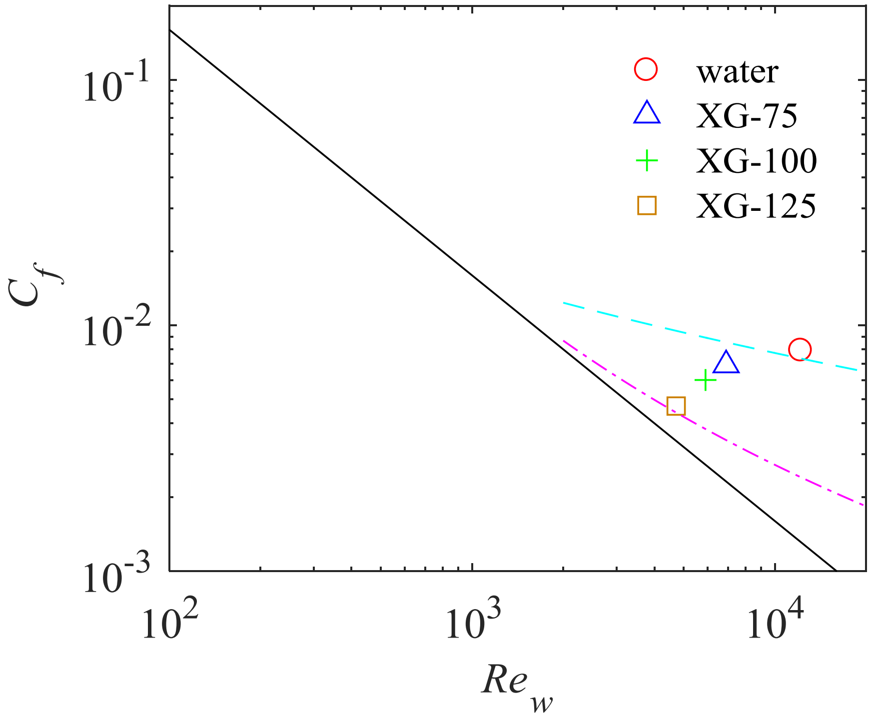

Figure 5-2. The effect of XG polymer concentration on Fanning friction factors obtained from experimental measurements. Solid line shows $C_f = 16/Re_w$ (laminar flow), Prandtl-Karman equation for turbulent flows (---), Virk's asymptote (-·-·-).

Table 5-1. Drag reduction and channel flow scaling for water and the XG polymer solutions. DR% is calculated based on τ_w.

	C_f	DR%	τ_w (Pa)	τ_w^* (Pa)	u_τ (m/s)	μ_w (Pa.s)	λ (μm)	d$<U>/dy$ (1/s)
water	0.0079	0	1.602	1.37	0.0400	0.89×10^{-3}	22.2	1800
XG-75	0.0069	17	1.331	1.14	0.0365	1.53×10^{-3}	42.0	870
XG-100	0.0060	36	1.037	0.89	0.0322	1.7×10^{-3}	52.9	610
XG-125	0.0047	45	0.880	0.75	0.0296	2.2×10^{-3}	74.4	400

5.4 Results and discussion

In this study, the turbulent structure of XG polymer solutions is investigated to identify the different mechanisms contributing to drag reduction. Additionally, the turbulent structures in the non-Newtonian polymer solutions are compared with those found in Newtonian turbulent channel flow. The mean velocity, higher order turbulence statistics, velocity fluctuations in different quadrants, and length scale of the turbulent structures are investigated. Proper Orthogonal Decomposition (POD) is also utilized to further characterize the spatial pattern of the energetic turbulent modes.

5.4.1 Mean velocity profile

The profiles of mean streamwise velocity $\langle U\rangle$ normalized by U_b across half the channel for water and the XG solutions are presented in Figure 5-3(a). The velocity gradient (d$\langle U\rangle$/dy) at the wall reduces with increasing XG concentration. This results in the observed reduction of wall-shear stress in Table 5-1. The profiles also tend toward a parabolic distribution similar to a laminar channel flow. However, the flow is still in the turbulent regime as was shown earlier based on the Fanning plot of Figure 5-2. At a constant flow rate, an increase in polymer concentration reduces the near-wall velocity while increasing the velocity in the core of the flow.

The profiles of $U^+ = \langle U\rangle/u_\tau$, plotted against wall-normal distance $y^+ = y/\lambda$, are shown using a semi-logarithmic scale in Figure 5-3(b). The friction velocity (u_τ) and wall unit (λ) of each polymer are presented in Table 5-1. The water profile follows the von-Karman log law ($U^+ = 1/\kappa\ ln\ y + B$) with $\kappa = 0.4$ and $B = 5.5$, confirming its fully developed state (Abubakar *et al.* 2014). The U^+ profiles for the water and polymer solutions overlap within the viscous sublayer ($y^+ < 5$) while the polymer solutions continue to follow the law of the wall at larger values of y^+. A considerable dependence of U^+ on XG concentration is observed beyond the viscous sublayer ($y^+ \sim 15$). A thicker viscous sublayer and buffer layer, and an upward shift of the log-layer are observed with increasing polymer concentration. This indicates larger viscous dissipation by the smallest eddies in the near-wall region while the balance between production and viscous dissipation (i.e., log layer) occurs farther away from the wall. A log-layer is observed for XG-75 within $35 < y^+ < 120$ with fitted $\kappa = 0.4$, which is similar to the Newtonian flow. However, for XG-100, κ reduces to 0.32 while the log-layer is approximately bounded by $40 < y^+ < 90$. No distinct log-layer is observed for the maximum drag reduction case of XG-125. Virk *et al.* (1970) postulated an additional "interactive zone" which connects the Newtonian-type viscous and turbulent zones. This is different from a Newtonian turbulent wall flow in which the viscous sublayer and the turbulent log-layer are connected only via a buffer region. The amount of drag reduction was associated with the extent of the interactive zone. Virk *et al.* (1970) also anticipated that the ultimate drag reduction is achieved when the interactive zone extends to the channel centerline, as is observed here for the XG-125 condition, as shown in Figure 5-3(b). It should be noted XG-125 reaches the maximum drag reduction (MDR) asymptote ($u^+ = 11.7 \ ln \ y^+ -17$) proposed by (Virk *et al.* 1970).

The current investigation is carried out at a constant flow rate while the addition of polymers decreases the friction velocity and increases fluid viscosity at the wall. Therefore, Re_τ reduces to 117, 93, 66 for XG-75, XG-100, and XG-125. In order to distinguish the effect of reduction in Re_τ from drag reducing effect of polymers, mean velocity profile from DNS of Newtonian flow by Tsukahara *et al.* (2005) at $Re_\tau = 70$ is added to Figure 5-3(b). The added mean velocity profile follows is close to the profile of XG-75 at $Re_\tau = 117$. Therefore, the effect of polymer is beyond merely reduction of Re_τ or laminarization of the flow field.

The maximum drag reduction (MDR) is valid for both flexible and rigid polymer solutions. However, these two polymer types approach MDR in different ways with increase of concentration according to Procaccia et al. (Procaccia *et al.* 2008). The mean velocity profile of flexible polymers follows the MDR asymptote until a crossover point where it becomes parallel to the Newtonian log-law with $\kappa = 0.4$ and $B = 5.5$ (i.e., Newtonian plug). The crossover point is further away from the wall as DR of the flexible polymer increases. On the other hand, the semi-logarithmic profile of rigid polymers prior to MDR does not follow the MDR near the wall. It falls between the Newtonian log-law and MDR profiles. The results of current study in Figure 5-3(b) and also Escudier et al. (Escudier *et al.* 2009) confirm this trend for rigid polymers. The exception to this trend is the result of Warholic et al. (Warholic *et al.* 1999), which shows mean velocity of a flexible polymer is between the Newtonian log-law and MDR profile before reaching MDR.

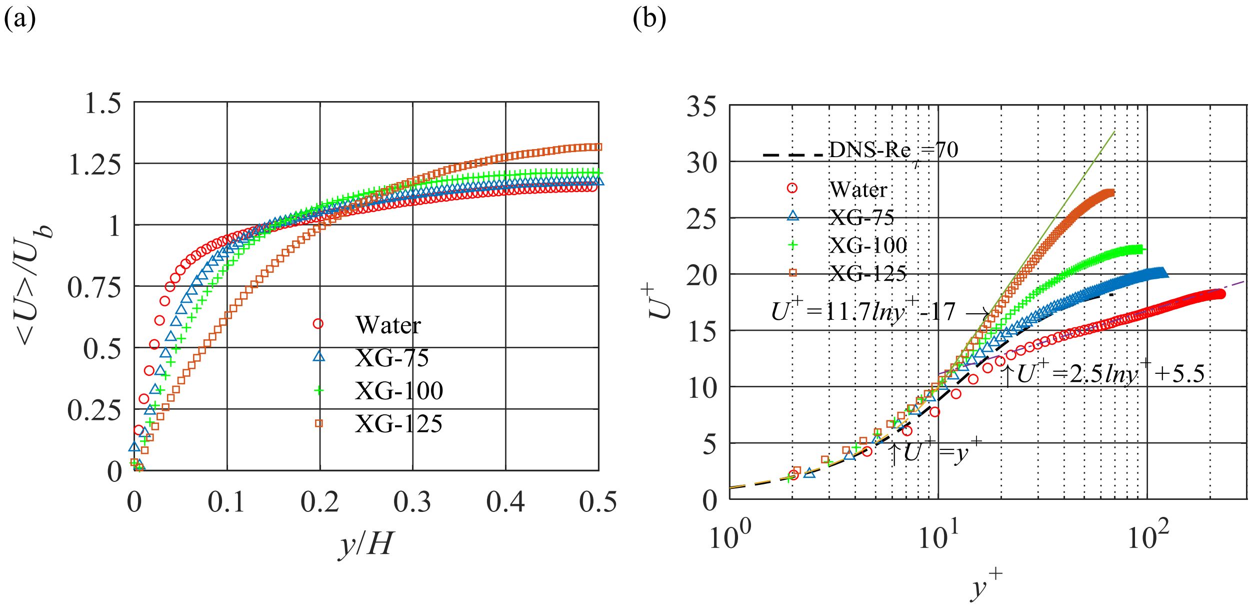

Figure 5-3. The effect of XG polymer concentration on mean streamwise velocity profiles (a) normalized by the bulk velocity versus location/H across the channel, and (b) normalized by friction velocity and plotted against y^+. Only one out of five data points is presented for clarity of the plot. The law of the wall ($U^+=y^+$), log-law of Newtonian flows ($U^+=2.5\ln y^+ + 5.5$), and Virk's asymptote ($U^+=11.7\ln y^+ - 17$) are also indicated in this figure. Profiles of U^+ from DNS of Tsukahara *et al.* (2005) at $Re_\tau = 70$ in water are also shown for comparison.

5.4.2 Reynolds stresses

The dimensionless streamwise normal Reynolds stress profiles, $\langle u^2\rangle/u^2_{\tau 0}$ are shown in Figure 5-4(a). The measurement in Newtonian flow is also compared with the DNS results of Tsukahara *et al.* (2005) at $Re_\tau = 180$ due to the unavailability of DNS at $Re_\tau = 220$. The DNS data is normalized using its corresponding $u_{\tau 0}$ at $Re_\tau = 180$. There is an overlap between the DNS and PIV measurement in water for $y^+>40$ while PIV underestimates $\langle u^2\rangle/u_{\tau 0}$ closer to the wall. The latter is associated with the limited spatial-resolution of PIV in resolving the small-scale near-wall structures. The spatial-resolution issue is alleviated for polymer solutions since λ increases significantly with increasing polymer concentration (see Table 5-1). The first few data points at

$y^+<10$ are expected to be erroneous as $\langle u^2\rangle$ does not converge to zero. This is mainly due to presence of mirrored particle images in the near-wall interrogations windows. The $\langle u^2\rangle$ peak is farther away from the wall for the polymeric solutions, which indicates a thicker buffer layer as it was also observed in the semi-log plot of Figure 5-3(b). Previous experiments also confirm that the location of the $\langle u^2\rangle$ peak moves away from the wall as the extent of DR increases (Escudier *et al.* 2009; Warholic *et al.* 1999, 2001; Wei & Willmarth 1992). As discussed below, however, the variation of the peak value with increasing polymer concentration (or increasing DR) does not seem to follow a monotonous trend.

An analysis of the peak value of $\langle u^2\rangle$ is conducted here for polymeric flows at constant flow rate. The variation of $\langle u^2\rangle$ is also considered when normalized using the inner scaling of Newtonian flow ($u_{\tau 0}$) instead of the friction velocity of each polymer solution. This is applied to avoid variation of $\langle u^2\rangle$ due to change in friction velocity at a similar flow rate. The value of the $\langle u^2\rangle$ peak in Figure 5-4(a) increases by ~10% as the XG concentration increases and reaches maximum at 100 ppm of XG. When the polymer concentration is increased to 125 ppm, the peak value of $\langle u^2\rangle$ is seen to reduce significantly, to the point that it is at approximately the same level as the Newtonian flow. Warholic *et al.* (1999) used a polyacrylamide polymer (Percol 727, a copolymer of PAM and sodium acrylamide) and divided their investigation to low (<40%) and high DR regimes. In the lower DR regime they observed an initial increase (~2%) of $\langle u^2\rangle$ peak for 14% DR and another increase (~2%) of $\langle u^2\rangle$ peak for 19% DR followed by a 4% decrease of non-normalized $\langle u^2\rangle$ peak. At higher DR of 63%, they observed up to 60% reduction in the peak $\langle u^2\rangle$ value. Wei & Willmarth (1992) observed about ±10% variation in peak $\langle u^2\rangle$ value in DR range of 30 to 40% using PEO polymer. Escudier *et al.* (2009) also observed an increase of dimensional $\langle u^2\rangle$ peak until 59% DR followed by a sudden large reduction at 67% DR for XG polymer solution at high concentrations (300 to 1500 ppm).

The peak value of $\langle u^2\rangle$ for all polymer solutions is as large as the peak value for water. The value of $\langle u^2\rangle^{0.5}$ (i.e., streamwise turbulence intensity) at the peak location is also about $0.15U_b$, which confirms the flow is still turbulent. Escudier *et al.* (2009) measured $\langle u^2\rangle^{0.5}/U_b$ of about 0.02-0.03 in a laminar flow (Probably due to TS (Tollmien–Schlichting) waves) which increased up to 0.1

to 0.15 after transition to turbulent for a polymeric flow. These indicate that the flow field in all polymer solutions is turbulent.

The wall-normal component of normal Reynolds stresses, $\langle v^2 \rangle$, normalized using $u_{\tau 0}$ are plotted as a function of the wall-normal distance y^+_0 in Figure 5-4(b). The PIV measurements of $\langle v^2 \rangle$ in water agree with the DNS of $Re_\tau = 180$ at $y^+>25$. The overestimation in the near-wall is again associated with the presence of mirrored particle images. The $\langle v^2 \rangle$ profile and the peak value of each profile attenuate with increasing XG concentration. The location of the $\langle v^2 \rangle$ peak is also displaced away from the wall. The effect of polymer concentration on the peak $\langle v^2 \rangle$ value is observed to be non-linear as there is a large attenuation from water (Newtonian) to 75 ppm of XG followed by a slight reduction at 100 ppm, and another significant reduction at 125 ppm. The reduction of $\langle v^2 \rangle$ profiles with increasing drag reduction agrees with the results of Warholic *et al.* (1999, 2001) presented for both low and high drag reduction regimes. They observed ~85% attenuation for 69% DR and also displacement of the peak location away from the wall. Wei & Willmarth (1992) observed ~40% reduction in the $\langle v^2 \rangle$ peak at 39% DR. Escudier *et al.* (2009) observed reduction of the $\langle v^2 \rangle$ peak with increase of XG ppm (also DR).

The profile of Reynolds shear stress, $\langle uv \rangle$, is shown in Figure 5-4(c). The PIV measurement of $\langle uv \rangle$ at $Re_\tau = 220$ is not expected to overlap with the DNS data at $Re_\tau=180$ since the wall shear stress is different. The slope of the $\langle uv \rangle$ profile at the centerline of the channel is also expected to decrease with increase of Re_τ as observed in Figure 5-4(c). However, that PIV measurement underestimated $\langle uv \rangle$ peak since the peak for $Re_\tau = 220$ should be slightly larger than that of $Re_\tau=180$. This is associated with the finite spatial resolution and correlation noise between u and v components. The peak value reduces with increasing polymer concentration while the peak location monotonously shifts away from the wall. Warholic *et al.* (1999) also observed attenuation and displacement of $\langle uv \rangle$ peak away from the wall with the increase of the drag reduction. They observed up to 94% reduction of the $\langle uv \rangle$ peak at 69% DR. The measurements of Wei & Willmarth (1992) demonstrated ~54% reduction in the peak $\langle uv \rangle$ at 39% DR. In addition, Escudier *et al.* (2009) observed $\langle uv \rangle$ decreases with increasing DR; in fact they reported that the Reynolds shear stresses essentially become negligible at 67% DR.

The DNS of Tsukahara *et al.* (2005) at $Re_\tau = 70$ is also presented in Figure 5-4 in order to evaluate the effect of reduction in Re_τ. This DNS data is normalized using the $u_{\tau 0}$ used for normalization of the polymer flows. The peak value of $\langle u^2 \rangle$, $\langle v^2 \rangle$ and $\langle uv \rangle$ for Newtonian DNS at $Re_\tau = 70$ is significantly smaller than those of XG-125 at $Re_\tau = 67$. This indicates that the observed trend is not due to the variation of Re_τ. In fact, the Newtonian flow at $Re_\tau = 70$ is laminar while the flow of XG-125 at $Re_\tau = 67$ is still turbulent.

The analysis of the results of the present study and comparison of these results with those reported in the literature both indicate that when polymer drag reduction occurs, the peaks of the normal and shear Reynolds stresses move away from the wall, indicating a thicker viscous sublayer and buffer layer. There also is a consistent reduction of $\langle v^2 \rangle$ and $\langle uv \rangle$ with increasing DR. The current results and some previous experiments (Warholic *et al.* (1999) and Escudier *et al.* (2009)) show the same trend in variation of $\langle u^2 \rangle$ with DR percentage. The presence of large $\langle u^2 \rangle$ and small $\langle v^2 \rangle$ at maximum DR show a larger anisotropy compared to Newtonian turbulent channel flow.

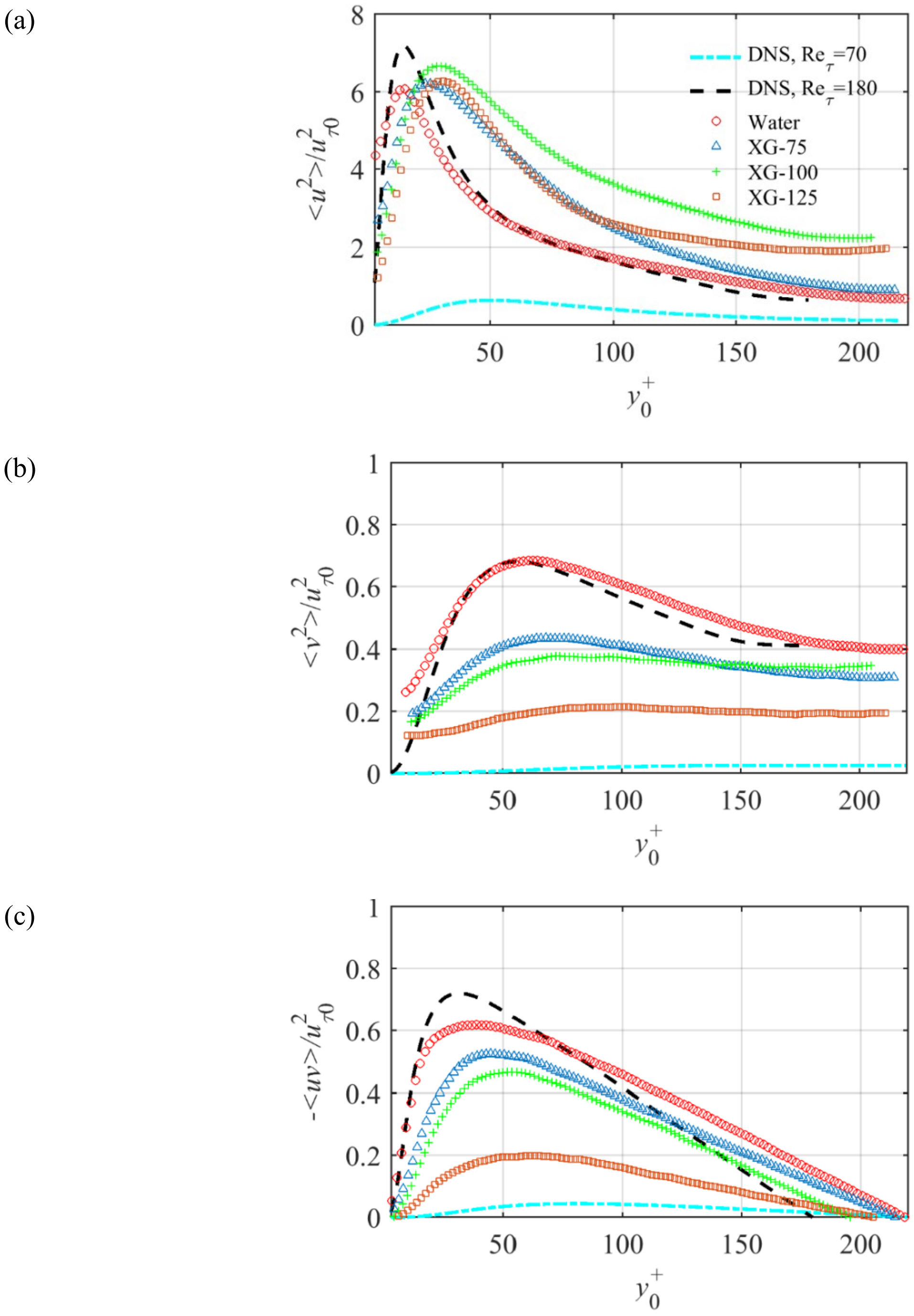

Figure 5-4. The effect of XG polymer concentration on the (a) streamwise (b) wall-normal, and (c) shear Reynolds stresses normalized by the reference friction velocity of water ($u_{\tau 0}$) and plotted against wall-normal distance normalized by the reference inner scale (λ_0). The DNS of Newtonian channel flow by Tsukahara *et al.* (2005) at Re_τ= 180 is provided to evaluate the uncertainties of PIV measurement in water at Re_τ= 220. This DNS data is normalized with its corresponding friction velocity ($u_{\tau 0}$) at Re_τ= 180. The DNS data of Tsukahara *et al.* (2005) at Re_τ= 70 is also presented to investigate the effect of Re_τ variation of polymeric flows. This DNS data is normalized using $u_{\tau 0}$ at Re_τ= 220 similar to the polymer flows. Both DNS data are presented for channel height of the current experiment.

5.4.3 High-order turbulence statistics

The triple products of velocity fluctuations can identify the direction of the transport of turbulent kinetic energy. The transport of streamwise component of turbulent kinetic energy (i.e., $\langle u^2 \rangle$) by u and v velocity fluctuations for XG-75, 100, and 125 ppm is demonstrated in Figure 5-5(a), (b), and (c), respectively. The triple products and the wall-normal distance are normalized by the reference friction velocity ($u_{\tau 0}$) and wall unit (λ_0) of the Newtonian flow. The triple products from PIV measurements of water flow and also $\langle u^3 \rangle$ from the simulations of Iwamoto *et al.* (2002) at $Re_\tau = 150$ and 300 are presented in all plots for comparison. Although the trend of $\langle u^3 \rangle$ for water is similar to that obtained from the simulations, the magnitudes are different due to the smaller aspect ratio of the channel and the spatial averaging of the PIV. The near-wall peak in the DNS profiles, which occurs at about $y^+_0 \sim 7$, is not seen in the PIV data for water due to finite spatial resolution and signal truncation within the near-wall interrogation windows (Theunissen *et al.* 2008). The lack of near-wall peak of $\langle u^3 \rangle / u_{\tau 0}{}^3$ for XG-75 is also associated with bias error of PIV in the near wall region ($y^+_0 < 10$). However, the near-wall peak is away from the wall and out of the biased error region of PIV for the solutions with higher polymer concentrations (XG-100 and XG-125), as it is observed at $y^+_0 \sim 15$ and 25 in Figure 5-5(b) and (c), respectively.

The positive values of $\langle u^3 \rangle / u_{\tau 0}{}^3$ and small negative values of $\langle u^2 v \rangle / u_{\tau 0}{}^3$ in the near wall region of $y^+_0 < 13$ show the dominance of the sweep events ($u > 0$, $v < 0$), while the negative value of $\langle u^3 \rangle / u_{\tau 0}{}^3$ and the positive value of $\langle u^2 v \rangle / u_{\tau 0}{}^3$ indicate the dominance of ejection events ($u < 0$, $v > 0$) at $y^+_0 > 13$ for the Newtonian flow. The transition between these two sweep and ejection dominated regions is indicated by the solid (red) vertical line in Figure 5-5. This transition line for the XG-75 solution is indicated by dashed (blue) vertical line, which is displaced farther from the wall to $y^+_0 = 20$. The local minimum of $\langle u^3 \rangle / u_{\tau 0}{}^3$, which shows strong ejection motions, intensifies and is also displaced from the wall for XG-75. A similar shift of $\langle u^2 v \rangle / u_{\tau 0}{}^3$ peaks away from the wall is observed for XG-75 although the magnitudes are smaller. Wei & Willmarth (1992) investigated the skewness of u, defined as $\langle u^3 \rangle / \langle u^2 \rangle^{3/2}$, for different polymer solutions with DR in the range of 30-40%. Their results showed that the transition between the sweep dominated region in the immediate vicinity of the wall and the ejection dominated region occurred at $y^+_0 \sim 20$. They also observed that the negative peak is intensified and displaced from the wall with increasing DR. The presence of these two regions was also observed by Warholic *et al.* (2001).

The transport mechanism of $\langle u^2\rangle$ for XG-100 in Figure 5-5(b) is similar to that of XG-75 while the transition between sweep and ejection (vertical dashed line) is shifted farther from the wall to y^+_0=34. The positive $\langle u^3\rangle$ peak for XG-100 is found at y^+_0=15 while the negative $\langle u^3\rangle$ peak intensifies and shifts farther from the wall compared to XG-75. The negative and positive peaks of $\langle u^2v\rangle$ for XG-100 are also displaced away from the wall. The positive $\langle u^3\rangle$ peak for XG-125 in Figure 5-5(c) has significantly intensified and moved away from the wall to y^+_0= 25. The transition of sweep and ejection regions occurs at y^+_0=80. There is no negative peak in $\langle u^3\rangle$ profile of XG-125 while the negative values extend to the channel centerline. The trend of $\langle u^2v\rangle/u_{\tau 0}^3$ for XG-125 is the same as that of XG-75 and XG-100 while the relatively small peaks are farther shifted away from the wall.

The increase in XG concentration (and consequent increase in DR) has resulted in the extension of the end of the sweep dominated region from y^+_0= 13 (Newtonian) to y^+_0=80 (XG-125), where an ejection dominated region starts. The intensity of the positive $\langle u^3\rangle$ peak also increases with increasing polymer concentration which indicates stronger positive *u* fluctuations. The core of the ejection dominated region (i.e., negative peak of $\langle u^3\rangle$) shows the center of the buffer layer (y^+_0~20) for the water results. The negative peak of $\langle u^3\rangle$ is displaced away from the wall for XG-75 and XG-100 while it has almost disappeared for XG-125. The $\langle u^3\rangle$ profile in Figure 5-5 also allows for the investigation of the degree of asymmetry in the distribution of *u* fluctuations. The increase in XG concentration (and DR) has resulted in larger positive *u* fluctuations in the near wall region while the negative *u* fluctuations seem to attenuate and are displaced toward central region of the channel. However, evaluation of the fourth order moment (i.e., flatness) is required to identify if the larger positive/negative $\langle u^3\rangle$ peak is caused by a large number of small *u* fluctuations or a smaller number of intense *u* fluctuations.

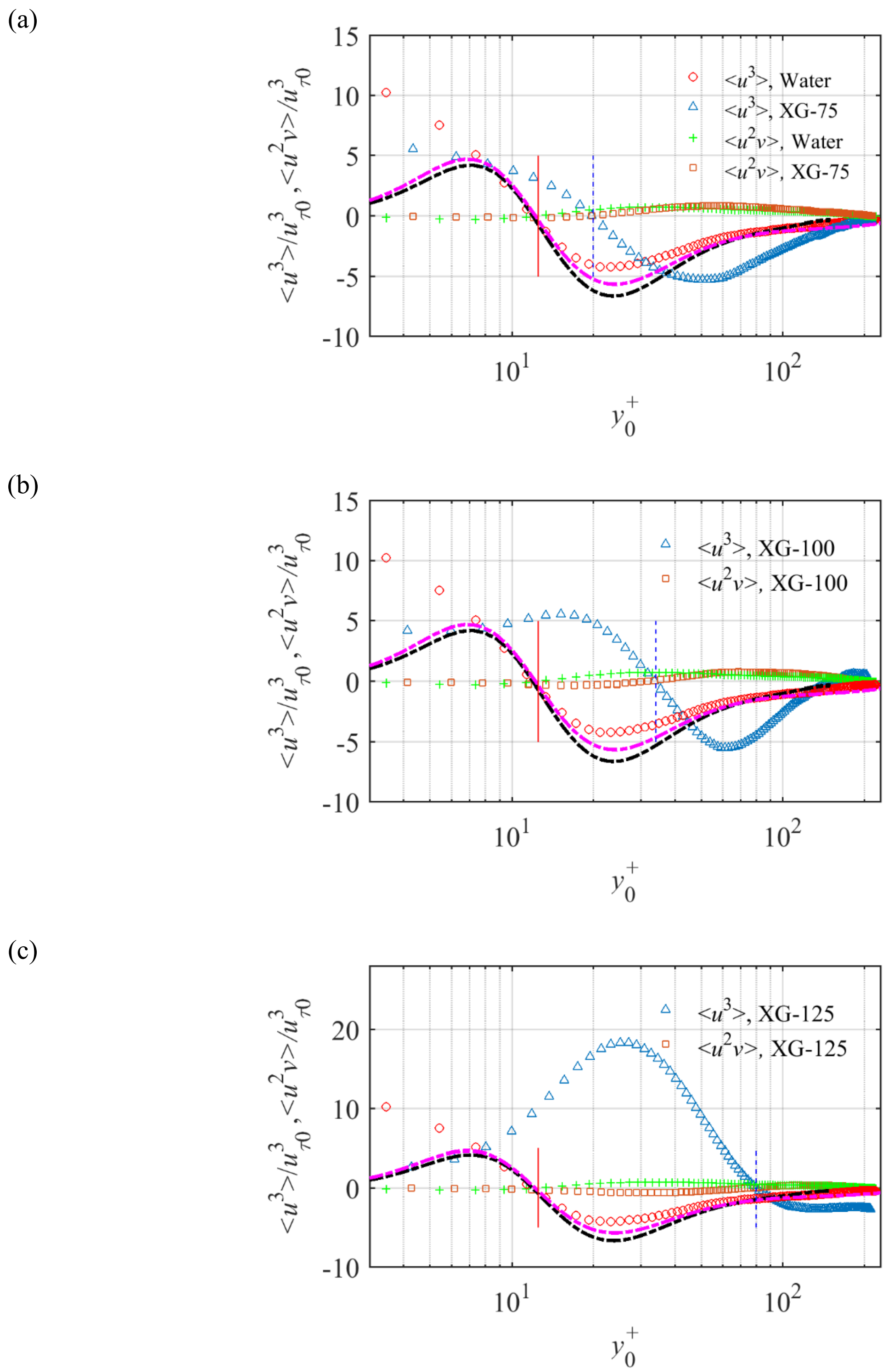

Figure 5-5. The triple products of u and v calculated to investigate the transport direction of streamwise turbulent kinetic energy. Profiles of $\langle u^3 \rangle$ and $\langle u^2 v \rangle$ for (a) XG-75 (b) XG-100, (c) XG-125 are shown. Profiles of $\langle u^3 \rangle$ from DNS of Iwamoto *et al.* (2002) at $Re_\tau = 150$ (---) and 300 (-·-·-) and PIV measurement in water are also shown for comparison. The vertical solid (red) and dashed (blue) lines indicate the location of transition from a sweep dominated to an ejection dominated region for water and polymer solution, respectively.

As shown in Figure 5-6, the peak value of $\langle u^4\rangle/u_{\tau 0}{}^4$ is assumed to be at about $y^+{}_0$~15 for water which indicates presence of u fluctuations with larger amplitude. The near-wall data ($y^+{}_0$<10) are not shown due to the effects of significant bias error in the fourth-order moment. The peak location of $\langle u^4\rangle$ has moved to $y^+{}_0$~28 for all XG concentrations. The magnitude of $\langle u^4\rangle$ increases with increasing polymer concentration, indicating presence of a greater number of intense positive u fluctuations.

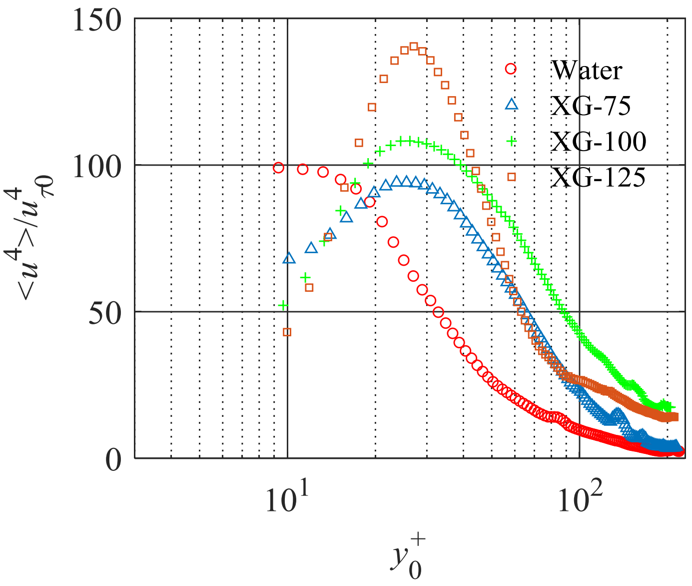

Figure 5-6. Profiles showing $\langle u^4\rangle/u_{\tau 0}{}^4$ for water and polymer solutions.

5.4.4 Quadrant of turbulent fluctuations

The contribution of ejection and sweep motions to total turbulence production is investigated using conditional averaging of the Reynolds shear stress, $\langle uv\rangle$, based on the sign of u and v fluctuations (Wallace *et al.* 1972). The conditional average is indicated as uv_{Qi} where i varies from 1 to 4 referring to the four quadrants of the u vs v plot in the counter clockwise direction. Figure 5-7 demonstrates uv_{Qi} normalized with the reference (water) friction velocity. It should be noted that uv_{Q2} and uv_{Q4} have a negative sign and result in turbulence production, while uv_{Q1} and uv_{Q3} events with a positive sign result in damping turbulence production (Kim *et al.* 1987).

The conditional average of the uv_{Q1} in Figure 5-7(a) shows the contribution of u>0 and v>0 fluctuations to $\langle uv\rangle$. In the near wall region ($y^+{}_0$<13), uv_{Q1} decreases with increasing XG concentration. Within the layer $13<y^+_0<80$, uv_{Q1} increases with increasing polymer concentration. There is also a positive peak in this region which becomes more pronounced and moves away from the wall at higher polymer concentrations. At $y^+_0>80$, the XG-100 solution has the largest value of uv_{Q1} of the 3 polymer concentrations tested

In Figure 5-7(b), the profiles of uv_{Q2} are shown. Recall that uv_{Q2} is associated with ejection, a major contributor to turbulence production. Generally, as can be seen in Figure 5-7(b), the intensity of ejection motions increases with increasing wall normal distance, reaches a maximum, and decreases gradually until the centerline of the channel is reached. The peak value of uv_{Q2} is attenuated with increasing XG concentration and the location of the peak moves away from the wall. The magnitude of uv_{Q2} decreases with increasing XG concentration, implying the reduction of turbulence production due to ejection.

Figure 5-7(c) shows that uv_{Q3} events decrease with increasing XG concentration in $y^+_0 \leq 35$, which results in increasing turbulence production. It should be noted that the value of uv_{Q3} for XG-125 is less than water in $y^+_0 \leq 100$. The location of the maximum peak of uv_{Q3} events moves away from the wall for XG-75 and XG-100, while the peak disappears for XG-125. For the regions far away from the wall, the value of uv_{Q3} of polymer solution is greater than water, showing the reduction of turbulence production for polymer solution.

Values of uv_{Q4}, shown in Figure 5-7(d), indicate the contribution of sweep motions to turbulence production. For water, values of uv_{Q4} decrease with increasing wall normal distance for $y^+_0\leq10$, stays constant until about $y^+_0=50$ followed by a gradual reduction until the channel centerline. In the vicinity of the wall (i.e. within the region $y^+_0<15$), an increase in XG concentration results in smaller contribution of sweep events to the total Reynolds stress. The uv_{Q4} profile for the XG-75 solution follows a similar trend as was observed for water but the values are attenuated across the channel. However, further increases in XG concentration produce larger values of uv_{Q4} in the region $15 < y^+_0 < 100$.

The results for water, shown in Figure 5-7, confirm the dominance of sweep events at $y^+_0<13$ and then the greater contribution of ejection to Reynolds shear stress at $y^+_0>13$. This is in agreement with the results of Kim et al. (Kim *et al.* 1987) that showed this transition from sweep-to-ejection occurs at about $y^+_0=12$ for Newtonian flows. Evaluation of the uv_{Qi} in the four quadrants shows that the significance of ejection is significantly reduced in the polymeric solutions relative to the Newtonian (water) flow. A consistent reduction of contribution of ejection was observed in Figure 5-7(b) with increase of ppm (increase of DR). The second largest contributor to the Reynolds shear stress (i.e., sweeps) also appear to attenuate at the near-wall region (y^+_0<13) with increase of DR. The sweeps also appear to initially attenuate with increase of polymer concentration at about y^+_0~40 while they intensify at the maximum DR (which was obtained with the XG-125 polymer solution).

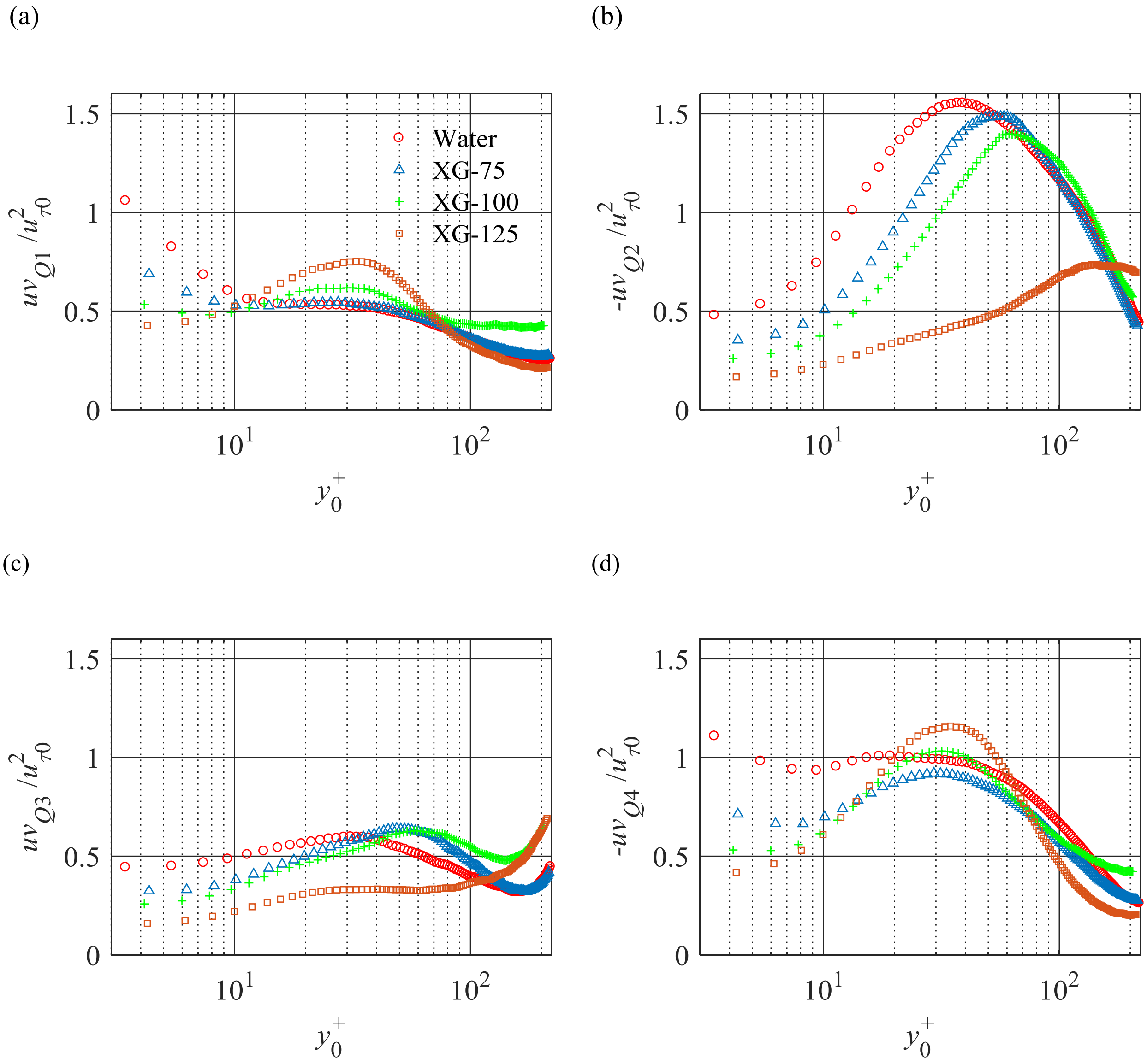

Figure 5-7. Evaluation of the conditional averages of the four quadrants (a) uv_{Q1}, (b) uv_{Q2}, (c) uv_{Q3}, and (d) uv_{Q4}.

The effect of XG polymer concentration on turbulent fluctuations is further investigated using joint probability density functions (i.e., quadrant analysis) determined at two wall-normal locations. The results are presented in Figure 5-8. The first location was chosen at y^+_0=25 to investigate the turbulence at the positive peak location of $\langle u^3\rangle$ for XG-125 in Figure 5-5(c). The second location, y^+_0=140, is in the outer layer.

Figures 5-8(a) and (b) show that the JPDF in the second (ejection) and fourth (sweep) quadrants are larger than the first and third quadrants for the water flow. The positive and negative u velocity fluctuations become weaker with increasing wall-normal distance (Figure 5-8(b)) while the positive and negative v velocity fluctuations approximately have the same magnitude. The angle of the ejection/sweep motions (principal axis of Reynolds stress tensor) with respect to the wall becomes larger as the wall-normal distance increases. In addition, the sweeps of the fourth quadrant occupy a smaller area at y^+_0=140, which indicates attenuation of intense sweep motions.

The quadrant analysis of the flow of the XG-75 solution, presented in Figures 5-8(c) and (d), show reduction of the magnitude of v fluctuations and increase of the strength of u fluctuations in both wall-normal locations in comparison with the Newtonian flow. The same trend is also observed for the XG-100 solution, shown in Figures 5-8(e) and (f). As a result, the angle of principal axis of u-v plot with respect to the wall decreases, which shows shallower sweep/ejection motions at y^+_0=25.

The JPDF analysis shows a different pattern of turbulence fluctuations at the point of MDR (obtained with the XG-125 solution). These results can be found in Figures 5-8(g) and (h). The magnitude of v fluctuation has further decreased at both wall-normal locations relative to the XG-75 and XG-100 cases, while v distribution remains symmetric. At y^+_0=25, a highly skewed distribution of u is observed. There is a large number of weak u<0 fluctuations at about $u/u_{\tau 0}$ = -2 while there is a small number of u>0 fluctuations with maximum intensity of about $8u_{\tau 0}$. The principal axis is also almost horizontal which indicates a lack of inclined shear-layer found in Newtonian wall flows. At y^+_0=140 for XG-125 solution, the u fluctuations are still stronger than the v fluctuations. However, the distribution shows that stronger u fluctuations ($u > 3u_{\tau 0}$ or $u < -3u_{\tau 0}$) seems to occur along with positive v.

Walker & Tiederman (1990) and Fu *et al.* (2014) observed a similar JPDF with symmetric contours with respect to the *u*-axis (i.e. symmetric *v* fluctuations) for a turbulent channel flow with flexible PAM and PEO polymers. Fu *et al.* (2014) showed that the angle of the principal axis of shear stress with respect to the *u*-axis varies from -2º to -8º as y^+_0 varies from 50 to 200 for a channel flow with an average PEO polymer concentration of 14 ppm. This is a more acute (shallow) principal axis angle than that observed for water at the same Reynolds number (i.e., -8º to -18º). Kim & Sirviente (2005) also observed approximate alignment of the principal axes of Reynolds stresses with the *u*-axis. These investigations support the JPDF analysis presented here for the XG-75 and XG-100 solutions, as the results described above are associated with conditions where the point of MDR has not yet been reached, and exhibit considerable residual $\langle uv \rangle$ across the channel. The current investigation depicts further skewness of *u* in JPDF at the MDR condition of XG-125. The skewness is characterized by a large number of small negative *u* fluctuation and small number of large positive *u* fluctuations at the y^+_0~25.

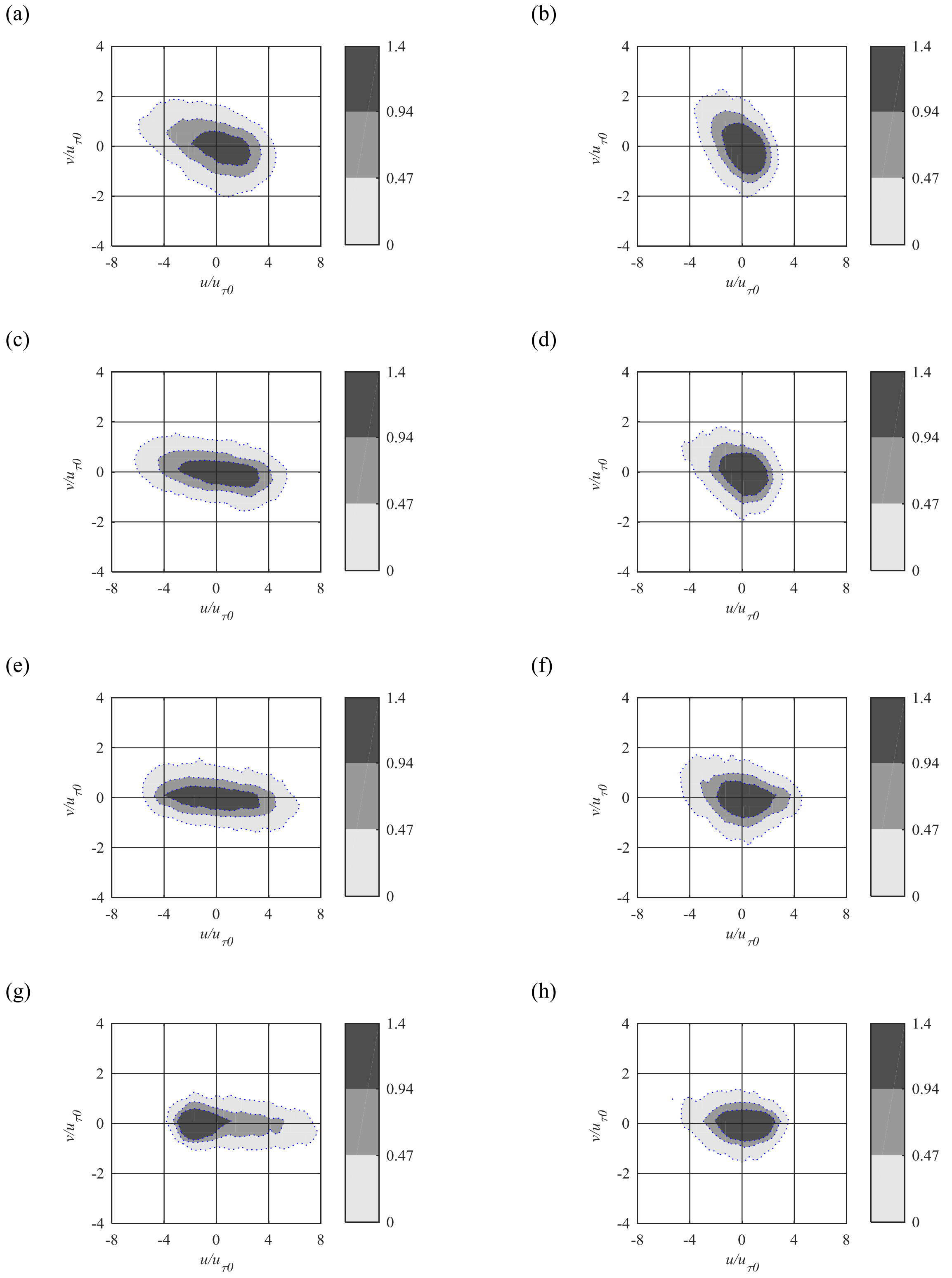

Figure 5-8. The JPDF of turbulent motions in water (a and b), XG-75 (c and d), XG-100 (e and f), and XG-125 (g and h). The figures on the left (a, c, e, and g) correspond to y^+_0 = 25 and the figures on the right (b, d, f, h) correspond to y^+_0=140.

5.4.5 Length scales of XG polymer solutions

The length scales of turbulent structures are analyzed here using spatial correlation. White *et al.* (2004) showed that the polymer additives increase the spanwise spacing of the low and high speed streaks. Li *et al.* (2006) used DNS to obtain spatial correlations of streamwise velocity fluctuations in the streamwise and spanwise directions. They showed that longer computational domains are required to capture length scales of polymer solutions. In addition, they observed that the length scales of u fluctuations in streamwise direction for MDR are larger than those for water solution. However, it appears that length scales in channel flows of drag-reducing polymer solutions, in both the streamwise and wall-normal directions, have not experimentally been explored. The streamwise and wall-normal spatial-correlations of u and v are determined using

$$C_{u_iu_i,x} = \frac{< u_i(x, y_0)u_i(x+\Delta x, y_0) >}{< u_i(x, y_0)^2 >} \tag{5.1}$$

$$C_{u_iu_i,y} = \frac{< u_i(x_0, y)u_i(x_0, y+\Delta y) >}{< u_i(x_0, y)^2 >} \tag{5.2}$$

where x_0 and y_0 indicate the center point of spatial correlation while the index i refers to u (i=1) and v (i=2). Figures 5-9(a) and (b) show $C_{uu,x}$ at y^+_0 =25 and 140 for water and for the XG solutions. The streamwise displacement (Δx) is normalized based on the wall unit ($\delta x^+_0=\Delta x/\lambda_0$). The spatial-correlation in the x direction increases with increasing XG concentration, implying longer streamwise coherence of the turbulent structures. Figures 5-9(c) and (d) demonstrate that the streamwise coherence of v is smaller than u for both the water and polymer solutions. It is also observed in Figure 5-9(c) that at y^+_0=25, $C_{vv,x}$ attenuates with polymer concentration. Therefore, the length scale of v fluctuations becomes smaller in the x direction with increasing DR. The spatial-correlation at y^+_0= 140, shown in Figure 5-9(d), indicates larger streamwise length scales of v fluctuations for the XG-75 and XG-100 solutions relative to water. The XG-125 solution shows a sudden reduction of $C_{vv,x}$ for $\delta x^+_0 < 20$ followed by a gradual reduction beyond this point.

Figures 5-10(a) and (b) present wall-normal spatial-correlations of u and v fluctuations. In Figure 5-10(a), it can be seen that the $C_{uu,y}$ profile shows increasing spatial coherence of u fluctuations in the y direction with an increase of XG concentration from 75 to 100 ppm. A further increase to

125 ppm results in formation of alternating low and high speed streaks (or layers) in the wall-normal direction since $C_{uu,y}$ changes sign at y^+_0=50 and 150. The distance between the center of alternative positive and negative *u* layers is estimated to be about 75-100λ_0. The spatial-correlation of *v* in the *y* direction, as shown in Figure 5-10(b), is approximately the same for water and XG-75 and XG-100, while there is a sudden reduction of wall-normal length scales for XG-125 solution.

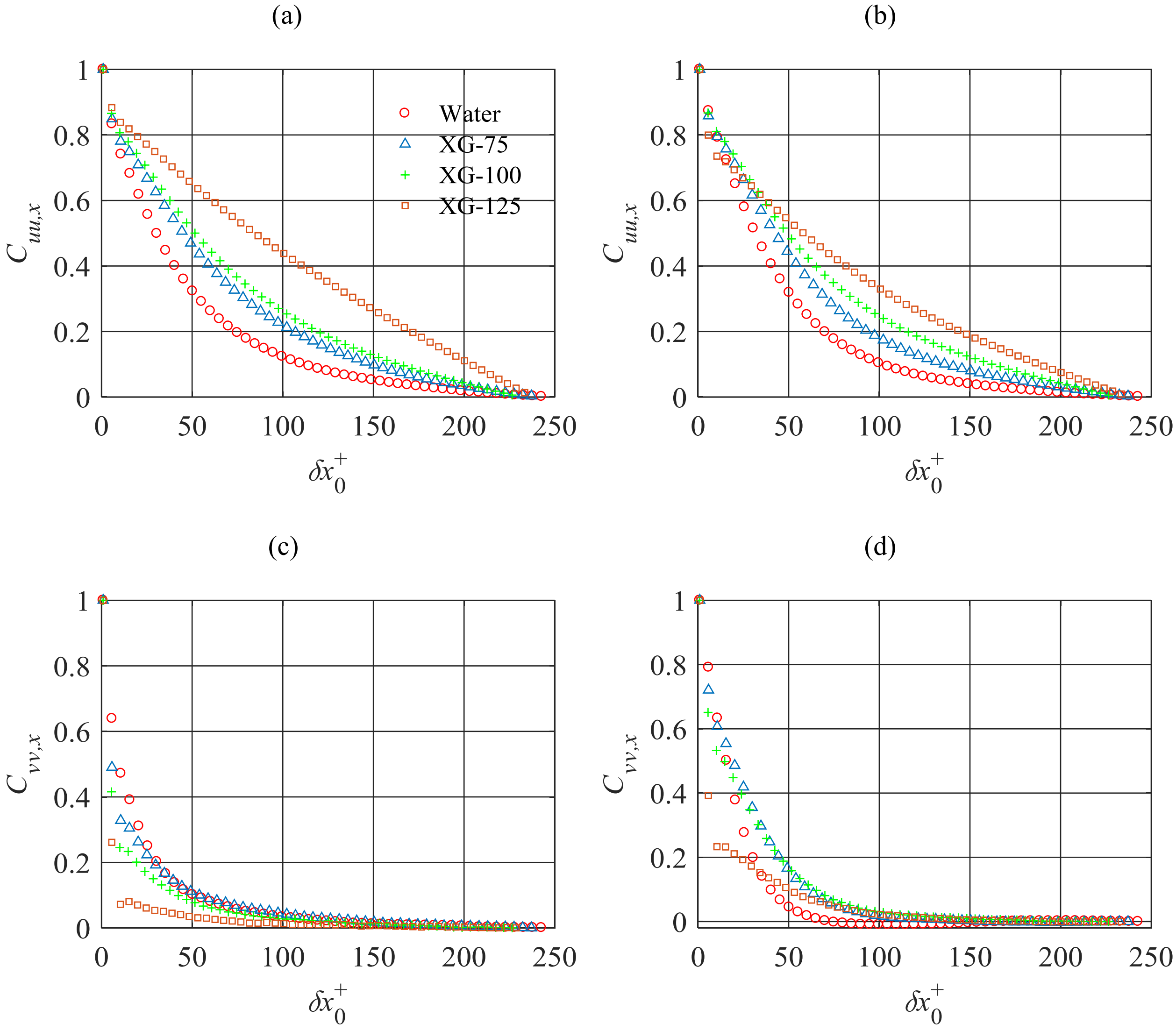

Figure 5-9. Spatial-correlation of streamwise (a and b) and wall-normal (c and d) in the *x* direction. Two wall-normal locations of y^+_0 =25 (a, c) and y^+_0 =140 (b, d) are shown. Only one out of five data points is presented for clarity.

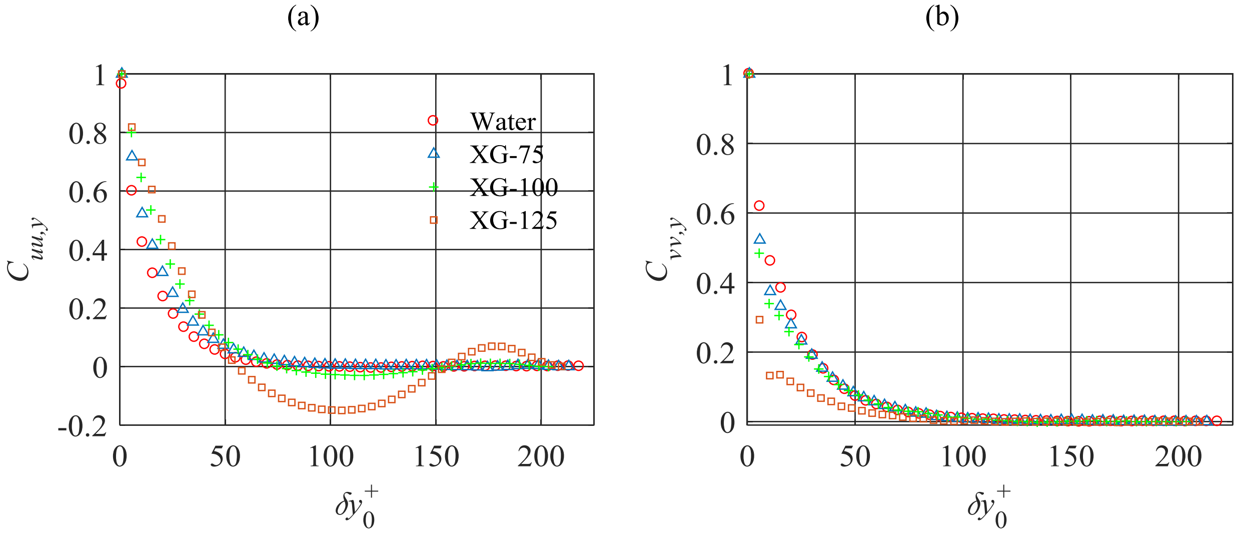

Figure 5-10. The effect of XG concentration on the spatial correlation of (a) streamwise and (b) wall-normal fluctuations in the *y* direction. Only one out of five data points is presented for clarity.

5.4.6 Spatial organization of energetic modes

The POD method decomposes the velocity fluctuation field to the dominant eigenmodes, which present spatial description of turbulent structures carrying most of the flow energy (Lumley 1967; Sirovich 2016). The snap-shot POD method is applied here to a half-channel domain (from the wall to the centerline) based on the algorithm proposed by Lumley (1967) and Meyer *et al.* (2007). The velocity fluctuations are decomposed into a sum of modes and temporal coefficients as follows:

$$u(x,t) = \sum_{k=1}^{N} a^k(t)\phi^k(x) \tag{5.3}$$

where $u(x,t)$, N, $a^k(t)$, and $\varphi^k(x)$ are the velocity fluctuations, the number of snapshots, time coefficient, and normalized modes, respectively . The *u* and *v* fluctuations are appended into one matrix followed by forming an autocovariance matrix. The eigenvalues are ordered in descending order and the energy of each mode is determined by its eigenvalue normalized by the sum of all eigenvalues (Meyer *et al.* 2007). The modes are normalized as

$$\phi^i = \frac{\sum_{n=1}^{N} A_n^i u^n}{\left\| \sum_{n=1}^{N} A_n^i u^n \right\|}, \quad i = 1, 2, ..., N. \tag{5.4}$$

where A^i_n is the nth component of the eigenvector corresponding to the relevant eigenvector. Figure 5-11 demonstrates the energy distribution for the first twenty modes. The first two modes of velocity fluctuations are dominant for water and the polymer solutions. The energy of the first two modes increases with the increasing polymer concentration. The two modes comprise 28% of the total turbulent kinetic energy for water while for XG-125 they represent 61% of the total energy. Each of the remaining modes has a smaller energy (< 4%) for water and the polymer solutions.

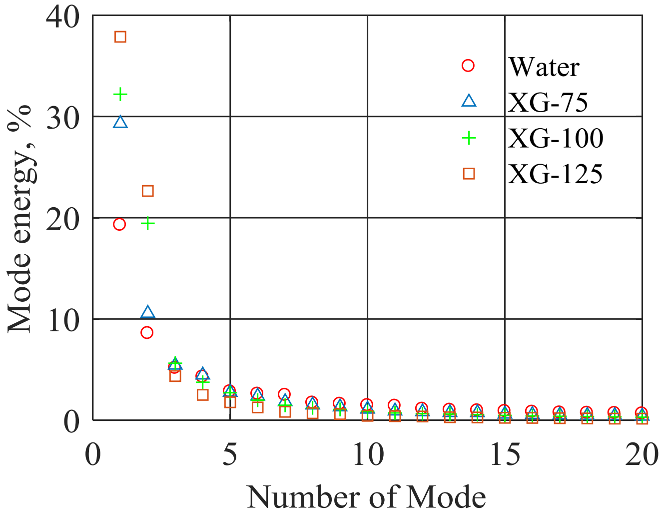

Figure 5-11. POD mode analysis for water and the XG polymer solutions.

The first two dominant modes are shown in Figure 5-12 for water and polymer solutions. It should be noted that the POD modes only describe the spatial pattern of the energetic modes and the sign of $a^k(t)$ coefficient for each snap-shot has to be taken into account in interpreting the direction and detailed description of the coherent motions. The first mode for water in Figure 5-12(a) captures large-scale ejection or sweep of fluid depending on the sign of the $a^1(t)$. The second mode in Figure 5-12(b) resembles the shear layer structure of Newtonian flows assuming a negative $a^2(t)$. The reverse vectors of this mode (i.e. $a^2(t) < 0$) show a strong ejection motion opposed by a sweep motion from the core of the channel. The interaction of the ejection and sweep motions results in the formation of a shear layer (Robinson 1991). The angle of the shear layer at y^+_0= 20 is about 8º with respect to the channel wall which is in good agreement with the value (= 10º) reported by Kreplin & Eckelmann (1979). The first and second modes of the XG-75 solution are similar to those of water. However, the angle of the shear layer is smaller. The trend continues for XG-100, as shown in Figure 5-12(e) and (f), as weaker ejection or sweep is present in the first mode and the angle of the shear layer becomes smaller. At the point of MDR (i.e. for the XG-125 solution), the two modes are both horizontal with no indications of an inclined shear layer. An intense sweep or ejection motion (depending on the sign of $a^1(t)$) is observed in the first mode which uniformly spans the whole field-of-view. The second mode of XG-125 also shows a strong horizontal shear layer at about y^+_0~ 50. These modes indicate presence of layers of low and high streamwise momentum which are elongated in the x-direction at the MDR limit. Cai *et al.* (2009) also showed that the first POD mode captures ejection of low momentum fluid and sweep of high momentum fluid, and the inclination angle of 30 ppm cetyltrimethyl ammonium chloride (CTAC) solution is smaller than that of water. Their results indicated that the second mode captured the ejection of low momentum fluid. The current study confirms the reduction of the inclination angle of the coherent structures during drag reduction and the presence of horizontal shear layers between low and high speed fluid at the MDR.

5.4.7 Power spectra

The velocity fields from PIV is used to analyze the distribution of energy in wavenumber (k=2π/λ, where λ is wavelength) domain for the Newtonian and the non-Newtonian solutions. The power spectral density (PSD) of streamwise velocity versus k at y^+=25 is shown in Figure 5-13. The PSD of water flow has larger energy and distributed over a wide range of wavenumber within the dynamic spatial range of the PIV system. The additional of the polymers has reduced the energy content of all the wavenumbers while the broadband shape of the PSD is maintained. There is no appearance of a peak potentially due to Tollmien-Schlichting instabilities as the polymer concentration is increased.

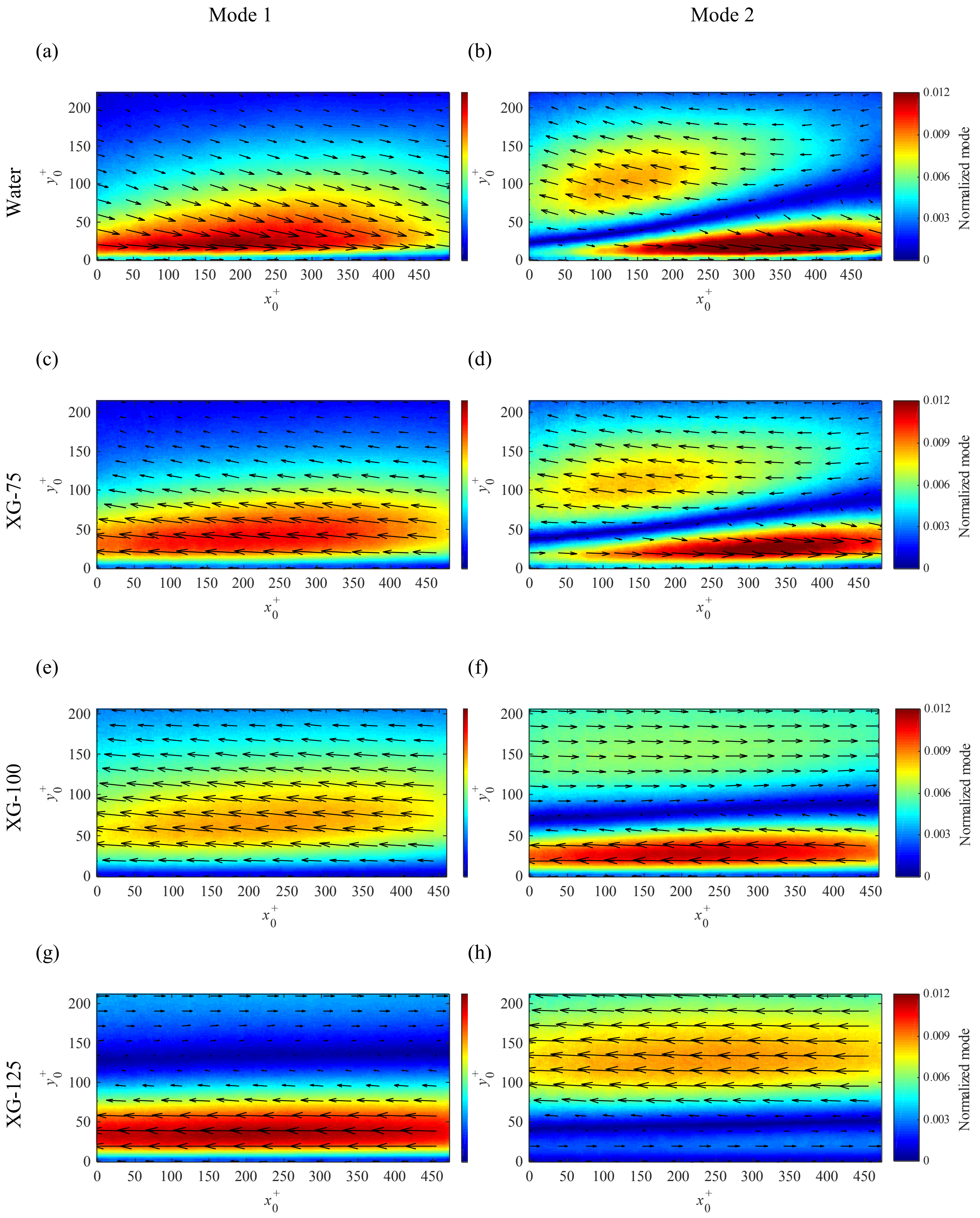

Figure 5-12. Dominant first and second POD modes for (a, b) water and polymer solutions of (c, d) XG-75, (e, f) XG-100, and (g, h) XG-125.

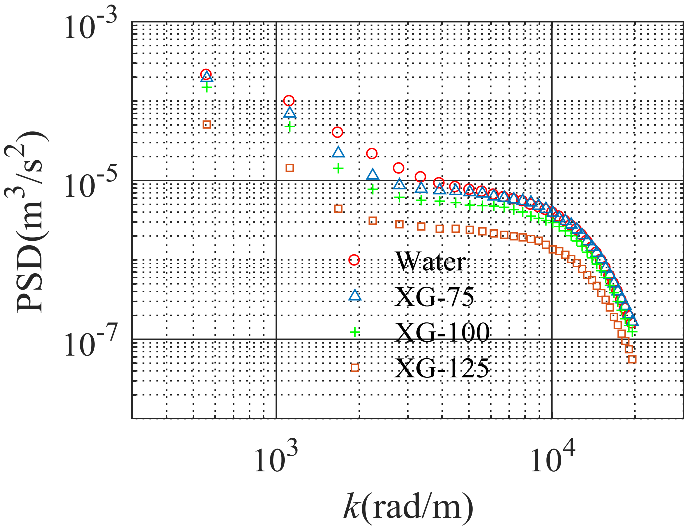

Figure 5-13. PSD of water and polymer solutions at y^+=25.

5.5 Conclusion

The turbulent structures of XG polymer solutions in the channel flow were experimentally investigated and compared with those found in Newtonian flow at a Reynolds number of *Re* = 7,200. The logarithmic layer moves away from the wall with increasing XG polymer concentration. The streamwise Reynolds stresses are as large as those of the Newtonian flow while the wall-normal Reynolds stresses and Reynolds shear stresses are significantly attenuated. The spatial-correlation of the fluctuating velocity field shows that an increase in XG concentration increases the spatial coherence of *u* fluctuations in the *x*-direction while *v* fluctuations are not affected and stay localized. The length scales of streamwise velocity fluctuation in wall-normal direction show the formation of low and high speed streak. Proper orthogonal decomposition (POD) confirms the results of the length scales of streamwise velocity fluctuation in wall-normal direction.

Chapter 6. Turbulence mechanisms of rigid and flexible polymers at an identical drag reduction and turbulent structures at maximum drag reduction

6.1 Introduction

As mentioned previously, polymers are classified into two structure groups known as flexible and rigid polymers. Polyacrylamide (PAM), as a flexible synthetic polymer made from acrylamide subunits, has a wide range of applications in water treatment, papermaking process, and for flocculation of solid particles dispersed in a liquid (Han *et al.* 2017; Xiong *et al.* 2018). Among rigid polymers, Xanthan Gum (XG), a natural bio polymer made by the Xanthomonas camperstris, has been used in the petroleum industry to enhance oil recovery (Abdulbari *et al.* 2014). Both of PAM and XG have been used as drag reducers in turbulent flows (Sandoval *et al.* 2015; Soares *et al.* 2015; Virk 1975).

As mentioned before, two DR mechanisms have generally been suggested in the literature for the flexibility of polymers known as viscous theory and elastic theory. Both viscous and elastic theories have been proposed for flexible polymers and they may not be valid for rigid polymers with a negligible chain flexibility (Pereira *et al.* 2013) is still under investigation.

The addition of polymers into Newtonian flows alters the structures of low and high speed streaks, and vortices (White & Mungal 2008). The number and strength of quasi-streamwise vortices decrease with increasing DR (White & Mungal 2008). In addition, the streamwise velocity streaks become thickened in polymer solutions (White *et al.* 2004; White & Mungal 2008). The author, as mentioned in Chapter 5, captured the formation of low and high speed streaks in wall-normal direction for XG solutions at DR of 45% at Re_w=7200 (in Newtonian flow) using spatial correlation and proper orthogonal decomposition (POD). It was observed that the low and high speed streaks are more elongated in the streamwise direction. The inclined shear layer structure, which is a major source for producing turbulence in Newtonian flow, was completely suppressed at DR = 45%. Choueiri *et al.* (2018) obtained MDR for both concentrations of 20 ppm and 60 ppm. The flow structures were completely different while both of them had the same friction factor. The PAM solution at 20 ppm was intermittent, which indicated localized bursts were separated by more quiescent regions. However, the flow at 60 ppm was dominated by streamwise elongated streaks. It should be noted that the results of Choueiri *et al.* (2018) are obtained in transitional flow where EII is a dominant instability. On the other hand, Dubief *et al.* (2013), using DNS, investigated the turbulent structures at MDR (~ 61%) in the channel flow with $Re = 6000$. The simulations of Dubief *et al.* (2013) showed the presence of small spanwise vortical structures in near wall. The same structure at MDR was observed in DNS results of Samanta *et al.* (2013). Further experiments and numerical works are needed to address turbulent structures of MDR at turbulent flow (high $Re \sim 20{,}000$).

None of the experimental and numerical works tried to compare turbulent structures of rigid and flexible polymers at an identical pressure drop, while also keeping the flow rate constant. The DR at a constant flow rate can be calculated as $\text{DR}\% = (1-\Delta P_{\text{polymer}}/\Delta P_{\text{water}})\times 100$. Hence polymer solutions with the same pressure drop produce identical DR.

The first objective of this investigation is to compare the turbulent structures of rigid and flexible polymer solutions at an identical DR (pressure drop). The planar-PIV and stereo-PIV are used to capture turbulent structures of polymer solutions. Mean velocity profiles, Reynolds stresses, and spatial correlations in x and y directions are obtained using the Planar-PIV, while spatial correlation in z direction is achieved using stereo-PIV. The streamwise and spanwise vorticity fluctuations along polymer stress of polymer solutions are experimentally characterized. The second objective of this investigation is to characterize the turbulent structures at MDR and compare them with those found in Newtonian flow. The turbulent length scales of the polymer solutions at MDR and those for water are compared to evaluate their differences in turbulent structures.

6.2 Flow condition

Experiments were carried out in a channel flow (discussed in Chapter 3) of Newtonian (water) and non-Newtonian (rigid and flexible polymer solutions) flows at the same flow rate and at an identical DR (pressure drop). In addition, the experiments were conducted for Newtonian flow with the same pressure drop with polymer solutions (water-ΔP constant). Measurements were performed using high-speed planar and stereoscopic PIV systems. Turbulent structures of flexible polymer solutions at MDR were compared with those found in Newtonian flow at the same flow rate.

The experiments were conducted at the same flow rate (~1.2 L/s) while Reynolds number for Newtonian flow was 22,500 ($Re = U_b H/\upsilon = 22{,}500$). The wall shear stress is obtained using $\tau_w{}^* = \Delta P(WH)/(2L(W+H))$, where $L = 700$ mm and ΔP is the pressure drop for flow of water. The wall shear stress of Newtonian flow at $Re = 22{,}500$ is estimated $\tau_{w0} \sim 10.65$ Pa. The reference friction velocity is calculated as $u_{\tau 0} = (\tau_{w0}/\rho)^{0.5} \sim 0.1032$ m/s. The estimated wall unit and Reynolds number based on the friction velocity are $\lambda_0 = \upsilon/u_{\tau 0} = 8.62$ μm and $Re_\tau = u_{\tau 0}H/(2\upsilon) = 580$. Another experiment in Newtonian flow at $Re = 17{,}000$ (flow rate ~ 0.9 L/s), which has the same pressure drop as the polymer solutions, was conducted to compare turbulent structures of Newtonian flow with polymer solutions.

In this study, two polymers with different structures (rigid and flexible) were selected. The flexible PAM polymer chosen in this investigation is Superfloc A-150 (SF) from Kemira company (Kemira n.d.). SF has high molecular weight (1-20 million Daltons) with high anionic charge, and commonly used in mining applications (Kemira n.d.). The XG polymer with non-linear structure was selected as the rigid polymer. The structure of XG and the procedure of polymer solution preparation were explained in greater detail in Chapter 3.

6.3 Polymer characterization

At first, DR of XG solutions at different concentrations was investigated at mass flow rate of 1.2 kg/s. XG at 200 ppm was chosen as the optimum case because DR was rather high (~ 37%) and the solution was transparent for PIV measurements. The SF solution at 25 ppm was selected to achieve a similar DR with XG. The DR started from 60% and reached to 37% within 2 hours due to mechanical degradation. For experiments at MDR, SF at 45 ppm was selected because of larger DR (~ 58%) and negligible degradation during PIV measurement. The DR% and mass flow rate for these polymer solutions are shown in Table 6-1. The results for water at the same mass flow rate (water-$\dot{m}$ constant) and at the same pressure drop (water-ΔP constant) with polymer solutions are also presented in Table 6-1.

Shear viscosity of water and polymer solutions were measured using a rheometer with a double gap cylinder (RheolabQC, Anton Paar) up to a shear rate of 1000 1/s. As shown in Figure 6-1, XG at 200 ppm and SF at 45 ppm have shear thinning behavior while SF at 25 ppm (degraded solution which leads to 37% DR) and water behave like Newtonian solutions. However, the range of shear rate in the channel flow is beyond the rheometer limitation. As shown in Figure 6-1, the shear viscosity of SF at 45 ppm tends to be constant at higher shear rates. Hence, the shear viscosity at the wall for Newtonian flow, SF at 25 ppm and SF at 45 ppm is determined and presented in Table 6-1. The shear viscosity at the wall for XG at 200 ppm is calculated as $\mu_w = \tau_w/(d\langle U\rangle/dy)$. The same procedure applied to Newtonian flow is used to estimate the wall shear stress of polymer solutions using pressure drop measurement. The high-spatial resolution PIV was used to estimate the shear rate at the wall ($d\langle U\rangle/dy = 3520$), by applying a linear regression on the velocity points near the wall. The friction velocity ($u_\tau = (\tau_w/\rho)^{0.5}$) and wall unit of polymer solutions ($\lambda = \upsilon_w/u_\tau$) are calculated and presented in Table 6-1. The mass flow rate, Reynolds number, and friction Reynolds number for water and polymer solutions, based on their corresponding shear viscosity at the wall and friction velocity, are also presented in Table 6-1. For brevity, XG at 200 ppm, degraded SF at 25 ppm, and SF at 45 ppm are specified with XG-200, SF-25, and SF-45, respectively.

Figure 6-2 shows the Fanning friction factor versus Reynolds number ($Re_w = \rho U_b D_h/\mu_w$) for water-$\dot{m}$ constant, water-ΔP constant, and polymer solutions. The friction factor for both water solutions follows Prandtl-Karman equation for turbulent flows. As mentioned above, XG-200 and SF-25 solutions have an identical DR (pressure drop) which leads to the same shear stress at the wall and the same friction factor. However, Re_w of these polymer solutions are different due to different μ_w. As shown in Figure 6-2, the friction factor of SF-45 follow the Virk asymptote and proves that MDR is achieved.

Virk et al. (1975, 1997) investigated drag reduction performance using collapsed and extended polyelectrolytes. Two extremes of drag reduction behavior were obtained. The first one (Type A) relates to flexible, random-coiling, and deformable polymer, while the second one (Type B) relates to relatively rigid, elongated, and undeformable polymer. In Type A, the $C_f^{-1/2}$ starts from a common onset point on the Prandtl-Karman line and its value increases with increasing polymer concentration. Drag reduction for polymers in Type A category is an increasing function of $ReC_f^{1/2}$. On the other hand, in Type B, the $C_f^{-1/2}$ starts from maximum drag reduction asymptote and stays parallel with Prandtl-Karman line. Drag reduction for polymer solutions located in Type B category is independent of $ReC_f^{1/2}$.

Table 6-1. Drag reduction percentage and inner scaling properties of water and polymer solutions.

	DR %	τ_w (Pa)	u_τ (m/s)	λ (µm)	μ_w (Pa.s)	Mass Flow rate (kg/s)	Re_w number	Friction Re_w number
Water-$\dot{m}$ constant	0	10.65	0.103	8.62	0.89×10^{-3}	1.2	22,500	580
Water-ΔP constant	0	6.69	0.082	10.88	0.89×10^{-3}	0.9	17,000	460
XG at 200 ppm	37	6.69	0.082	23.23	1.90×10^{-3}	1.2	10,500	215
SF at 25 ppm	37	6.69	0.082	13.57	1.11×10^{-3}	1.2	18,000	370
SF at 45 ppm	58	4.47	0.067	29.90	2.00×10^{-3}	1.2	10,000	168

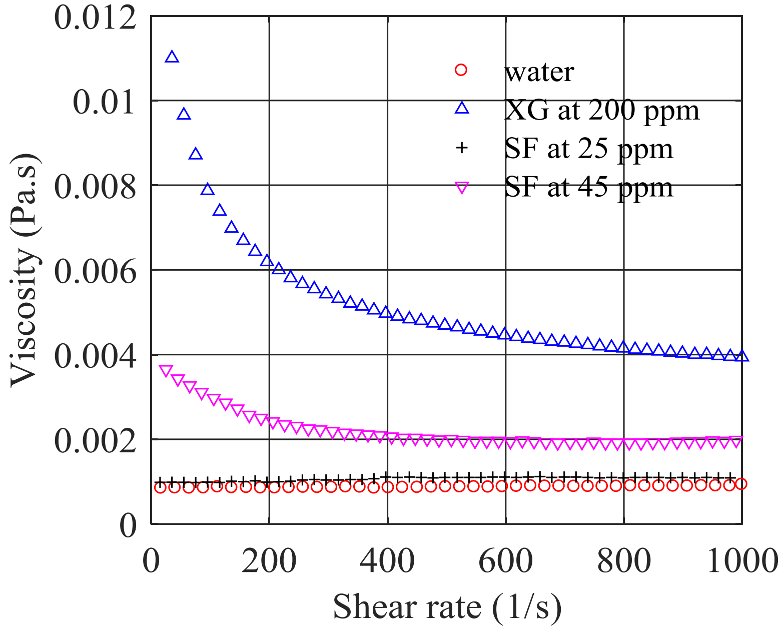

Figure 6-1. Shear viscosity of water and polymer solutions. The shear thinning behavior is observed in XG and SF at 45 ppm, while water and degraded SF at 25 ppm shows Newtonian behavior.

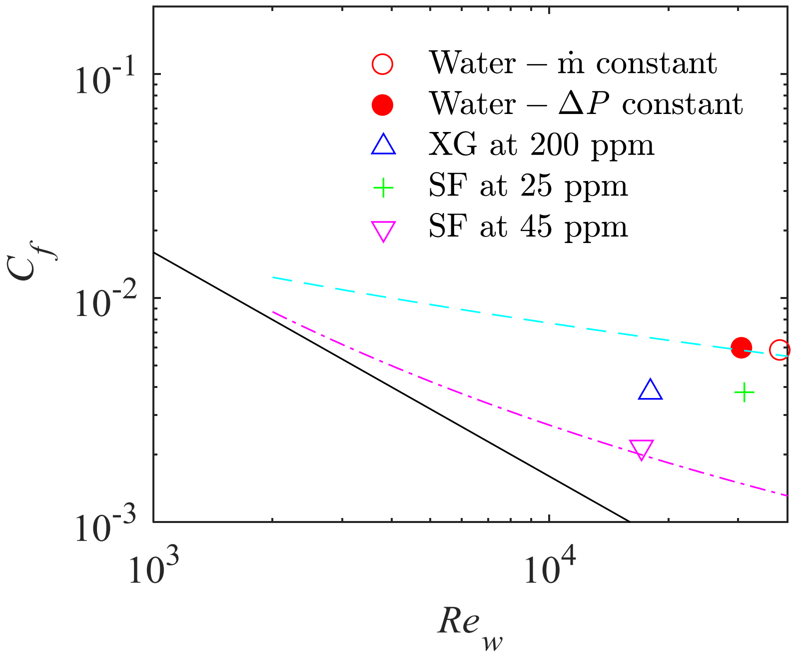

Figure 6-2. The fanning friction factor for water-$\dot{m}$ constant, water-ΔP constant, and polymer solutions. Solid line shows $C_f = 16/Re_w$ (laminar flow), Prandtl-Karman equation for turbulent flows (---), Virk's asymptote (-·-·-).

6.4 Results and discussion

Turbulent structures of SF and XG polymer solutions at similar DR (or similar pressure drop) are experimentally investigated to evaluate different DR mechanisms in flexible and rigid polymer solutions. In addition, the turbulent structures at MDR are compared with those found in Newtonian turbulent channel flow also at the same flow rate. The mean velocity profile, Reynolds stresses, polymer stress, quadrants of velocity fluctuations, length scale of the turbulent structures, and vorticity fluctuations, are investigated in Newtonian and non-Newtonian turbulent channel flow.

6.4.1 Mean velocity profile

The streamwise mean velocity profiles normalized by the bulk velocity, $\langle U\rangle/U_b$, across half the channel for water and polymer solutions are shown in Figure 6-3(a). With the addition of polymer solutions, the near-wall velocity decreases while the velocity in the core of the flow increases. The reduction is larger for XG-200 solution than it is for the SF-25 solution.

The profiles of streamwise mean velocity normalized by the friction velocity, $U^+ = \langle U\rangle/u_\tau$, as a function of wall-normal distance, $y^+ = y/\lambda$, for Newtonian and non-Newtonian flow are demonstrated in Figure 6-3(b). The wall unit (λ) and friction velocity (u_τ) of water and polymer solutions are presented in Table 6-1. The profiles of U^+ for both water flows (water-$\dot{m}$ constant and water-ΔP constant) overlap from $y^+ \sim 8$ and follow the von-Karman log law ($U^+ = 1/\kappa \ln y + B$), where κ and B are 0.4 and 5.5, respectively. The U^+ profiles for XG-200 and SF-25 follow the law of wall until $y^+ \sim 11$ and they approximately overlap up to $y^+ \sim 40$. The viscous sublayer and buffer layer are thickened with the addition of polymer solutions and the log-layers are shifted upward at a similar slope relative to the Newtonian flow ($\kappa = 0.4$). A log-layer is observed for XG-200 within $80 < y^+ < 215$ with fitted $\kappa = 0.4$ and $B = 14$, while for SF-25, the log-layer is approximately bounded by $70 < y^+ < 350$ with fitted $\kappa = 0.4$ and $B = 12.5$. As mentioned before, DR obtained for polymer solutions is 37% which falls in the category of low drag reduction (LDR) region presented by Warholic *et al.* (1999). In LDR, the log-layer of the mean velocity profile is shifted upward and the slope remains unchanged, which is in agreement with the results obtained here.

Procaccia *et al.* (2008) showed that rigid and flexible polymer solutions approach the MDR asymptote ($u^+ = 11.7\, ln\, y^+ - 17$) in different ways with the increase of concentration. The semi-logarithmic profile of rigid polymers prior to MDR falls between the Newtonian log-law and MDR. However, the U^+ profiles of flexible polymers follow the MDR asymptote until a crossover point, then deviate and follow the Newtonian log-law. The location of the crossover point is displaced farther away from the wall with increasing polymer concentration and DR. On the other hand, the results of Warholic *et al.* (1999) showed that the U^+ profiles of flexible polymer solutions are placed between the Newtonian log-law and MDR before achieving MDR. The U^+ profiles of XG-200 and SF-25 are placed between the Newtonian log-law and MDR and confirm the results of Warholic *et al.* (1999).

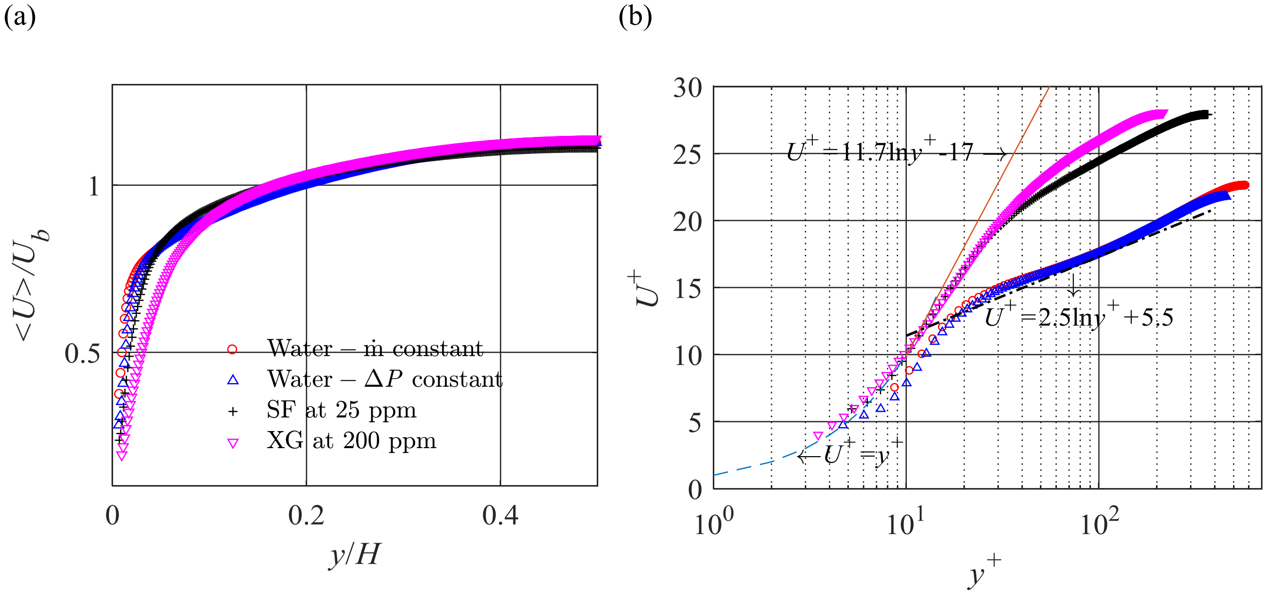

Figure 6-3. The effect of XG-200 and SF-25 polymer solutions on mean streamwise velocity profiles (a) normalized by the bulk velocity as a function of y/H, and (b) normalized by friction velocity and plotted as a function of y^+. The experimental results are compared with the law of the wall ($U^+ = y^+$), log-law of Newtonian flows ($U^+ = 2.5\ln y^+ + 5.5$), and Virk's asymptote ($U^+ = 11.7\ln y^+ - 17$).

6.4.2 Reynolds stresses

The streamwise Reynolds stresses, $\langle u^2 \rangle$ profiles, normalized with the friction velocity of water-$\dot{m}$ constant ($u_{\tau 0}$) as a function of y^+_0 (= y/λ_0, where $\lambda_0 = \upsilon/u_{\tau 0}$) are shown in Figure 6-4(a). This normalization helps to isolate the variation of normalized streamwise Reynolds stress profiles from the change in friction velocity of water-ΔP constant and polymer solutions. The PIV measurements for water-$\dot{m}$ constant are compared with the DNS results of Moser *et al.* (1999) at

Re_τ = 590. The DNS results are normalized using their corresponding friction velocity at Re_τ = 590. There is good agreement between the DNS results and PIV measurements across the channel. The data points near the wall at $y^+ < 20$ are assumed to be erroneous and they are removed because the $\langle u^2\rangle/u^2_{\tau 0}$ profiles do not converge to zero. This is related to the presence of mirrored particle images in the near wall region. The $\langle u^2\rangle/u^2_{\tau 0}$ profile of water-$\dot{m}$ constant is larger than those found in water-ΔP constant across the channel as they have higher flow rate (higher bulk velocity). Both polymer solutions have larger $\langle u^2\rangle/u^2_{\tau 0}$ at $34 < y^+_0 < 170$ relative to water-$\dot{m}$ constant, which indicates turbulent flow of the polymer solutions. The XG-200 has higher $\langle u^2\rangle/u^2_{\tau 0}$ in comparison with SF-25 at $y^+_0 > 50$. The $\langle u^2\rangle/u^2_{\tau 0}$ peak of XG-200 is displaced away from the wall which shows a thicker buffer layer, while the peak in SF-25 is not observed due to the noise in the near wall measurements. A thicker buffer layer was also observed in the semi-log plot of Figure 6-3(b) and in the results of previous experiments (Warholic *et al.* 1999). The $\langle u^2\rangle/u^2_{\tau 0}$ peak of XG-200 is at approximately the same position as water-$\dot{m}$ constant and it is in agreement with the results of current research presented in Section 4.1 where they observed $\langle u^2\rangle/u^2_{\tau 0}$ peak of different concentrations (or different DR) of XG solution stays approximately unchanged.

The wall-normal Reynolds stress profiles, $\langle v^2\rangle$, normalized with $u_{\tau 0}$ for Newtonian and non-Newtonian solutions are shown in Figure 6-4(b). There is good agreement between the PIV measurements of $\langle v^2\rangle$ in water-$\dot{m}$ constant and DNS results of Moser *et al.* (1999) at Re_τ = 590 across the channel. The magnitude of $\langle v^2\rangle/u^2_{\tau 0}$ profiles in water-$\dot{m}$ constant is larger than observed in water-ΔP constant across the channel. The $\langle v^2\rangle/u^2_{\tau 0}$ profiles of XG-200 and SF-25 are approximately the same and their magnitudes are considerably decreased relative to water-$\dot{m}$ constant and water-ΔP constant. The peaks of $\langle v^2\rangle/u^2_{\tau 0}$ profiles in XG-200 and SF-25 move away from the wall, which indicates the increase of buffer layer thickness. The addition of polymer solutions reduces the $\langle v^2\rangle/u^2_{\tau 0}$ peak by 65%; however, this reduction is almost the same for both polymer solutions.

The profiles of Reynolds shear stress, $\langle uv\rangle$, normalized with $u_{\tau 0}$ are shown in Figure 6-4(c). The $\langle uv\rangle/u^2_{\tau 0}$ profiles for water-$\dot{m}$ constant have a good agreement with DNS results of Re_τ=590 at $y^+ > 80$, while PIV underestimates the magnitude of $\langle uv\rangle/u^2_{\tau 0}$ near the wall. This is due to the limited spatial-resolution of PIV in recognizing the small-scale structures near the wall. The $\langle uv\rangle/u^2_{\tau0}$ profiles are reduced for the polymer solutions. The $\langle uv\rangle/u^2_{\tau0}$ profiles of polymer solutions and water-ΔP constant are approximately the same at $y^+_0 > 120$. One way to obtain shear stress at the wall is to extrapolate the $\langle uv\rangle$ profiles at $y^+_0 = 0$, therefore the same $\langle uv\rangle/u^2_{\tau0}$ profiles indicate identical shear stress at the wall. On the other hand, shear stress at the wall has a proportional relationship with pressure drop ($\tau_w^*=(\Delta P\ WH)/(2L(W+H))$), which was already kept constant. The peak of $\langle uv\rangle/u^2_{\tau0}$ profiles decreases about 50% with adding polymer solutions and their magnitudes are approximately equal.

Analysis of the results of Figure 6-4 indicates that the streamwise Reynolds stresses of XG-200 and SF-25 have large difference in magnitude, while wall-normal Reynolds stresses and Reynolds shear stresses are approximately similar when polymer solutions have an identical DR.

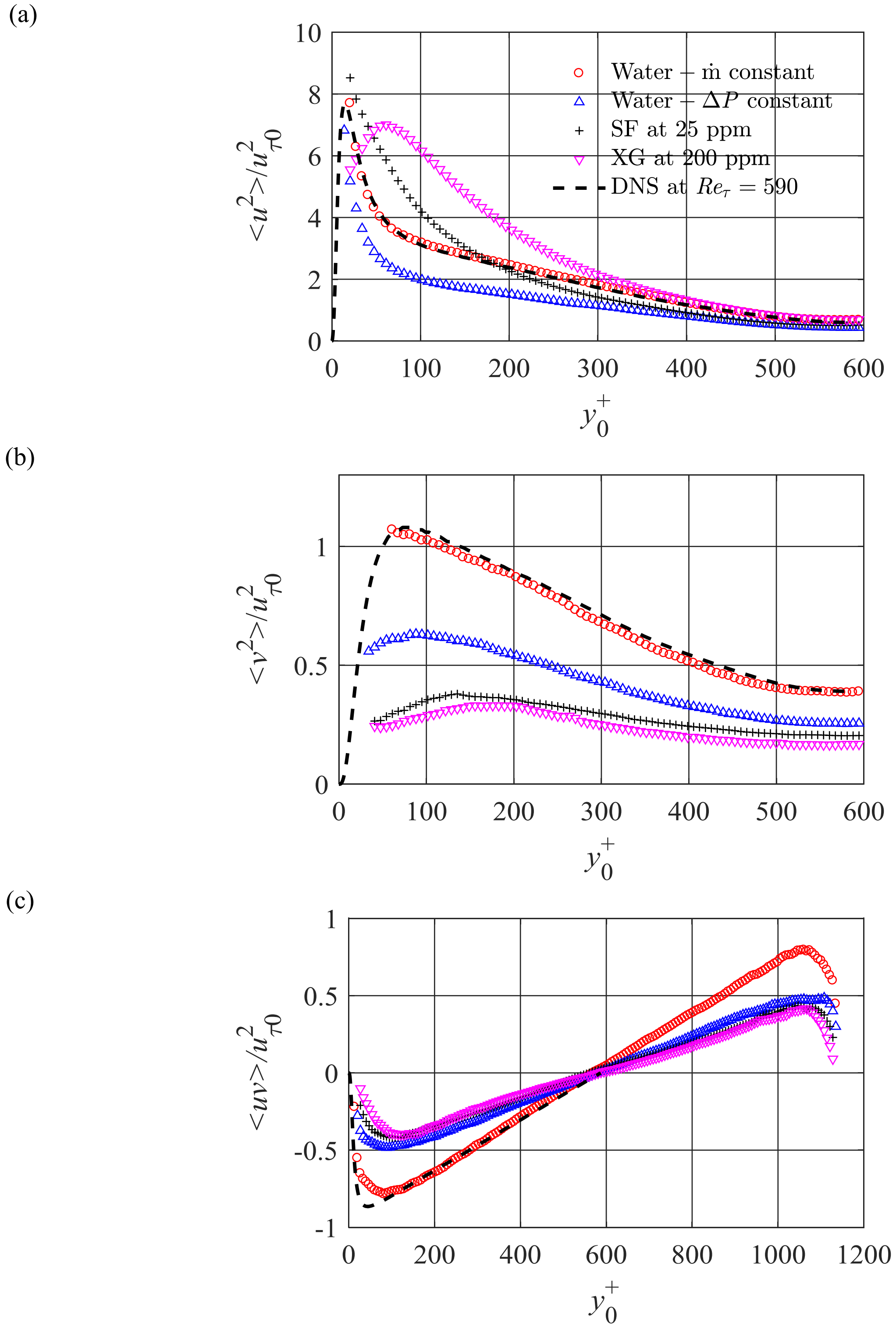

Figure 6-4. The effect of XG-200 and SF-25 polymer solutions on the (a) streamwise (b) wall-normal, and (c) shear Reynolds stresses normalized by the reference friction velocity of water ($u_{\tau 0}$) at 1.2 L/s flow rate as a function of wall-normal distance normalized by the reference inner scale (λ_0). The uncertainties of PIV measurement in water-$\dot{\boldsymbol{m}}$ constant at Re_τ = 580 are evaluated with DNS result of Moser *et al.* (1999) at Re_τ= 590. This DNS is normalized with its corresponding friction velocity at Re_τ= 590.

6.4.3 Polymer stress characterization

The polymer stress profiles, $\langle \tau_p \rangle$, of non-Newtonian flows normalized with the shear stress of polymer solutions (τ_w) presented in Table 6-1 are shown in Figure 6-5. The polymer stress is estimated using the mean momentum balance in 2D channel flow. The polymer stresses of XG-200 and SF-25 are obtained using

$$\frac{\tau_p}{\tau_w} = \tau_p^+ = \frac{\tau_t - (\tau_s + \tau_{Re})}{\tau_w} \tag{6.1}$$

Where $\tau_t = \tau_w\,(1\text{-}y/H)$ is total shear stress of polymer solutions. The viscous stress, $\mu_s\, d\langle U \rangle/dy$, and Reynolds stress, $-\rho\langle uv \rangle$, are indicated with τ_μ and τ_R, respectively. There is a large reduction in polymer stresses near the wall ($y^+_0 < 120$) with increasing y^+_0, followed by an approximately constant region until the half channel height. The polymer stress of XG-200 is larger relative to SF-25 at $y^+_0 < 120$, while they have approximately similar polymer stress at $120 < y^+_0 < 600$.

The trend of polymer stress observed here agrees with the trend of Warholic *et al.* (1999) at LDR, where they showed the polymer stress is larger near the wall ($y/H < 0.1$) and then after a large reduction stays approximately constant across the channel.

Analysis of Figure 6-5 shows that rigid and flexible polymer solutions at similar DR share approximately similar magnitudes of polymer stress at $y^+_0 > 120$, while the polymer stress of XG-200 is larger than that found in SF-25 at $y^+_0 < 120$.

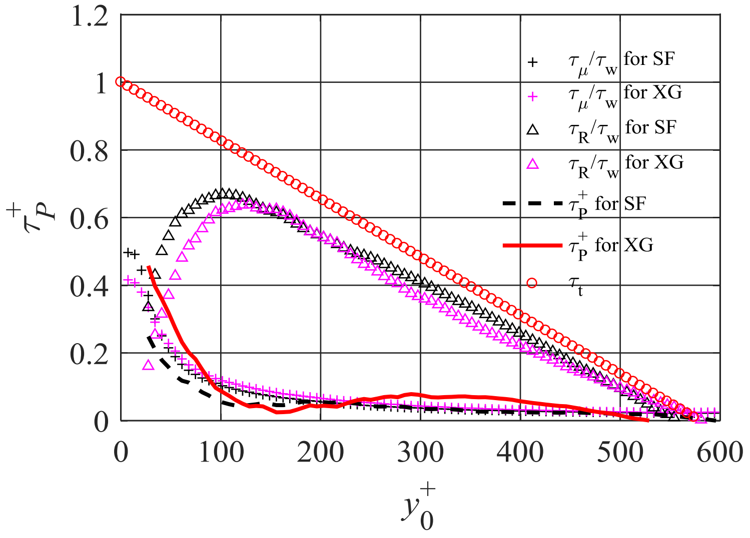

Figure 6-5. Total stress, Reynolds stress, viscous stress, and polymer stresses of XG-200 and SF-25 when polymer solutions have similar DR. Polymer stress of XG-200 is larger relative to SF-25 at $y^+_0 < 80$.

6.4.4 Quadrant of velocity fluctuations

The effect of polymer solutions at similar DR on the velocity fluctuations is investigated using joint probability density functions (JPDF). The difference of $\langle u^2 \rangle / u^2_{\tau 0}$ values in Newtonian and non-Newtonian flows, as shown in Figure 6-4, is large enough at $y^+_0 = 80$, which makes this location a good position to study JPDF. The JPDF of Newtonian and non-Newtonian flows at $y^+_0 = 80$ are shown in Figure 6-6. As shown in Figures 6-6(a) and (b), the JPDF in the second (ejection) and fourth (sweep) quadrants is stronger than the first and third quadrants in Newtonian flows. The positive and negative u and v velocity fluctuations of water-$\dot{m}$ constant are larger relative to water-ΔP constant due to the larger *Re*. The angles of the ejection/sweep motions (principal axis of JPDF contour) for water-$\dot{m}$ constant and water-ΔP constant are approximately similar. The sweep and ejection of water-$\dot{m}$ constant occupy a larger area in comparison with water-ΔP constant due to larger bulk velocity.

Figures 6-6(c) and (d) show that polymer solutions reduce the magnitude of v fluctuations and increase the magnitude of u fluctuations. The angles of the ejection/sweep motions in polymer solutions with respect to the wall decrease. This indicates the reduction of sweep/ejection motions in polymer solutions. The attenuation of v fluctuations is larger in XG-200 in comparison with SF-25, while XG-200 has larger u fluctuations relative to SF-25. This is in agreement with the magnitude of $\langle u^2\rangle/u^2_{\tau 0}$ and $\langle v^2\rangle/u^2_{\tau 0}$ at $y^+_0 = 80$ observed in Figure 6-4(a) and (b) for XG-200 and SF-25.

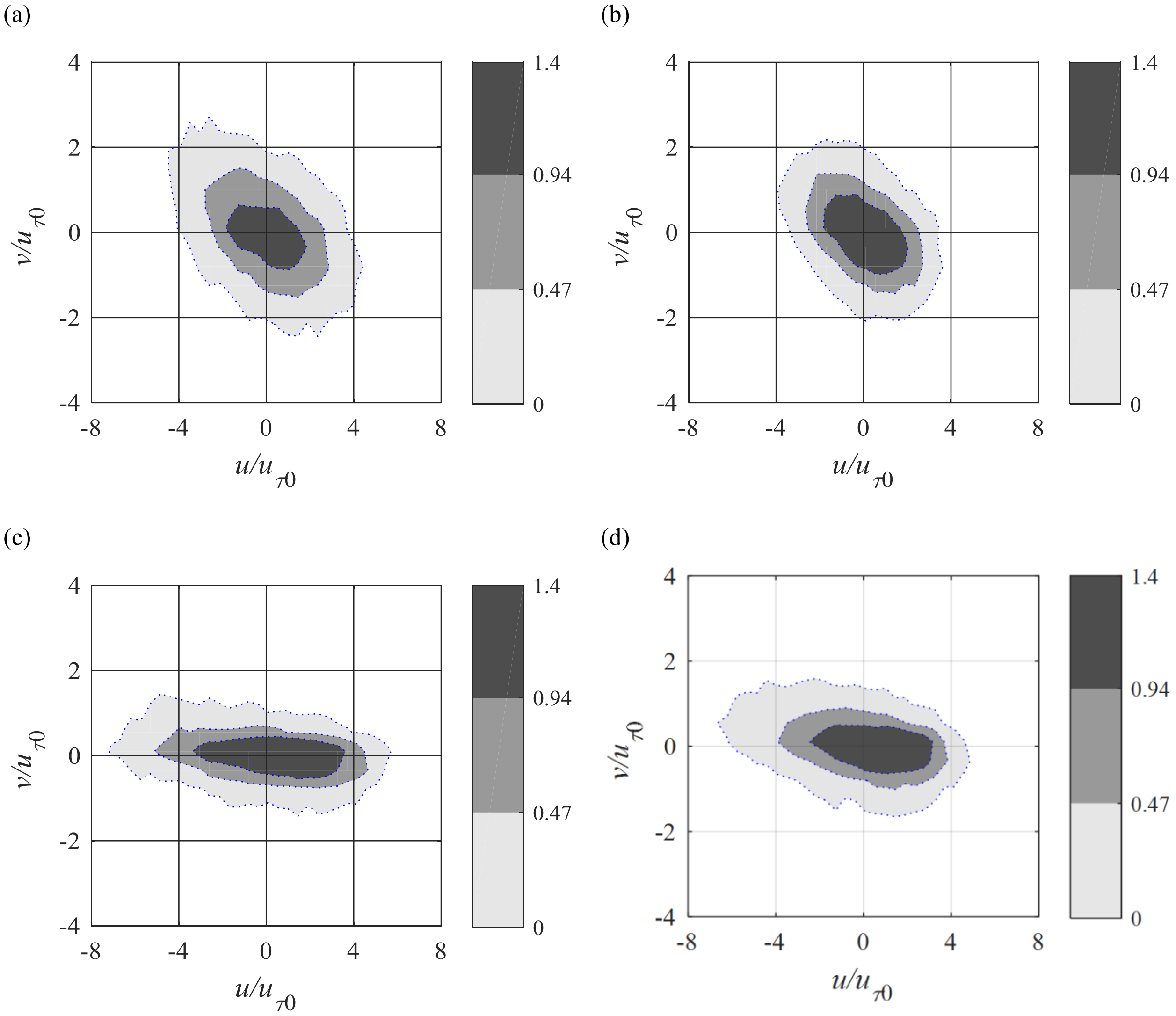

Figure 6-6. The JPDF of velocity fluctuations in (a) water-$\dot{m}$ constant (b) water-ΔP constant, (c) XG-200, (d) SF-25 at $y^+_0 = 80$. The reduction of v fluctuations is larger in XG-200 in relative to SF-25, while XG-200 has higher u fluctuations in comparison with SF-25.

6.4.5 Length scales of Newtonian and non-Newtonian flows

The length scales of Newtonian and non-Newtonian flows are investigated using two-point spatial correlation of streamwise velocity. The streamwise, wall-normal, and spanwise spatial-correlations are defined as

$$C_{uu,x} = \frac{\langle u(x, y_0)u(x + \Delta x, y_0)\rangle}{\langle u(x, y_0)^2\rangle} \tag{6.2}$$

$$C_{uu,y} = \frac{\langle u(x_0, y)u(x_0, y + \Delta y)\rangle}{\langle u(x_0, y)^2\rangle} \tag{6.3}$$

$$C_{uu,z} = \frac{\langle u(y_0, z)u(y_0, z + \Delta z)\rangle}{\langle u(y_0, z)^2\rangle} \tag{6.4}$$

where x_0 and y_0 show the reference point of two-point spatial correlation. Two-point spatial correlations of u fluctuations in x ($C_{uu,x}$) and y ($C_{uu,y}$) directions at $y^+_0 = 80$ are obtained from the planar PIV and are shown in Figure 6-7(a) and (b), while Figure 6-7(c) indicates the spatial correlations of streamwise velocity fluctuations in z ($C_{uu,z}$) direction at $y^+_0 = 129$, obtained from the stereo PIV. The streamwise, wall-normal, and spanwise displacements (Δx, Δy, and Δz) are normalized using the reference wall unit ($\delta x^+_0=\Delta x/\lambda_0$, $\delta y^+_0=\Delta y/\lambda_0$, and $\delta z^+_0=\Delta z/\lambda_0$). The $C_{uu,x}$ of water-$\dot{m}$ constant and water-ΔP constant are approximately the same, while it increases for polymer solutions. As shown in Figure 6-7(a), the XG-200 has larger $C_{uu,x}$ relative to SF-25 which indicates longer streamwise coherence in turbulent structures. The $C_{uu,x}$ does not reach zero at maximum δx^+_0 (~300) due to the limited field of view. The $C_{uu,y}$ in Figure 6-7(b) shows the same trend, however the magnitude of variation is low in comparison with the variation of $C_{uu,x}$.

The $C_{uu,z}$ of water-$\dot{m}$ constant and water-ΔP constant are approximately the same while polymer solutions have larger values. The $C_{uu,z}$ of XG-200 is larger than the $C_{uu,z}$ of SF-25 at $\delta z^+_0<175$, implying the presence of longer streamwise coherence (thicker high streak). The $C_{uu,z}$ in Newtonian flows changes sign at $\delta z^+_0=74$ due to the presence of alternating low and high speed streaks in the spanwise direction. The changes of sign and the location of the minimum in $C_{uu,z}$ for polymer solutions occur at a distance further away from the wall which indicates the presence of thicker buffer layer.

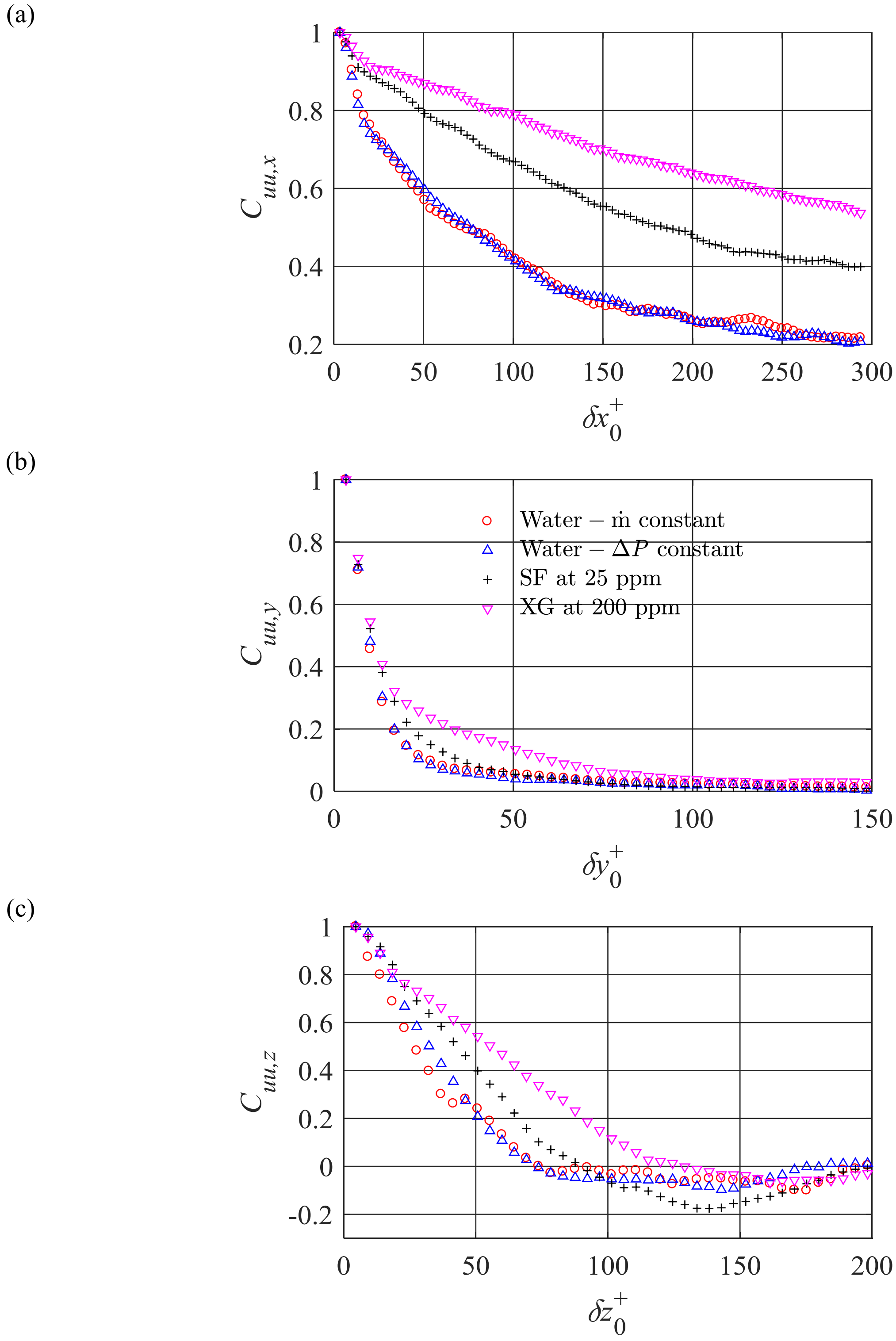

Figure 6-7. Spatial-correlation of streamwise velocity fluctuations in (a) x direction at y^+_0 = 80 (b) y direction at the middle of channel and (c) z direction y^+_0 = 129. The XG-200 has larger streamwise coherence in all directions relative to SF-25.

6.4.6 Vorticity fluctuations

The vorticity fluctuations are defined as the curl of the velocity fluctuations vector and are obtained using

$$\omega_x = \frac{\partial w}{\partial y} - \frac{\partial v}{\partial z},\ \omega_y = \frac{\partial u}{\partial z} - \frac{\partial w}{\partial x},\ \omega_z = \frac{\partial v}{\partial x} - \frac{\partial u}{\partial y} \tag{6.5}$$

where ω_x, ω_y, and ω_z are streamwise, wall-normal, and spanwise vorticity fluctuations, respectively. The vorticity fluctuations are normalized here using the reference inner time scale ($\upsilon/u^2_{\tau 0}$, where υ is the kinematic viscosity of water). This is applied to avoid the variation of normalized vorticity fluctuations due to the change of friction velocity and viscosity of polymer solutions. The normalized spanwise and streamwise vorticity fluctuations are shown in Figure 6-8. The normalized spanwise vorticity fluctuations ($\langle\omega_z\rangle\upsilon/u^2_{\tau 0}$) of water-$\dot{m}$ constant at $Re_\tau = 580$, as shown in Figure 6-8(a), agree with the DNS results of Abe *et al.* (2002) at $Re_\tau = 640$. The $\langle\omega_z\rangle\upsilon/u^2_{\tau 0}$ profiles in water-ΔP constant are smaller in relative to water-$\dot{m}$ constant due to the lower flow rate (lower bulk velocity). The addition of polymer solutions reduces the magnitude of $\langle\omega_z\rangle\upsilon/u^2_{\tau 0}$ across the channel. The reduction of $\langle\omega_z\rangle\upsilon/u^2_{\tau 0}$ by XG-200 relative to water-$\dot{m}$ constant at y^+_0=21 is around 36.1% while SF-25 reduces $\langle\omega_z\rangle\upsilon/u^2_{\tau 0}$ by approximately 11.6% at the same location. The $\langle\omega_z\rangle\upsilon/u^2_{\tau 0}$ profiles of water-ΔP constant at $Re_\tau = 460$ fall between the DNS results of Abe *et al.* (2002) at $Re_\tau = 395$ and 640, and these $\langle\omega_z\rangle\upsilon/u^2_{\tau 0}$ profiles are approximately the same as the profiles for SF-25. The $\langle\omega_z\rangle\upsilon/u^2_{\tau 0}$ profiles from DNS at $Re_\tau = 395$ and 640 have a large difference in magnitude at y^+_0=7 and they converge with respect to each other with increasing y^+_0. This trend is observed in the $\langle\omega_z\rangle\upsilon/u^2_{\tau 0}$ profiles of Newtonian and non-Newtonian flows in the current study.

Figure 6-8(b) indicates that the normalized streamwise vorticity fluctuations ($\langle\omega_x\rangle\upsilon/u^2_{\tau 0}$) in Newtonian flow at $Re_\tau = 580$ follow the DNS results of Abe *et al.* (2002) at $Re_\tau = 640$. The $\langle\omega_x\rangle\upsilon/u^2_{\tau 0}$ profiles of water-ΔP constant are located between DNS results of $Re_\tau = 395$ and 640. The addition of polymer solutions decreases the $\langle\omega_x\rangle\upsilon/u^2_{\tau 0}$ profiles of water-$\dot{m}$ constant across the channel (~ 20% at y^+_0=120). The $\langle\omega_x\rangle\upsilon/u^2_{\tau 0}$ profiles in XG-200 and SF-25 are approximately the same.

The reduction of $\langle\omega_x\rangle\upsilon/u^2_{\tau0}$ profiles with the addition of polymer solutions can be related to the vortex retardation mechanism presented by Kim *et al.* (2007) (Dallas *et al.* 2010). It should be noted that both $\langle\omega_z\rangle\upsilon/u^2_{\tau0}$ and $\langle\omega_x\rangle\upsilon/u^2_{\tau0}$ values reduce across the channel with the addition of polymer solutions. Therefore DR mechanisms should take into account both $\langle\omega_z\rangle\upsilon/u^2_{\tau0}$ and $\langle\omega_x\rangle\upsilon/u^2_{\tau0}$ profiles.

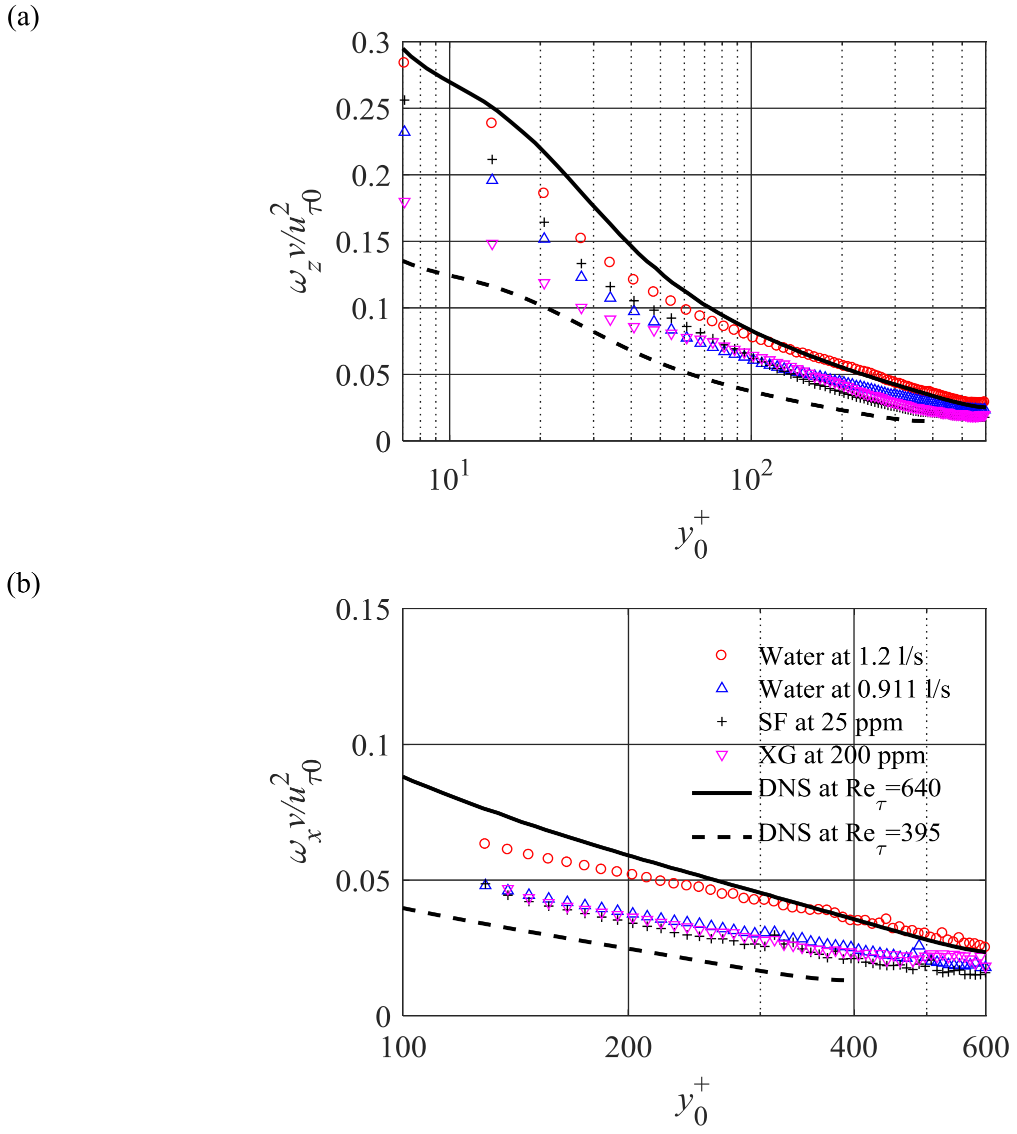

Figure 6-8. The vorticity fluctuations of Newtonian and non-Newtonian flow in (a) spanwise direction and (b) streamwise direction. The PIV measurements in water-$\dot{\boldsymbol{m}}$ constant at $Re_\tau = 580$ are evaluated with DNS result of Abe et al. (2002) at $Re_\tau = 640$. The normalized spanwise vorticity fluctuations of SF-25 is larger than those found in XG-200 at $y^+_0 < 50$, while polymer solutions approximately have the same normalized streamwise vorticity fluctuations.

6.4.7 Flow structure at MDR

Turbulent structures of streamwise velocity fluctuations at MDR are compared with those found in Newtonian flow. A second-order regression with a kernel of four has been applied to smooth the streamwise fluctuating field and remove the noisy data points. The organization of low-speed and high-speed streaks is temporally visualized using stereo-PIV from $0.1H$ to the middle of channel ($0.5H$). The low-speed and high-speed streaks are recognized as negative and positive u velocity fluctuations of $u/U_b = \pm 0.03$ strength. Figure 6-9(a) and (b) show the presence of low-speed and high-speed streaks for both water-$\dot{m}$ constant and SF-45 solution. The low-speed and high-speed streaks are alternately elongated as they evolve temporally. The visualization of Figure 6-9(a) and (b) shows that low and high-speed streaks in SF-45 solution have longer and thicker structure in comparison with water-$\dot{m}$ constant.

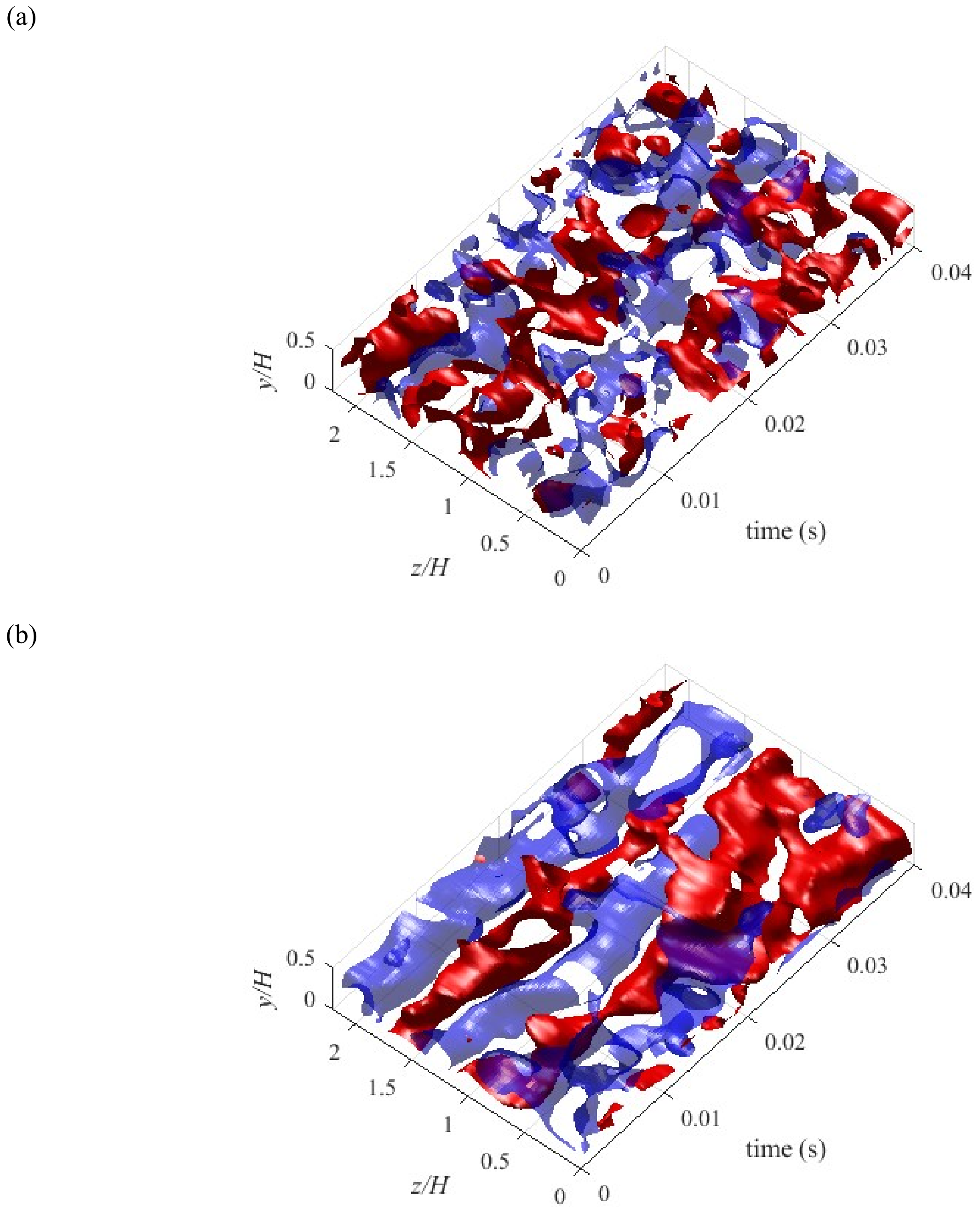

Figure 6-9. Organization of low-speed (transparent blue/light grey) and high-speed (red/dark grey) streaks visualized by iso-surfaces of $u/U_b = \pm 0.03$ for (a) water-$\dot{m}$ constant (b) SF-45 (MDR).

Figure 6-10(a) and (b) show two-point spatial correlations of u fluctuations in y ($C_{uu,y}$) and z ($C_{uu,z}$) directions at $y^+_0 = 113$. The $C_{uu,y}$ of SF-45 shown in Figure 6-10(a) is larger than that of water-$\dot{m}$ constant at $\delta y^+_0 < 200$. In addition, Figure 6-10(b) shows that SF-45 has higher $C_{uu,z}$ at $\delta z^+_0 < 200$ in relative to water-$\dot{m}$ constant. The increase of $C_{uu,y}$ and $C_{uu,z}$ values in SF-45 solution indicate thicker coherent structures at MDR compared to Newtonian flow. This is in agreement with the length scale behavior observed in Figure 6-7. The increase of $C_{uu,z}$ in SF-45 solution agrees with the formation of thicker low-speed and high-seed structures visualized in Figure 6-9(b).

As mentioned above, the $C_{uu,y}$ of SF-45 solution shown in Figure 6-10(a) is always positive, while the results in Section 5.4.5 showed that the $C_{uu,y}$ of XG at DR = 45% included the negative correlation implying the formation of low and high speed streaks in the wall-normal direction. The trend observed in the results presented in Section 5.4.5 might be associated with low Reynolds number ($Re_H \sim 7200$) set in Newtonian flow and the flow regime can be transitional flow with the addition of 125 ppm XG solution.

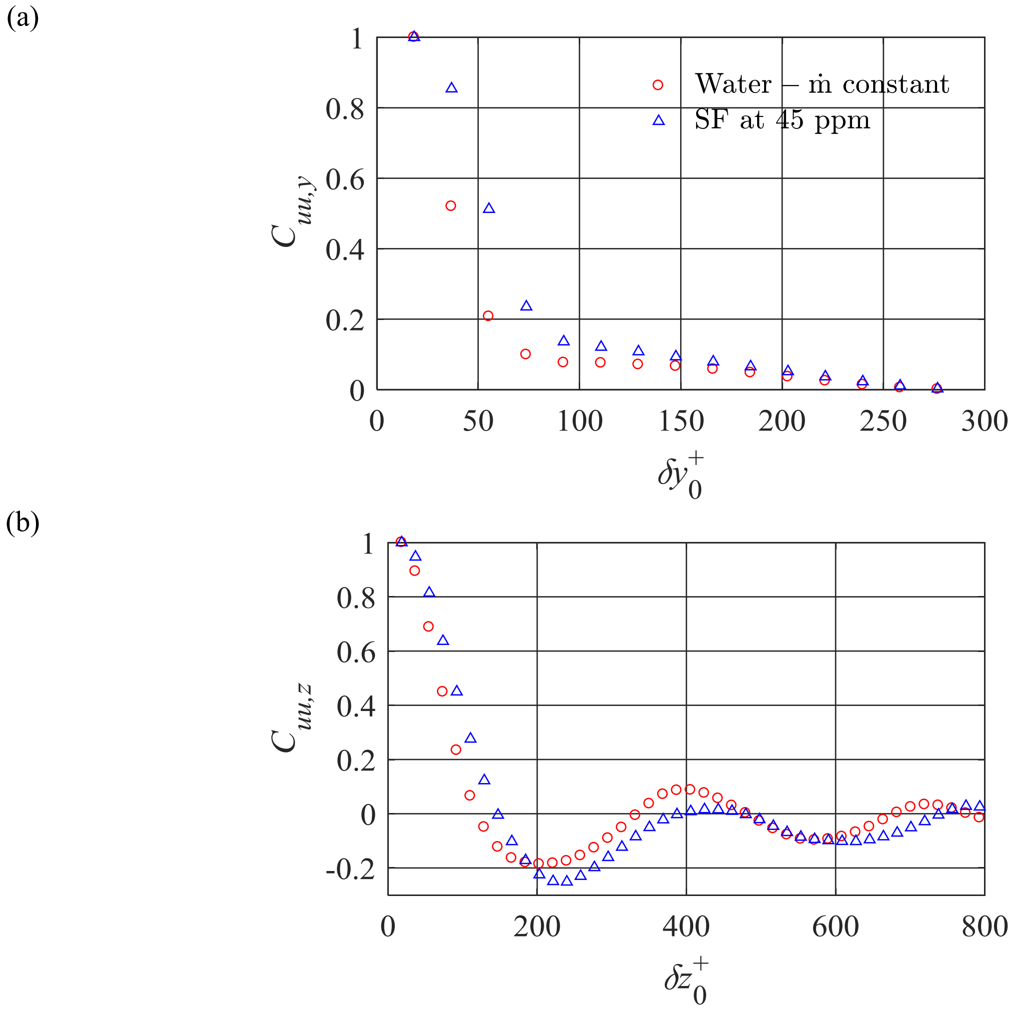

Figure 6-10. Spatial-correlation of streamwise velocity fluctuations in (a) y direction at the middle of channel and (b) z direction y^+_0 = 113. The SF-45 has higher streamwise coherence in y and z directions relative to Newtonian flow.

6.5 Conclusion

Turbulent structures of drag-reducing polymers with rigid and flexible molecular structures at similar DR (pressure drop) were experimentally investigated and compared with those found in Newtonian flows at the same flow rate (water-$\dot{m}$ constant) and at the same pressure drop (water-ΔP constant). The streamwise Reynolds stresses of XG were greater than those of SF at $y^+_0 > 50$, while the wall-normal Reynolds stresses and Reynolds shear stresses of polymer solutions were approximately the same. The polymer stress of XG due to larger shear viscosity was larger than the polymer stress of SF at $y^+_0 < 120$, while they approximately had the same polymer stress at $y^+_0 > 120$. The magnitude of streamwise and spanwise vorticity fluctuations reduced for both polymer solutions. The XG solution decreased the magnitude of spanwise vorticity fluctuations more than the SF solution at $y^+_0 < 50$, while both polymer solutions had the similar effect on the magnitude of streamwise vorticity fluctuations. The spatial-correlation of streamwise velocity fluctuations in polymer solutions were increased in all the directions, which indicates longer streamwise coherence of the turbulent structures, and this increase in XG solution was larger than that in SF solution. In addition, turbulent structures of SF solution at maximum drag reduction (MDR) were experimentally characterized relative to those found in Newtonian flow. The low and high speed streaks were elongated and thickened in the contrast with those found in Newtonian flow.

Chapter 7. Conclusion and future work

7.1 Conclusion

To replace synthetic polymers with bio polymers, an understanding of DR mechanisms for flexible and rigid polymers is necessary. DR mechanisms are experimentally investigated by comparing turbulent structures of rigid and flexible polymer solutions. At first, the relation between drag reduction (DR) and mechanical degradation with the rheology of polyacrylamides (PAM), polyethylene oxide (PEO), xanthan gum (XG), and carboxymethyl cellulose (CMC) solutions was experimentally investigated. Each polymer solution was prepared at a different concentration to produce the same shear viscosity. This methodology was chosen to isolate the effect of shear viscosity. The viscoelastic properties of the polymer solutions were investigated using a capillary break-up extensional rheometer (CaBER) and oscillatory shear measurements at the same solution concentration used for drag reduction tests of each polymer solution.

The DR performance of each solution and its mechanical degradation was measured in a turbulent pipe flow at Re = 13,100, based on bulk velocity and pipe diameter. The flexible polymers (PAM and PEO) produced larger DR than the rigid polymers (XG and CMC). However, DR of PEO quickly reduced to zero due to mechanical degradation, while XG and CMC demonstrated negligible mechanical degradation. As expected, DR and mechanical degeneration were both independent of shear viscosity; all polymer solutions had the same shear viscosity but exhibited different DR performance.

This investigation highlights the importance of viscoelasticity of the polymer solutions, both in the linear and non-linear regimes, as characterized by oscillatory shear viscosity and CaBER measurements, respectively. Drag reduction was proportional to both relaxation time and Weissenberg number (Wi) obtained from CaBER measurements. We also observed a correlation between the magnitude of extensional viscosity at high strain rates (similar strain rate as the corresponding pipe flow) and DR of the polymer solutions. The rapid and significant mechanical degradation of the PEO solution was associated with its strain-rate thinning behavior as seen from reduction of its extensional viscosity with increase of strain rate. The PAM solutions, which were relatively resistant to mechanical degradation, showed strain-rate hardening behavior. The PAM polymers had the largest G' and G'', while the PEO had the lowest values. The G' and G'' modulus for rigid XG and CMC solutions fell between the values for PEO and PAM. In general, it was observed that solutions with larger G'/G'' result in larger DR due to their stronger elastic behavior. The rheological measurements (extensional viscosity measurements and oscillatory tests) are proposed to initially categorize DR performance of a wide range of polymer solutions. The polymer solutions with larger magnitude in storage and loss modulus or relaxation time are determined. This process significantly reduces the number of pressure drop measurements in the flow loop. However, the ultimate DR performance for selected polymers can be characterized by pressure drop measurements because shear rate in the flow loop is needed for DR prediction.

There are a few studies about bio polymers in the literature; however turbulent structures are not completely discussed. Hence, planar-PIV was used to investigate turbulent structures of XG solutions at different concentrations. The addition of rigid XG polymer to water at different concentrations has resulted in significant changes in the turbulent structures measured during channel flow at Re = 7200. There is a monotonic change of turbulence statistics with increasing polymer concentration, with turbulence production at a minimum when the point of maximum drag reduction (MDR) is reached. The investigations of the present study showed that the logarithmic layer, where turbulence production is balanced by the viscous dissipation of turbulence, shifts away from the wall with increasing XG concentration. This shift of the logarithmic layer is associated with reduction of near-wall turbulence production at all DR cases. The semi-log profile of mean velocity prior to MDR falls between the Newtonian log-law and MDR profiles. This is in contrast to most of the previous observations of flexible polymers, which have a crossover point from MDR asymptote in the near-wall to a profile parallel to Newtonian log-law. At the MDR condition, turbulence production is so small that the logarithmic layer disappears and the mean velocity follows Virk's asymptote (Virk 1971). The reduction of turbulence production is mainly associated with changes in ejection motions (second quadrant of u-v plot) although there is a small increase of turbulence production by sweep motions (fourth quadrant). At the MDR, streamwise Reynolds stress is as large as that of the Newtonian flow. This is contrary to flexible polymers showing significant reduction of streamwise Reynolds stress at MDR. Wall-normal and shear Reynolds shear stresses of XG solution were also significantly attenuated, which agrees with the trend of flexible polymers.

Investigation of the triple products of velocity fluctuations showed that the narrow sweep-dominated region in the immediate vicinity of the wall extends farther away from the wall with increasing polymer concentration. The outer boundary of the sweep-dominated layer moves from $13\lambda_0$ in the Newtonian flow to $80\lambda_0$ at MDR. The asymmetric behavior of positive u fluctuations (i.e., positive $<u^3>$) increases with increasing polymer XG concentration. This positive skewness ($<u^3>/<u^2>^{3/2}$) extends in the wall-normal direction and intensifies at larger DR values. The largest positive skewness is observed at MDR at y^+_0~25 where the largest flatness (Kurtosis or $<u^4>/<u^2>^2$) of u fluctuations is also observed.

The quadrant analysis at $y^+_0=25$ shows that the addition of polymers inclines the principal axis of v versus u plot from about 15 degrees (clockwise with respect to negative u-axis) in the Newtonian flow to almost zero (horizontal) at MDR. The JPDF of fluctuations becomes symmetric with respect to the u axis at MDR. A large number of negative and weak u fluctuations ($-3u_\tau < u < -u_\tau$) along with a relatively smaller number of positive larger u fluctuations ($u > 6u_\tau$) are observed at MDR. The spatial-correlation of the fluctuating velocity field shows that an increase in XG concentration increases the spatial coherence of u fluctuations in the x-direction while v fluctuations are not affected and stay localized. The length scales of streamwise velocity fluctuations in wall-normal direction show the formation of low and high speed streaks. Proper orthogonal decomposition (POD) confirms the results of the length scales of streamwise velocity fluctuations in wall-normal direction. The first energetic mode at MDR (obtained with 125 ppm XG polymer) shows streamwise elongated layers with positive and negative u fluctuations. The inclined shear layer structure of Newtonian wall flows, which plays a major role in turbulence production, is not present in the energetic POD modes of the flow at MDR.

To further investigate DR mechanisms of rigid and flexible polymers, comparison of the two types should be made at conditions where they produce an identical DR. Hence, investigations of rigid and flexible polymer solutions at similar DR were conducted and the turbulent structures were compared with those found in Newtonian flow. The mean velocity profile had a larger slope with the flexible polymer solutions than that of the rigid polymer solution. The rigid polymer solution increased the streamwise Reynolds stresses in the comparison with the flexible polymer at $y^+_0 > 50$, while both rigid and flexible polymers had an approximately similar effect on the wall-normal Reynolds stresses and Reynolds shear stresses. The quadrant analysis at $y^+_0 = 80$ for both XG and SF solutions showed that the magnitude of v fluctuations attenuated while the magnitude of u fluctuations increased. The inclination of the principal axis of v as a function of u plot to horizontal line was observed for polymer solutions. The rigid polymer included larger polymer stress near the wall ($y^+_0 < 120$) in relative to the flexible polymer while they approximately provided similar polymer stresses far away from the wall ($y^+_0 > 120$). The rigid and flexible polymer solutions similarly reduced the magnitude of streamwise vorticity fluctuations, while the rigid polymer decreased the magnitude of spanwise vorticity fluctuations larger in contrast with the flexible polymer at $y^+_0 < 50$. The rigid polymer increased the spatial-correlation of u fluctuations more compared to the flexible polymer. Therefore, based on the comparison of parameters mentioned above, the significant differences are existed between DR mechanisms of rigid and flexible polymers even when they produce an identical DR.

The investigation of turbulent structures for synthetic and bio polymers is the first step to determine their DR mechanism. Now the only way to increase DR of a bio polymer is to increase the concentration, and MDR usually occurs at very high concentration. To achieve MDR using very low concentration of a bio polymer, DR mechanism has to be completely understood and the molecular structure of bio polymers should be optimized to provide this condition.

In addition, turbulent structures for Newtonian flow and polymer solutions at MDR were characterized. The low-speed and high-speed streaks in the flexible polymer solution at MDR have thicker and elongated structures relative to the Newtonian flow. The spatial-correlation of u fluctuations in y and z directions also confirmed the visualization of the low-speed and high-speed streaks at MDR. The elongated and thicker low-speed and high-speed streaks at MDR suggest the presence of elasto-inertial instability (EII).

In summary, DR mechanisms of rigid and flexible polymer solutions were studied by comparing turbulent structures and the results indicated clear differences, even when they produce an identical DR.

7.2 Future work

The effect of flexible and rigid polymers on turbulent structures can be further investigated using tomographic PIV. The production and dissipation term of kinetic energy budget for both polymer solutions are obtained and compared. In addition, these experimental results are used to verify DNS results available in the literature. Moreover, the ratio of the convective time scale of streamwise vorticity fluctuation to vortex rotation time for both rigid and flexible polymers can be experimentally obtained and compared with those obtained from DNS results. As previously mentioned, the mechanism of MDR is not completely understood; therefore this study should be carried out at both LDR and MDR states.

DR mechanisms of flexible polymer solutions presented by Lumley (1967) and De Gennes (1986) can be further investigated using tomographic PIV. Based on DR mechanism of Lumley (1967), the extensional viscosity is an important parameter in evaluating DR mechanism of flexible polymer solutions. The concentration of flexible polymers with linear and non-linear chains is adjusted to produce solutions with identical extensional viscosity. DR performance of flexible polymers at similar extensional viscosity shows dependency of DR mechanism on the hypothesis of De Gennes (1986). Tomographic PIV is used to compare turbulent structures of flexible polymer solutions at similar extensional viscosity. In addition, DR mechanisms of flexible polymers can be further investigated at identical DR (at both LDR and MDR states). This helps to clarify DR mechanisms of flexible polymers and find out whether they share the same DR mechanism or not.

References

Abdulbari, H. A., Shabirin, A., & Abdurrahman, H. N. (2014). Bio-polymers for improving liquid flow in pipelines-a review and future work opportunities. *Journal of Industrial and Engineering Chemistry*, **20**(4), 1157–1170.

Abe, H., Kawamura, H., & Matsuo, Y. (2002). Direct numerical simulation of a fully developed turbulent channel flow with respect to the Reynolds number dependence. *Journal of Fluids Engineering*, **123**(2), 382–393.

Abubakar, A., Al-Wahaibi, T., Al-Wahaibi, Y., Al-Hashmi, A. R., & Al-Ajmi, A. (2014). Roles of drag reducing polymers in single- and multi-phase flows. *Chemical Engineering Research and Design*, **92**(11), 2153–2181.

Anna, S. L., & McKinley, G. H. (2002). Elasto-capillary thinning and breakup of model elastic liquids. *Journal of Rheology*, **45**(1), 115–138.

BASF, O. (2013). Magnafloc® 5250- mining solutions- BASF corporation.

Benzi, R., Angelis, E. De, Victor, S. L., & Procaccia, I. (2005). Identification and calculation of the universal asymptote for drag reduction by polymers in wall bounded turbulence, **194502** (November), 1–4.

Bewersdorff, H.-W., & Singh, R. P. (1988). Rheological and drag reduction characteristics of xanthan gum solutions, **627**, 617–627.

Cai, W. H., Li, F. C., Zhang, H. N., Hishida, K. (2009). Study on the characteristics of turbulent drag-reducing channel flow by particle image velocimetry combining with proper orthogonal decomposition analysis. *Physics of Fluids*, **21**(11), 1–12.

Campo-Deaño, L., & Clasen, C. (2010). The slow retraction method (SRM) for the determination of ultra-short relaxation times in capillary breakup extensional rheometry experiments. *Journal of Non-Newtonian Fluid Mechanics*, **165**(23–24), 1688–1699.

Choueiri, G. H., Lopez, J. M., & Hof, B. (2018). Exceeding the asymptotic limit of polymer drag reduction. *Physical Review Letters*, **120**(12), 124501 (1-6).

Dallas, V., Vassilicos, J. C., & Hewitt, G. F. (2010). Strong polymer-turbulence interactions in viscoelastic turbulent channel flow. *Physical Review E - Statistical, Nonlinear, and Soft Matter Physics*, **82**(6), 1–19.

Den Toonder J.M.J. , Draad A.A., Kuiken, G. D. C. and Nieuwstadt F. T. M. (1995). Degradation effects of dilute polymer solutions on turbulent drag reduction in pipe flows. *Applied Scientific Research*, **55 (1)**, 63–82.

Dinic, J., Zhang, Y., Jimenez, L. N., & Sharma, V. (2015). Extensional relaxation times of dilute, aqueous polymer solutions. *ACS Macro Letters*, **4**(7), 804–808.

Dontula, P., Pasquali, M., Scriven, L. E., & Macosko, C. W. (1997). Can extensional viscosity be measured with opposed-nozzle devices? *Rheologica Acta*, **36**(4), 429–448.

Dubief, Y., Terrapon, V. E., & Soria, J. (2013). On the mechanism of elasto-inertial turbulence. *Physics of Fluids*, **25**(11), 110817 (1-16).

Dubief, Y., White, C. M., Terrapon, V. E., Shaqfeh, E. S. G., Moin, P., & Lele, S. K. (2004). On the coherent drag-reducing and turbulence-enhancing behaviour of polymers in wall flows. *Journal of Fluid Mechanics*, **514**, 271–280.

Entov, V. M., & Hinch, E. J. (1997). Effect of a spectrum of relaxation times on the capillary thinning of a filament of elastic liquid, **72**, 31–53.

Escudier, M. P., Gouldson, I. W., Pereira, A. S., Pinho, F. T., & Poole, R. J. (2001). On the reproducibility of the rheology of shear-thinning liquids. *Journal of Non-Newtonian Fluid Mechanics*, **97**(2–3), 99–124.

Escudier, M. P., Nickson, A. K., & Poole, R. J. (2009). Turbulent flow of viscoelastic shear-thinning liquids through a rectangular duct: Quantification of turbulence anisotropy. *Journal of Non-Newtonian Fluid Mechanics*, **160**(1), 2–10.

Escudier, M. P., Presti, F., & Smith, S. (1998). Drag reduction in the turbulent pipe flow of polymers. *Journal of Non-Newtonian Fluid Mechanics*, **81**(3), 197–213.

F. Olsson, J. Y. (1993). Some properties of the upper for viscoelastic fluid flow, **48**, 125–145.

Fu, Z., Otsuki, T., Motozawa, M., Kurosawa, T., Yu, B., & Kawaguchi, Y. (2014). Experimental investigation of polymer diffusion in the drag-reduced turbulent channel flow of inhomogeneous solution. *International Journal of Heat and Mass Transfer*, **77**, 860–873.

Gampert, B., Braemer, T., Eich, T., & Dietmann, T. (2005). Rheo-optical investigations and near-wall turbulence structure of polymer solutions in turbulent channel flow. *Journal of Non-Newtonian Fluid Mechanics*, **126**(2–3 SPEC. ISS.), 115–121.

Gennes, P. G. DE. (1986). Towards a scaling theory of drag reduction. *Physica*, **140A**, 9–25.

Hadri, F., Besq, A., Guillou, S., & Makhloufi, R. (2011). Temperature and concentration influence on drag reduction of very low concentrated CTAC / NaSal aqueous solution in turbulent pipe flow. *Journal of Non-Newtonian Fluid Mechanics*, **166**(5–6), 326–331.

Han, W. J., & Choi, H. J. (2017). Role of bio-based polymers on improving turbulent flow characteristics: materials and application. *Polymers*, **9**, **209**(6), 1–23.

Han, W. J., Dong, Y. Z., & Choi, H. J. (2017). Applications of water-Soluble Polymers in turbulent drag reduction. *Processes*, **5**(4), 24.

Hénaut, I., Glénat, P., Cassar, C., Gainville, M., Hamdi, K., & Pagnier, P. (2012). Mechanical degradation kinetics of polymeric DRAs. © *BHR Group 2012 Multiphase 8*, 59–71.

Housiadas, K. D., & Beris, A. N. (2004). Characteristic scales and drag reduction evaluation in turbulent channel flow of nonconstant viscosity viscoelastic fluids. *Physics of Fluids*, **16**(5), 1581–1586.

Interthal, W., & Wilski, H. (1985). Drag reduction experiments with very large pipes. *Colloid & Polymer Science*, **263**(3), 217–229.

Iwamoto, K., Suzuki, Y., & Kasagi, N. (2002). Reynolds number effect on wall turbulence : toward effective feedback control. *International Journal of Heat and Fluid Flow*, **23**, 678–689.

J.L. Lumley. (1967). The structure of inhomogeneous turbulent flow. *Atmospheric Turbulence and Radio Wave Propagation (Ed. A. M. Yaglom & V. I. Tatarski)*, 166–178.

J.W. Hoyt. (1989). Drag reduction by polymers and surfactants. *American Institute of Aeronautics and Astronautics*, 413–432.

Jaffar, A. and P. R. J. (2011). Drag reduction of biopolymer flows. *Journal of Applied Sciences*, **11(9)**, 1544–1551.

Japper-Jaafar, A., Escudier, M. P., & Poole, R. J. (2009). Turbulent pipe flow of a drag-reducing rigid "rod-like" polymer solution. *Journal of Non-Newtonian Fluid Mechanics*, **161**(1–3), 86–93.

Jubran, B. A., Zurigat, Y. H., & Goosen, M. F. A. (2007). Drag reducing agents in multiphase flow pipelines : Recent trends and future needs drag, **6466**, 1403–1424.

Kemira. (n.d.). Superfloc® flocculants & coagulants.

Kim, C. A., Choi, H. J., Kim, C. B., & Jhon, M. S. (1998). Drag reduction characteristics of polysaccharide xanthan gum. *Macromolecular Rapid Communications*, **19**(8), 419–422.

Kim, J., Moin, P., & Moser, R. (1987). Turbulence statistics in fully developed channel flow at low reynolds number. *Journal of Fluid Mechanics*, **177**, 133–166.

Kim, K., Li, C. F., Sureshkumar, R., Balachandar, S., & Adrian, R. J. (2007). Effects of polymer stresses on eddy structures in drag-reduced turbulent channel flow. *Journal of Fluid Mechanics*, **584**, 281–299.

Kim, K., & Sirviente, A. I. (2005). Turbulence structure of polymer turbulent channel flow with and without macromolecular polymer structures. *Experiments in Fluids*, **38**(6), 739–749.

Kreplin, H.-P., & Eckelmann, H. (1979). Propagation of perturbations in the viscous sublayer and adjacent wall region. *Journal of Fluid Mechanics*, **95**(2), 305–322.

Lee, K., Kim, C. A., Lim, S. T., Kwon, D. H., Choi, H. J., & Jhon, M. S. (2002). Mechanical degradation of polyisobutylene under turbulent flow. *Colloid Polymer Science*, 779–782.

Li, C. F., Sureshkumar, R., & Khomami, B. (2006). Influence of rheological parameters on polymer induced turbulent drag reduction. *Journal of Non-Newtonian Fluid Mechanics*, **140**(1–3), 23–40.

Li, C. F., Sureshkumar, R., & Khomami, B. (2015). Simple framework for understanding the universality of the maximum drag reduction asymptote in turbulent flow of polymer solutions. *Physical Review E - Statistical, Nonlinear, and Soft Matter Physics*, **92**(4), 1–6.

Liberatore, M. W., Baik, S., McHugh, A. J., & Hanratty, T. J. (2004). Turbulent drag reduction of polyacrylamide solutions: effect of degradation on molecular weight distribution. *Journal of Non-Newtonian Fluid Mechanics*, **123**(2–3), 175–183.

Lumley, J. L. (1967). Drag reduction by additives. *Annual Review of Fluid Mechanics*, **1**(1), 367–384.

McKinley, G. H., & Tripathi, A. (2002). How to extract the newtonian viscosity from capillary breakup measurements in a filament rheometer. *Journal of Rheology*, **44**(3), 653–670.

Meinhart, C. D., Wereley, S. T., & Santiago, J. G. (2000). A PIV algorithm for estimating time-averaged velocity fields. *Journal of Fluids Engineering*, **122**(2), 285–289.

Meyer, K. E., Pedersen, J. M., & Ȯzcan, O. (2007). A turbulent jet in crossflow analysed with proper orthogonal decomposition. *Journal of Fluid Mechanics*, **583**(2007), 199–227.

Miller, E., Clasen, C., & Rothstein, J. P. (2009). The effect of step-stretch parameters on capillary breakup extensional rheology (CaBER) measurements. *Rheologica Acta*, **48**(6), 625–639.

Min, T., Choi, H., & Yoo, J. Y. (2003). Maximum drag reduction in a turbulent channel flow by polymer additives. *Journal of Fluid Mechanics*, **492**(492), 91–109.

Morrison, F. A. (2001). *Understanding rheology*, Oxford University Press.

Moser, R. D., Kim, J., & Mansour, N. N. (1999). Direct numerical simulation of turbulent channel flow up to Re_τ=590. *Physics of Fluids*, **11**(4), 943–945.

Nakken, T., Tande, M., & Elgsaeter, A. (2001). Measurements of polymer induced drag reduction and polymer scission in taylor flow using standard double-gap sample holders with axial symmetry. *Journal of Non-Newtonian Fluid Mechanics*, **97**(1), 1–12.

Owolabi, B. E., Dennis, D. J. C., & Poole, R. J. (2017). Turbulent drag reduction by polymer additives in parallel-shear flows. *Journal of Fluid Mechanics*, **827**, 1–12.

Papagianni, M., Psomas, S. K., Batsilas, L., Paras, S. V., Kyriakidis, D. A., & Liakopoulou-Kyriakides, M. (2001). Xanthan production by xanthomonas campestris in batch cultures. *Process Biochemistry*, **37**(1), 73–80.

Pereira, A. S., Andrade, R. M., & Soares, E. J. (2013). Drag reduction induced by flexible and rigid molecules in a turbulent flow into a rotating cylindrical double gap device: comparison between poly (ethylene oxide), polyacrylamide, and xanthan gum. *Journal of Non-Newtonian Fluid Mechanics*, **202**, 72–87.

Pereira, A. S., & Soares, E. J. (2012). Polymer degradation of dilute solutions in turbulent drag reducing flows in a cylindrical double gap rheometer device. *Journal of Non-Newtonian Fluid Mechanics*, **179–180**, 9–22.

Procaccia, I., L'Vov, V. S., & Benzi, R. (2008). Colloquium: Theory of drag reduction by polymers in wall-bounded turbulence. *Reviews of Modern Physics*, **80**(1), 225–247.

Ptasinski, P. K., Boersma, B. J., Nieuwstadt, F. T. M., Hulsen, M. A., Van den Brule, H. A. A., & Hunt, J. C. R. (2003). Turbulent channel flow near maximum drag reduction: simulations, experiments and mechanisms. *Journal of Fluid Mechanics*, **490**(490), 251–291.

Ptasinski, P. K., Nieuwstadt, F. T. M., Van Den Brule, B. H. A. A., & Hulsen, M. A. (2001). Experiments in turbulent pipe flow with polymer additives at maximum drag reduction. *Flow, Turbulence and Combustion*, **66**(2), 159–182.

Renardy, M. (1995). A numerical study of the asymptotic evolution and breakup of Newtonian and viscoelastic jets. *Journal of Non-Newtonian Fluid Mechanics*, **59**(2–3), 267–282.

Robinson, S. (1991). Coherent motions in the turbulent boundary layer. *Annual Review of Fluid Mechanics*, **23**(1), 601–639.

Rodd, L. E., Scott, T. P., Cooper-White, J. J., & McKinley, G. H. (2005). Capillary break-up rheometry of low-viscosity elastic fluids. *Applied Rheology*, **15**(1), 12–27.

S. B. Pope. (2000). *Turbulent flows*, Cambridge: Cambridge University Press. doi:10.1016/S0010-2180(01)00244-9

Samanta, D., Dubief, Y., Holzner, M., Hof, B. (2013). Elasto-inertial turbulence. *Proceedings of the National Academy of Sciences*, **110**(30), 10557–10562.

Sandoval, G. A. B., Trevelin, R., Soares, E. J., Silveira, L., Thomaz, F., & Pereira, A. S. (2015). Polymer degradation in turbulent drag reducting flows in pipes. *Thermal Engineering*, **4**, 3–6.

Sandoval, G., & Soares, E. J. (2016). Effect of combined polymers on the loss of efficiency caused by mechanical degradation in drag reducing flows through straight tubes. *Rheologica Acta*, **55**(7), 559–569.

Schramm, G. (1994). *A practical approach to rheology and rheometry*, Karlsruhe: Haake.

Scientific, T. (2006). Instruction manual, HAAKE CaBER 1, Thermo Electron (Karlsruhe) GMBH.

SIGMA-ALDRICH. (n.d.). Product specification- poly (ethylene oxide)- average Mv ~ 8,000,000, powder.

Singh, R. P., Jai, S. K., & Lan, N. (1991). Drag reduction, flocculation and rheological characteristics of contemporary, grafted polysaccharides. *Polymer Science Themes*, In: Sivara, New Dehli: Polymer Science Contemporary Themes.

Sirovich, L. (2016). Turbulence and the dynamics of coherent structures. III. Dynamics and scaling. *Quarterly of Applied Mathematics*, **45**(3), 583–590.

Soares, E. J., Sandoval, G. A. B., Silveira, L., Pereira, A. S., Trevelin, R., & Thomaz, F. (2015a). Loss of efficiency of polymeric drag reducers induced by high Reynolds number flows in tubes with imposed pressure. *Physics of Fluids*, **27**(12), 125105 (1-23).

Soares, E. J., Sandoval, G. A. B., Silveira, L., Pereira, A. S., Trevelin, R., & Thomaz, F. (2015b). Loss of efficiency of polymeric drag reducers induced by high Reynolds number flows in tubes with imposed pressure. *Physics of Fluids*, **27**(12). doi:10.1063/1.4937594

Sohn, J. I., Kim, C. A., Choi, H. J., & Jhon, M. S. (2001). Drag-reduction effectiveness of xanthan gum in a rotating disk apparatus. *Carbohydrate Polymers*, **45**(1), 61–68.

Stanislas, M., Perret, L., & Foucaut, J. M. (2008). Vortical structures in the turbulent boundary layer: a possible route to a universal representation. *Journal of Fluid Mechanics*, **602**, 327–382.

TA-Instruments. (2019). Discovery Hybrid Rheometer.

Teng, H., Liu, N., Lu, X., & Khomami, B. (2018). Turbulent drag reduction in plane couette flow with polymer additives: a direct numerical simulation study. *Journal of Fluid Mechanics*, **846**, 482–507.

Theunissen, R., Scarano, F., & Riethmuller, M. L. (2008). On improvement of PIV image interrogation near stationary interfaces. *Experiments in Fluids*, **45**(4), 557–572.

Toonder, J. M. J. Den. (1995). *Drag reduction by polymer additives in a turbulent pipe flow: laboratory and numerical experiments*.

Tsukahara, T., Seki, Y., Kawamura, H., & and D. Tochio. (2005). DNS of turbulent channel flow at very low Reynolds numbers. *In Proc. of the Forth Int. Symp. on Turbulence and Shear Flow Phenomena*, Williamsburg, USA.

Vanapalli, S. A., Ceccio, S. L., & Solomon, M. J. (2006). Universal scaling for polymer chain scission in turbulence. *Proceedings of the National Academy of Sciences*, **103**(45), 16660–16665.

Virk, P. S., Sherman, D. C., & Wagger, D. L. (1997). Additive equivalence during turbulent drag reduction. *AIChE Journal*, **43**(12), 3257–3259.

Virk, P. S. (1971). An elastic sublayer model for drag reduction by dilute solutions of linear macromolecules. *Journal of Fluid Mechanics*, **45**(3), 417–440.

Virk, P. S. (1975). Drag reduction by collapsed and extended polyelectrolytes. *Nature,* **253**, 109–110.

Virk, P. S. (1975). Drag reduction fundamentals. *AIChE Journal*, **21**(4), 625–656.

Virk, P. S., Merrill, E. W., Mickley, H. S., & Smith, K. A. (1967). The Toms phenomenon: turbulent pipe flow of dilute polymer solutions. *Journal of Fluid Mechanics*, **30**(02), 305–328.

Virk, P. S., Mickley, H. S., & Smith, K. A. (1970). The ultimate asymptote and mean flow structure in Toms' phenomenon. *Journal of Applied Mechanics*, **37**(2), 488.

Vonlanthen, R., & Monkewitz, P. A. (2013). Grid turbulence in dilute polymer solutions: PEO in water. *Journal of Fluid Mechanics*, **730**(2013), 76–98.

Walker, D. T., & Tiederman, W. G. (1990). Turbulent structure in a channel flow with polymer injection at the wall. *Journal of Fluid Mechanics*, **218**, 377–403.

Wallace, J. M., Eckelmann, H., & Brodkey, R. S. (1972). The wall region in turbulent shear flow. *Journal of Fluid Mechanics*, **54**(1), 39–48.

Warholic, M. D., Heist, D. K., Katcher, M., & Hanratty, T. J. (2001). A study with particle-image velocimetry of the influence of drag-reducing polymers on the structure of turbulence. *Experiments in Fluids*, **31**(5), 474–483.

Warholic, M. D., Massah, H., & Hanratty, T. J. (1999). Influence of drag-reducing polymers on turbulence: effects of Reynolds number, concentration and mixing. *Experiments in Fluids*, **27**(5), 461–472.

Wei, T., & Willmarth, W. W. (1992). Modifying turbulent structure with drag-reducing polymer additives in turbulent channel flows. *Journal of Fluid Mechanics*, **245**, 619–641.

White, C. M., & Mungal, M. G. (2008). Mechanics and prediction of turbulent drag reduction with polymer additives. *Annual Review of Fluid Mechanics*, **40**(1), 235–256.

White, C. M., Somandepalli, V. S. R., & Mungal, M. G. (2004). The turbulence structure of drag-reduced boundary layer flow. *Experiments in Fluids*, **36**(1), 62–69.

Wieneke, B. (2005). Stereo-PIV using self-calibration on particle images. *Experiments in Fluids*, **39**(2), 267–280.

Wyatt, N. B., Gunther, C. M., & Liberatore, M. W. (2011). Drag reduction effectiveness of dilute and entangled xanthan in turbulent pipe flow. *Journal of Non-Newtonian Fluid Mechanics*, **166**(1–2), 25–31.

Xi, L., & Graham, M. D. (2012). Intermittent dynamics of turbulence hibernation in Newtonian and viscoelastic minimal channel flows. *Journal of Fluid Mechanics*, **693**, 433–472.

Xiong, B., Loss, R. D., Shields, D. Kumar, M. (2018). Polyacrylamide degradation and its implications in environmental systems. *Npj Clean Water*, **1**(1), 1–9.

Y.A. Çengel, J. M. C. (2014). *Fluid mechanics : fundamentals and applications*, (3st ed.)., New York: McGraw-Hill.

Yarin, A. L. (1993). *Free liquid jets and films: hydroshears & rheology*, Interactio, Longman, Wiley, New York.

Appendices

Appendix A. Pump curve

A progressive cavity pump (Moyno, model 36704) was used to circulate the flow in the channel and pipe flow loops. The pump performance is shown in Figure A.1.

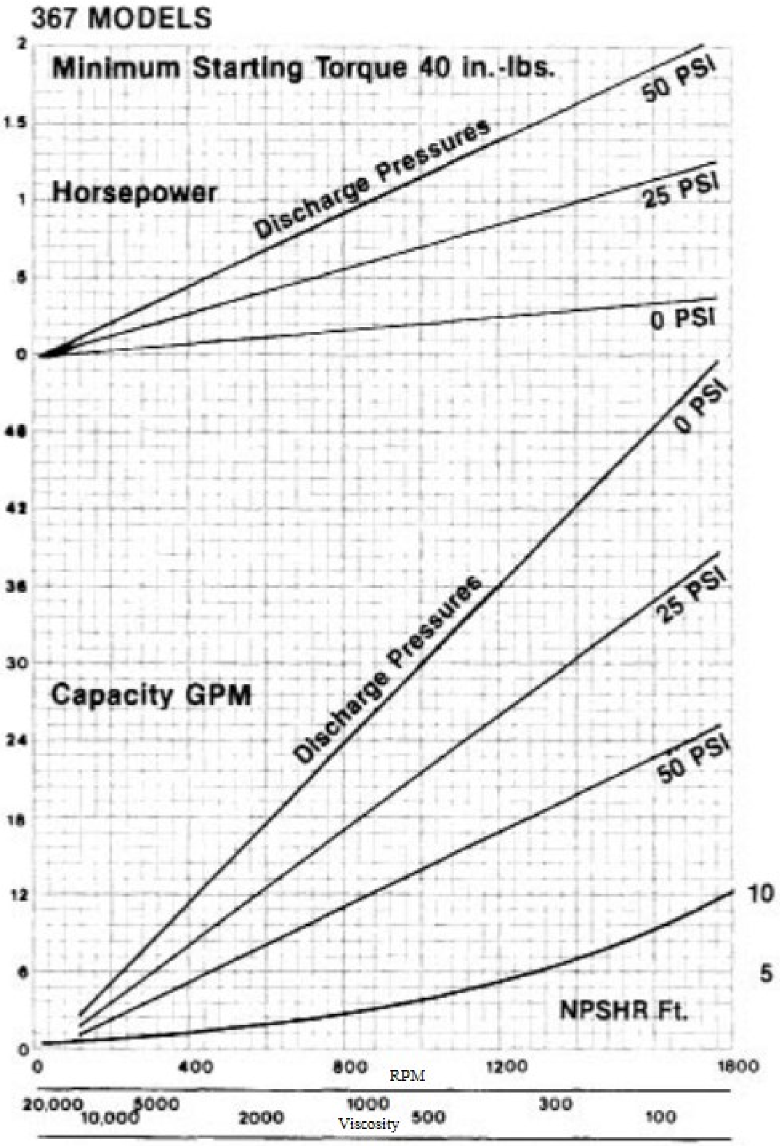

Figure A-1. The pump performance of A progressive cavity pump (Moyno, model 36704)

Appendix B. Polymer preparation procedure

The procedure of polymer preparation for rigid and flexible polymer solutions is detailed in this section. As previously mentioned, a high-concentration, master solution is prepared using a low shear magnetic stirrer. The required amount of polymer powder is accurately weighed (Mettler Toledo, AB104-S) with precision of 0.1 mg. The first step is to find out how much polymer powder is needed to make master solution. For example, to make a 20 ppm polymer solution in the loop, we have to multiply the desired concentration in the loop by the volume of tank. Therefore, the concentration of master solution would be 1400 ppm which is produced by adding 2.8 gr polymer powder in 2 Lit water. The polymer and water were gradually added to a beaker (~2 L) while the magnetic stirrer mixed the solution at 300-400 rpm. The procedure of master solutions preparation for flexible polymers is carried out at ambient temperature, while that for rigid polymers is conducted at 50 degrees. It helps rigid polymers to be homogenously dissolved in water. After 2 hours of mixing, a vacuum pump was applied to remove air bubbles from the solution. Then master solution was wrapped using a napkin and held for 24 hrs before to be used. This disappears all small bubbles in the master solution.

Appendix C. Loop operation

The experimental setup used in this research consists of pipe and channel flow loops (Figures 3-1 and 3-2, page 25). A Validyne differential pressure transducer with 0.5 psi diaphragm was used for the measuring the pressure drop. Pressure transducer was calibrated before using it in the flow loop. A known amount of pressure was applied to the pressure transducer (0-0.5 psi) and the corresponding voltage (0-10 Volts) was recorded. The span was adjusted to give 10 Volts for 0.5 psi. A sample calibration curve is illustrated in Figure C-1.

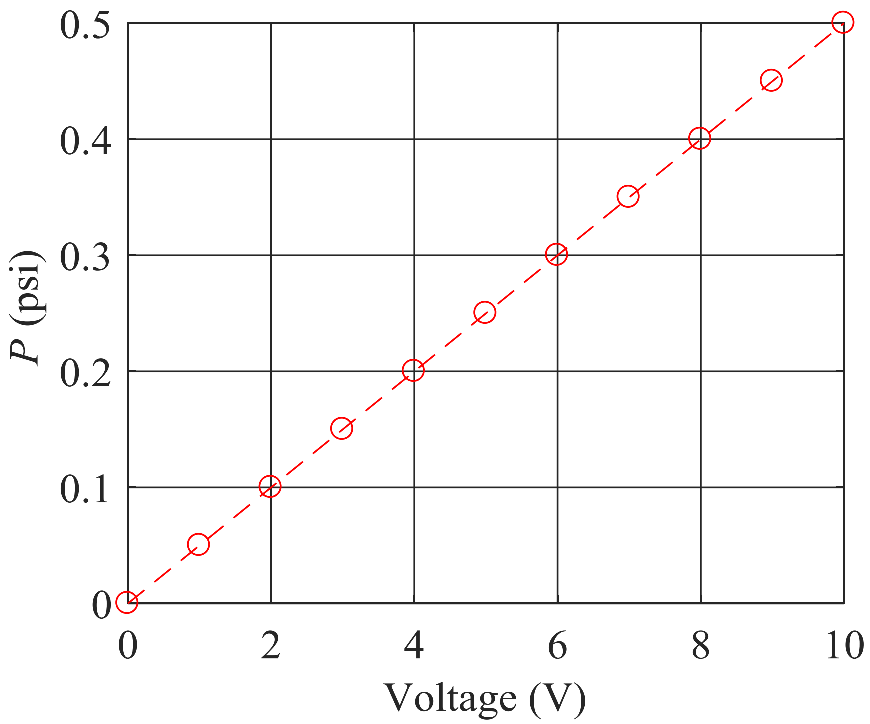

Figure C-1. Calibration curve for pressure transducer with 0.5 psi diaphragm.

The pressure drop measured by pressure transducer is converted from the voltage to psi using the calibration curve. A progressive cavity pump (Moyno, model 36704) and a variable frequency drive (VFD) were used to circulate the flow. The VFD runs the pump at the frequency range of 5-60 Hz and the flow rate increases with increasing the frequency. Flow rate was measured using a magnetic flow meter (Omega, FLR 8340D). This flowmeter measures flow rate from 4 to 40 gallon per minute (gpm).

After filling the tank with water, the flow was circulated ine the flow loop by running the pump at low frequency of VFD. All the sections were checked to figure out whether the leakage is in there or not. Then, the frequency of VFD was gradually increased to de-air water. This procedure was done around 30 minutes. Then, the frequency was reduced to the frequency of real experiment. The pump run the flow about 1 hour at this frequency to make sure the flow is steady state. Then, the polymer solutions were added to the tank and were mixed into the water using a rod. It took around 5 minutes for master polymer solutions to be homogenously mixed into water. After making desired concentration in the loop, the experiments were carried out. After finishing the experiments, the loop was properly washed and the pressure drop measurement for water was conducted to make sure there is no polymer left in the flow loop.

Appendix D. Design of flow loop

Soildwork software was used to design both pipe and channel flow loop. The 2D drawings were prepared which involve of design of the channel and pipe test section, flanges, O-rings, expansion, contractions, and settling chambers.

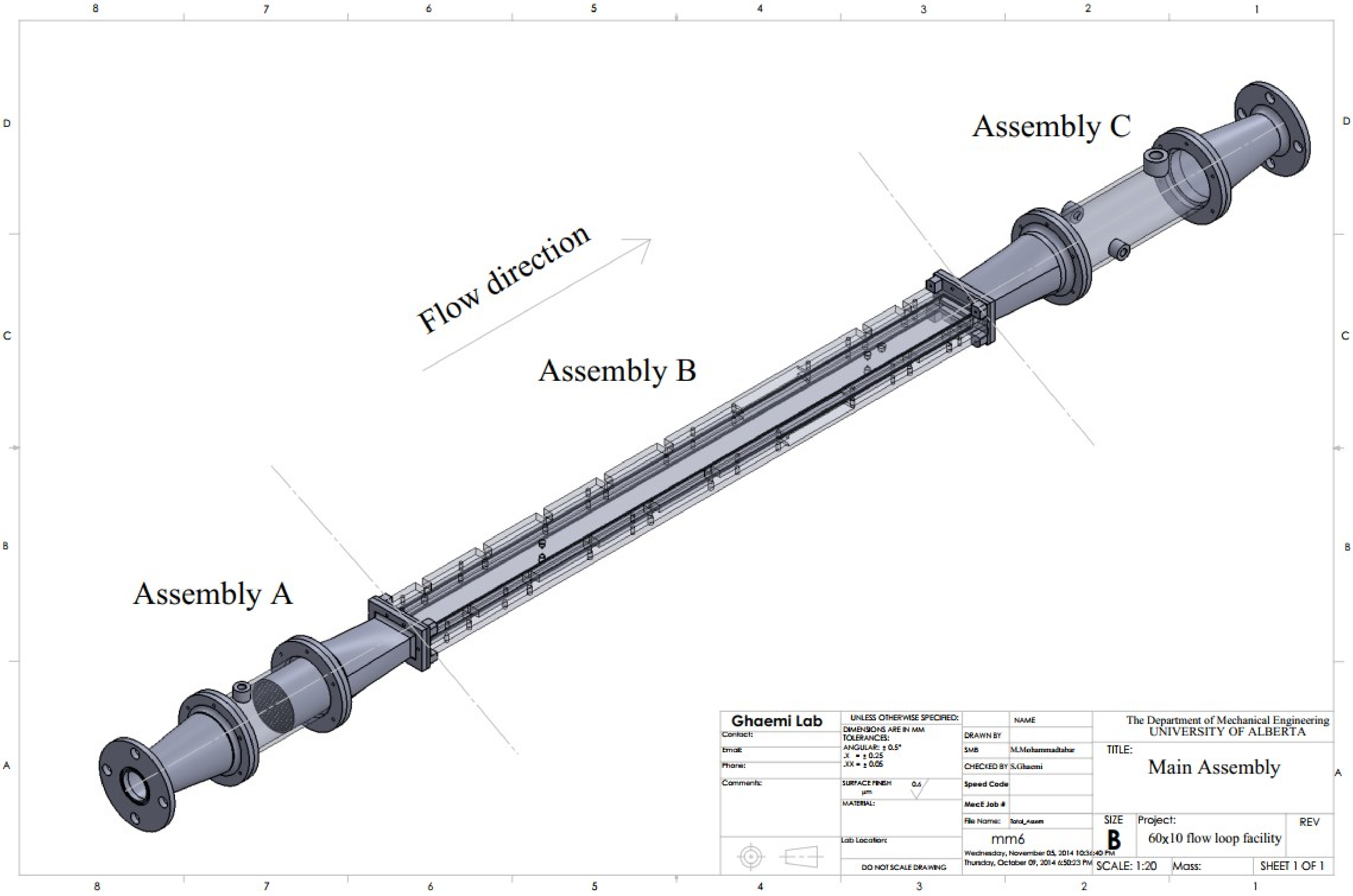

Ghaemi Lab
Contact:
Email:
Phone:
Comments:

UNLESS OTHERWISE SPECIFIED:
DIMENSIONS ARE IN MM
TOLERANCES:
ANGULAR: ± 0.5°
.X = ± 0.25
.XX = ± 0.05
SURFACE FINISH µm 0.6
MATERIAL:
Lab Location:
DO NOT SCALE DRAWING

NAME
DRAWN BY
SMB M.Mohammadtabar
CHECKED BY S.Ghaemi
Speed Code
MecE Job #
File Name: Total_Assem
mm6
Wednesday, November 05, 2014 10:36:40 PM
Thursday, October 09, 2014 6:50:23 PM

The Department of Mechanical Engineering
UNIVERSITY OF ALBERTA
TITLE: Main Assembly
SIZE B
Project: 60x10 flow loop facility
REV
SCALE: 1:20
Mass:
SHEET 1 OF 1

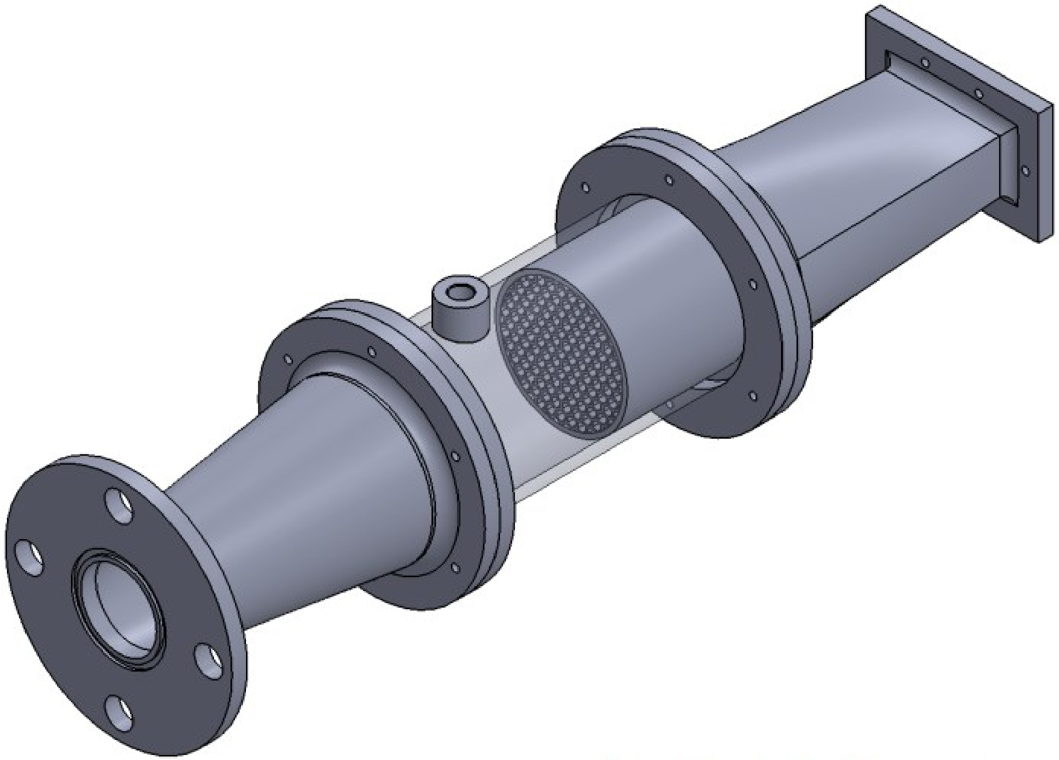

Ghaemi Lab
Contact:
Email:
Phone:
Comments:

UNLESS OTHERWISE SPECIFIED:
DIMENSIONS ARE IN MM
TOLERANCES:
ANGULAR: ± 0.5°
.X = ± 0.25
.XX = ± 0.05
SURFACE FINISH µm 0.6
MATERIAL:
Lab Location:
DO NOT SCALE DRAWING

	NAME
DRAWN BY	
SMB	M.Mohammadtaher
CHECKED BY	S.Ghaemi
Speed Code	
MecE Job #	
File Name:	Assem2

mm6
Tuesday, October 28, 2014 2:18:46 PM
Sunday, October 05, 2014 1:52:26 PM

The Department of Mechanical Engineering
UNIVERSITY OF ALBERTA

TITLE:
Assembly A

SIZE B
Project: 60x10 flow loop facility
REV
SCALE: 1:5
Mass:
SHEET 1 OF 1

ITEM NO.	PART NUMBER	DESCRIPTION	QTY.
A.1	Contraction to pipe		1
A.2	Flange for pipe		2
A.3	Buffer zone		1
A.4	1/4 O-Let		1
A.5	Honeycomb		1
A.6	Cover of honeycomb		1
A.7	Contraction to test section		1

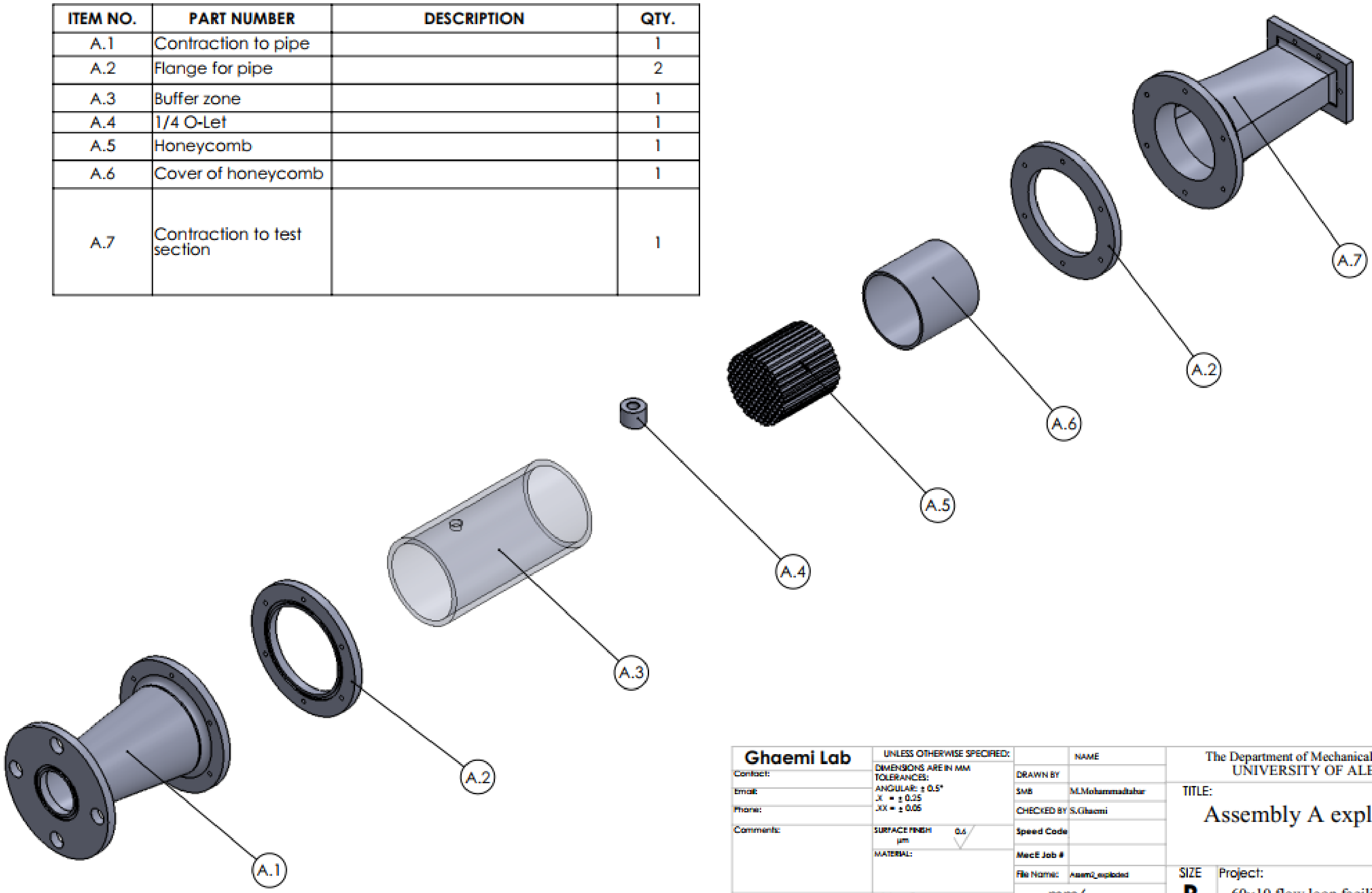

Ghaemi Lab	UNLESS OTHERWISE SPECIFIED:	NAME	The Department of Mechanical Engineering UNIVERSITY OF ALBERTA
Contact:	DIMENSIONS ARE IN MM TOLERANCES: ANGULAR: ± 0.5° .X = ± 0.25 .XX = ± 0.05	DRAWN BY	TITLE: Assembly A exploded
Email:		SMB M.Mohammadtabar	
Phone:		CHECKED BY S.Ghaemi	
Comments:	SURFACE FINISH µm 0.6	Speed Code	
	MATERIAL:	MecE Job #	
		File Name: Assem2_exploded	SIZE B Project: 60x10 flow loop facility REV
	Lab Location:	mm6 Tuesday, October 28, 2014 2:19:07 PM Sunday, October 05, 2014 1:52:26 PM	
	DO NOT SCALE DRAWING		SCALE: 1:20 Mass: SHEET 1 OF 1

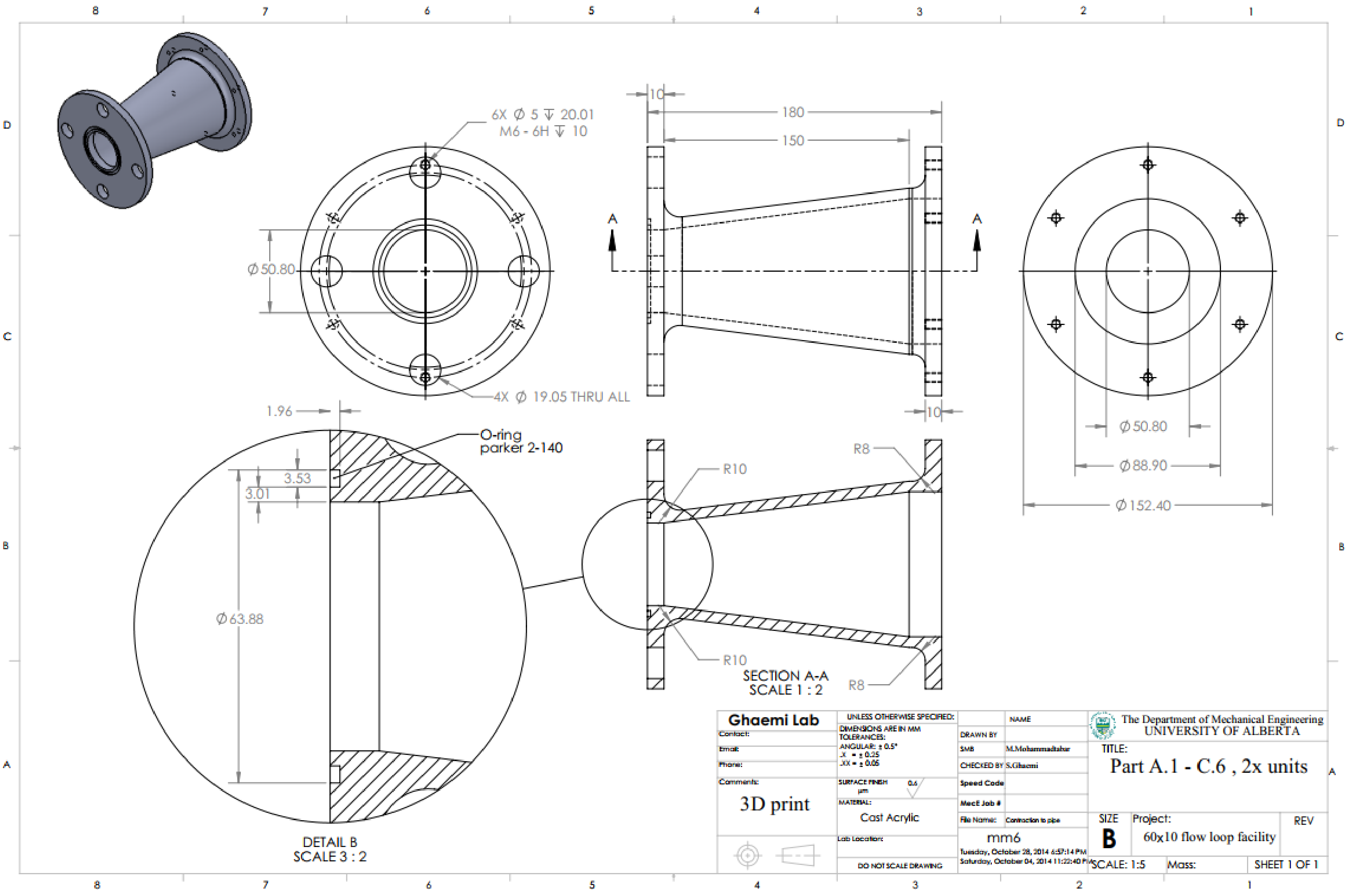

Ghaemi Lab
Contact:
Email:
Phone:
Comments:
3D print

UNLESS OTHERWISE SPECIFIED:
DIMENSIONS ARE IN MM
TOLERANCES:
ANGULAR: ± 0.5°
.X = ± 0.25
.XX = ± 0.05
SURFACE FINISH μm 0.6
MATERIAL:
Cast Acrylic
Lab Location:
DO NOT SCALE DRAWING

	NAME
DRAWN BY	
SMB	M.Mohammadtabar
CHECKED BY	S.Ghaemi
Speed Code	
MecE Job #	
File Name:	Contraction to pipe

mm6
Tuesday, October 28, 2014 6:57:14 PM
Saturday, October 04, 2014 11:22:40 PM

The Department of Mechanical Engineering
UNIVERSITY OF ALBERTA
TITLE:
Part A.1 - C.6 , 2x units
SIZE **B**
Project:
60x10 flow loop facility
REV
SCALE: 1:5
Mass:
SHEET 1 OF 1

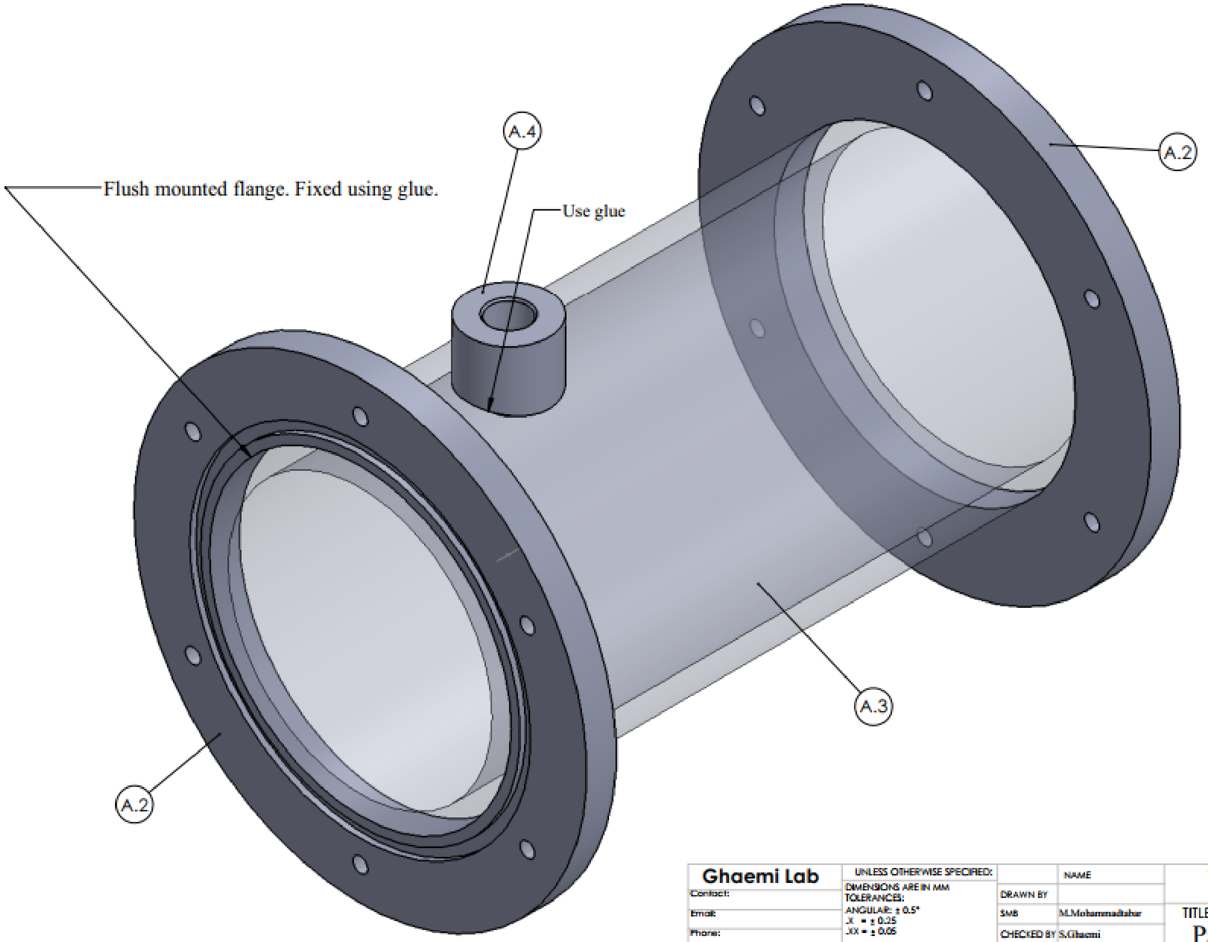

Ghaemi Lab
Contact:
Email:
Phone:
Comments:

UNLESS OTHERWISE SPECIFIED:
DIMENSIONS ARE IN MM
TOLERANCES:
ANGULAR: ± 0.5°
.X = ± 0.25
.XX = ± 0.05
SURFACE FINISH μm 0.6
MATERIAL:
Lab Location:
DO NOT SCALE DRAWING

	NAME
DRAWN BY	
SMB	M.Mohammadtabar
CHECKED BY	S.Ghaemi
Speed Code	
MecE Job #	
File Name:	Assem3_Buffer zone +flange

mm6
Tuesday, October 28, 2014 2:18:57 PM
Sunday, October 05, 2014 1:52:26 PM

The Department of Mechanical Engineering
UNIVERSITY OF ALBERTA

TITLE:
Parts A.2 , A.3, and A.4

SIZE
B
Project:
60x10 flow loop facility
REV
SCALE: 1:5
Mass:
SHEET 1 OF 1

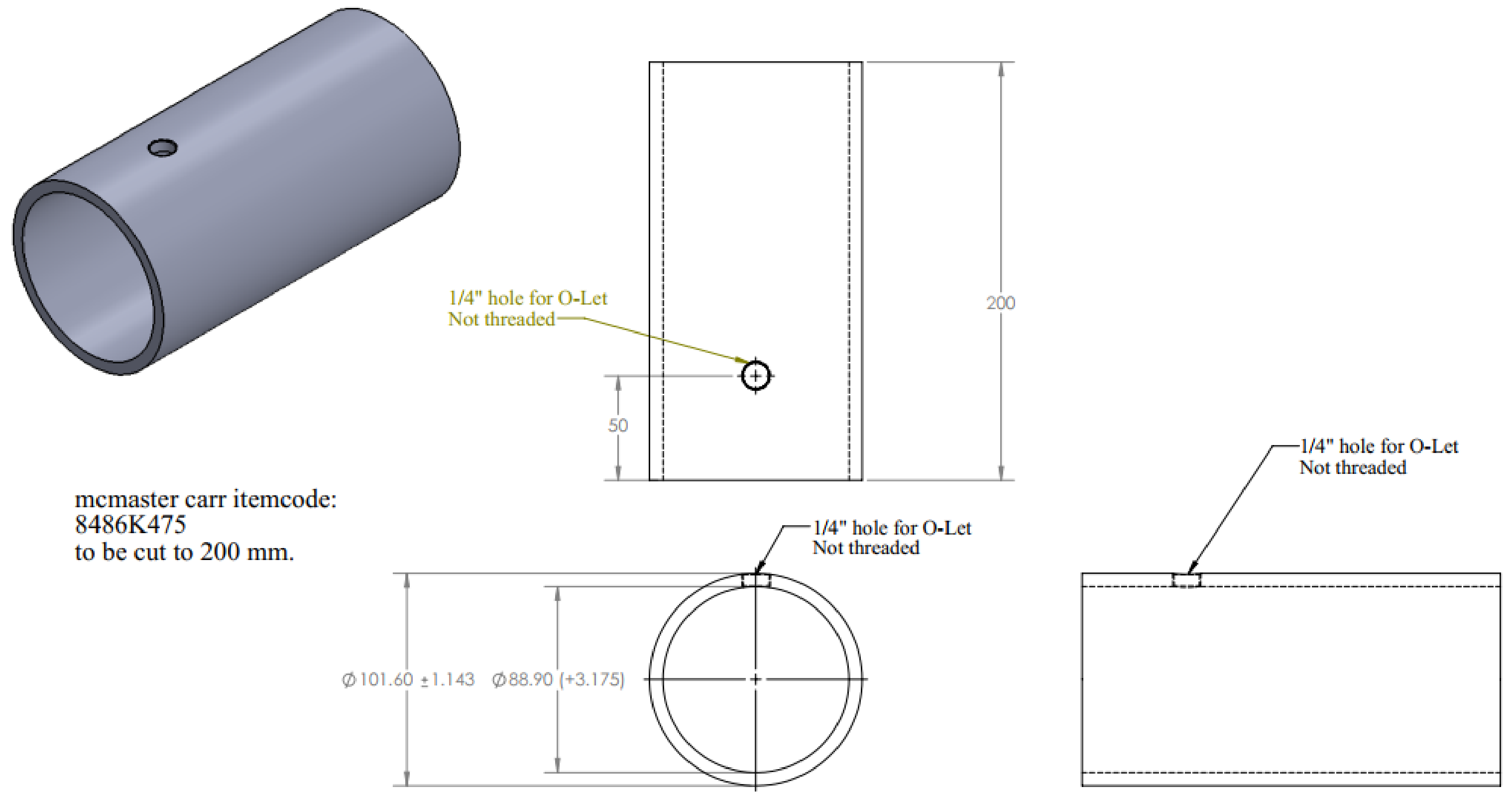

mcmaster carr itemcode:
8486K475
to be cut to 200 mm.

Ghaemi Lab
Contact:
Email:
Phone:
Comments:
Mcmaster
8486k475

UNLESS OTHERWISE SPECIFIED:
DIMENSIONS ARE IN MM
TOLERANCES:
ANGULAR: ± 0.5°
.X = ± 0.25
.XX = ± 0.05
SURFACE FINISH µm 0.6
MATERIAL:
Cast Acrylic
Lab Location:
DO NOT SCALE DRAWING

	NAME
DRAWN BY	
SMB	M.Mohammadtaher
CHECKED BY	S.Ghaemi
Speed Code	
MecE Job #	
File Name:	bufferzone

mm6
Monday, October 27, 2014 3:05:54 PM
Saturday, October 04, 2014 12:06:52 PM

The Department of Mechanical Engineering
UNIVERSITY OF ALBERTA

TITLE:
Part A.3

SIZE **B**
Project:
60x10 flow loop facility
REV
SCALE: 1:2
Mass:
SHEET 1 OF 1

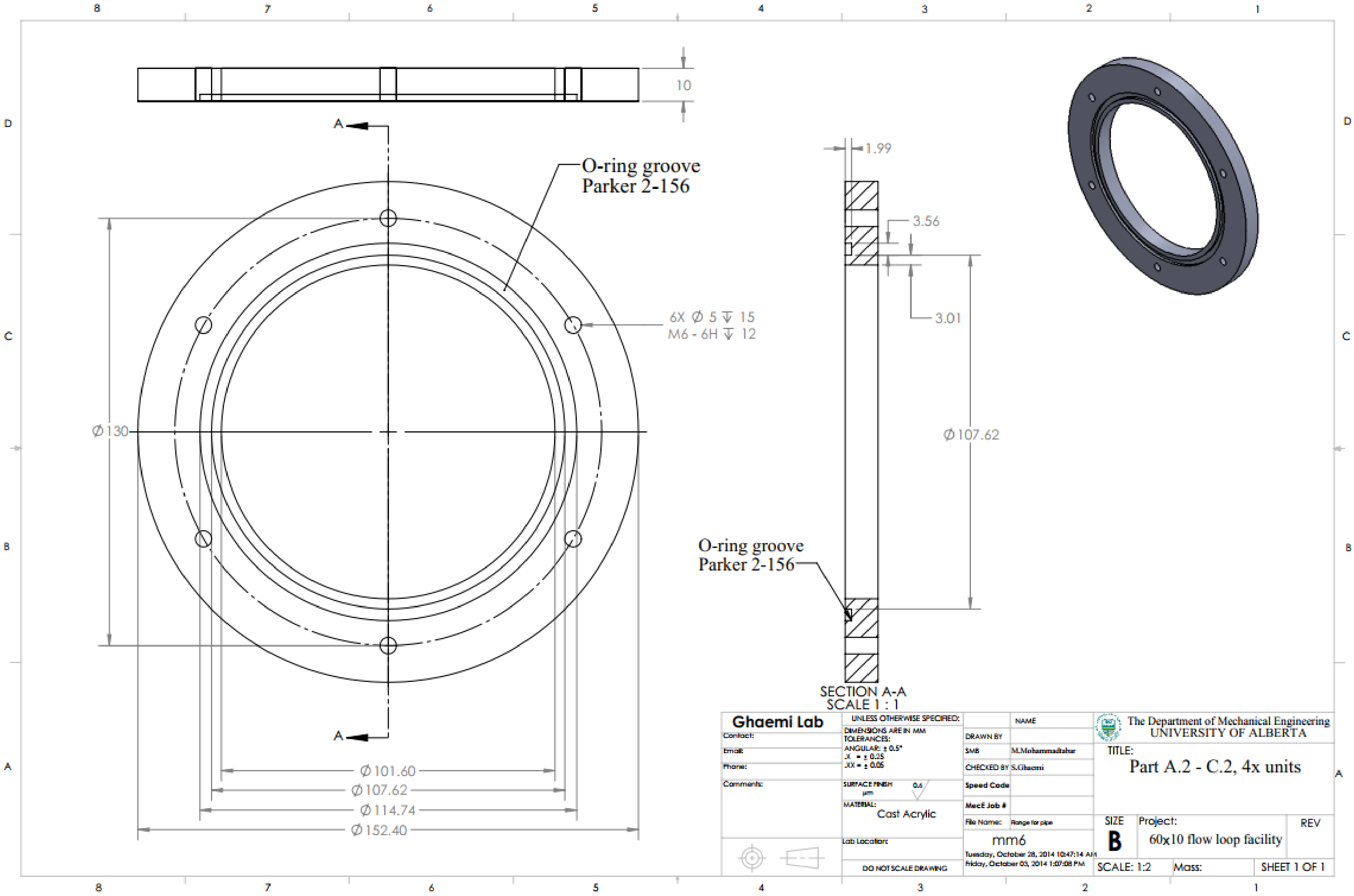
10
A
O-ring groove
Parker 2-156
6X Ø 5 ↧ 15
M6 - 6H ↧ 12
Ø 130
A
Ø 101.60
Ø 107.62
Ø 114.74
Ø 152.40
1.99
3.56
3.01
Ø 107.62
O-ring groove
Parker 2-156
SECTION A-A
SCALE 1 : 1
Ghaemi Lab
Contact:
Email:
Phone:
Comments:
UNLESS OTHERWISE SPECIFIED:
DIMENSIONS ARE IN MM
TOLERANCES:
ANGULAR: ± 0.5°
.X = ± 0.25
.XX = ± 0.05
SURFACE FINISH µm 0.6
MATERIAL:
Cast Acrylic
Lab Location:
DO NOT SCALE DRAWING
NAME
DRAWN BY
SMB M.Mohammadtabar
CHECKED BY S.Ghaemi
Speed Code
MecE Job #
File Name: Flange for pipe
mm6
Tuesday, October 28, 2014 10:47:14 AM
Friday, October 03, 2014 1:07:08 PM
The Department of Mechanical Engineering
UNIVERSITY OF ALBERTA
TITLE:
Part A.2 - C.2, 4x units
SIZE
B
Project:
60x10 flow loop facility
REV
SCALE: 1:2
Mass:
SHEET 1 OF 1
8
7
6
5
4
3
2
1
D
C
B
A

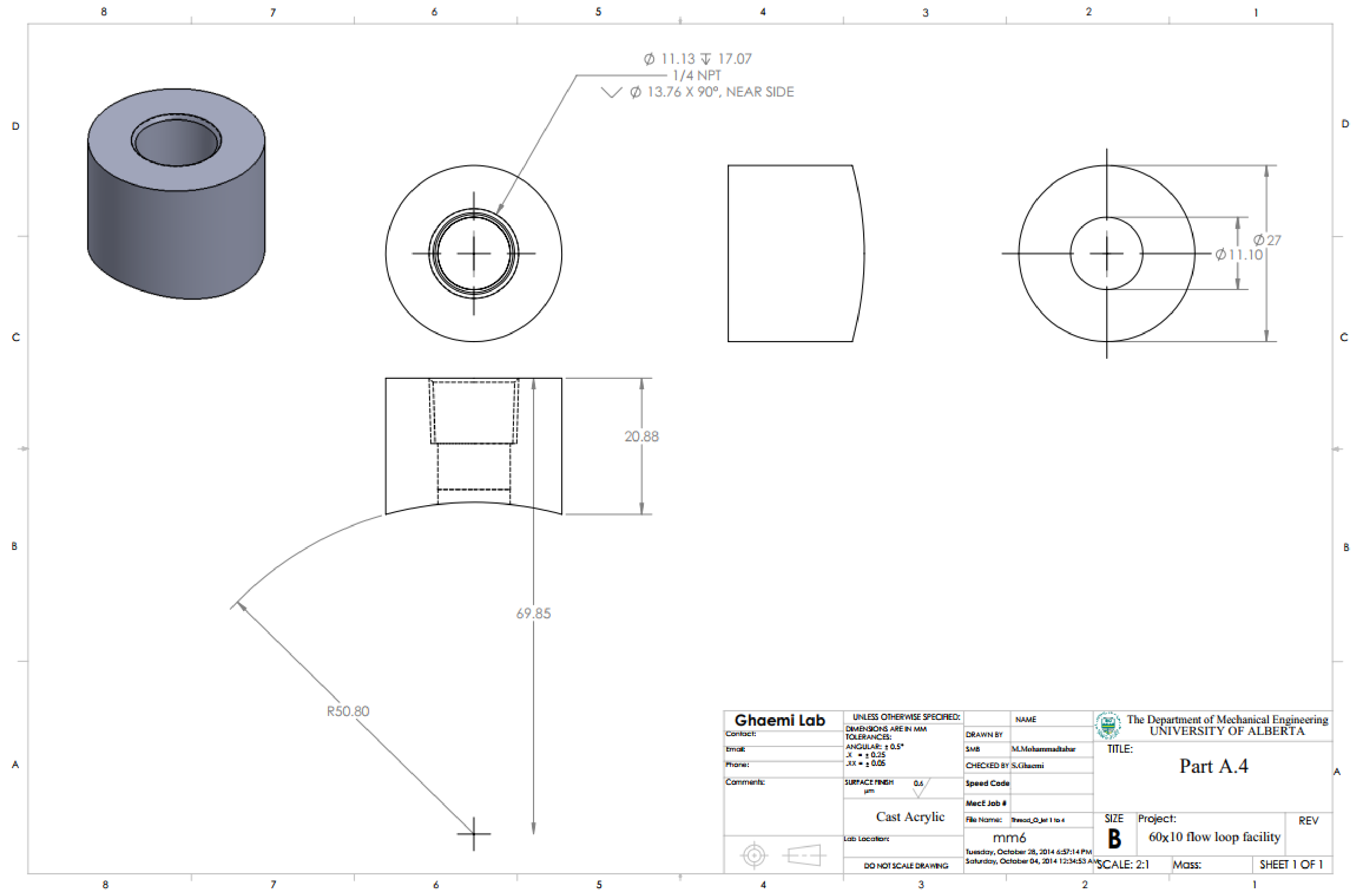

Ghaemi Lab

Contact:
Email:
Phone:
Comments:

UNLESS OTHERWISE SPECIFIED:
DIMENSIONS ARE IN MM
TOLERANCES:
ANGULAR: ± 0.5°
.X = ± 0.25
.XX = ± 0.05

SURFACE FINISH µm 0.6

Cast Acrylic

Lab Location:

DO NOT SCALE DRAWING

	NAME
DRAWN BY	
SMB	M.Mohammadtabar
CHECKED BY	S.Ghaemi
Speed Code	
MecE Job #	
File Name:	Thread_O_let 1 to 4

mm6
Tuesday, October 28, 2014 6:57:14 PM
Saturday, October 04, 2014 12:34:53 AM

The Department of Mechanical Engineering
UNIVERSITY OF ALBERTA

TITLE:
Part A.4

SIZE B
Project: 60x10 flow loop facility
REV
SCALE: 2:1
Mass:
SHEET 1 OF 1

After cutting the Honeycob sheet to 82.55 mm (3.25") it can be inserted by tight fit. Then the assembly will be fixed inside the part A.3. Using a removable glue(e.g., Silicone glue).

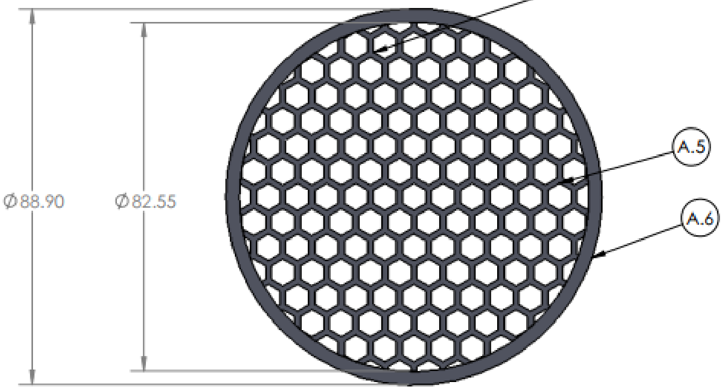

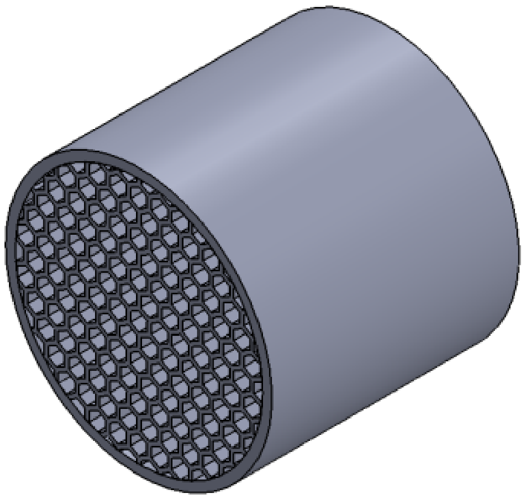

Ghaemi Lab
Contact:
Email:
Phone:
Comments:

UNLESS OTHERWISE SPECIFIED:
DIMENSIONS ARE IN MM
TOLERANCES:
ANGULAR: ± 0.5°
.X = ± 0.25
.XX = ± 0.05
SURFACE FINISH µm 0.6
MATERIAL:
Lab Location:
DO NOT SCALE DRAWING

	NAME
DRAWN BY	
SMB	M.Mohammadtaher
CHECKED BY	S.Ghaemi
Speed Code	
MecE Job #	
File Name:	Assem2_Honey comb+Cover

mm6
Tuesday, October 28, 2014 2:19:16 PM
Sunday, October 05, 2014 1:52:26 PM

The Department of Mechanical Engineering
UNIVERSITY OF ALBERTA

TITLE:
Part A.5-A.6

SIZE **B**
Project: 60x10 flow loop facility
REV
SCALE: 1:2
Mass:
SHEET 1 OF 1

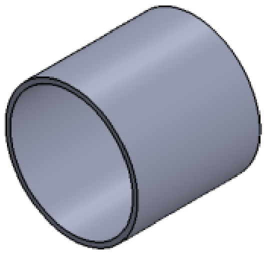

mcmaster:
8486K371

to be cut to 82.55 mm (3.25")
length from a pipe with
inner diameter of 3.25 inches
and outer diameter of 3.5 inches.
will be glued inside part A.3

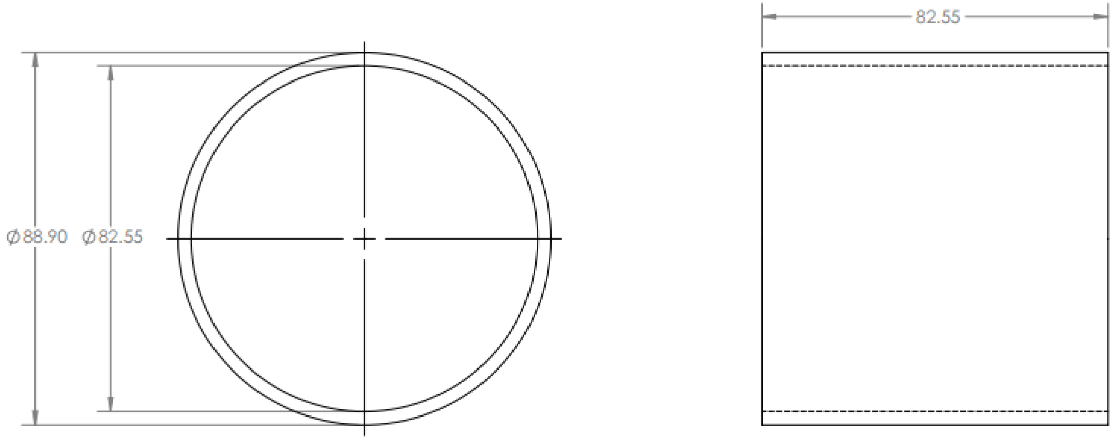

Ghaemi Lab
Contact:
Email:
Phone:
Comments:
Mcmaster
8486k371

UNLESS OTHERWISE SPECIFIED:
DIMENSIONS ARE IN MM
TOLERANCES:
ANGULAR: ± 0.5°
.X = ± 0.25
.XX = ± 0.05
SURFACE FINISH μm 0.6
MATERIAL:
Cast Acrylic
Lab Location:
DO NOT SCALE DRAWING

	NAME
DRAWN BY	
SMB	M.Mohammadtabar
CHECKED BY	S.Ghaemi
Speed Code	
MecE Job #	
File Name:	Cover of honeycomb

mm6
Wednesday, October 15, 2014 7:48:30 PM
Friday, October 03, 2014 10:34:26 PM

The Department of Mechanical Engineering
UNIVERSITY OF ALBERTA
TITLE:
PartA.6
SIZE B
Project:
60x10 flow loop facility
REV
SCALE: 1:2
Mass:
SHEET 1 OF 1

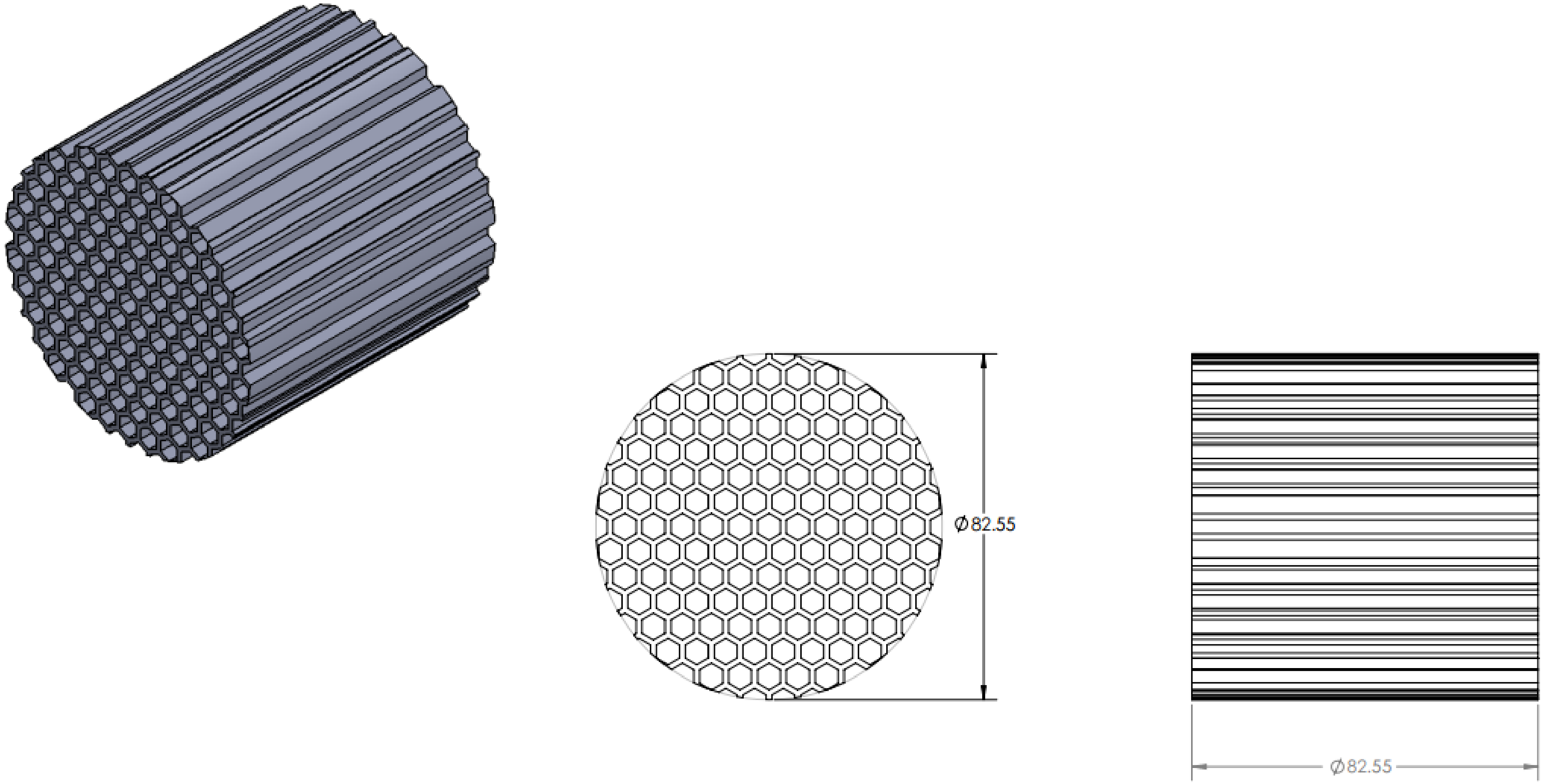

Ghaemi Lab
Contact:
Email:
Phone:
Comments:

UNLESS OTHERWISE SPECIFIED:
DIMENSIONS ARE IN MM
TOLERANCES:
ANGULAR: ± 0.5°
.X = ± 0.25
.XX = ± 0.05
SURFACE FINISH µm 0.6
MATERIAL:
Lab Location:
DO NOT SCALE DRAWING

NAME
DRAWN BY
SMB M.Mohammadtabar
CHECKED BY S.Ghaemi
Speed Code
MecE Job #
File Name: Honeycomb
mm6
Friday, October 17, 2014 9:39:46 PM
Friday, October 03, 2014 6:23:32 PM

The Department of Mechanical Engineering
UNIVERSITY OF ALBERTA
TITLE:
Part A.5
SIZE B
Project: 60x10 flow loop facility
REV
SCALE: 1:2
Mass:
SHEET 1 OF 1

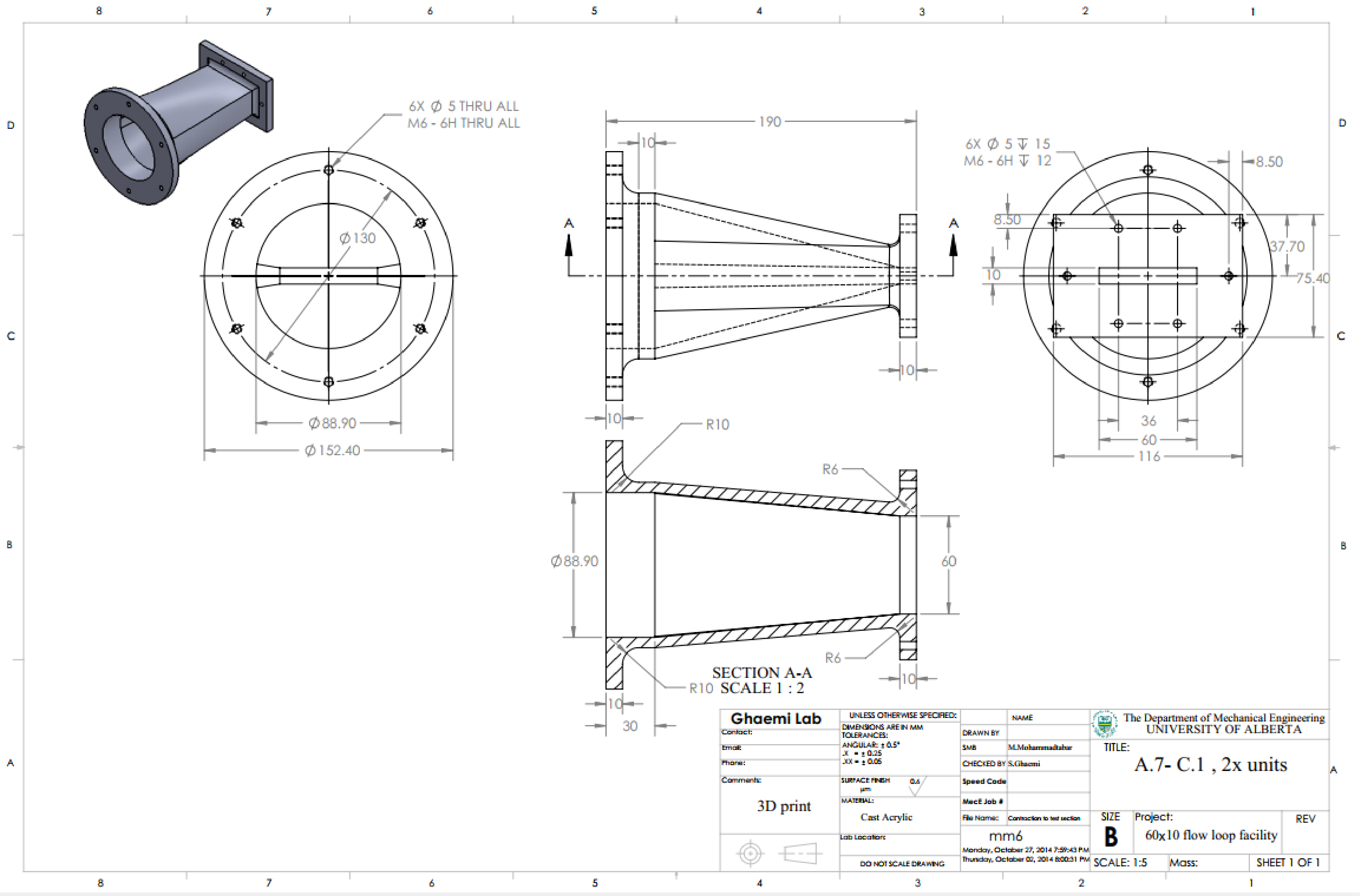

Ghaemi Lab
Contact:
Email:
Phone:
Comments:
3D print

UNLESS OTHERWISE SPECIFIED:
DIMENSIONS ARE IN MM
TOLERANCES:
ANGULAR: ± 0.5°
.X = ± 0.25
.XX = ± 0.05
SURFACE FINISH µm 0.6
MATERIAL:
Cast Acrylic
Lab Location:
DO NOT SCALE DRAWING

	NAME
DRAWN BY	
SMB	M.Mohammadtabar
CHECKED BY	S.Ghaemi
Speed Code	
MecE Job #	
File Name:	Contraction to test section

mm6
Monday, October 27, 2014 7:59:43 PM
Thursday, October 02, 2014 8:00:31 PM

The Department of Mechanical Engineering
UNIVERSITY OF ALBERTA

TITLE:
A.7- C.1 , 2x units

SIZE B
Project:
60x10 flow loop facility
REV
SCALE: 1:5
Mass:
SHEET 1 OF 1

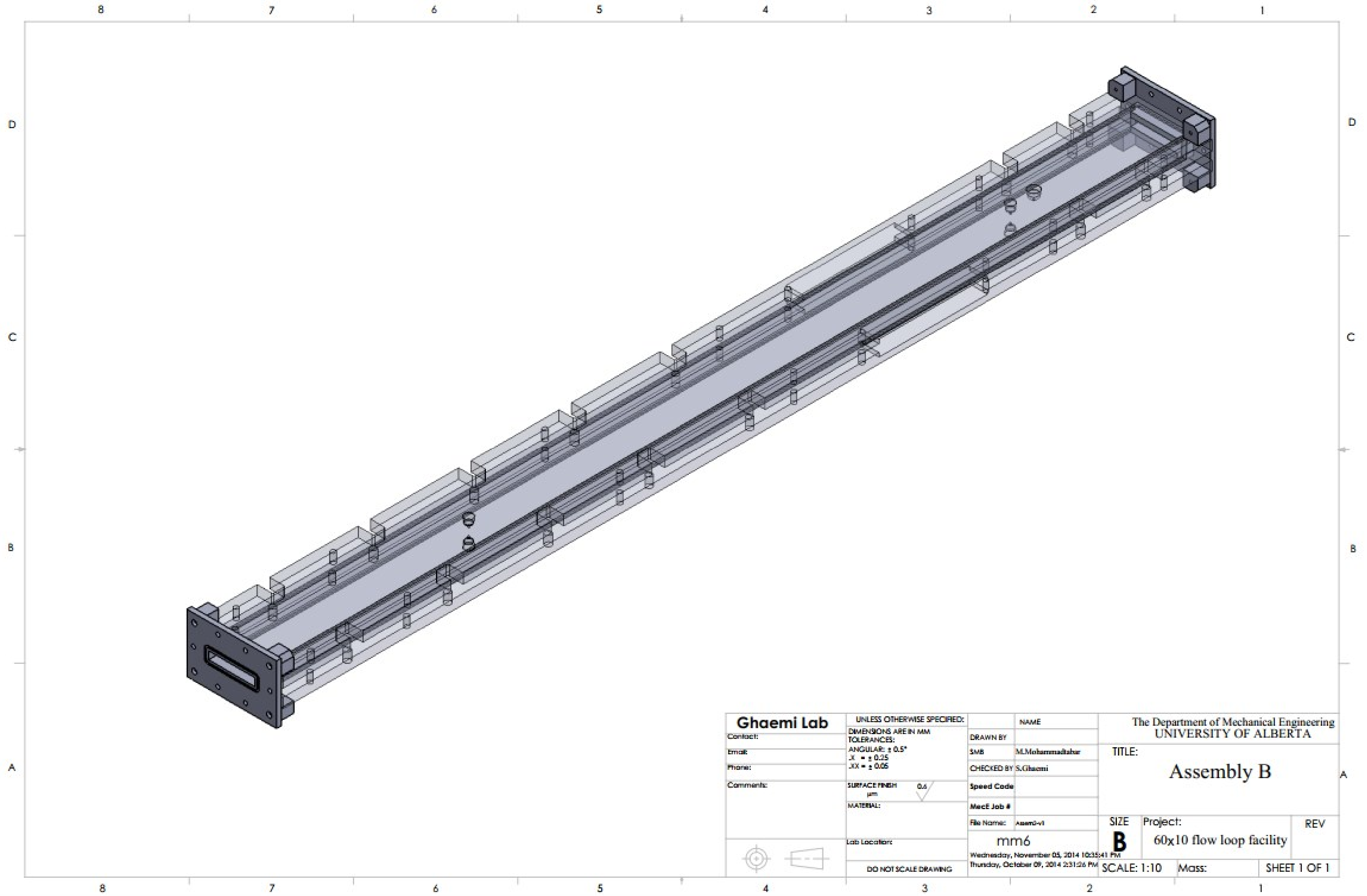

Ghaemi Lab
Contact:
Email:
Phone:
Comments:

UNLESS OTHERWISE SPECIFIED:
DIMENSIONS ARE IN MM
TOLERANCES:
ANGULAR: ± 0.5°
.X = ± 0.25
.XX = ± 0.05
SURFACE FINISH µm 0.6
MATERIAL:
Lab Location:
DO NOT SCALE DRAWING

	NAME
DRAWN BY	
SMB	M.Mohammadtaher
CHECKED BY	S.Ghaemi
Speed Code	
MecE Job #	
File Name:	Assem0-v1

mm6
Wednesday, November 05, 2014 10:35:41 PM
Thursday, October 09, 2014 2:31:26 PM

The Department of Mechanical Engineering
UNIVERSITY OF ALBERTA

TITLE:
Assembly B

SIZE B
Project: 60x10 flow loop facility
REV
SCALE: 1:10
Mass:
SHEET 1 OF 1

ITEM NO.	PART NUMBER	DESCRIPTION	QTY.
B.1	Bottom of channel 2_v1		1
B.2	Side of channel 2_v1		2
B.3	Top of channel 2_v1		1
B.4	end plate2_v1		2
B.5	little box 2-v1		8

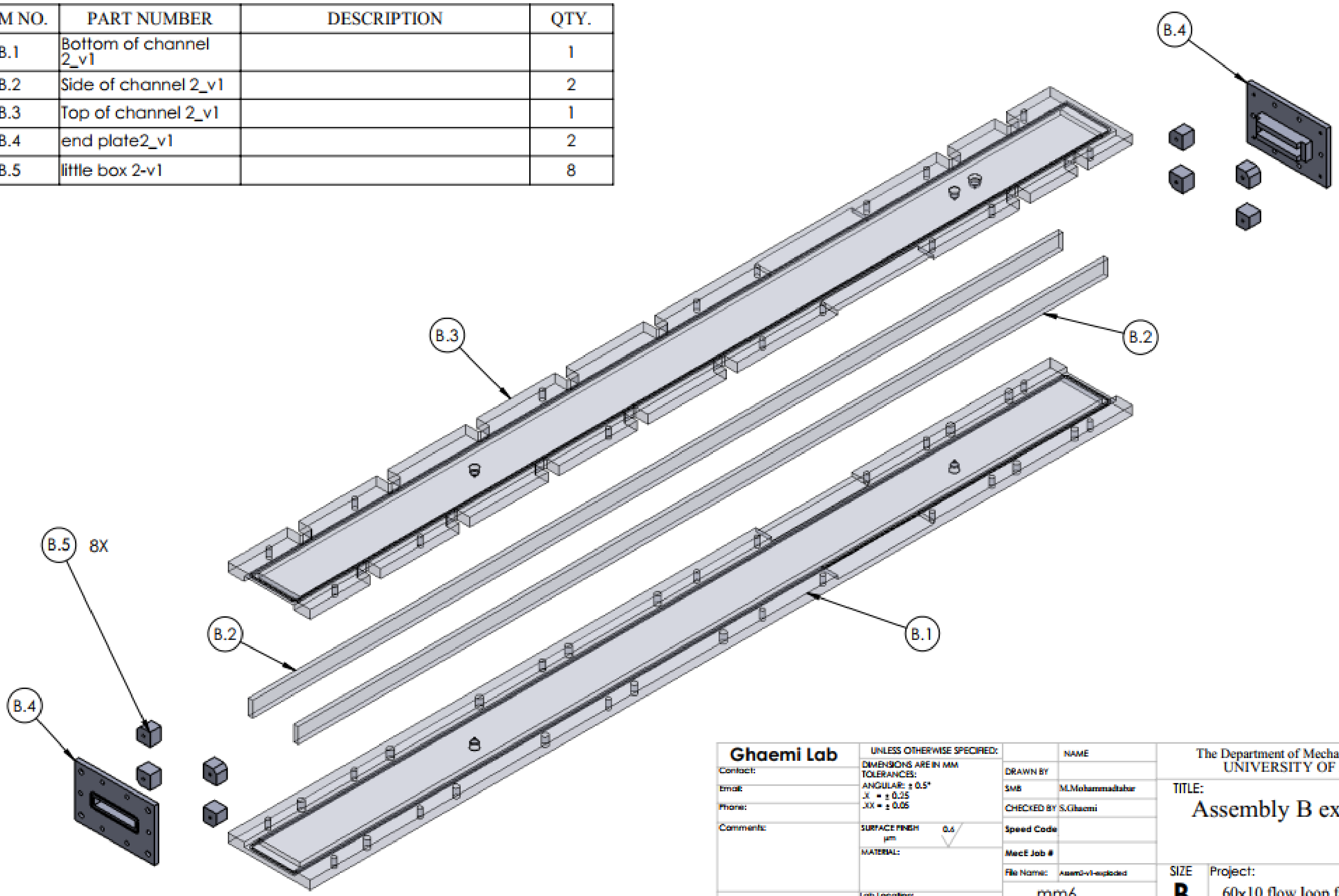

Ghaemi Lab
Contact:
Email:
Phone:
Comments:

UNLESS OTHERWISE SPECIFIED:
DIMENSIONS ARE IN MM
TOLERANCES:
ANGULAR: ± 0.5°
.X = ± 0.25
.XX = ± 0.05
SURFACE FINISH μm 0.6
MATERIAL:
Lab Location:
DO NOT SCALE DRAWING

	NAME
DRAWN BY	
SMB	M.Mohammadtabar
CHECKED BY	S.Ghaemi
Speed Code	
MecE Job #	
File Name:	Assem0-v1-exploded

mm6
Wednesday, November 05, 2014 10:35:53 PM
Thursday, October 09, 2014 2:31:26 PM

The Department of Mechanical Engineering
UNIVERSITY OF ALBERTA

TITLE:
Assembly B exploded

SIZE B
Project: 60x10 flow loop facility
REV

SCALE: 1:20
Mass:
SHEET 1 OF 1

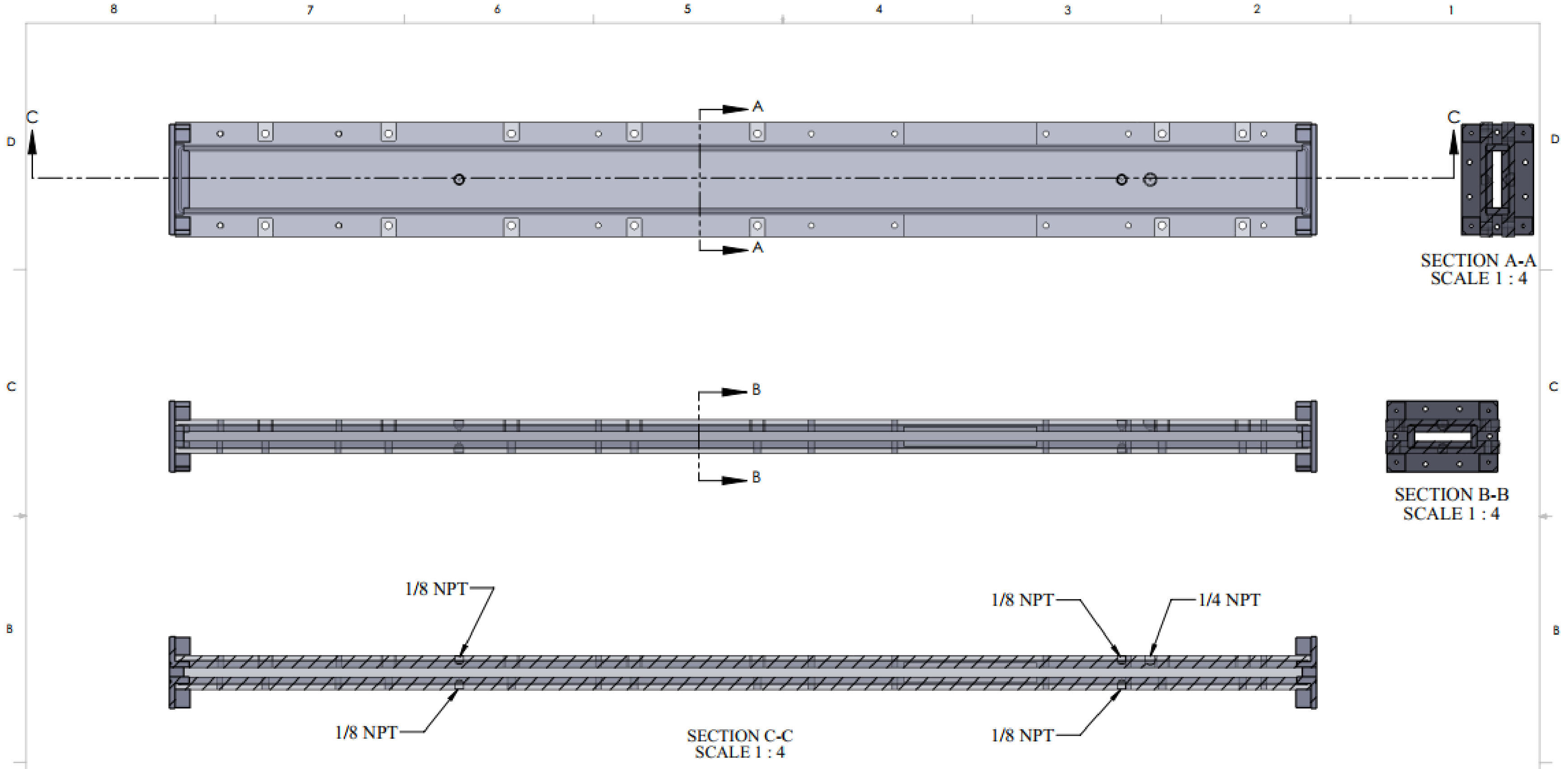

Ghaemi Lab
Contact:
Email:
Phone:
Comments:

UNLESS OTHERWISE SPECIFIED:
DIMENSIONS ARE IN MM
TOLERANCES:
ANGULAR: ± 0.5°
.X = ± 0.25
.XX = ± 0.05
SURFACE FINISH µm 0.6
MATERIAL:
Lab Location:
DO NOT SCALE DRAWING

	NAME
DRAWN BY	
SMB	M.Mohammadtabar
CHECKED BY	S.Ghaemi
Speed Code	
MecE Job #	
File Name:	Assem3-v1

mm6
Wednesday, November 05, 2014 10:35:41 PM
Thursday, October 09, 2014 2:31:26 PM

The Department of Mechanical Engineering
UNIVERSITY OF ALBERTA

TITLE:
Assembly B

SIZE B
Project: 60x10 flow loop facility
REV
SCALE: 1:10
Mass:
SHEET 1 OF 1

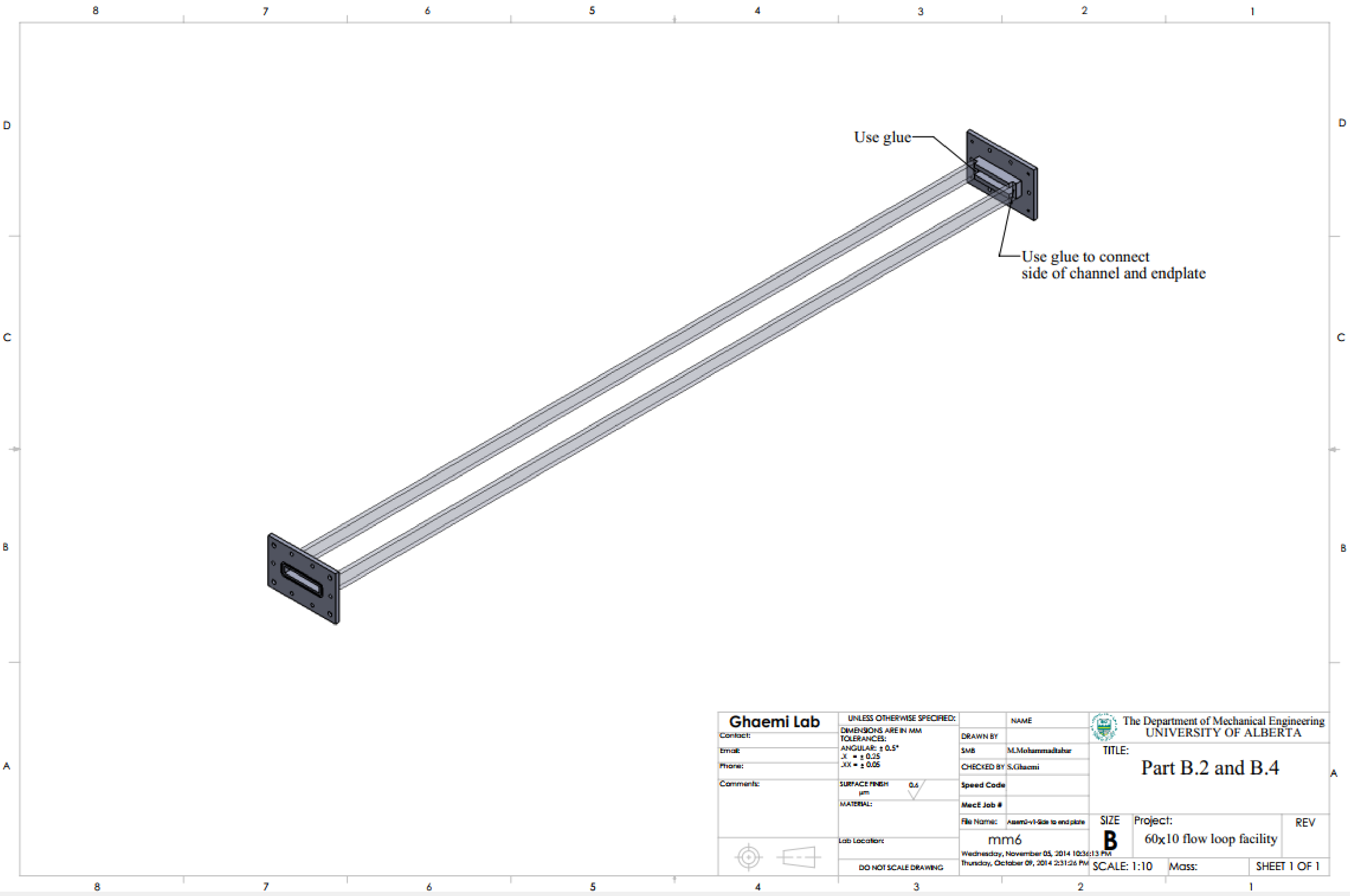

Use glue

Use glue to connect
side of channel and endplate

Ghaemi Lab
Contact:
Email:
Phone:
Comments:

UNLESS OTHERWISE SPECIFIED:
DIMENSIONS ARE IN MM
TOLERANCES:
ANGULAR: ± 0.5°
.X = ± 0.25
.XX = ± 0.05
SURFACE FINISH µm 0.6
MATERIAL:
Lab Location:
DO NOT SCALE DRAWING

	NAME
DRAWN BY	
SMB	M.Mohammadtabar
CHECKED BY	S.Ghaemi
Speed Code	
MecE Job #	
File Name:	Assem3-v1-Side to end plate

mm6
Wednesday, November 05, 2014 10:36:13 PM
Thursday, October 09, 2014 2:31:26 PM

The Department of Mechanical Engineering
UNIVERSITY OF ALBERTA

TITLE:
Part B.2 and B.4

SIZE B
Project: 60x10 flow loop facility
REV
SCALE: 1:10
Mass:
SHEET 1 OF 1

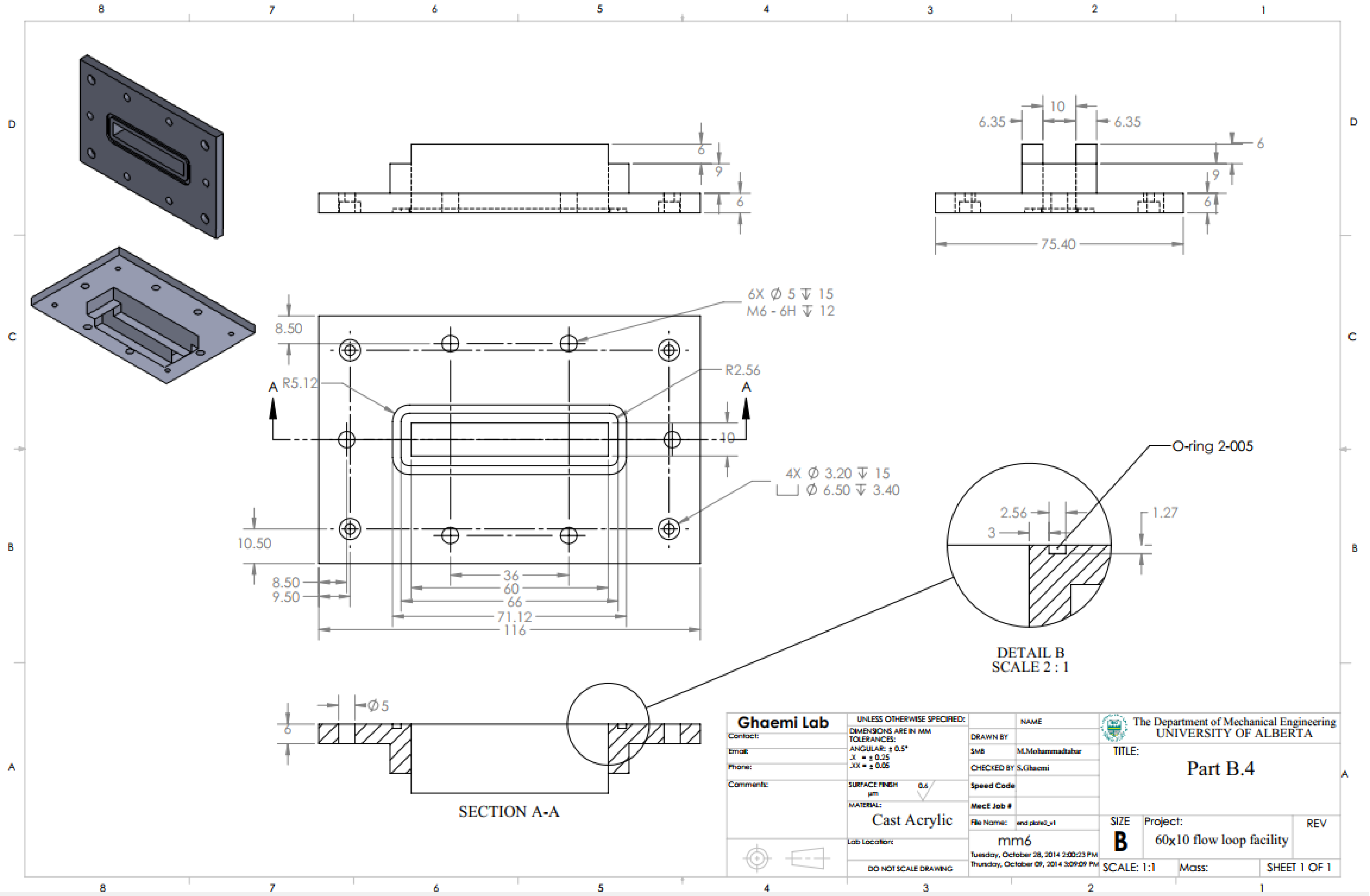
6.35
10
6.35
6
9
6
75.40
6X Ø 5 ↧ 15
M6 - 6H ↧ 12
8.50
R5.12
R2.56
A
A
10
4X Ø 3.20 ↧ 15
⌴ Ø 6.50 ↧ 3.40
10.50
8.50
9.50
36
60
66
71.12
116
O-ring 2-005
2.56
3
1.27
DETAIL B
SCALE 2 : 1
Ø5
6
SECTION A-A
Ghaemi Lab
Contact:
Email:
Phone:
Comments:
UNLESS OTHERWISE SPECIFIED:
DIMENSIONS ARE IN MM
TOLERANCES:
ANGULAR: ± 0.5°
.X = ± 0.25
.XX = ± 0.05
SURFACE FINISH µm 0.6
MATERIAL:
Cast Acrylic
Lab Location:
DO NOT SCALE DRAWING
NAME
DRAWN BY
SMB M.Mohammadtabar
CHECKED BY S.Ghaemi
Speed Code
MecE Job #
File Name: end plate2_v1
mm6
Tuesday, October 28, 2014 2:00:23 PM
Thursday, October 09, 2014 3:09:09 PM
The Department of Mechanical Engineering
UNIVERSITY OF ALBERTA
TITLE:
Part B.4
SIZE
B
Project:
60x10 flow loop facility
REV
SCALE: 1:1
Mass:
SHEET 1 OF 1

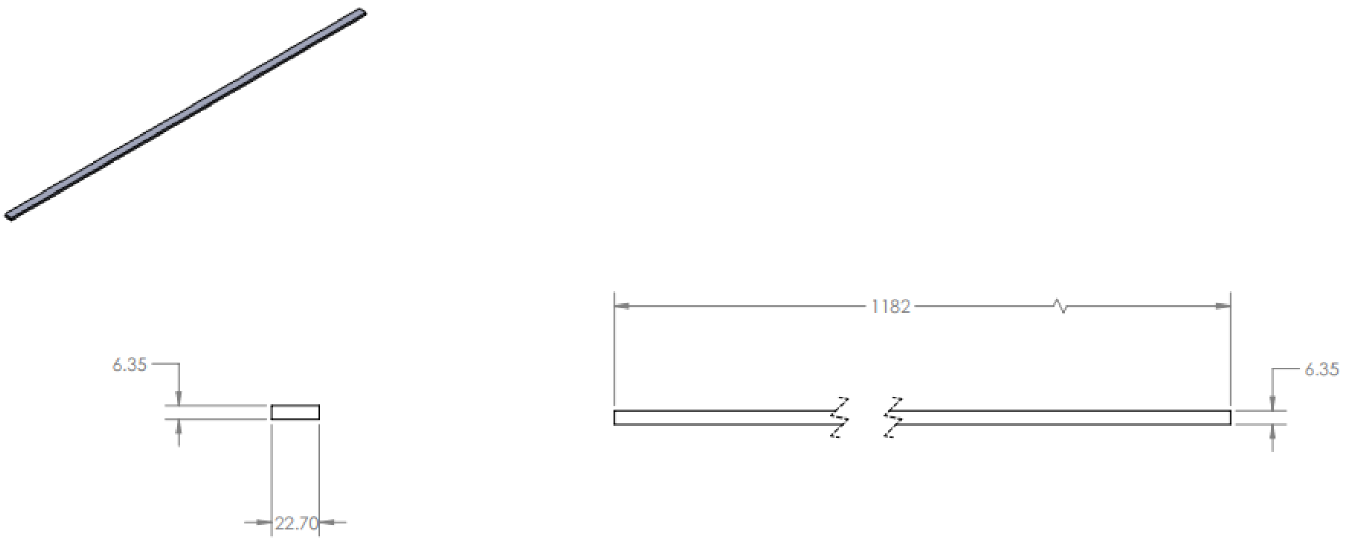

Ghaemi Lab
Contact:
Email:
Phone:
Comments:

UNLESS OTHERWISE SPECIFIED:
DIMENSIONS ARE IN MM
TOLERANCES:
ANGULAR: ± 0.5°
.X = ± 0.25
.XX = ± 0.05
SURFACE FINISH µm 0.6
MATERIAL:
Glass
Lab Location:
DO NOT SCALE DRAWING

	NAME
DRAWN BY	
SMB	M.Mohammadtabar
CHECKED BY	S.Ghaemi
Speed Code	
MecE Job #	
File Name:	Side of channel 2_v1

mm6
Monday, October 27, 2014 11:02:51 PM
Sunday, September 28, 2014 11:50:14 PM

The Department of Mechanical Engineering
UNIVERSITY OF ALBERTA

TITLE:
Part B.2

SIZE
B
Project:
60x10 flow loop facility
REV
SCALE: 1:10
Mass:
SHEET 1 OF 1

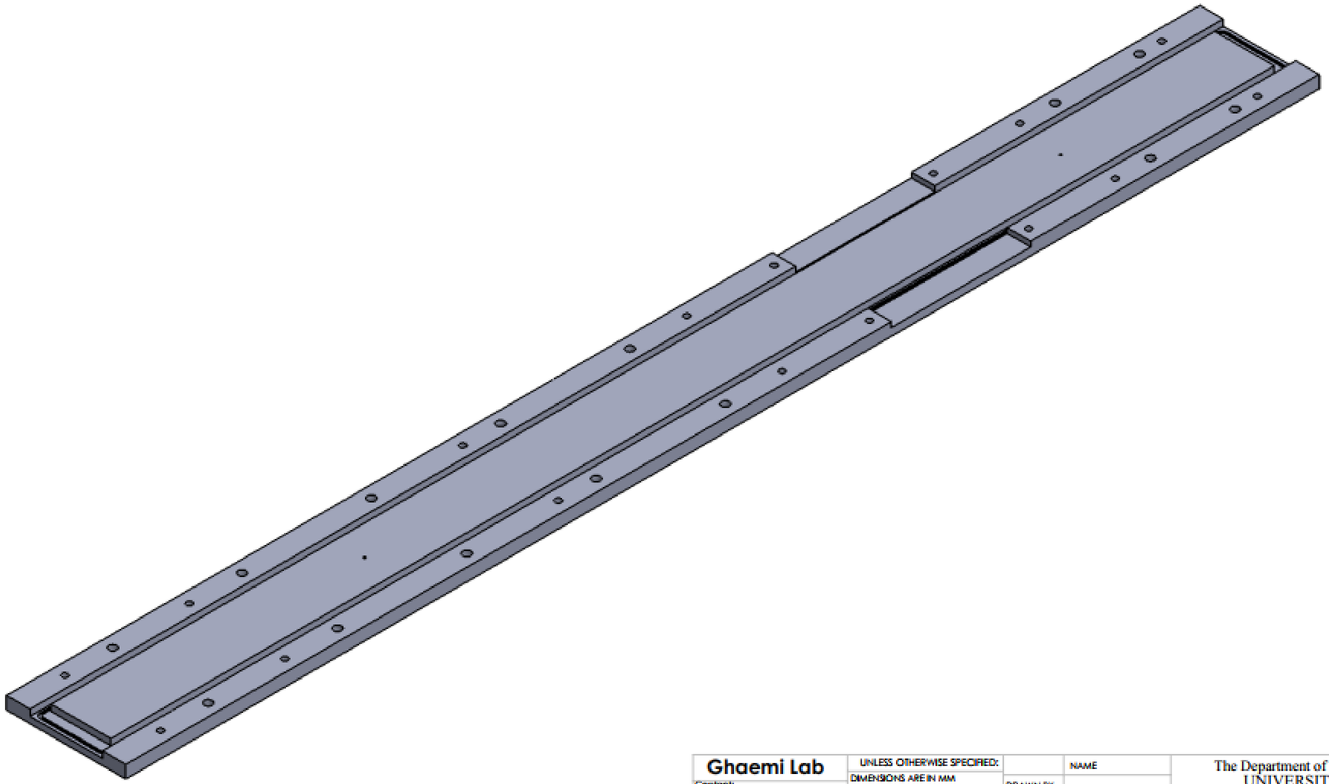

Ghaemi Lab
Contact:
Email:
Phone:
Comments:

UNLESS OTHERWISE SPECIFIED:
DIMENSIONS ARE IN MM
TOLERANCES:
ANGULAR: ± 0.5°
.X = ± 0.25
.XX = ± 0.05
SURFACE FINISH µm 0.6
MATERIAL:
Cast Acrylic
Lab Location:
DO NOT SCALE DRAWING

	NAME
DRAWN BY	
SMB	M.Mohammadtabar
CHECKED BY	S.Ghaemi
Speed Code	
MecE Job #	
File Name:	Bottom of channel 2_v1

mm6
Wednesday, November 05, 2014 10:34:29 PM
Wednesday, September 24, 2014 11:01:55 AM

The Department of Mechanical Engineering
UNIVERSITY OF ALBERTA

TITLE:
Part B.1

SIZE
B
Project:
60x10 flow loop facility
REV
SCALE: 1:10
Mass:
SHEET 1 OF 1

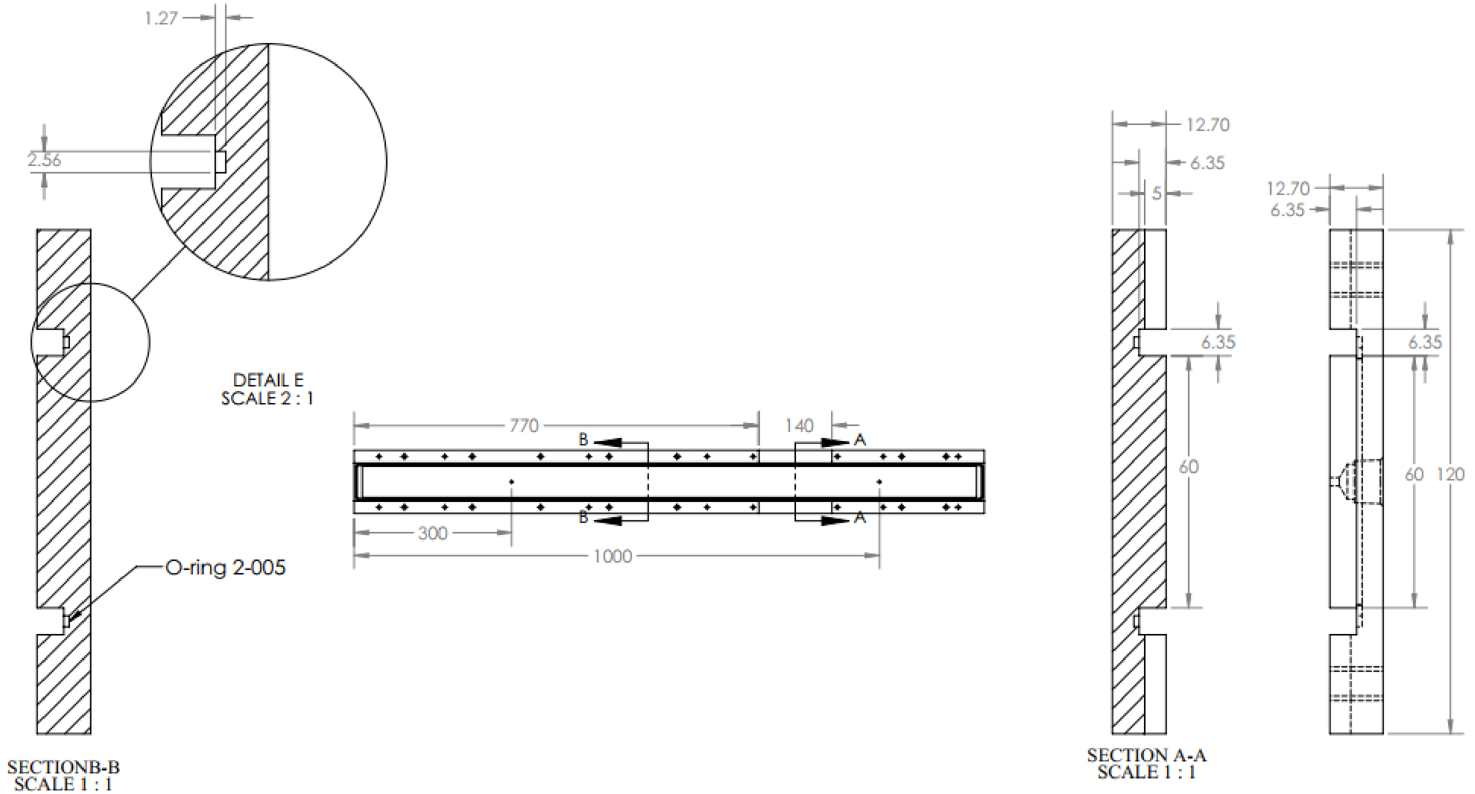

Ghaemi Lab
Contact:
Email:
Phone:
Comments:

UNLESS OTHERWISE SPECIFIED:
DIMENSIONS ARE IN MM
TOLERANCES:
ANGULAR: ± 0.5°
.X = ± 0.25
.XX = ± 0.05
SURFACE FINISH µm 0.6
MATERIAL:
Cast Acrylic
Lab Location:
DO NOT SCALE DRAWING

	NAME
DRAWN BY	
SMB	M.Mohammadtabar
CHECKED BY	S.Ghaemi
Speed Code	
MecE Job #	
File Name:	Bottom of channel 2_v1

mm6
Wednesday, November 05, 2014 10:34:29 PM
Wednesday, September 24, 2014 11:01:55 AM

The Department of Mechanical Engineering
UNIVERSITY OF ALBERTA
TITLE:
Part B.1
SIZE B
Project: 60x10 flow loop facility
REV
SCALE: 1:10
Mass:
SHEET 1 OF 1

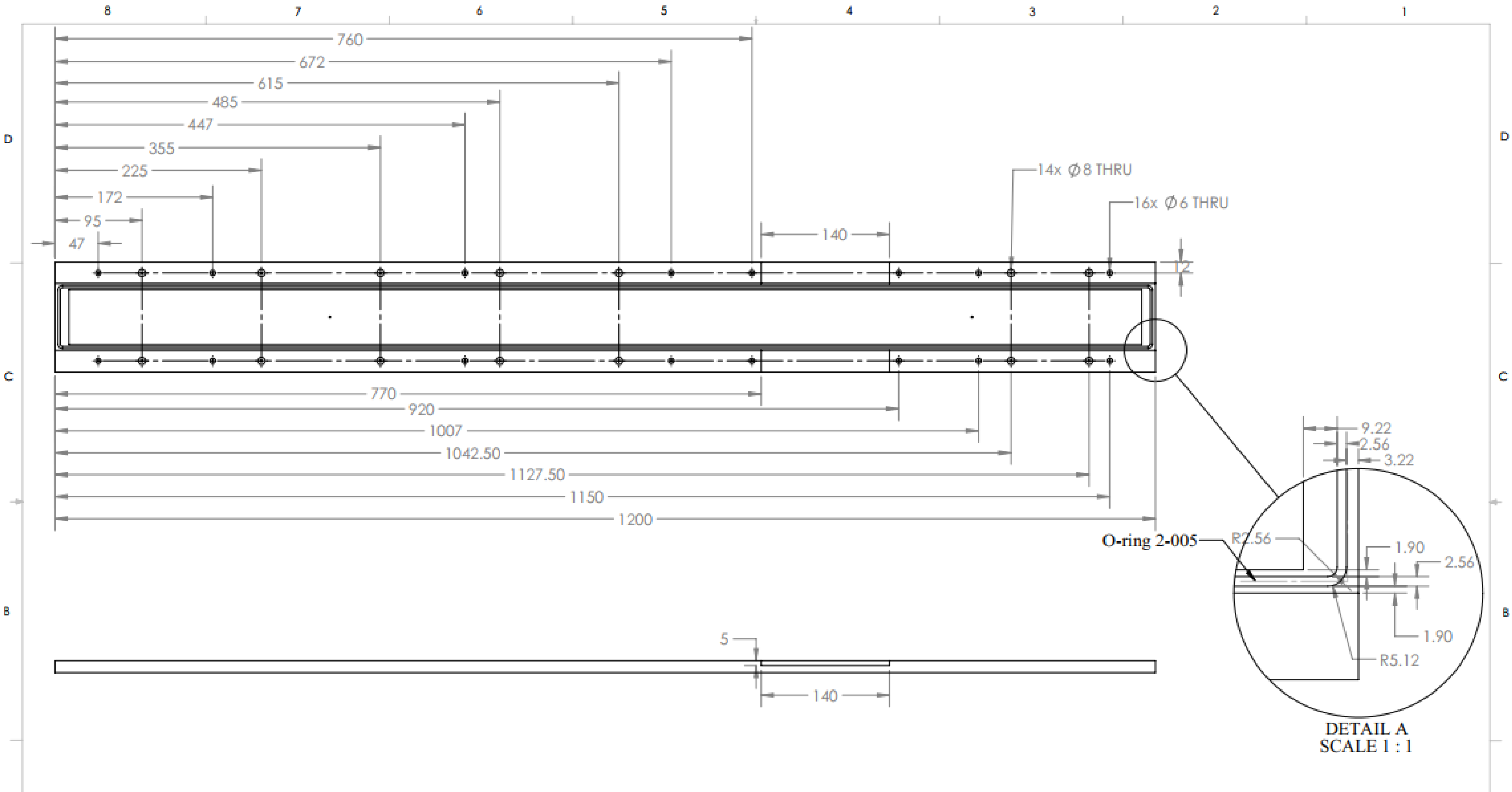

DETAIL A
SCALE 1 : 1

Ghaemi Lab
Contact:
Email:
Phone:
Comments:

UNLESS OTHERWISE SPECIFIED:
DIMENSIONS ARE IN MM
TOLERANCES:
ANGULAR: ± 0.5°
.X = ± 0.25
.XX = ± 0.05
SURFACE FINISH µm 0.6
MATERIAL:
Cast Acrylic
Lab Location:
DO NOT SCALE DRAWING

	NAME
DRAWN BY	
SMB	M.Mohammadtabar
CHECKED BY	S.Ghaemi
Speed Code	
MecE Job #	
File Name:	Bottom of channel 2_v1

mm6
Wednesday, November 05, 2014 10:34:29 PM
Wednesday, September 24, 2014 11:01:[illegible]

The Department of Mechanical Engineering
UNIVERSITY OF ALBERTA

TITLE:
Part B.1

SIZE
B
Project:
60x10 flow loop facility
REV
SCALE: 1:10
Mass:
SHEET 1 OF 1

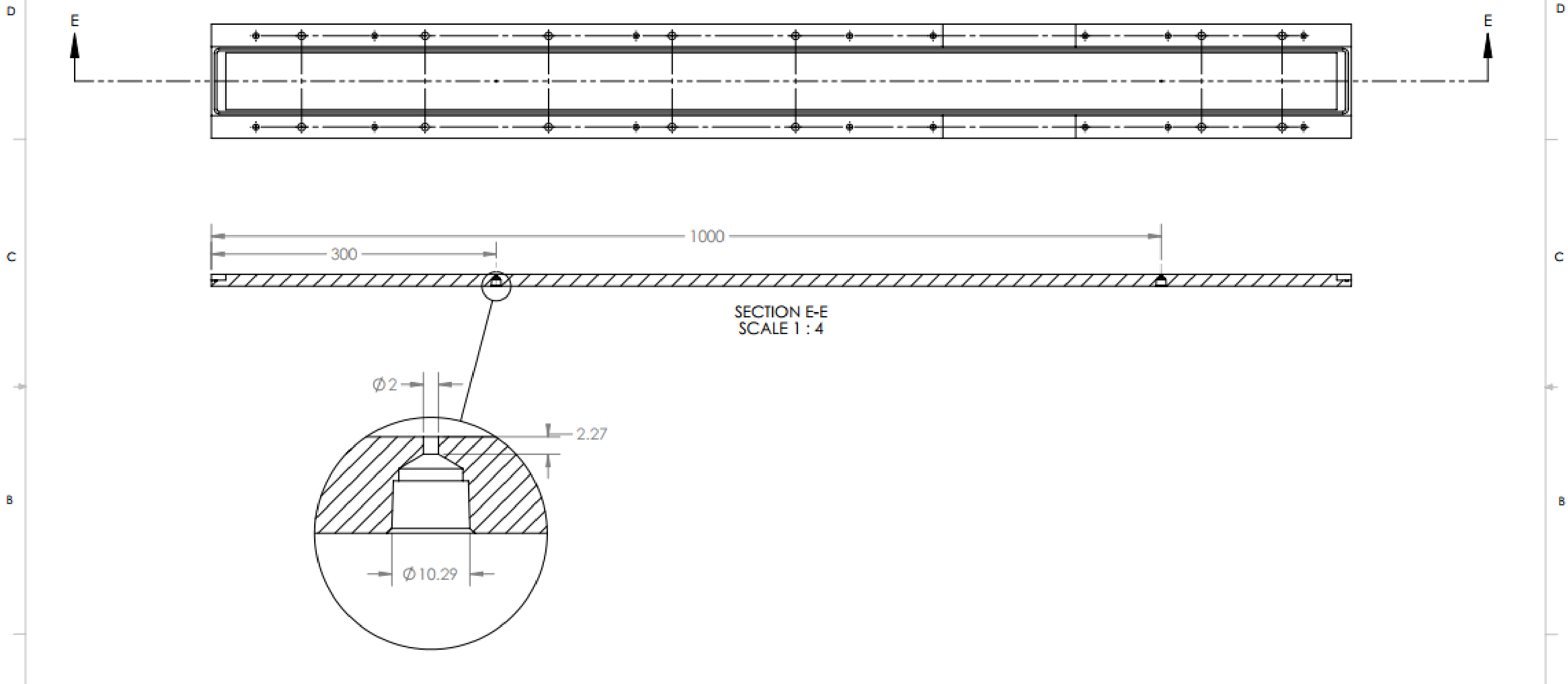

DETAIL G
SCALE 2 : 1

Ghaemi Lab	UNLESS OTHERWISE SPECIFIED:		NAME	The Department of Mechanical Engineering UNIVERSITY OF ALBERTA
Contact:	DIMENSIONS ARE IN MM TOLERANCES: ANGULAR: ± 0.5° .X = ± 0.25 .XX = ± 0.05	DRAWN BY		TITLE: Part B.1
Email:		SMB	M.Mohammadtabar	
Phone:		CHECKED BY	S.Ghaemi	
Comments:	SURFACE FINISH µm 0.6	Speed Code		
	MATERIAL: Cast Acrylic	MecE Job #		
		File Name:	bottom of channel 2_v1	SIZE B Project: 60x10 flow loop facility REV
	Lab Location:	mm6 Wednesday, November 05, 2014 10:34:29 PM Wednesday, September 24, 2014 11:01:55 AM		
	DO NOT SCALE DRAWING			SCALE: 1:10 Mass: SHEET 1 OF 1

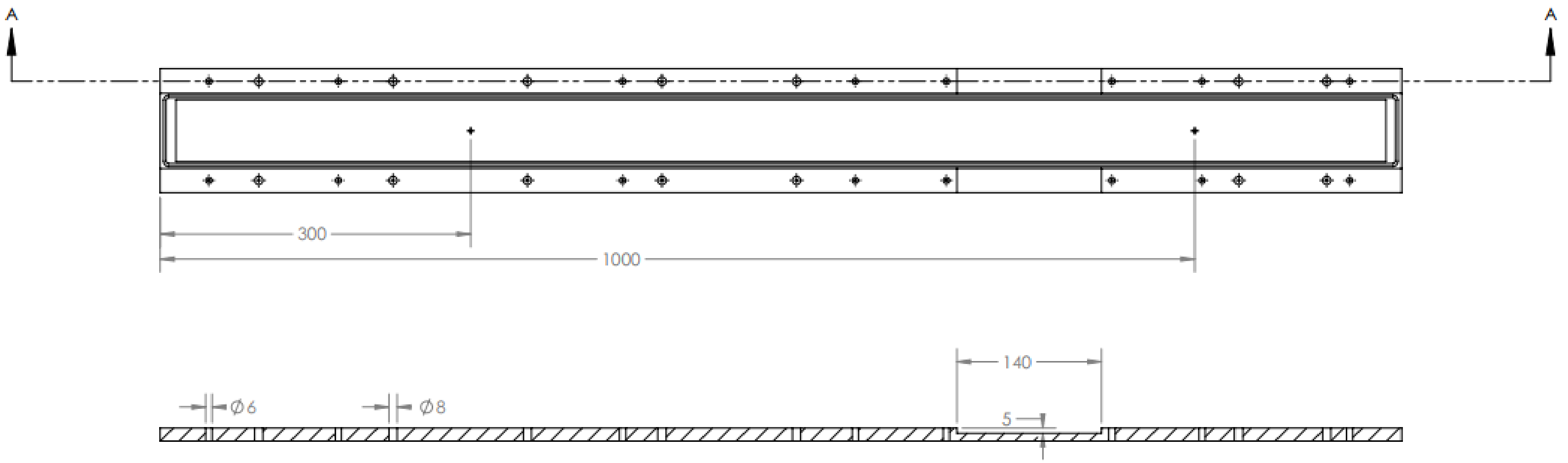

SECTION A-A
SCALE 1 : 4

Ghaemi Lab
Contact:
Email:
Phone:
Comments:

UNLESS OTHERWISE SPECIFIED:
DIMENSIONS ARE IN MM
TOLERANCES:
ANGULAR: ± 0.5°
.X = ± 0.25
.XX = ± 0.05
SURFACE FINISH µm 0.6
MATERIAL:
Cast Acrylic
Lab Location:
DO NOT SCALE DRAWING

	NAME
DRAWN BY	
SMB	M.Mohammadtabar
CHECKED BY	S.Ghaemi
Speed Code	
MecE Job #	
File Name:	Bottom of channel 2_v1

mm6
Wednesday, November 05, 2014 10:34:29 PM
Wednesday, September 24, 2014 11:01:[illegible] AM

The Department of Mechanical Engineering
UNIVERSITY OF ALBERTA

TITLE:
Part B.1

SIZE B
Project:
60x10 flow loop facility
REV
SCALE: 1:10
Mass:
SHEET 1 OF 1

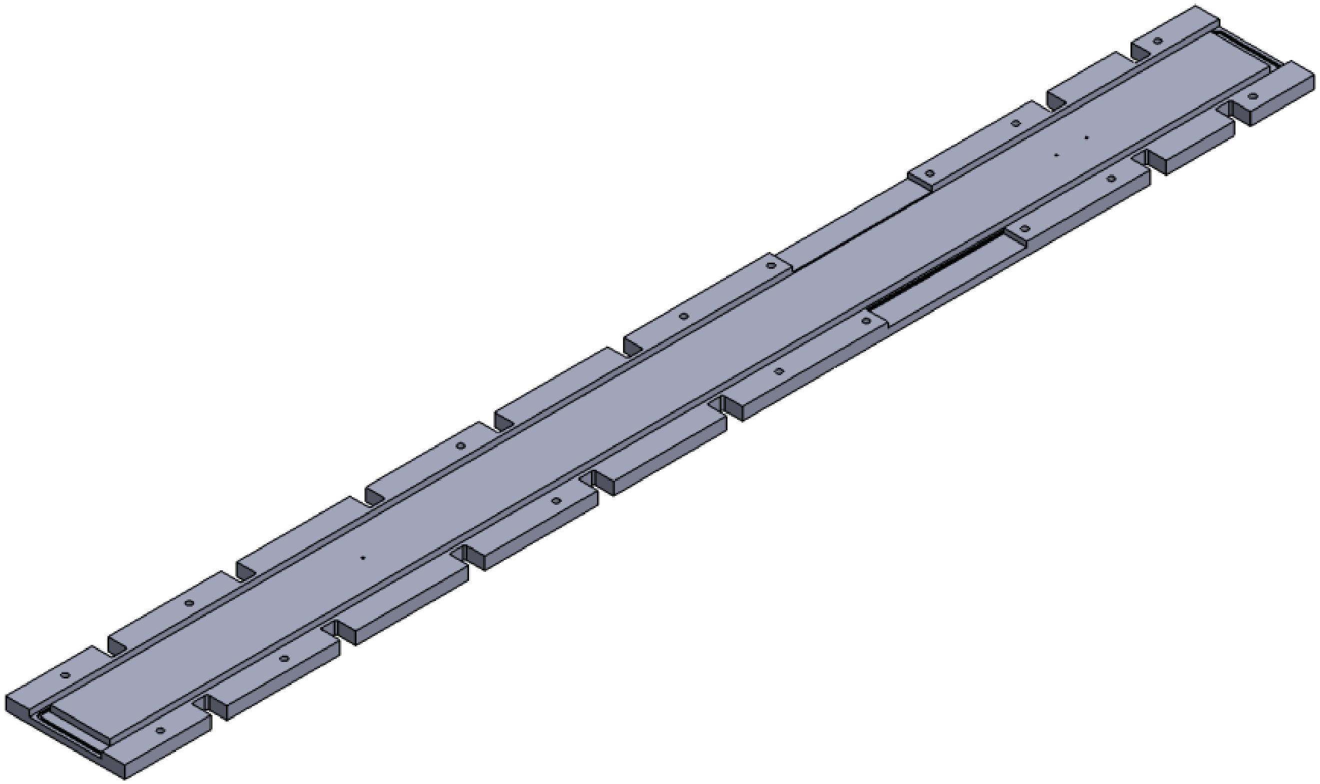

Ghaemi Lab	UNLESS OTHERWISE SPECIFIED:		NAME	The Department of Mechanical Engineering UNIVERSITY OF ALBERTA
Contact:	DIMENSIONS ARE IN MM TOLERANCES: ANGULAR: ± 0.5° .X = ± 0.25 .XX = ± 0.05	DRAWN BY		TITLE: Part B.3
Email:		SMB	M.Mohammadtabar	
Phone:		CHECKED BY	S.Ghaemi	
Comments:	SURFACE FINISH µm 0.6	Speed Code		
	MATERIAL: Cast Acrylic	MecE Job #		
		File Name:	Top of channel 3_v1	SIZE B · Project: 60x10 flow loop facility · REV
	Lab Location:	mm6 Wednesday, October 29, 2014 4:16:13 PM Saturday, September 27, 2014 5:13:04 PM		
	DO NOT SCALE DRAWING			SCALE: 1:10 · Mass: · SHEET 1 OF 1

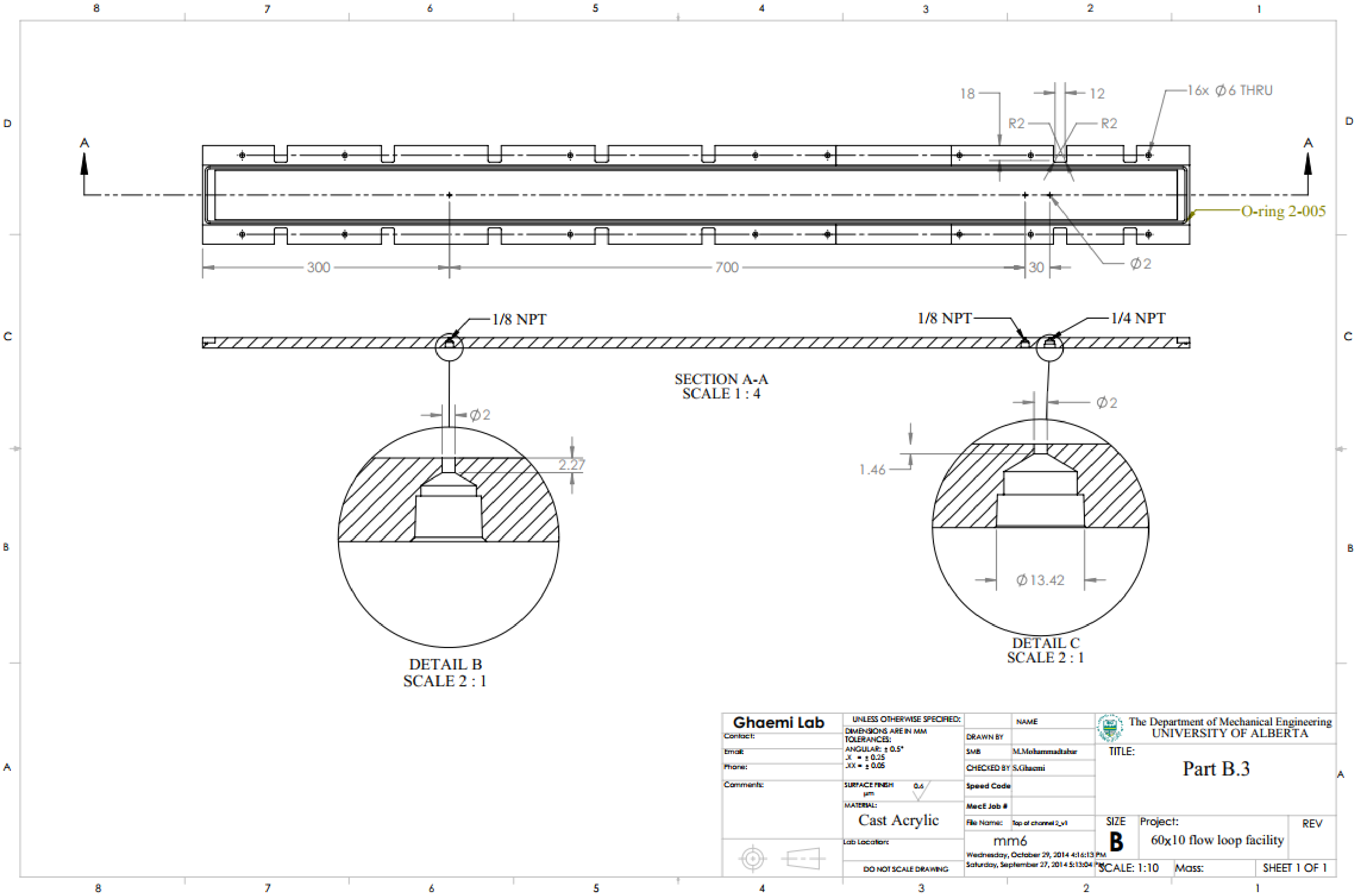

Ghaemi Lab	UNLESS OTHERWISE SPECIFIED:		NAME	The Department of Mechanical Engineering UNIVERSITY OF ALBERTA
Contact:	DIMENSIONS ARE IN MM TOLERANCES: ANGULAR: ± 0.5° .X = ± 0.25 .XX = ± 0.05	DRAWN BY		TITLE: Part B.3
Email:		SMB	M.Mohammadtabar	
Phone:		CHECKED BY	S.Ghaemi	
Comments:	SURFACE FINISH µm 0.6	Speed Code		
	MATERIAL: Cast Acrylic	MecE Job #		
		File Name:	Top of channel 3_v1	SIZE B
	Lab Location:	mm6		Project: 60x10 flow loop facility
	DO NOT SCALE DRAWING	Wednesday, October 29, 2014 4:16:13 PM Saturday, September 27, 2014 5:13:04 PM		SCALE: 1:10

REV

Mass:

SHEET 1 OF 1

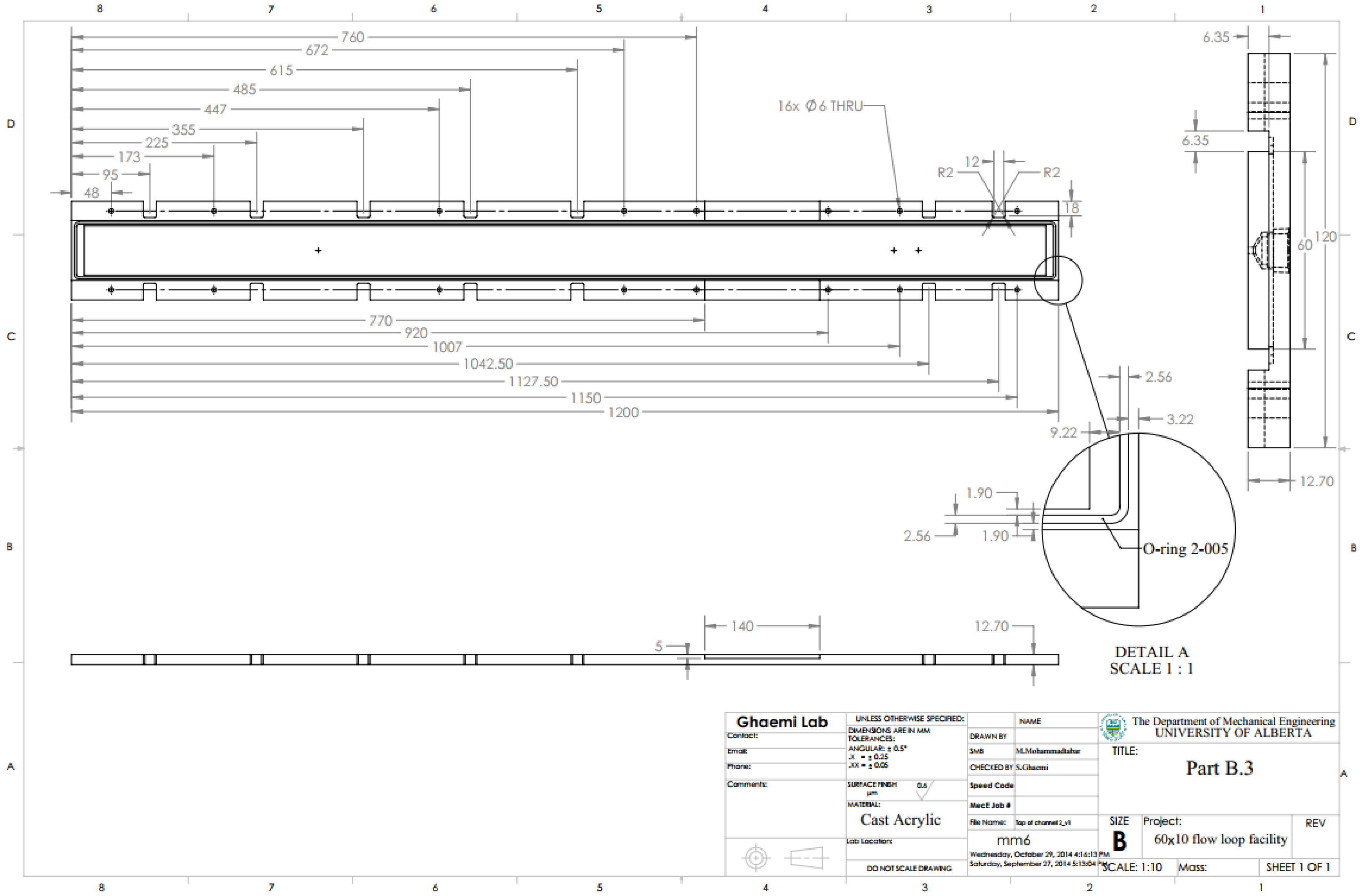

Ghaemi Lab
Contact:
Email:
Phone:
Comments:

UNLESS OTHERWISE SPECIFIED:
DIMENSIONS ARE IN MM
TOLERANCES:
ANGULAR: ± 0.5°
.X = ± 0.25
.XX = ± 0.05
SURFACE FINISH µm 0.6
MATERIAL:
Cast Acrylic
Lab Location:
DO NOT SCALE DRAWING

	NAME
DRAWN BY	
SMB	M.Mohammadtabar
CHECKED BY	S.Ghaemi
Speed Code	
MecE Job #	
File Name:	Top of channel 2_v1

mm6
Wednesday, October 29, 2014 4:16:13 PM
Saturday, September 27, 2014 5:13:04 PM

The Department of Mechanical Engineering
UNIVERSITY OF ALBERTA
TITLE:
Part B.3
SIZE B
Project: 60x10 flow loop facility
REV
SCALE: 1:10
Mass:
SHEET 1 OF 1

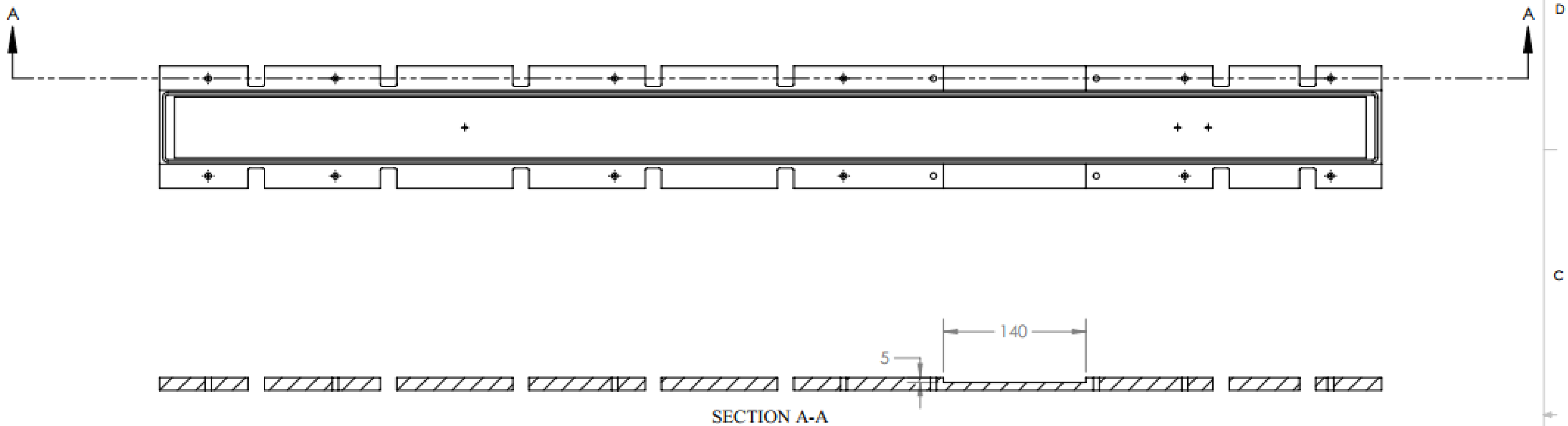

SECTION A-A
SCALE 1 : 4

Ghaemi Lab
Contact:
Email:
Phone:
Comments:

UNLESS OTHERWISE SPECIFIED:
DIMENSIONS ARE IN MM
TOLERANCES:
ANGULAR: ± 0.5°
.X = ± 0.25
.XX = ± 0.05
SURFACE FINISH µm 0.6
MATERIAL:
Cast Acrylic
Lab Location:
DO NOT SCALE DRAWING

	NAME
DRAWN BY	
SMB	M.Mohammadtabar
CHECKED BY	S.Ghaemi
Speed Code	
MecE Job #	
File Name:	Top of channel 2_v1

mm6
Wednesday, October 29, 2014 4:16:13 PM
Saturday, September 27, 2014 5:13:04 PM

The Department of Mechanical Engineering
UNIVERSITY OF ALBERTA

TITLE:
Part B.3

SIZE
B
Project:
60x10 flow loop facility
REV
SCALE: 1:10
Mass:
SHEET 1 OF 1

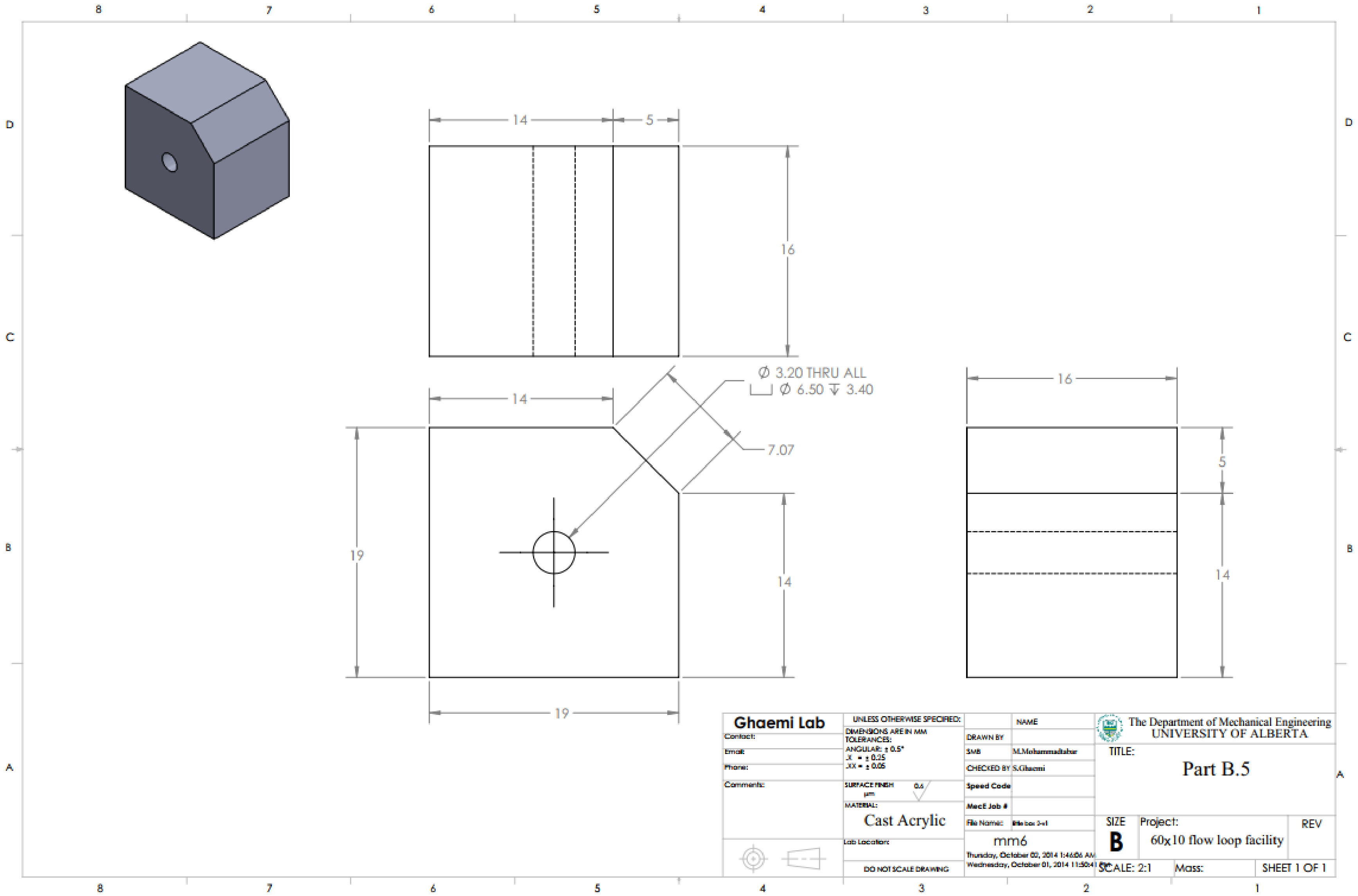

Ghaemi Lab
Contact:
Email:
Phone:
Comments:

UNLESS OTHERWISE SPECIFIED:
DIMENSIONS ARE IN MM
TOLERANCES:
ANGULAR: ± 0.5°
.X = ± 0.25
.XX = ± 0.05
SURFACE FINISH µm 0.6
MATERIAL:
Cast Acrylic
Lab Location:
DO NOT SCALE DRAWING

	NAME
DRAWN BY	
SMB	M.Mohammadtabar
CHECKED BY	S.Ghaemi
Speed Code	
MecE Job #	
File Name:	little box 3-v1

mm6
Thursday, October 02, 2014 1:46:06 AM
Wednesday, October 01, 2014 11:50:41 PM

The Department of Mechanical Engineering
UNIVERSITY OF ALBERTA

TITLE:
Part B.5

SIZE
B
Project:
60x10 flow loop facility
REV
SCALE: 2:1
Mass:
SHEET 1 OF 1

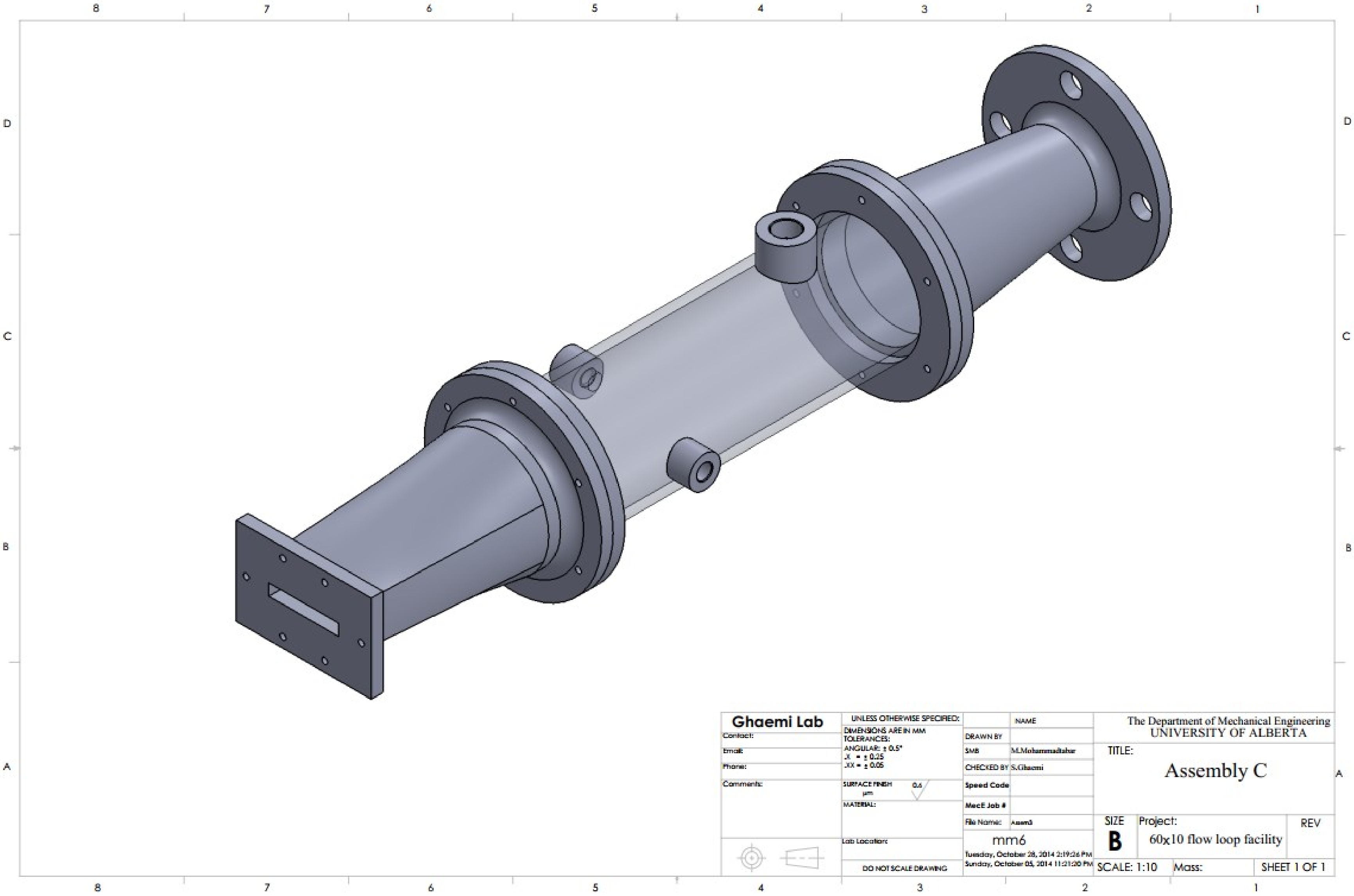

Ghaemi Lab
Contact:
Email:
Phone:
Comments:

UNLESS OTHERWISE SPECIFIED:
DIMENSIONS ARE IN MM
TOLERANCES:
ANGULAR: ± 0.5°
.X = ± 0.25
.XX = ± 0.05
SURFACE FINISH µm 0.6
MATERIAL:
Lab Location:
DO NOT SCALE DRAWING

	NAME
DRAWN BY	
SMB	M.Mohammadtaher
CHECKED BY	S.Ghaemi
Speed Code	
MecE Job #	
File Name:	Assem3

mm6
Tuesday, October 28, 2014 2:19:26 PM
Sunday, October 05, 2014 11:21:20 PM

The Department of Mechanical Engineering
UNIVERSITY OF ALBERTA

TITLE:
Assembly C

SIZE **B**
Project: 60x10 flow loop facility
REV
SCALE: 1:10
Mass:
SHEET 1 OF 1

ITEM NO.	PART NUMBER	DESCRIPTION	QTY.
C.1	Contraction to test section		1
C.2	Flange for pipe		2
C.3	Thread_O_let 1 to 4		1
C.4	Buffer zone 2		2
C.5	Thread_O_let 1 to 2		1
C.6	Contraction to pipe		1

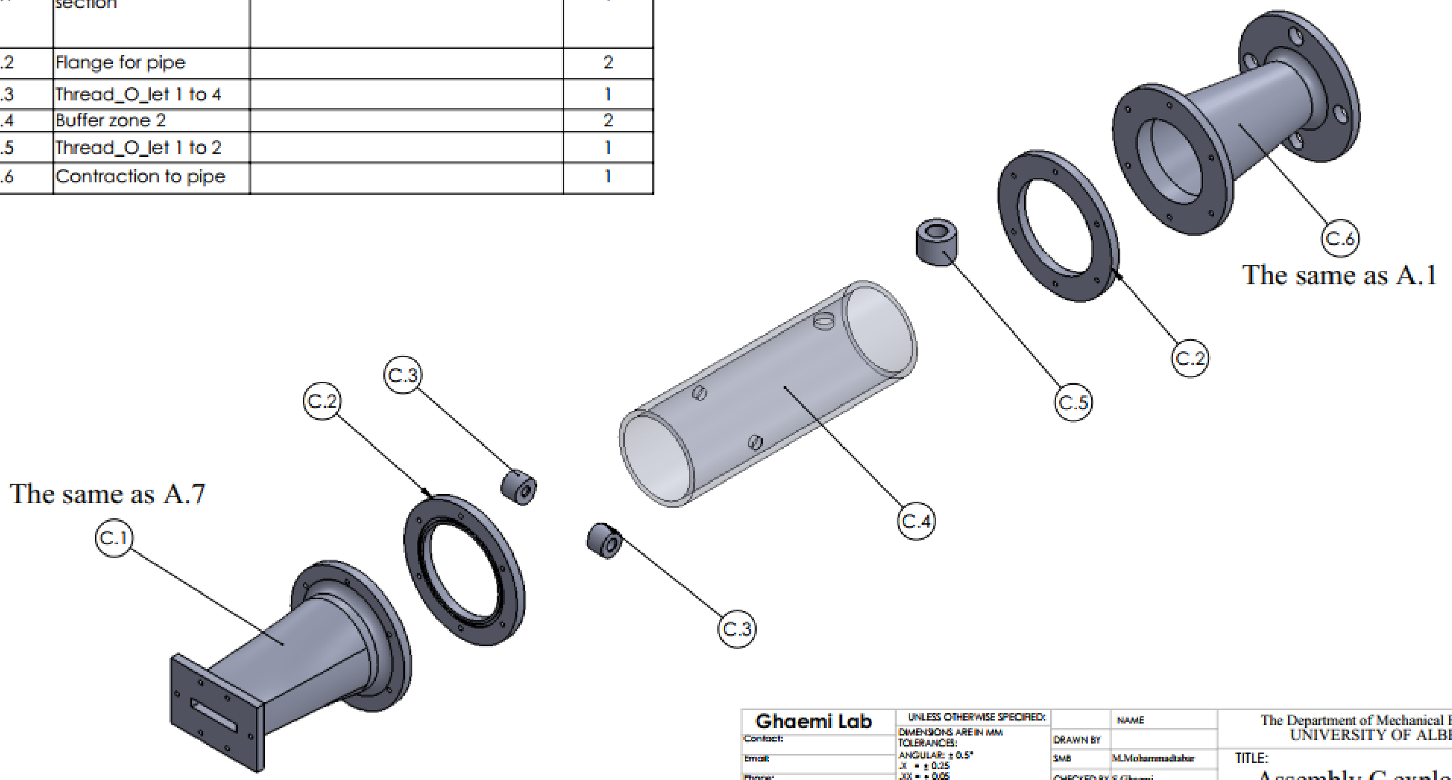

Ghaemi Lab Contact: Email: Phone: Comments:	UNLESS OTHERWISE SPECIFIED: DIMENSIONS ARE IN MM TOLERANCES: ANGULAR: ± 0.5° .X = ± 0.25 .XX = ± 0.05 SURFACE FINISH µm 0.6 MATERIAL: Lab Location: DO NOT SCALE DRAWING	NAME DRAWN BY SMB M.Mohammadtabar CHECKED BY S.Ghaemi Speed Code MecE Job # File Name: Assem3-exploded mm6 Tuesday, October 28, 2014 2:19:35 PM Sunday, October 05, 2014 11:21:20 PM	The Department of Mechanical Engineering UNIVERSITY OF ALBERTA TITLE: Assembly C exploded SIZE B Project: 60x10 flow loop facility REV SCALE: 1:20 Mass: SHEET 1 OF 1

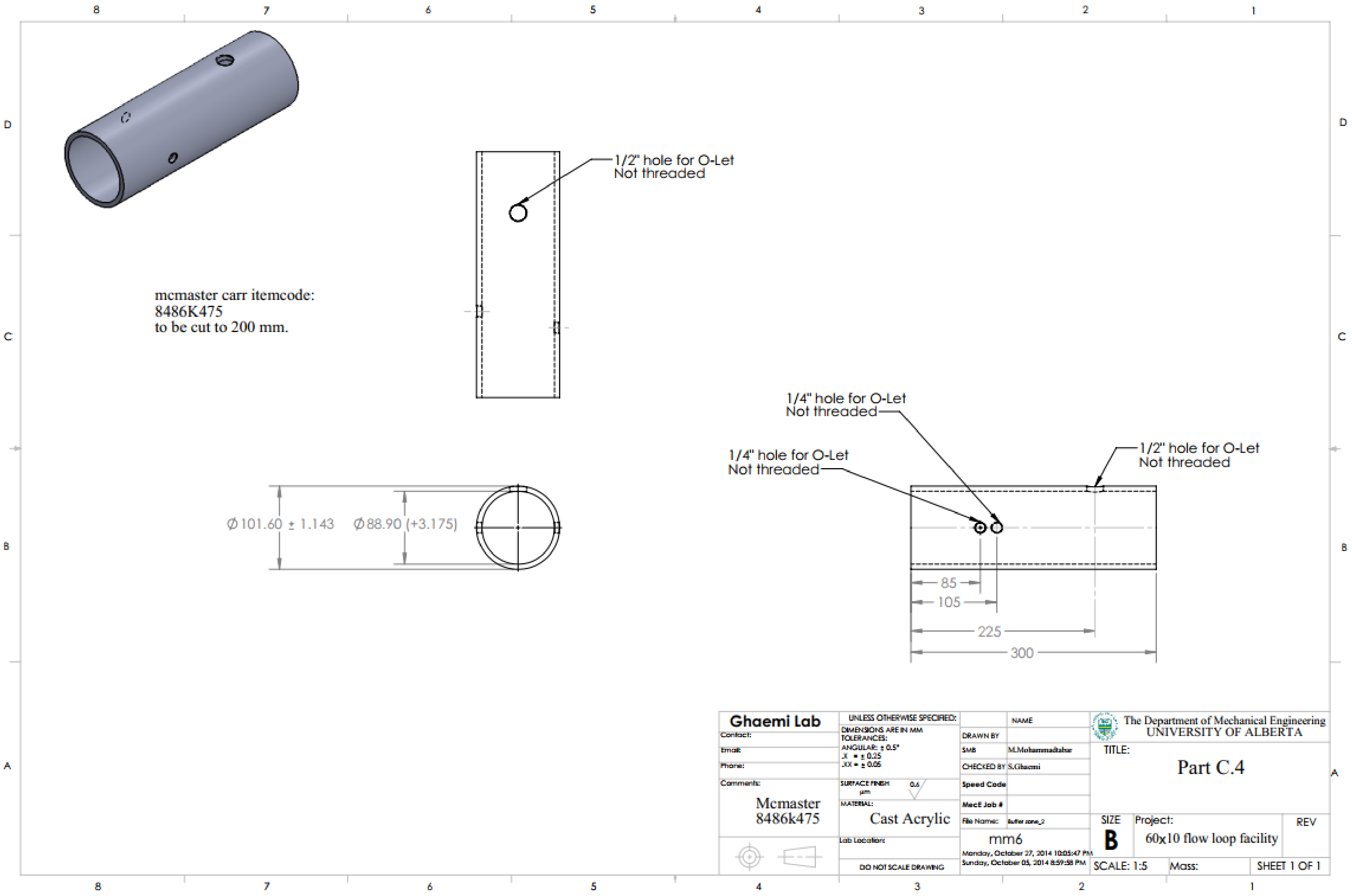

mcmaster carr itemcode:
8486K475
to be cut to 200 mm.

Ghaemi Lab
Contact:
Email:
Phone:
Comments:
Mcmaster
8486k475

UNLESS OTHERWISE SPECIFIED:
DIMENSIONS ARE IN MM
TOLERANCES:
ANGULAR: ± 0.5°
.X = ± 0.25
.XX = ± 0.05
SURFACE FINISH µm 0.6
MATERIAL:
Cast Acrylic
Lab Location:
DO NOT SCALE DRAWING

	NAME
DRAWN BY	
SMB	M.Mohammadtabar
CHECKED BY	S.Ghaemi
Speed Code	
MecE Job #	
File Name:	buffer zone_2

mm6
Monday, October 27, 2014 10:05:47 PM
Sunday, October 05, 2014 8:59:58 PM

The Department of Mechanical Engineering
UNIVERSITY OF ALBERTA
TITLE:
Part C.4
SIZE
B
Project:
60x10 flow loop facility
REV
SCALE: 1:5
Mass:
SHEET 1 OF 1

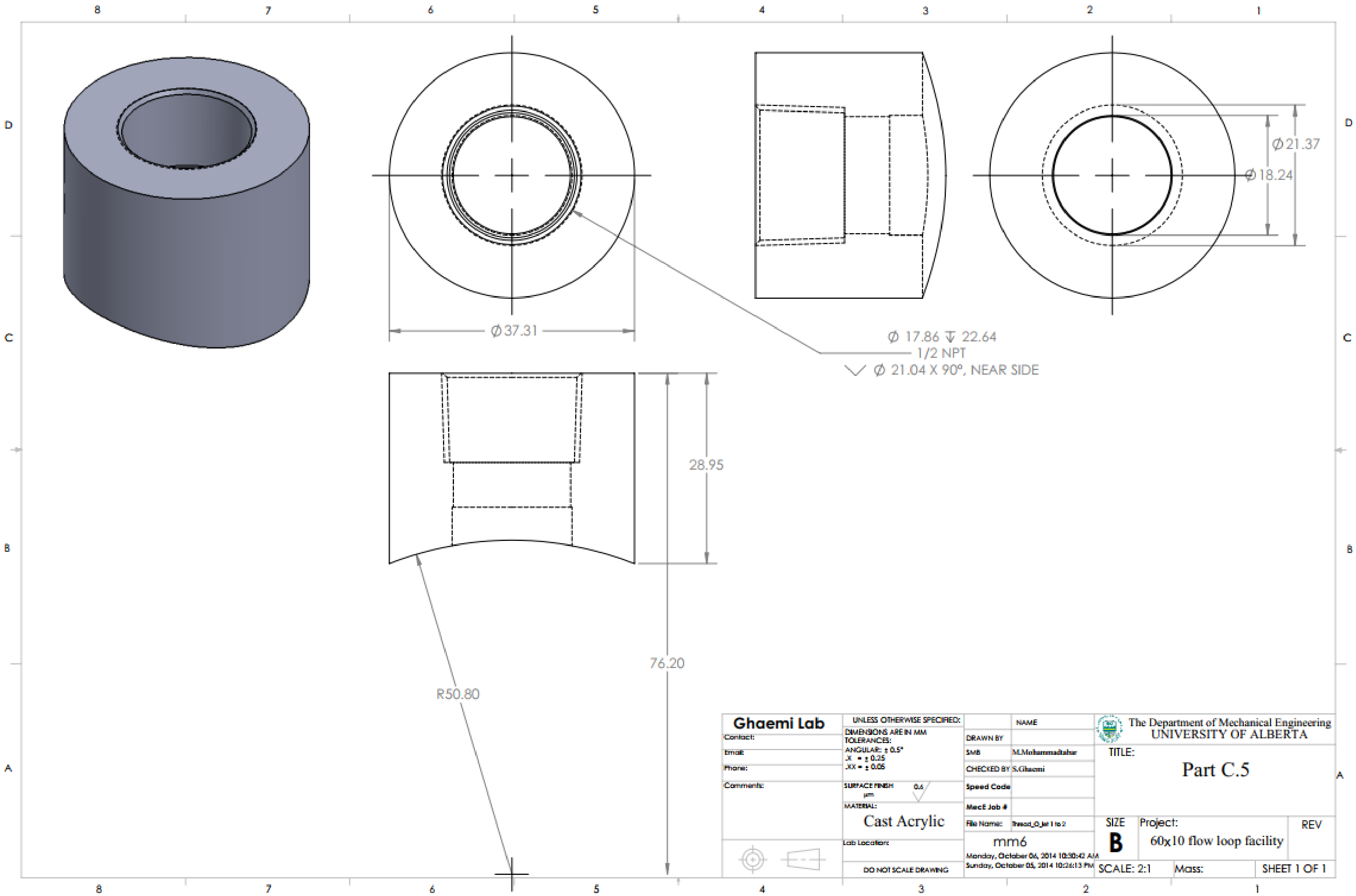

Ghaemi Lab
Contact:
Email:
Phone:
Comments:

UNLESS OTHERWISE SPECIFIED:
DIMENSIONS ARE IN MM
TOLERANCES:
ANGULAR: ± 0.5°
.X = ± 0.25
.XX = ± 0.05
SURFACE FINISH µm 0.6
MATERIAL:
Cast Acrylic
Lab Location:
DO NOT SCALE DRAWING

	NAME
DRAWN BY	
SMB	M.Mohammadtabar
CHECKED BY	S.Ghaemi
Speed Code	
MecE Job #	
File Name:	Thread_O_Jet 1 to 2

mm6
Monday, October 06, 2014 10:30:42 AM
Sunday, October 05, 2014 10:26:13 PM

The Department of Mechanical Engineering
UNIVERSITY OF ALBERTA

TITLE:
Part C.5

SIZE
B
Project:
60x10 flow loop facility
REV
SCALE: 2:1
Mass:
SHEET 1 OF 1

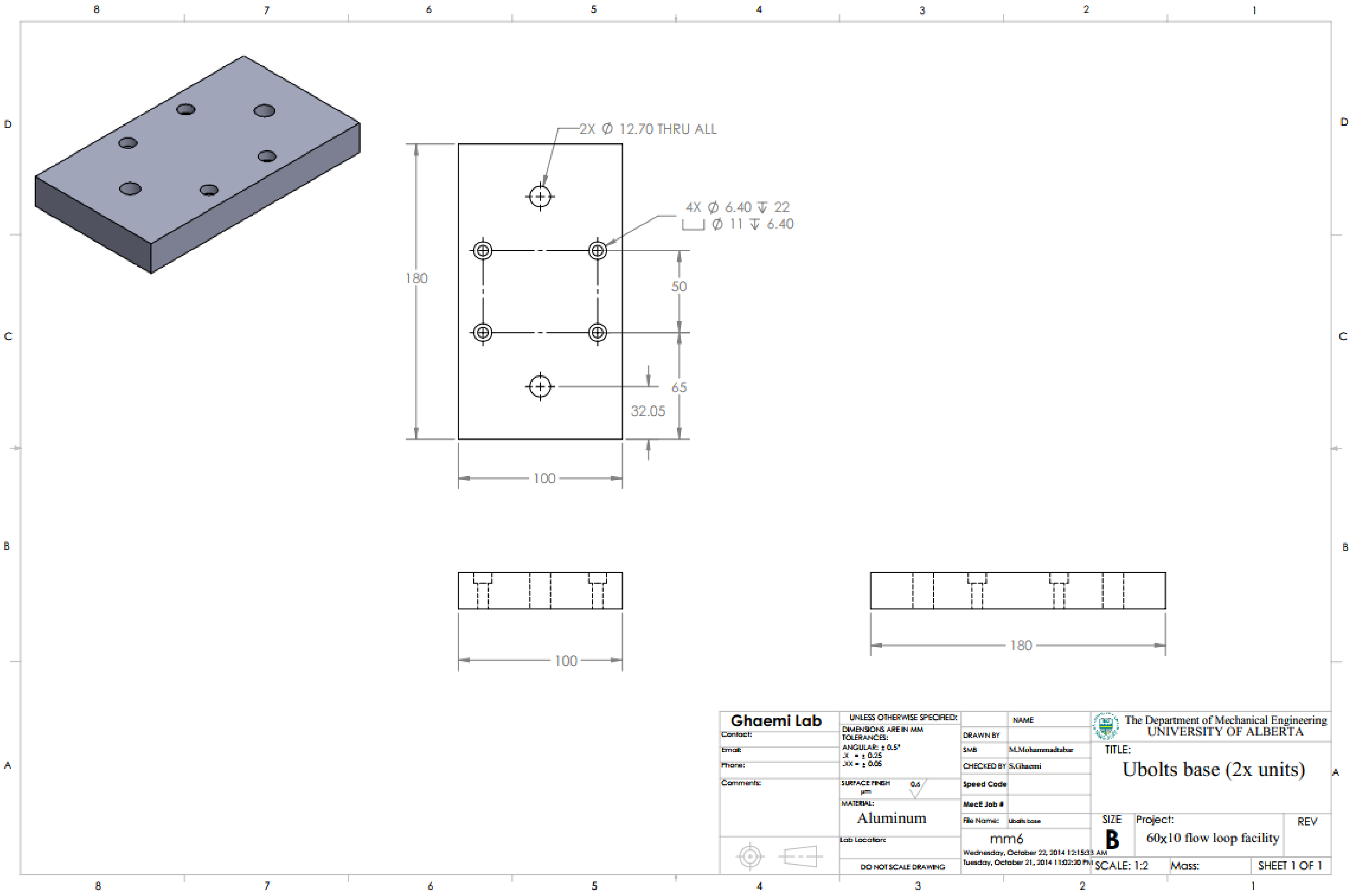
2X ⌀ 12.70 THRU ALL
4X ⌀ 6.40 ↧ 22
⌴ ⌀ 11 ↧ 6.40
180
50
65
32.05
100
100
180
Ghaemi Lab
Contact:
Email:
Phone:
Comments:
UNLESS OTHERWISE SPECIFIED:
DIMENSIONS ARE IN MM
TOLERANCES:
ANGULAR: ± 0.5°
.X = ± 0.25
.XX = ± 0.05
SURFACE FINISH µm
0.6
MATERIAL:
Aluminum
Lab Location:
DO NOT SCALE DRAWING
NAME
DRAWN BY
SMB M.Mohammadtabar
CHECKED BY S.Ghaemi
Speed Code
MecE Job #
File Name: Ubolts base
mm6
Wednesday, October 22, 2014 12:15:33 AM
Tuesday, October 21, 2014 11:02:20 PM
The Department of Mechanical Engineering
UNIVERSITY OF ALBERTA
TITLE:
Ubolts base (2x units)
SIZE
B
Project:
60x10 flow loop facility
REV
SCALE: 1:2
Mass:
SHEET 1 OF 1

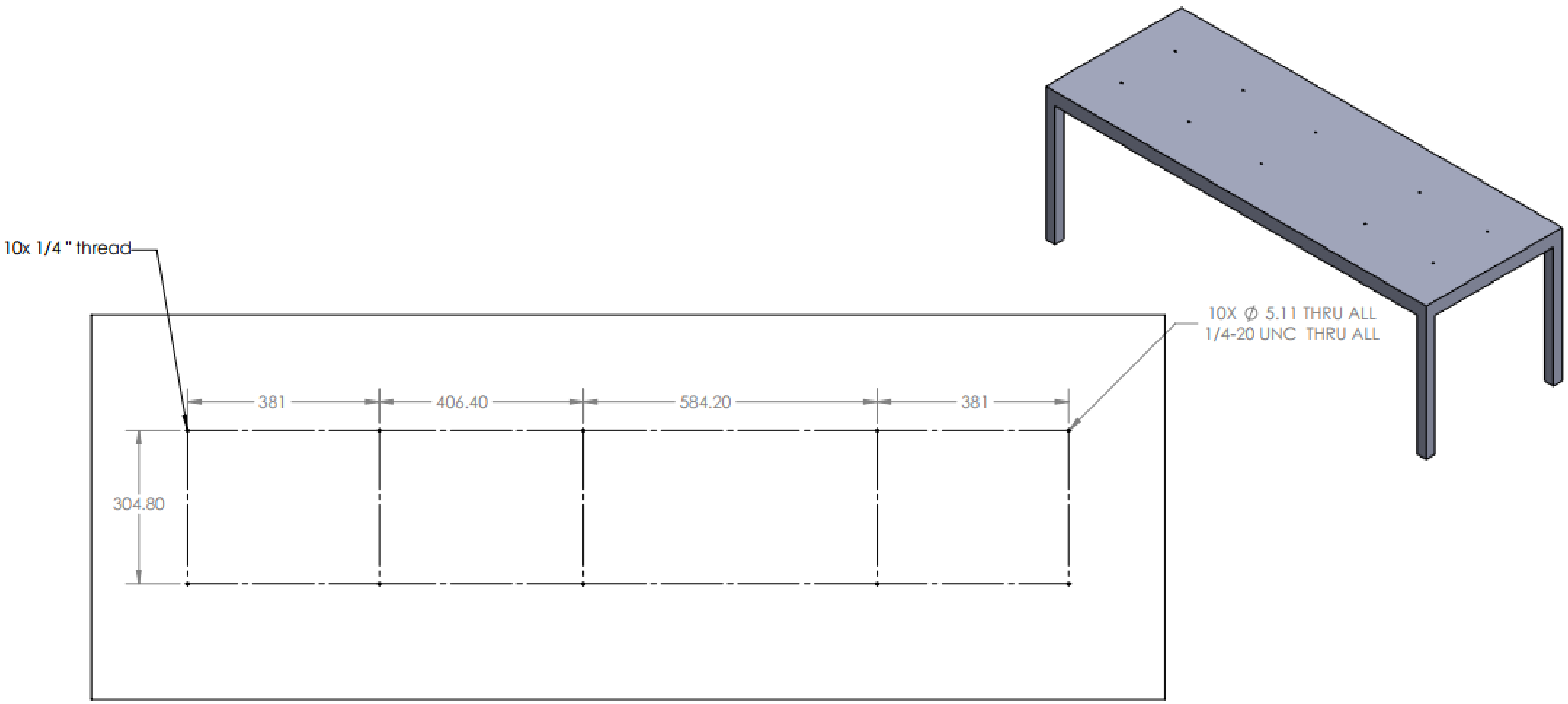

Ghaemi Lab

Contact:

Email:

Phone:

Comments:

UNLESS OTHERWISE SPECIFIED:

DIMENSIONS ARE IN MM

TOLERANCES:

ANGULAR: ± 0.5°

.X = ± 0.25

.XX = ± 0.05

SURFACE FINISH µm 0.6

MATERIAL:

Lab Location:

DO NOT SCALE DRAWING

	NAME
DRAWN BY	
SMB	M.Mohammadtaher
CHECKED BY	S.Ghaemi
Speed Code	
MecE Job #	
File Name:	hole on table

mm6

Tuesday, October 28, 2014 4:21:49 PM

Tuesday, October 28, 2014 2:51:40 PM

The Department of Mechanical Engineering
UNIVERSITY OF ALBERTA

TITLE:

Hole on the table

SIZE B

Project: 60x10 flow loop facility

REV

SCALE: 1:20

Mass:

SHEET 1 OF 1

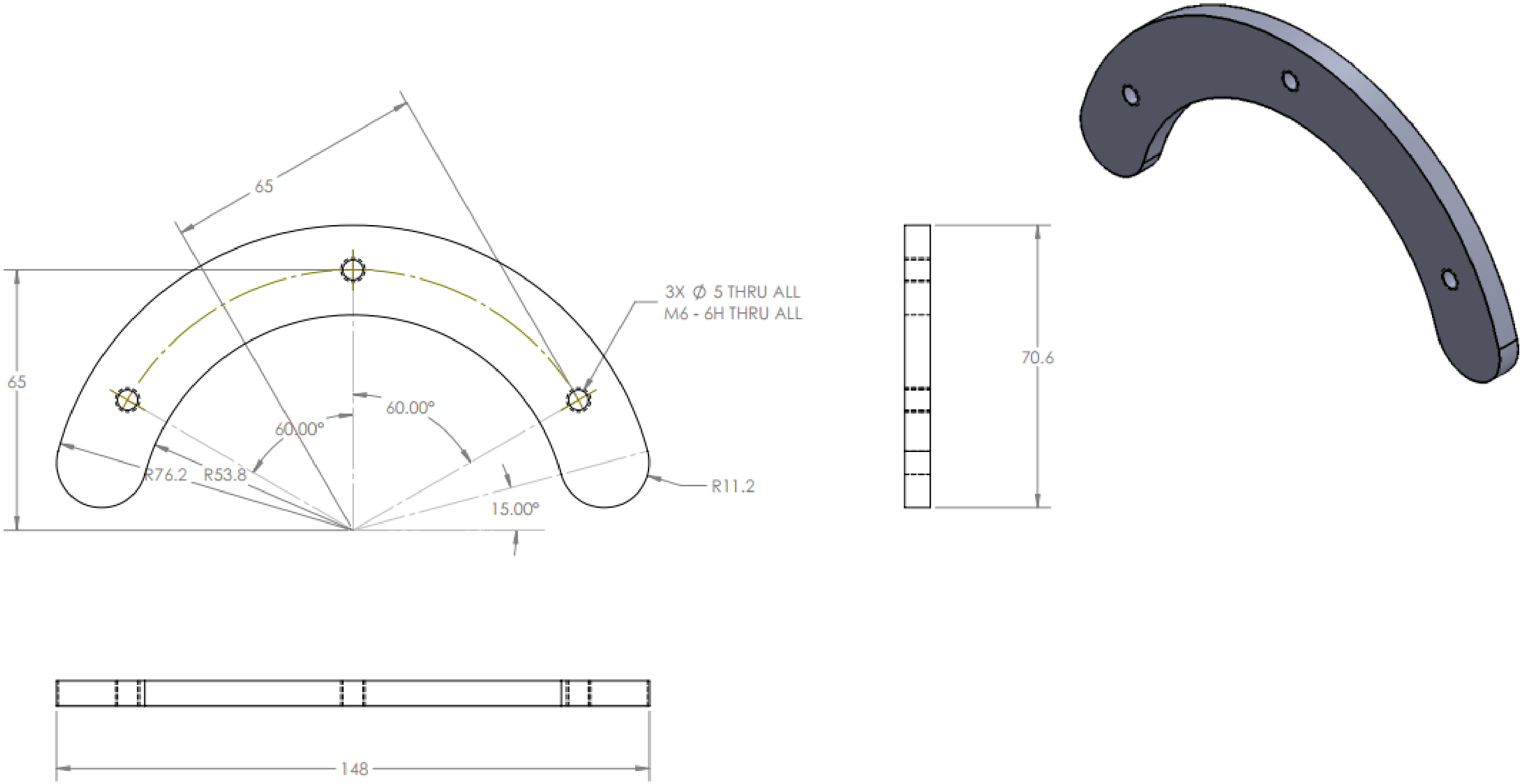

Ghaemi Lab
Contact:
Email:
Phone:
Comments:

UNLESS OTHERWISE SPECIFIED:
DIMENSIONS ARE IN MM
TOLERANCES:
ANGULAR: ± 0.5°
.X = ± 0.25
.XX = ± 0.05
SURFACE FINISH µm 0.6
MATERIAL:
Lab Location:
DO NOT SCALE DRAWING

	NAME
DRAWN BY	
SMB	M.Mohammadtabar
CHECKED BY	S.Ghaemi
Speed Code	
MecE Job #	
File Name:	Washer for contraction to test section

mm6
Friday, May 15, 2015 4:10:32 PM
Thursday, May 14, 2015 10:22:48 PM

The Department of Mechanical Engineering
UNIVERSITY OF ALBERTA

TITLE:
Washer for contraction to test section

SIZE B
Project: 60x10 flow loop facility
REV
SCALE: 1:1
Mass:
SHEET 1 OF 1

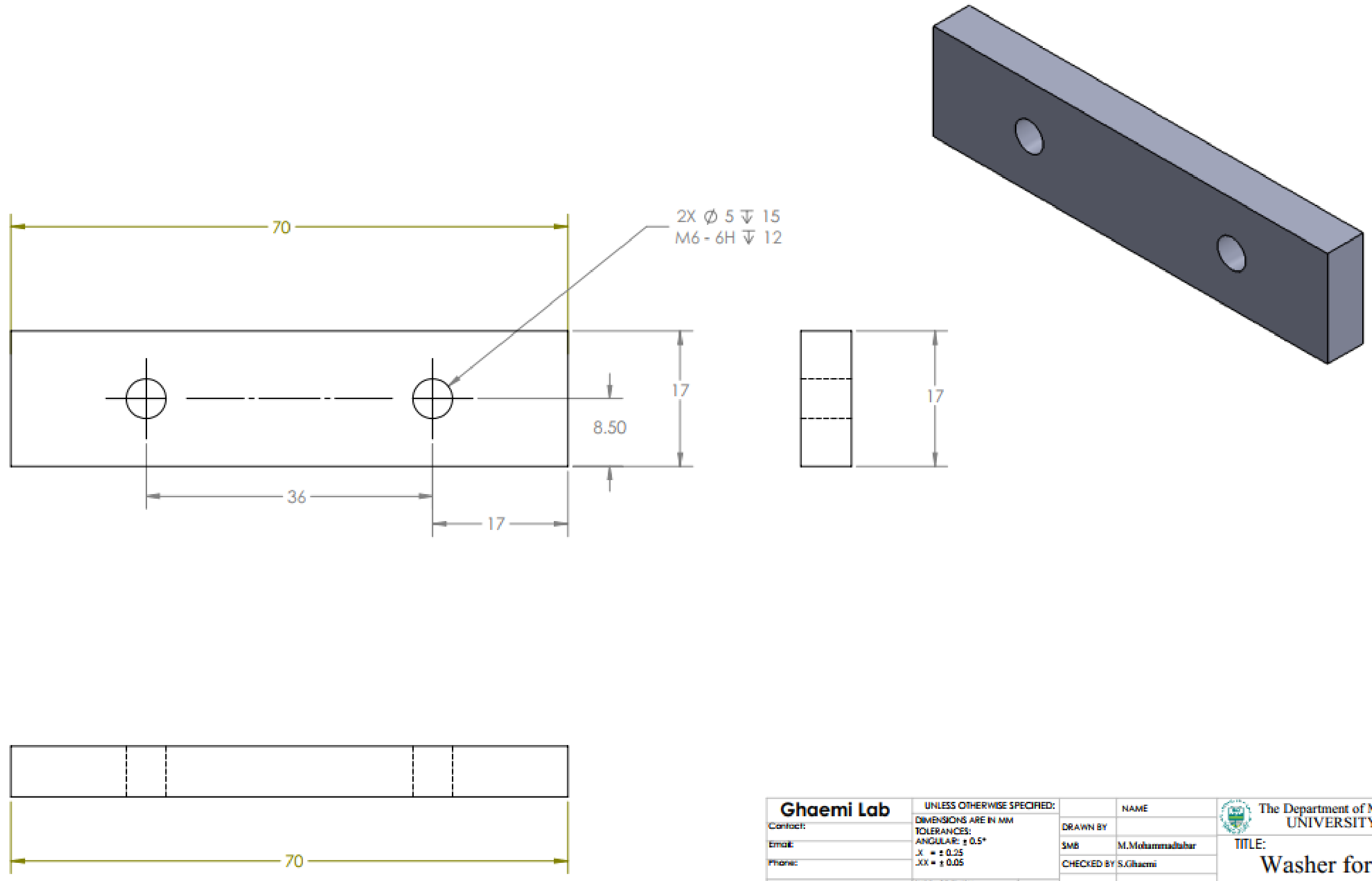

Ghaemi Lab
Contact:
Email:
Phone:
Comments:

UNLESS OTHERWISE SPECIFIED:
DIMENSIONS ARE IN MM
TOLERANCES:
ANGULAR: ± 0.5°
.X = ± 0.25
.XX = ± 0.05
SURFACE FINISH µm 0.6
MATERIAL:
Lab Location:
DO NOT SCALE DRAWING

	NAME
DRAWN BY	
SMB	M.Mohammadtabar
CHECKED BY	S.Ghaemi
Speed Code	
MecE Job #	
File Name:	Washer for end plate

mm6
Friday, May 15, 2015 3:02:22 PM
Thursday, May 14, 2015 7:56:09 PM

The Department of Mechanical Engineering
UNIVERSITY OF ALBERTA

TITLE:
Washer for end plate

SIZE **B**
Project: 60x10 flow loop facility
REV
SCALE: 2:1
Mass:
SHEET 1 OF 1

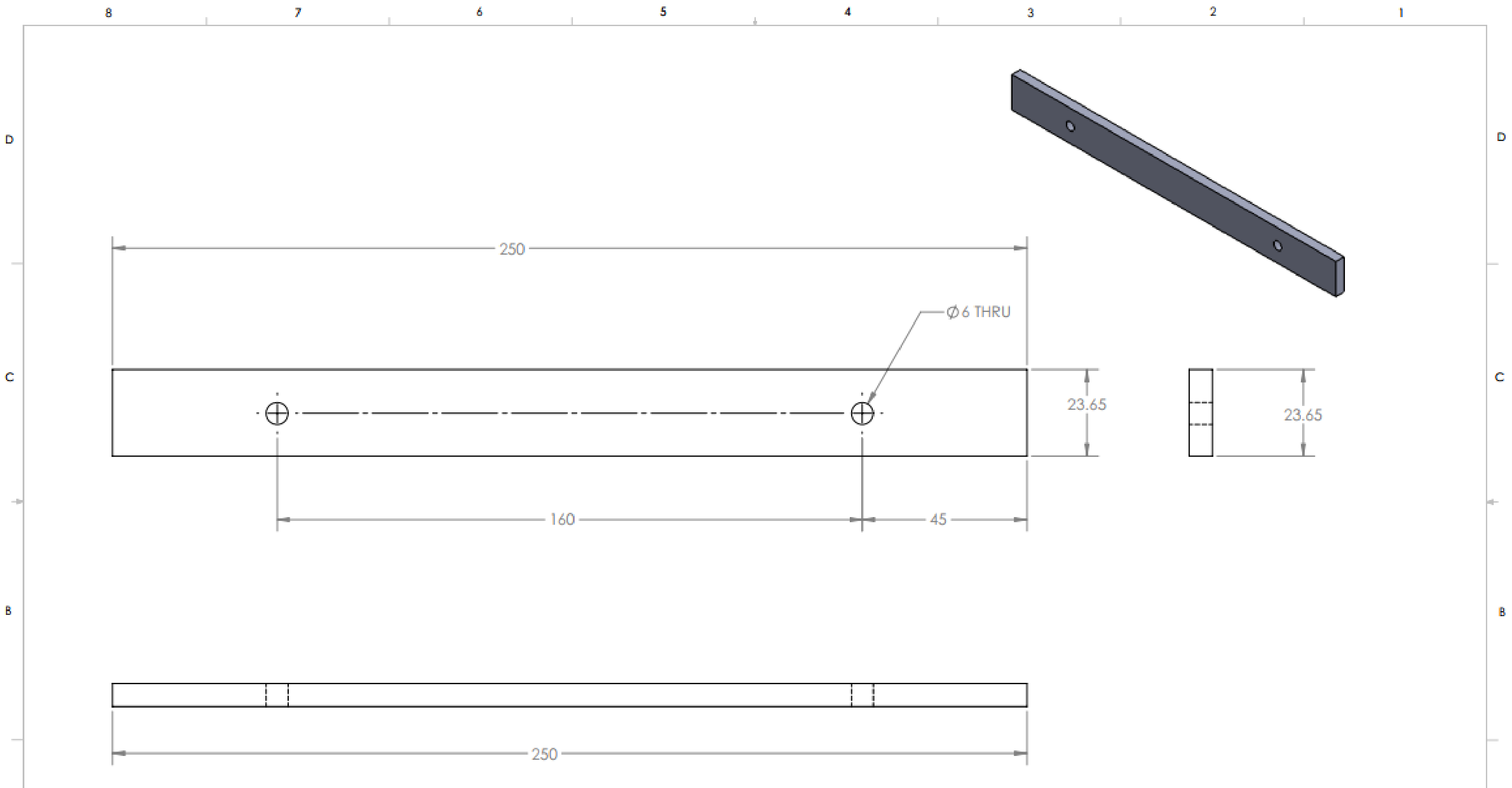

Ghaemi Lab	UNLESS OTHERWISE SPECIFIED:		NAME	The Department of Mechanical Engineering UNIVERSITY OF ALBERTA
Contact:	DIMENSIONS ARE IN MM TOLERANCES: ANGULAR: ± 0.5° .X = ± 0.25 .XX = ± 0.05	DRAWN BY		TITLE: Washer for Top plate
Email:		SMB	M.Mohammadtabar	
Phone:		CHECKED BY	S.Ghaemi	
Comments:	SURFACE FINISH µm 0.6	Speed Code		
	MATERIAL:	MecE Job #		
		File Name:	Washer for Top plate	SIZE B · Project: 60x10 flow loop facility · REV
	Lab Location:	mm6 Thursday, May 14, 2015 9:59:01 PM Thursday, May 14, 2015 8:28:27 PM		
	DO NOT SCALE DRAWING			SCALE: 1:2 · Mass: · SHEET 1 OF 1

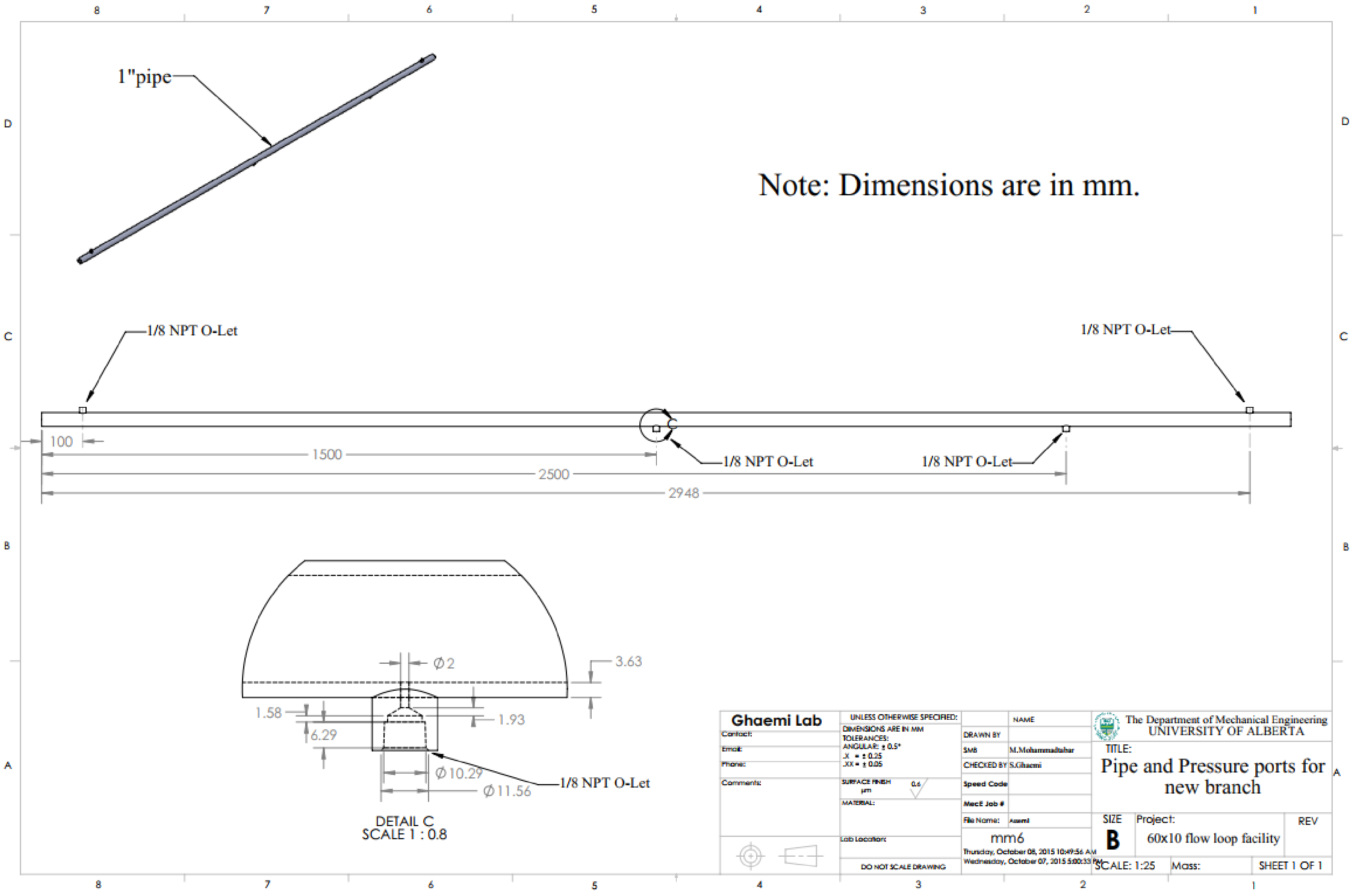

Ghaemi Lab
Contact:
Email:
Phone:
Comments:

UNLESS OTHERWISE SPECIFIED:
DIMENSIONS ARE IN MM
TOLERANCES:
ANGULAR: ± 0.5°
.X = ± 0.25
.XX = ± 0.05
SURFACE FINISH µm 0.6
MATERIAL:
Lab Location:
DO NOT SCALE DRAWING

	NAME
DRAWN BY	
SMB	M.Mohammadtabar
CHECKED BY	S.Ghaemi
Speed Code	
MecE Job #	
File Name:	Asemi

mm6
Thursday, October 08, 2015 10:49:56 AM
Wednesday, October 07, 2015 5:00:33 PM

The Department of Mechanical Engineering
UNIVERSITY OF ALBERTA

TITLE:
Pipe and Pressure ports for new branch

SIZE B
Project: 60x10 flow loop facility
REV
SCALE: 1:25
Mass:
SHEET 1 OF 1